Modelling, optimisation and scale up of a lab scale biomass solar gasifier

Houssame Boujjat

▶ **To cite this version:**

Houssame Boujjat. Modelling, optimisation and scale up of a lab scale biomass solar gasifier. Biotechnology. Université Grenoble Alpes [2020-..], 2020. English. NNT : 2020GRALI049 . tel-03426059

HAL Id: tel-03426059
https://theses.hal.science/tel-03426059

Submitted on 12 Nov 2021

HAL is a multi-disciplinary open access archive for the deposit and dissemination of scientific research documents, whether they are published or not. The documents may come from teaching and research institutions in France or abroad, or from public or private research centers.

L'archive ouverte pluridisciplinaire **HAL**, est destinée au dépôt et à la diffusion de documents scientifiques de niveau recherche, publiés ou non, émanant des établissements d'enseignement et de recherche français ou étrangers, des laboratoires publics ou privés.

THÈSE

Pour obtenir le grade de :

DOCTEUR DE L'UNIVERSITE GRENOBLE ALPES

Spécialité : **MÉCANIQUE DES FLUIDES, PROCÉDÉS, ÉNERGÉTIQUE**

Arrêté ministériel : 25 mai 2016

Présentée par :

« Houssame BOUJJAT »

Thèse dirigée par **Stéphane ABANADES, Directeur de recherche, CNRS-PROMES,** et codirigée par **Sylvain RODAT, Chargé de recherche, CNRS-PROMES et Valéry VUILLERME, Ingénieur Chercheur, CEA-GRENOBLE,** préparée au sein du **Laboratoire** des Systèmes Solaires et Thermodynamique (L2ST) du **CEA-GRENOBLE** dans **l'École Doctorale I-MEP2**

Modélisation, optimisation et extrapolation d'un réacteur solaire de gazéification de biomasse

Thèse soutenue publiquement le **«10/11/2020»**, devant le jury composé de :

M. Yann ROGAUME

Professeur, Université de Lorraine, Rapporteur

Mme. Claire COURSON

Maître de Conférences, Université de Strasbourg, Rapporteur

M. Guillain MAUVIEL

Professeur, Université de Lorraine, Président

M. Mustapha GOURMA

Associate Professor, Cranfield University, Examinateur

M. Stéphane ABANADES

Directeur de Recherche, CNRS-PROMES, Directeur de thèse

M. Sylvain RODAT

Chargé de Recherche, CNRS-PROMES, Encadrant de thèse

M. Valéry VUILLERME

Ingénieur Chercheur, CEA-GRENOBLE, Encadrant de thèse

M. Bruno GAGNEPAIN

Ingénieur, ADEME, Invité

DEDICATION

In memory of my father Mohammed.

To my lovely mother, Majida, who is the most important person in my life, for her unconditional love and care. Thank you for being the secret to my lifelong success. What a wonderful mom you are!

To my best friend and sister Wiame who inspires and encourages me. Thank you for giving me moral support, love and encouragement to do my research work successfully.

To my Uncle Ibrahim and his wife Fatima. I wish them long life.

To my family and my cousins for their sincere love.

To all my friends.

ACKOWLEDGMENT

I would like to express my sincere thanks and gratitude to my respected supervisors, Dr. Stéphane ABANADES, Dr. Sylvain RODAT and Dr. Valéry VUILLERME who have supported me during the journey of my Ph.D. I am most grateful to them for their constant help and excellent guidance that made my dissertation work possible. I extend my deep sense of indebtedness to them for their encouragement, high academic standards and achievements, constructive comments and mainly extensive motivation. Otherwise, this doctoral thesis would not have been possible without their support.

I express my warmest thanks to Nathalie DUPASSIEUX, head of the Laboratory of Solar Systems and Thermodynamics (L2ST) for her precious and most valuable support during my thesis.

I am very grateful to Dr. Bruno GAGNEPAIN from the French Environment and Energy Management Agency (ADEME) for his support and invaluable feedback on my research.

I extend my sincere thanks to all the members of PUMA3 laboratories (L2ST and LSED) of CEA-INES that enriched and encouraged me. Thank you for sharing your experience and knowledge with me!

I also warmly thank all the members of the Laboratory of Dry Process Thermoconversion of Carbonaceous Resources (L2CS) of CEA Grenoble and especially, Serge RAVEL, Marine PEYROT, Sylvie VALIN, Françoise DEFOORT and Christian PERRET for their availability, discussions and fruitful exchanges.

My gratitude goes to the honorable members of the Jury for agreeing to read the manuscript and to participate in the defense of this thesis. I would like to thank them very much for their extremely useful contribution.

I would like to thank also the University of Grenoble-Alpes (UGA) for giving me this great opportunity to carry out my doctoral research.

I must present my greatest thanks to ADEME for providing me with the funding support.

Finally, I wish to thank the wonderful administrative staff of CEA, INES, ADEME and UGA for being so helpful. I thank all those who contributed directly or indirectly to my dissertation.

RÉSUMÉ DE THÈSE

I.1 Introduction

Cette thèse vise à étudier un nouveau concept de gazéification solaire de l'échelle du laboratoire à l'échelle industrielle en combinant simulation numérique et expérimentation à haute température. Elle fait suite à la thèse de Q. Bellouard [1] (2014-2017) au cours de laquelle un premier réacteur solaire à jet a été conçu. Les premières expériences sur le réacteur ont montré des résultats très prometteurs qui confirment les avantages et les atouts de la technologie. Cependant, il reste un certain nombre de verrous scientifiques à lever constituant l'objectif de la présente thèse. Ces verrous scientifiques concernent la compréhension du fonctionnement du réacteur, y compris son hydrodynamique, le transfert de chaleur et la chimie. Des questions concernant la gestion du flux de chaleur variable pendant les périodes de forte et de faible irradiation solaire sont aussi posées. D'autres aspects portent sur la conversion de charges carbonées avec un fort taux de cendres telles que les déchets et enfin, sur le fonctionnement du réacteur à l'échelle du MW ainsi que sur la faisabilité technico-économique du procédé à grande échelle.

Afin d'apporter de nouveaux éléments sur le fonctionnement du réacteur et améliorer sa performance, sa flexibilité et son intégration industrielle, différents outils de simulation et d'expérimentation ont été mis au point. Le code commercial CFD (Computational Fluid Dynamics) Fluent© a été utilisé pour simuler le réacteur solaire en 2D et 3D. Des fonctions utilisateur (UDFs) en C++ ont été développées et utilisées comme compléments du solveur. Le logiciel Python a été utilisé pour simuler le fonctionnement dynamique du réacteur à l'échelle industrielle, et l'outil H2A du DOE [2] a été utilisé pour analyser la faisabilité technico-économique du procédé. De plus, le banc d'essai expérimental du réacteur solaire a été utilisé pour valider les approches numériques et réaliser des expériences complémentaires pour explorer de nouveaux modes de fonctionnement (hybridation par oxi-combustion, gazéification solaire de déchets et impact des matériaux de lit). Une nouvelle cavité transparente en PMMA (polyméthacrylate de méthyle) a également été conçue pour visualiser à température ambiante de nouvelles configurations hydrodynamiques visant à améliorer le fonctionnement du réacteur.

Dans ce résumé de thèse, nous présentons le réacteur solaire étudié et succinctement les résultats obtenus.

I.2 Dispositif expérimental

Le réacteur solaire étudié (REACSOL) utilise l'énergie solaire concentrée (à environ 10 000 soleils) pour convertir de la biomasse en un gaz de synthèse à haut pouvoir calorifique (Figure 1). Ce réacteur fonctionne à des températures supérieures à 1200°C. Les particules de bois sont transportées en continu par une vis sans fin. Elles tombent par gravité dans la cavité conique chaude jusqu'à l'injection complète de la charge. Un jet de gaz (Ar/H_2O) entraine les particules de biomasse

vers le haut puis ces particules redescendent de manière cyclique. Le diamètre de l'entrée du gaz du jet est de 2 mm permettant d'atteindre des vitesses d'environ 9 m/s. Les gaz produits traversent une unité d'épuration composée d'un bulleur et de deux filtres pour éliminer l'excès de vapeur et les particules de char/suies entraînées. La composition molaire du gaz de synthèse est ensuite analysée en continu à l'aide d'un analyseur de gaz en ligne. Ces mesures ont été vérifiées grâce à un chromatographe en phase gazeuse (CPG) équipé de deux colonnes utilisant l'argon comme gaz vecteur. Deux thermocouples (TC) mesurent directement la température interne de la cavité (T3 près du fond de la cavité dans la région conique et T1 au centre de la cavité) et un thermocouple (T2) mesure la température à la paroi externe de la cavité. Afin de protéger les TC des gaz réactifs, leurs pointes sont recouvertes d'un tube de protection en alumine. De plus un pyromètre optique a été utilisé et placé au centre du miroir parabolique. Le réacteur étudié est installé au foyer d'un four solaire parabolique situé au 6ème étage du bâtiment du CNRS-PROMES. Le haut du réacteur est composé d'une ouverture qui permet aux rayons solaires concentrés d'entrer dans la cavité et de chauffer le réacteur de manière directe ou indirecte (grâce à l'utilisation d'une plaque émettrice).

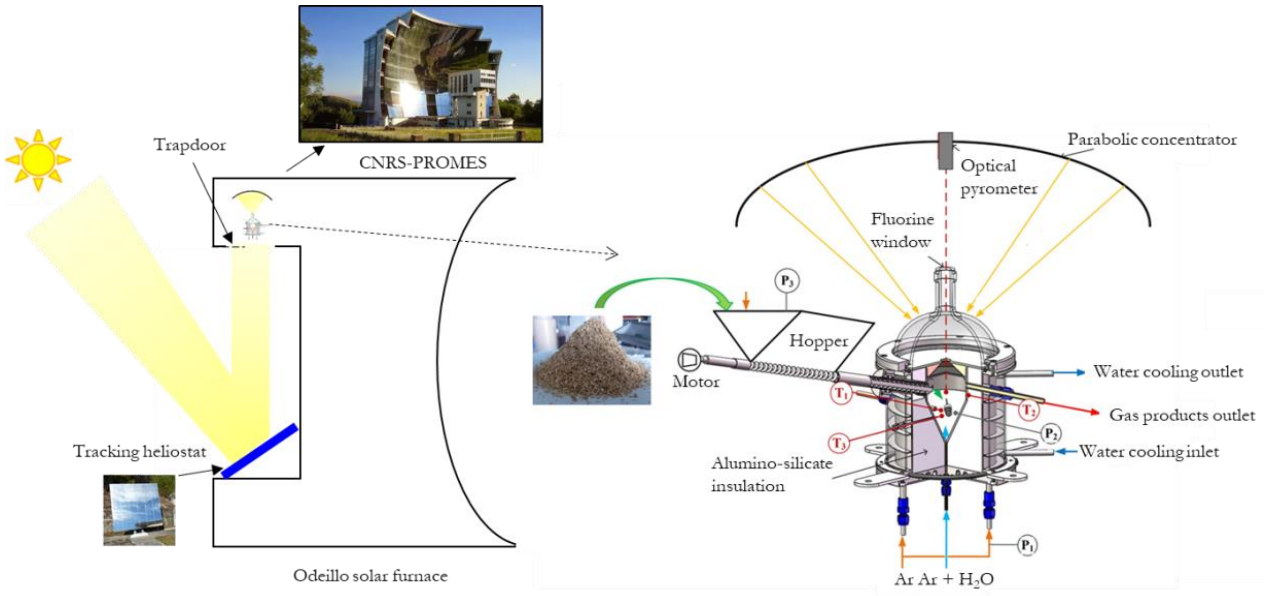

Figure 1 Schéma du réacteur solaire de gazéification

I.3 Modélisation multiphysique du réacteur solaire et validation expérimentale

Un modèle 3D global du réacteur solaire à l'échelle du laboratoire a été développé. Le modèle tient compte des équations couplées de la quantité de mouvement, du transfert de chaleur et de masse et des réactions chimiques (pyrolyse, gazéification/combustion hétérogène et cinétique de réaction en phase gazeuse) ainsi que de l'injection continue des particules. Les particules réactives ont été suivies dans l'espace et le temps à l'aide du modèle à phase discrète (Discrete Phase Modelling). Le modèle a permis d'analyser en détail les trajectoires des particules au cours de la conversion thermochimique solaire.

Des expériences allothermiques (chauffage solaire) de validation sur des particules de bois de hêtre millimétriques ont été réalisées en chauffage indirect et direct à 1200°C et comparées aux simulations. La Figure 2-a montre le contour de température au sein du réacteur en chauffage

indirect. La température de paroi avoisine les 1200°C pour une puissance solaire de 0,9 kW ce qui est en accord avec les mesures expérimentales. Le débit de biomasse injecté était de 1,2 g/min avec un débit de vapeur d'eau de 0,2 g/min. Le gaz était composé majoritairement d'H_2 et de CO à cause de la haute température. L'écart relatif maximal avec les expériences était inférieur à 10 % pour la composition du gaz de synthèse en sortie de réacteur.

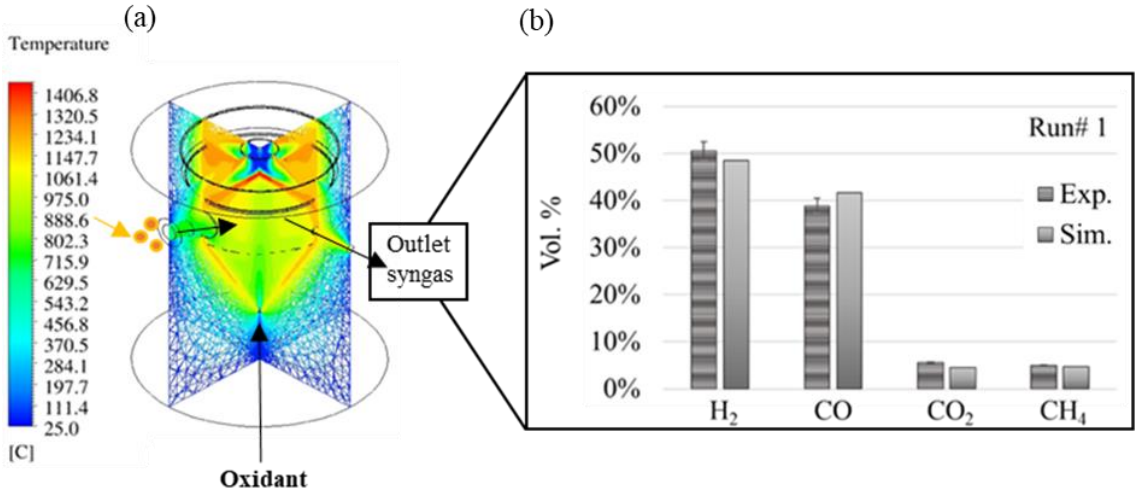

Figure 2 Contour de température en chauffage indirect et composition du gaz de synthèse (Exp. vs. Sim.)

Concernant les trajectoires des particules de bois, celles-ci décrivent un certain nombre de cycles au cours desquels elles sont pyrolysées et gazéifiées. Le mouvement cyclique vigoureux souhaité dans le réacteur a été confirmé par le modèle multiphysique comme le montre la Figure 3.

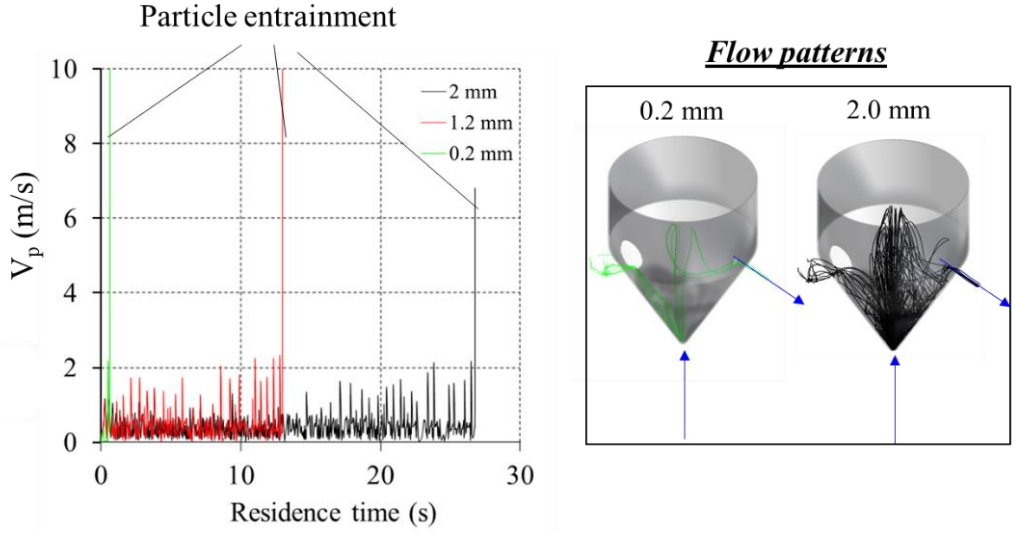

Figure 3 Vitesses de particules réactives en fonction du temps de séjour et trajectoires (diamètres initiaux 0,2 ; 1,2 et 2,0 mm)

Les résultats obtenus au cours de cette partie de la thèse ont donné un aperçu clair de la conversion solaire thermochimique des particules de bois dans la cavité directement ou indirectement irradiée par le soleil. Le modèle a confirmé la pertinence du réacteur à jet fonctionnant dans des conditions de chauffage solaire optimales grâce à des caractéristiques thermochimiques et hydrodynamiques spéciales et pertinentes. Enfin, des points d'amélioration

du modèle ont été identifiés. Une étude de sensibilité sur les différents paramètres physiques et numériques reste à réaliser afin de déterminer des données d'entrée optimisées permettant d'alléger le calcul sans perdre en précision. Une validation expérimentale sur des conditions opératoires plus variées est également à envisager dans la suite.

Les résultats obtenus ont été publiés dans l'*International Journal of Heat and Mass Transfer* [3].

I.4 Gestion de l'intermittence solaire : hybridation par oxi-combustion

Le modèle multiphysique 3D présenté dans la section précédente a été utilisé pour simuler un nouveau mode de chauffage hybride qui utilise des réactions de combustion in situ pour assister le chauffage solaire et résoudre le problème de la variabilité quotidienne de l'énergie solaire [4]. La faisabilité opérationnelle du procédé a d'abord été démontrée grâce à la modélisation numérique. La Figure 4-a montre le contour de température du réacteur directement irradié en chauffage allotherme sous 0,9 $kW_{solaire}$. L'injection d'une quantité supplémentaire de bois avec une quantité stœchiométrique d'O_2 a formé une flamme non pré-mélangée au niveau de la région centrale de la cavité où la température dépasse les 1800°C. En conséquence, la température moyenne de la paroi a augmenté de 52 °C (pour atteindre 1263°C).

Des expériences portant sur ce nouveau mode de chauffage ont été menées sur le banc expérimental. Les résultats obtenus représentent la première tentative réussie visant à contrôler un réacteur thermochimique hybride fonctionnant avec un apport solaire réel variable. La Figure 4-b montre la température du réacteur au cours d'un essai où la puissance solaire a été diminuée brutalement de 1,2 kW à 0,7 kW pour simuler le passage de nuages.

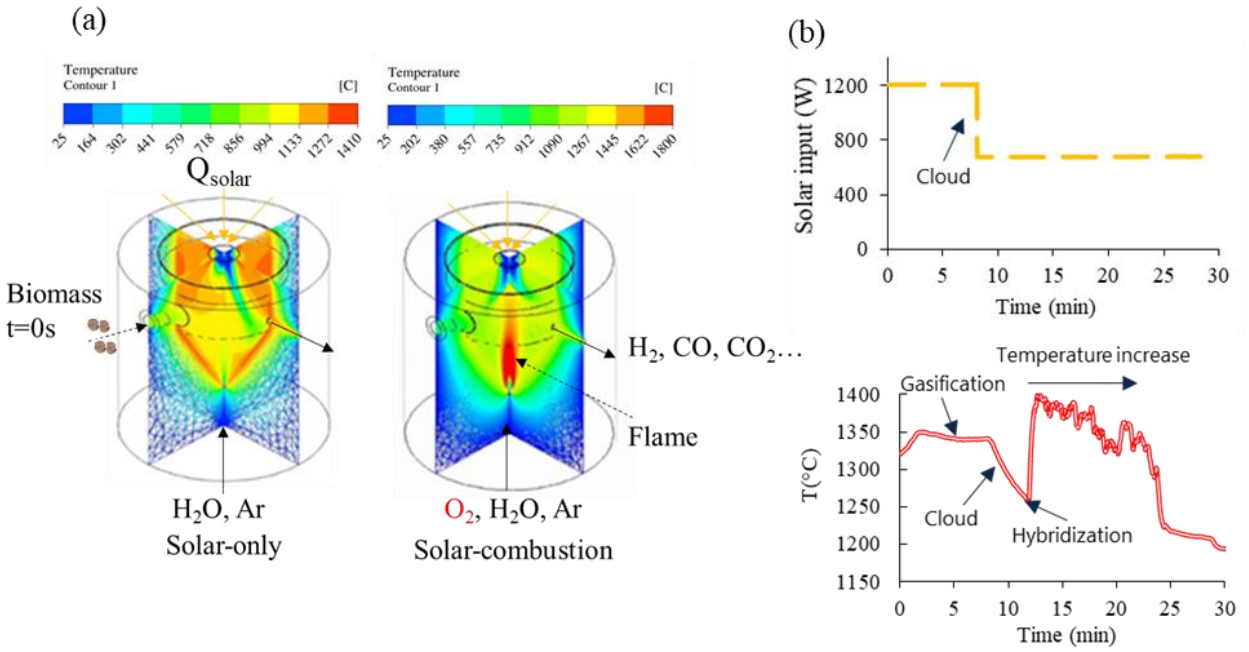

Figure 4 (a) Contour de température en chauffage alloterme (1,2 g/min de bois, 0,2 g/min d'eau) vs hybride (1,4 g/min de bois, 0,2 g/min d'eau, 0,25 NL/min d'O_2) ; (b) Résultats expérimentaux sur l'effet de l'hybridation sur la température du réacteur suite à une chute brutale de puissance solaire

Au départ, 1,2 g/min de bois et 0,2 g/min d'eau ont été injectés dans le réacteur. Ceci a entrainé une légère baisse de température à cause des réactions endothermiques de gazéification. La chute importante d'énergie solaire a provoqué une forte baisse de température d'environ 100°C pénalisant la production de gaz et les cinétiques de pyrogazéification/reformage. L'injection d'une quantité supplémentaire de bois de 0,2 g/min avec 0,25 NL/min d'O_2 a permis de rehausser la température du réacteur assurant ainsi une production continue de gaz avec un apport solaire faible. L'étude a montré que l'hybridation par oxy-combustion est une solution efficace pour maintenir la température de gazéification. Un impact important sur la qualité du gaz de synthèse (rapport H_2:CO et pouvoir calorifique) a néanmoins été observé. Cela peut être problématique et devrait être atténué grâce à un meilleur pilotage des entrées biomasse/oxydants afin d'optimiser la fiabilité et les performances du procédé. Un procédé solaire pouvant fonctionner en continu jour et nuit pourrait ainsi être envisagé.

Les résultats obtenus ont été publiés dans le journal *Energy* [5].

I.5 Etude exploratoire de la gazéification solaire de déchets

La gazéification solaire et hybride du bois de hêtre a été réalisée avec succès dans le réacteur solaire à jet. Cependant, des questions persistent quant à sa capacité à traiter des charges plus variées telles que les déchets et les plastiques. Ainsi, des expériences exploratoires ont été réalisées sur des particules de déchets sous forme de CSR (Combustibles Solides de Récupération). La Figure 5 montre le débit de production de gaz lors d'un essai en chauffage allotherme direct à 1,0 $kW_{solaire}$. Au cours de cet essai, environ 0,57 g/min de CSR ont été gazéifiés par 0,2 g/min d'eau à 1300°C.

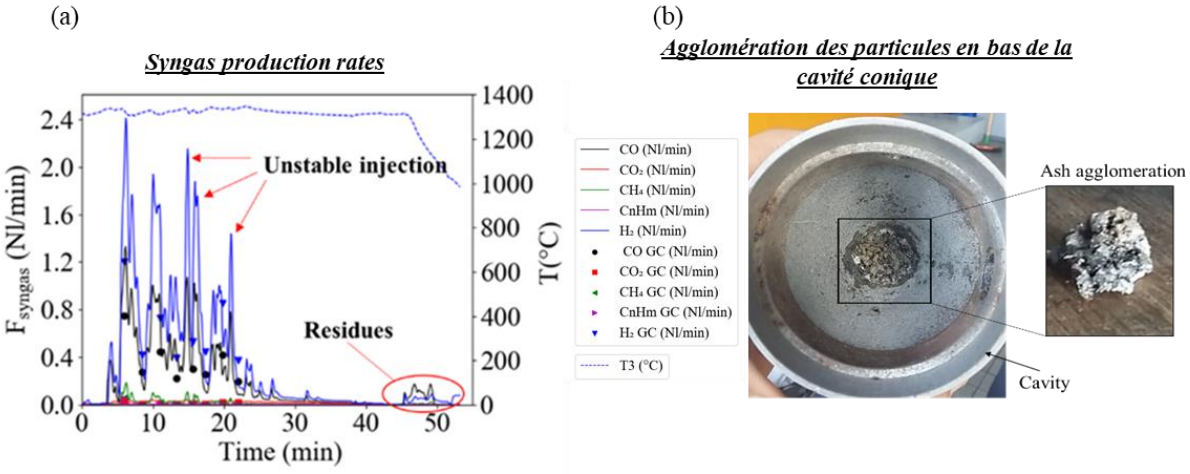

Figure 5 (a) Débit de production des principaux composants du gaz de synthèse; (b) agglomération des particules en bas du cône

Des performances globales très satisfaisantes ont été atteintes avec un rendement de gaz à froid (rapport entre l'énergie thermique du gaz de synthèse et celle de l'échantillon gazéifié) de 105% avec un taux de conversion du carbone supérieur à 88%. Deux points essentiels d'amélioration du procédé ont été identifiés suite aux expériences : l'injection instable des particules, mise en évidence par les pics de production de gaz dans la Figure 5 et l'agglomération des cendres en fusion en bas du cône au-dessus du tube d'injection d'oxydant. Des solutions ont été proposées afin d'assurer une injection de CSR plus stable et évacuer les cendres en fusion au cours de la conversion.

Les résultats obtenus ont été publiés dans le journal *Energies* [6].

I.6 Impact des matériaux de lit sur la conversion solaire

Dans le but d'améliorer le mélange au sein du réacteur, le temps de séjour solide/gaz ainsi que la conversion globale des particules, l'utilisation de matériaux inertes de lit comme moyen de transfert de chaleur est apparue judicieuse. Cette solution a d'abord été examinée à l'aide de simulations CFD 2D qui modélisent les particules inertes solides "spoutées" ou sous forme d'un lit fixe en interaction avec le rayonnement et l'écoulement gazeux (Figure 6-a). Les simulations ont confirmé le rôle bénéfique des particules inertes pour homogénéiser la température du réacteur et diminuer l'entrainement (par la sortie du réacteur) des particules réactives. L'écoulement a ensuite été étudié à température ambiante à l'aide d'une maquette froide transparente en PMMA (Figure 6-a). L'analyse a permis de déterminer les conditions minimales de jaillissement de différentes poudres et d'examiner la stabilité hydrodynamique de l'écoulement. Enfin, des expériences à 1200°C et à 1300°C ont été réalisées sur cinq matériaux de lit différents : Al_2O_3 3 mm; Al_2O_3 125 µm; SiC 300 µm, olivine 300 µm, sable 200 µm. La Figure 6-b montre l'impact des matériaux de lit sur le taux de conversion du carbone à 1200°C avec un débit de bois de 1,2 g/min et un débit d'eau de 0,2 g/min.

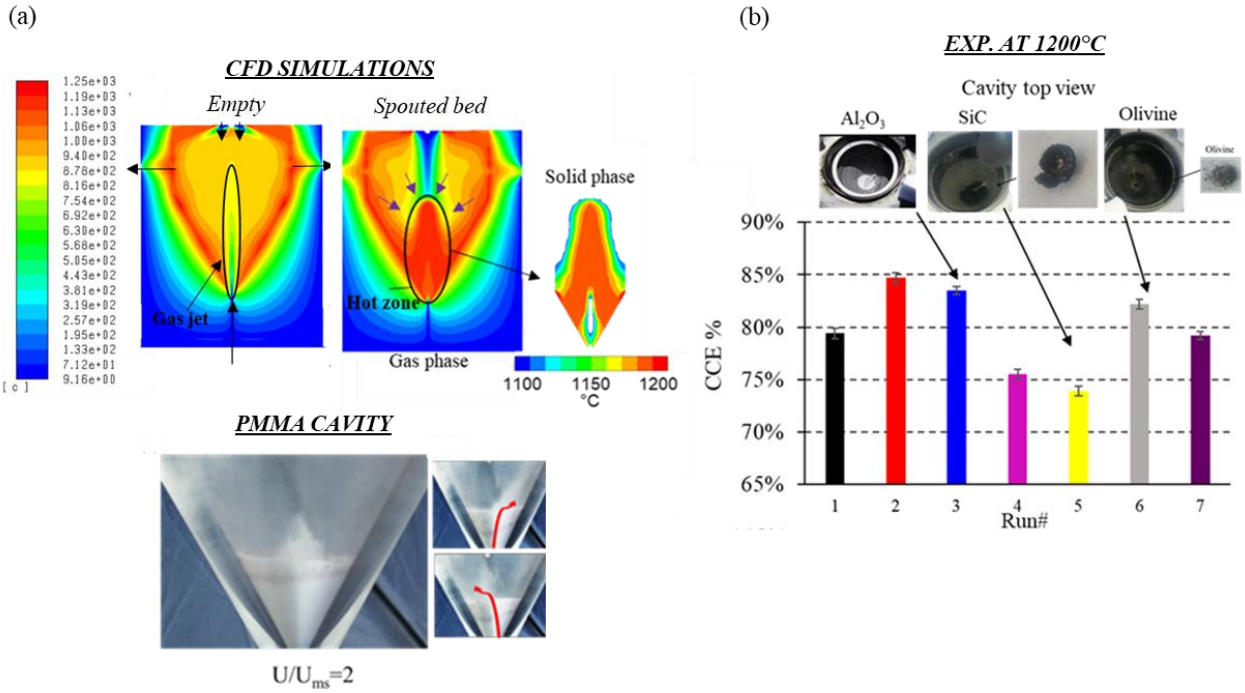

Figure 6 (a) Simulation CFD de l'impact d'une poudre d'alumine (10 g, 125 µm) sur le champ de température au sein de la cavité solaire ; visualisation de l'écoulement d'une poudre d'alumine à température ambiante; (b) impact de différentes poudres sur le taux de conversion du carbone du réacteur à 1200°C, 1,2 g/min de bois et 0,2 g/min d'eau

Les tests solaires ont montré une augmentation relative de la conversion du carbone maximale de 8 % en utilisant les particules d'Al_2O_3. L'impact sur la composition de gaz de synthèse est resté globalement très faible, avec une variation relative maximale inférieure à 7 % pour l'H_2. Ces premiers résultats soulignent l'importance du choix des matériaux du lit qui doivent résister à la fois à l'atmosphère hautement oxydante et à la température élevée pour assurer un fonctionnement optimal à long terme. Afin d'étudier plus en détail les matériaux du lit, il est important de quantifier avec précision la perte de masse à la fin les expériences; de plus, la

caractérisation de l'évolution des propriétés physico-chimiques des particules telles que la densité, la capacité thermique, l'émissivité, la composition, etc. pourrait fournir des informations clés et des données pertinentes sur leur comportement physique, leur durabilité et leur stabilité thermochimique.

Les résultats obtenus ont été publiés dans le journal *Chemical Engineering Science* [7].

I.7 Extrapolation et pilotage dynamique

Compte tenu des résultats prometteurs des simulations et des expériences, le réacteur a été extrapolé à l'échelle du MW pour la production industrielle de gaz de synthèse. Un modèle dynamique 0D du réacteur a été développé pour déterminer l'évolution de la température et des produits de gaz de synthèse pendant le fonctionnement continu. Trois stratégies de pilotage de l'alimentation en biomasse, vapeur et oxygène ont été proposées et étudiées : TOR (Tout Ou Rien), OPTI (OPTImized) et HYB (HYBridized). Les modes OPTI (allothermique) et HYB (solaire/autothermique) ont permis d'atteindre les plus hautes performances grâce au contrôle dynamique des débits d'injection qui stabilise la température du réacteur, minimise les pertes de chaleur et maximise la productivité. La température du réacteur au cours de trois jours consécutifs est présentée dans la Figure 7-a.

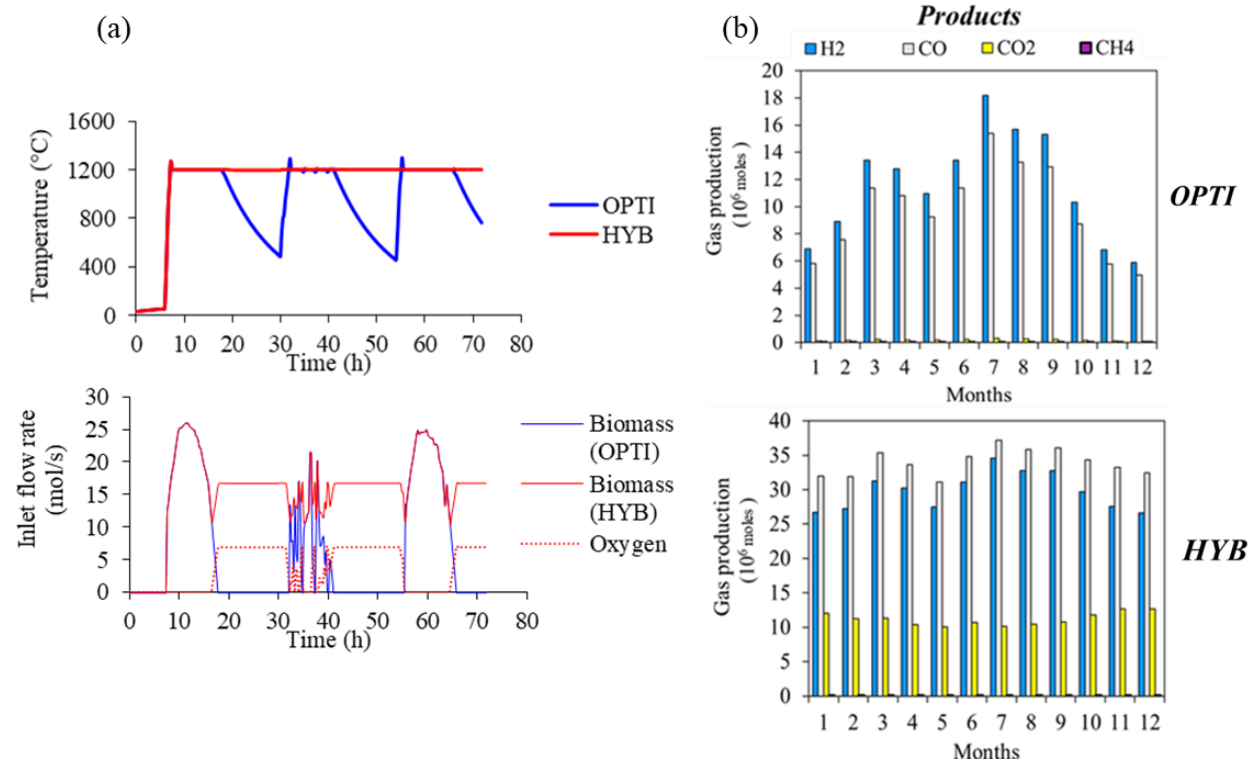

Figure 7 (a) Profil de température du réacteur au cours de trois jours consécutifs (4,5,6 Mai à Odeillo en France, données météorologiques générées par le logiciel commercial Meteonorm); (b) prédiction annuelle du volume produit de gaz de synthèse grâce au modèle 0D

Le mode OPTI permet de stabiliser la température du réacteur à 1200°C peu importe la ressource solaire grâce au pilotage dynamique de l'alimentation en biomasse et en vapeur (rapport débit d'eau sur débit de biomasse maintenu constant à 0.17) jusqu'à un certain point où la ressource solaire est tellement faible que l'injection de biomasse n'est plus possible à 1200°C et le réacteur s'arrête. Le mode HYB permet de maintenir la température du réacteur à

1200°C 24h/24 éliminant ainsi les phases de refroidissement et de chauffage (qui consomment en moyenne sur l'année environ 14% de l'énergie solaire totale reçue). De ce fait, ce mode de fonctionnement permet d'obtenir des rendements plus importants, surpassant ceux de la gazéification allothermique et autothermique conventionnelle. Des simulations annuelles ont été réalisées avec des données solaires moyennées sur 19 années. La Figure 7-b montre les volumes de gaz produits au cours de chaque mois de l'année. Ces prédictions ont été utilisées pour réaliser une étude technico-économique du procédé.

Les résultats obtenus ont été publiés dans l'*International Journal of Hydrogen Energy* [8].

I.8 Analyse technico-économique

Dans la dernière partie des travaux, la faisabilité économique du procédé à grande échelle pour la production centralisée de H_2 a été examinée. Le coût de production de H_2 par gazéification solaire, hybride et autothermique (non-solaire) de biomasse a été évalué en considérant différents scénarios économiques et en se basant sur la méthode du taux de rentabilité interne (Discounted cash flow rate of return).

En considérant un prix de référence de biomasse de 0,1 €/kg, et un prix de terrain de 12.9 €/m^2, les procédés solaires sont difficilement compétitifs avec le procédé conventionnel même en réduisant de façon importante le prix des matériaux et des composants solaires (Figure 8). Une étude de sensibilité détaillée sur les paramètres financiers et économiques les plus impactant a été réalisée. L'analyse a montré qu'une augmentation du coût de la biomasse d'un facteur 2 à 3 compromet significativement la rentabilité du procédé autothermique, au profit de la gazéification hybride et solaire.

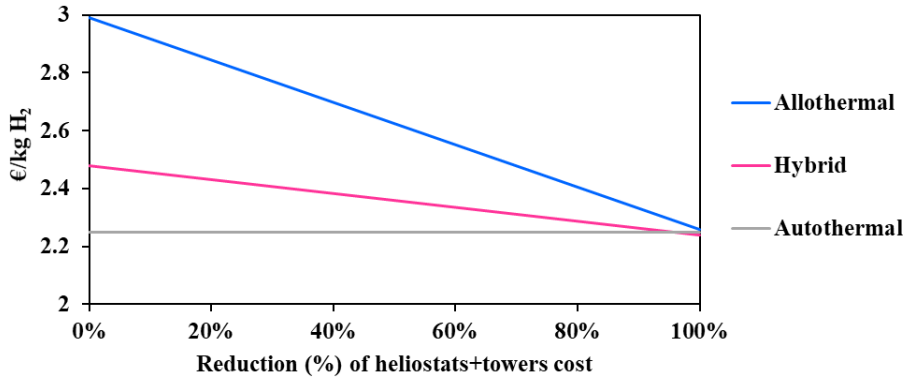

Figure 8 Impact de la réduction du coût des technologies solaires sur le prix minimum de l'hydrogène

Une étude comparative impliquant d'autres procédés solaires et non solaires a conclu à la rentabilité des procédés fossiles et en particulier le reformage du gaz naturel, qui montre un coût de l'H_2 inférieur à 1.28 €/kg (en tenant compte des coûts de la séquestration et du stockage du CO_2), contre 2,5 €/kg et 3,0 €/kg pour le procédé de gazéification de la biomasse hybride et solaire. Toutefois, compte tenu des réglementations environnementales de plus en plus strictes et de l'urgence du changement climatique, la voie durable connaît aujourd'hui une recherche et un développement approfondis pour gagner en efficacité et en rentabilité. Le déploiement massif de l'énergie solaire concentrée dans le monde entier au cours des prochaines années peut réduire considérablement le coût des matériaux et composants solaires (héliostats) et ainsi alléger le coût financier de la gazéification solaire.

I.9 Conclusion

Les travaux réalisés dans le cadre de cette thèse montrent l'intérêt et la rentabilité potentielle de l'utilisation de l'énergie solaire pour la valorisation des ressources carbonées par gazéification thermochimique et la production de carburants synthétiques propres. Au cours des dernières décennies, et en raison du changement climatique et de l'épuisement des combustibles fossiles, des progrès et des innovations techniques sont apparus pour assurer la conversion efficace de la ressource solaire. À ce jour, ce sont principalement les technologies de production directe d'électricité qui sont développées. Plus généralement, cette source d'énergie est non seulement prometteuse pour la gazéification, mais aussi pour la décarbonisation de processus chimiques endothermiques comme le reformage, la dissociation thermique, et aussi les processus métallurgiques nécessitant de très hautes températures. Il est donc important d'accorder une attention particulière à ces procédés innovants afin d'accélérer leur développement et leur déploiement à grande échelle. C'est ainsi que nous concluons avec la citation de T. Edison (1931) "*I'd put my money on the sun and solar energy. What a source of power! I hope we don't have to wait until oil and coal run out before we tackle that*".

REFERENCES

[1] Q. Bellouard, "theses.fr – Quentin Bellouard, Conversion de biomasse en vecteur énergétique par voie solaire thermochimique," 2017. http://www.theses.fr/s132650 (accessed Jul. 04, 2019).

[2] NREL H2A, "H2A: Hydrogen Analysis Production Models | Hydrogen and Fuel Cells | NREL," 2018. https://www.nrel.gov/hydrogen/h2a-production-models.html (accessed Jul. 07, 2020).

[3] H. Boujjat, S. Rodat, S. Chuayboon, and S. Abanades, "Numerical simulation of reactive gas-particle flow in a solar jet spouted bed reactor for continuous biomass gasification," *Int. J. Heat Mass Transf.*, vol. 144, p. 118572, Dec. 2019, doi: 10.1016/j.ijheatmasstransfer.2019.118572.

[4] S. Rodat, S. Abanades, H. Boujjat, and S. Chuayboon, "On the path toward day and night continuous solar high temperature thermochemical processes: A review," *Renew. Sustain. Energy Rev.*, vol. 132, p. 110061, Oct. 2020, doi: 10.1016/j.rser.2020.110061.

[5] H. Boujjat, S. Rodat, S. Chuayboon, and S. Abanades, "Experimental and numerical study of a directly irradiated hybrid solar/combustion spouted bed reactor for continuous steam gasification of biomass," *Energy*, vol. 189, p. 116118, Dec. 2019, doi: 10.1016/j.energy.2019.116118.

[6] H. Boujjat, S. Rodat, and S. Abanades, "Solar-hybrid Thermochemical Gasification of Wood Particles and Solid Recovered Fuel in a Continuously-Fed Prototype Reactor," *Energies*, vol. 13, no. 19, p. 5217, Jan. 2020, doi: 10.3390/en13195217.

[7] H. Boujjat, S. Rodat, S. Chuayboon, and S. Abanades, "Experimental and CFD investigation of inert bed materials effects in a high-temperature conical cavity-type reactor for continuous solar-driven steam gasification of biomass," *Chem. Eng. Sci.*, vol. 228, p. 115970, Dec. 2020, doi: 10.1016/j.ces.2020.115970.

[8] H. Boujjat, G. M. Yuki Junior, S. Rodat, and S. Abanades, "Dynamic simulation and control of solar biomass gasification for hydrogen-rich syngas production during allothermal and hybrid solar/autothermal operation," *Int. J. Hydrog. Energy*, Feb. 2020, doi: 10.1016/j.ijhydene.2020.01.072.

SUMMARY

FIGURES

TABLES

GENERAL INTRODUCTION

Gasification reactors have been on the market for more than a century, with current trends in chemicals, liquid fuels and power generation. These industrial reactors are based on the combustion of a part of the feedstock in order to provide the energy necessary to activate the strongly endothermic gasification reactions. This penalizes the material yield and the energy conversion efficiency. By combining concentrated solar energy and thermochemical gasification of biomass, it is possible to take advantage of both resources. Indeed, since high-temperature solar heat can be used to provide the enthalpy of the reaction, all the biomass can be converted into hydrogen and carbon monoxide (syngas). Solar gasification promotes biomass utilization and is an efficient way to store intermittent solar energy in the form of renewable, dispatchable and storable solar fuels.

Several experimental studies on allothermal solar gasification have demonstrated the feasibility and efficiency of the process at laboratory scale (Loutzenhiser & Muroyama, 2017). At the CEA, a first solar spouted bed reactor was built during the PhD work of Bellouard (2014-2017). This reactor was tested at the CNRS-PROMES solar furnace in Odeillo in France for the continuous steam conversion of millimetric beech wood particles at temperatures up to 1400°C. Although the first experimental tests on wood validated the design and demonstrated the viability of the solar process at laboratory scale, there are number of obstacles to address that constitute the objectives of the present thesis:

- The wood particles/gas flow hydrodynamics and its interaction with chemistry and radiation was only little discussed.
- The variable nature of solar energy and its impact on the reactor operation remains to be assessed.
- The ability of the reactor design to convert a more varied loads other than wood (e.g. waste, solid waste fuels, etc.) remains to be evaluated.
- The technical feasibility of the solar process at large scale and its economic/financial viability need to be investigated.

This manuscript presents the results obtained during my three-year doctoral thesis co-funded by the CEA and ADEME. I had also the opportunity, with the financial support of European projects (INSHIP, SFERA III) to carry out experiments at the CNRS PROMES solar furnace for two months in total in July 2018 and July 2019.

The manuscript is organized in five chapters. Chapter 1 is devoted to the literature survey, which presents relevant research studies in the field and provides the scientific/technical knowledge necessary to deal with the different aspects of the thesis. Chapter 2 is organized in three parts, the first one aims at providing a detailed understanding of the reactor operation thanks to 3D multiphysics numerical simulations with experimental validation. The second part assesses both experimentally and by simulation, the effects of process hybridization through partial feedstock oxy-combustion to tackle the issue of solar energy intermittency and the third part presents an exploratory study on waste (Solid Recovered Fuels or SRF) solar gasification.

Chapter 3 shows, thanks to numerical simulations and experimentations, the impact of different inert bed materials set initially inside the cavity on the performance of the reactor. Chapter 4 presents a dynamic model, which after a validation step, was used to simulate the reactor at large-scale. Finally, Chapter 5 presents a techno-economic analysis of the process based on dynamic model predictions. A comparative study with other solar and non-solar solar fuels production processes is presented.

I. CHAPTER 1

Background on concentrated solar energy, gasification and modelling

I.1 Introduction

In this work, a novel solar gasifier concept was studied from lab to industrial scale by combining numerical simulation and lab-scale experimentation. The present literature survey was conducted to provide the necessary knowledge and background and to properly grasp the thesis problem. Besides, it aimed at clarifying the state-of-the-art, determining the scientific locks and defining the main research axes to be pursued. It is organized as follows: Section I.2 presents an overview about concentrated solar energy, current solar energy systems and their performance metrics. Section I.3 is organized in three parts; the first part presents the main previously studied reactor designs, their advantages and limitations. The second part outlines the different management strategies proposed to deal with solar energy variations. The third part focuses on the scale-up of solar gasifiers. It presents a summary of pilot scale projects and recaps major large-scale system level simulations that couple the solar gasification concept with various energy and chemical processes. Section I.4 introduces spouted beds; it describes their main features and presents the previously studied spouted bed gasifiers. Finally, section I.5 tackles the main modelling approaches of pyrogasification with emphasis on models used in CFD (Computational Fluid Dynamics) simulation of gasifiers.

I.2 Concentrated Solar Energy

I.2.1 Overview

As solar energy is diluted, the direct solar flux received on Earth surface can hardly exceed 1000 $W.m^{-2}$. To capture this energy and transform it into heat, specific solar devices should be used. There are two main solar technologies that valorize the solar radiant energy into heat: flat-plate technologies (Pandey and Chaurasiya, 2017) and concentrators (Helman, 2017). The first kind is often used for domestic heating/air conditioning and in some cases, in industry for process heat generation. Due to excessive heat losses, these systems barely achieve 100-200°C. Solar concentrators enable to deliver energy at high temperature, which makes them crucial for many industrial and energy applications. Such technologies are based on the use of a receiver whose surface aperture is minimized (to reduce the thermal radiative losses) and optical systems, which collect and concentrate sunlight towards the receiver. There are two main areas of interest in concentrated solar energy: chemicals and power generation. Currently, power generation by concentrated solar energy (commonly referred to Concentrated Solar Power or CSP) is the most mature. CSP plants use the sunlight to heat a Heat Transfer Fluid (HTF), the latter exchanges energy with water, which becomes superheated and drives a conventional steam turbine-generator. Very often, to smooth out the energy delivery on cloudy and nocturnal hours, CSP plants are also equipped with thermal energy storage (TES) units making use of energy storage medium such as molten salt mixtures to store for several hours (e.g. 6-10 hours for a majority of active CSP projects) midday surplus sensible energy (Achkari and El Fadar, 2020).

I.2.2 CSP in the world

CSP is commercially available since 1984 (REN21, 2014) and it reached a world electrical production capacity of 5 500 MW in 2018 (REN21, 2019).Spain and USA are today the world leading countries in CSP, holding around 66% of the total power production capacity. Besides, more than third of major CSP projects are either under development or under construction especially in China, Chile, Australia, South Africa and MENA region, which denotes a growing interest in CSP worldwide (SolarPACES, 2020). The commercial viability of the plants depends on a large number of criteria, including the location of the power plants. In fact, solar concentration concerns exclusively the direct component of sunlight, which needs to be as high as possible. The best locations for CSP plants are therefore limited areas on Earth, which should guarantee a high level of DNI (Direct Normal Irradiance) all year round. The DLR (Deutsches Zentrum fur Luft-under Raumfahrt) drawn up a map of potential sites, which are auspicious for CSP (Figure I.1).

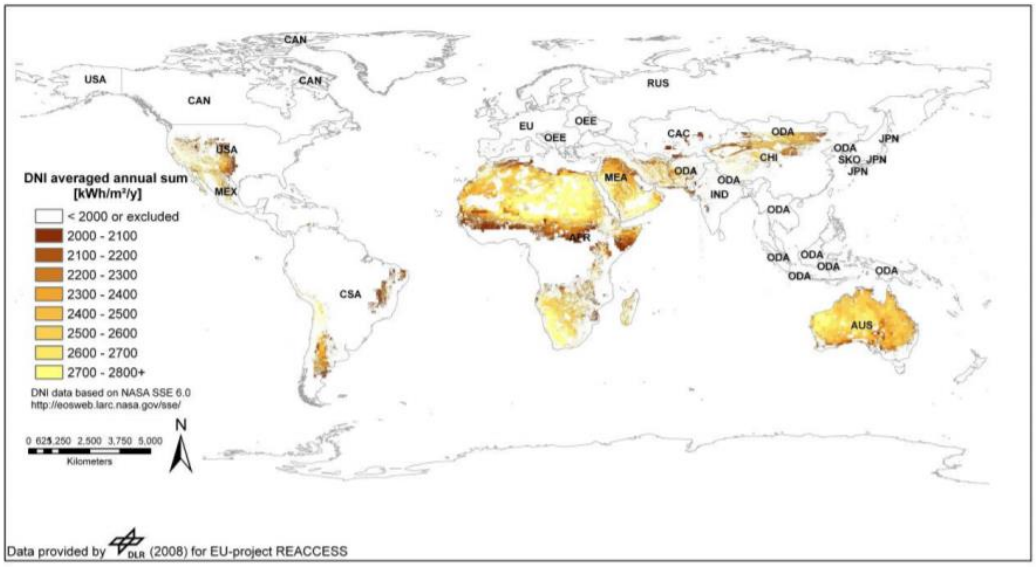

Figure I.1 Resulting map of the annual sum of direct normal irradiation for potential global CSP sites as identified within the EU-project REACCESS (Trieb, et al., 2009)

These sites are characterized by a DNI higher than 2000 $kWh.m^{-2}.year^{-1}$, a large open area (as flat as possible) with no property nearby, the presence of a power distribution network and a great supply of water. Note that under these conditions, only 1% of the Sahara desert surface is able to satisfy today's world electricity demand (Letcher, 2020).

I.2.3 Concentrating solar systems

Four CSP technologies are generally accepted and commercially available for the production of electricity (Figure I.2). Each technology has its own concentration level, which is expressed by the concentration ratio (C). From an energetic point of view, this ratio can be defined as the flux entering the collector over solar radiation hitting onto the receiver. However, the flux on the receiver is neither uniformly distributed, nor easily measurable. Besides, it varies during the day. For this reason, the geometrical concentration was introduced. This parameter is more convenient for practical engineering applications as it depends on the geometry of the

technology as manufactured. It is expressed as the ratio between the concentrator aperture surface and the surface of the receiver aperture.

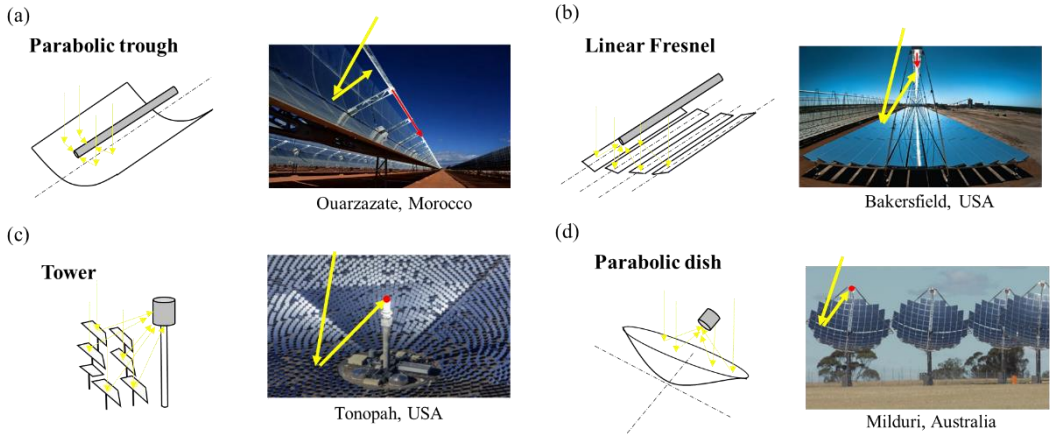

Figure I.2 Generally accepted CSP technology types

The maximum temperature level delivered by a CSP technology depends above all on this parameter. Parabolic Trough (PT) and Linear Fresnel (LF) reflectors (Figure I.2-a,b) are one-axis tracking and line-focusing technologies. Their operating range is 250-400°C with concentration ratios of about 50-100. Central receivers (i.e. tower configuration, Figure I.2-c) and parabolic dish concentrators (Figure I.2-d) are two-axis tracking and point-focusing technologies, and their concentration ratios can easily reach 1000 at the expense of a greater cost and complexity. This allows reaching higher temperatures at the receiver, which improves the solar-to-electric (STE) efficiency and reduces the energy costs (Fernández-García et al., 2014; IRENA, 2012; Weinstein et al., 2015). In the four configurations, the concentration ratio (and thus the receiver temperature) can be increased by adding further optical components such as 2D and 3D CPCs (Compounds Parabolic Collectors) (Tian et al., 2018).

Even if PT technologies dominated the market during the last two decades, tower plants show today an increasing interest. In fact, the total power capacity of tower plants under construction or development is twice that of PTs (Gauché et al., 2017). LF reflectors and dish collectors utilization remains marginal, except in some small projects worldwide.

The solar tower configuration gains attractiveness and shows a high potential for coupling with high temperature thermochemical processes at large scale (Weinstein et al., 2015; Yadav and Banerjee, 2016). This configuration presents various possible arrangements depending on the heliostats (i.e. tracking mirrors) layout and on the central receiver design/location (Figure I.3).

Figure I.3-a shows an external receiver with an aperture receiving radiation all around the circumference. This concept is used in a number of large-capacity tower plants such as Noor in Morocco and Ivanpah in California. Figure I.3-b depicts a cavity receiver mounted on the top of a tower with a polar heliostat field. The receiver is an insulated enclosure with an aperture irradiated from one side of the tower only. PS10 plant near Seville in Spain is the first ever built commercial solar tower plant and it is based on this principle.

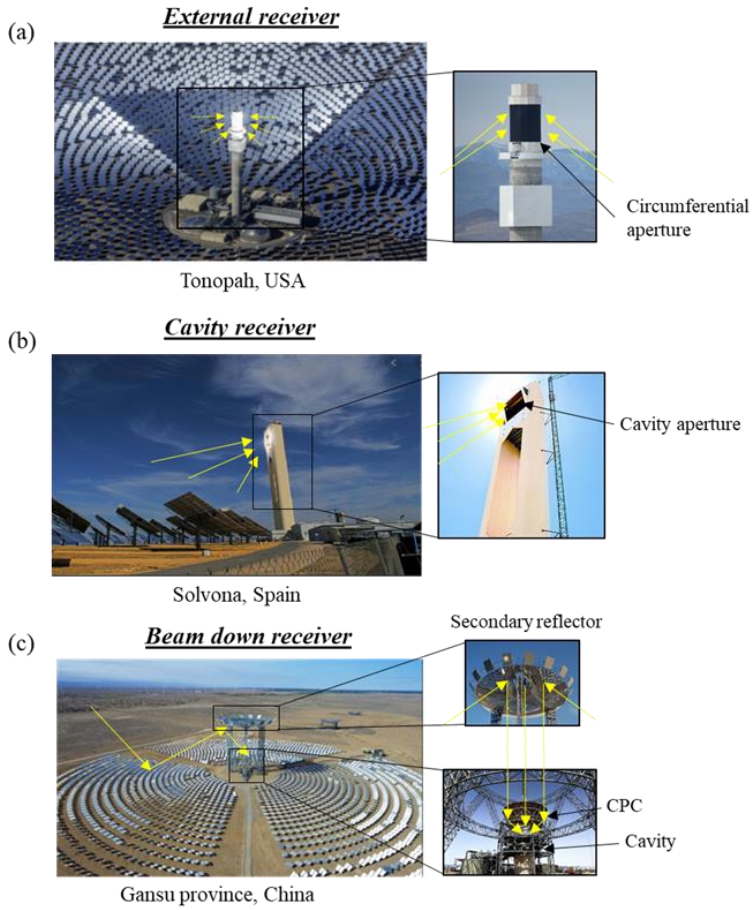

Figure I.3 Central receiver main configurations

The third possible configuration shown in Figure I.3-c makes use of the Cassegrain optical arrangement borrowed from telescopes. The cavity receiver is set on the ground and a secondary reflector at the top of the tower redirects the impinging light towards the receiver. This significantly reduces the weight and the cost of the tower, which thus supports only the secondary reflecting component (Yogev et al., 1998). A commercial plant taking use of beam-down/reflector technology was recently built (for the first time) in China (http://www.xinchen-csp.com/).

I.2.4 Performance metrics

Energy losses in CSP plants are basically of two types: optical and thermodynamic. The optical losses are due to different factors, which vary with the mirrors properties, the plant location and the period of the year. These losses are generally classified as follows: (i) the reflection losses are due to the non-perfect specular reflection on the mirrors surface, (ii) the cosine losses are due to the angle between the incident solar rays and the mirrors normal vector, (iii) the shading losses are caused by shading induced by some solar components relative to others (e.g. solar tower/heliostat field), (iv) the blockage losses occur when some reflectors block part of the reflected solar rays especially at low sun elevation angles, (v) the spillage losses are due to a proportion of irradiation that misses the receiver aperture because of tracking inaccuracies and mirrors shape defects, (vi) the attenuation losses are due to atmospheric scattering/absorption of radiation especially in large tower plants where the collector/receiver distance is high. With

this in mind, the plant optical efficiency (η_{opt}) can be written as the product of each factor efficiency, as depicted in Eq.I.1.

$$\eta_{opt} = \eta_{ref}.\eta_{cos}.\eta_{shading}.\eta_{blockage}.\eta_{spillage}.\eta_{atmo} \quad I.1$$

Accordingly, the optical efficiency of a solar plant is neither a fixed nor a predetermined value. It varies and decreases significantly during the day and throughout the years due to aggressive and repetitive stress factors such as temperature, humidity, saline mist, wind and sand storms (Pescheux et al., 2019). The maintenance of mirrors as well as their frequent washing are essential to guarantee a good conversion efficiency in the long-term. Globally, the lifetime of the solar mirrors is about 25–30 years (IRENA, 2017).

The overall CSP plants efficiency results from the combination of the optical efficiency, the receiver absorption efficiency and the thermodynamic efficiency of the cycle. Assuming that the solar receiver behaves like a grey body and that it only exchanges heat by radiation with outside, the efficiency of a solar receiver brought to the T_{rec} temperature can be written as a function of the geometric concentration $C=A_{mirrors}/A_{rec}$, the optical efficiency η_{opt}, the DNI and the receiver radiative properties (α and ε are the absorptivity and the emissivity of the receiver) (Eq.I.2).

$$\eta_{rec} = \frac{Q_{abs}}{Q_{rec}} = \frac{\alpha.Q_{rec} - Q_{loss}}{Q_{rec}} = \alpha - \frac{\varepsilon.\sigma_{rad}.A_{rec}.({T_{rec}}^4 - {T_{amb}}^4)}{\eta_{opt}.C.DNI.A_{rec}} \quad I.2$$

Where Q_{abs} and Q_{rec} represent the absorbed solar power and the one hitting onto the receiver, A_{rec} is the receiver surface (receiving the radiation) and DNI ($W.m^{-2}$) is the Direct Normal Irradiance, a measured solar data characterizing the flux received at Earth surface, which is perpendicular to sunlight. σ_{rad} is the Stefan-Boltzmann constant (~5.670 374.10^{-8} $W.m^{-2}.K^{-4}$).

The theoretical (maximum) thermal-to-electrical efficiency is given by the Carnot efficiency (Eq.I.3). Accordingly, the overall ideal plant efficiency is given by Eq.I.4, where T_{amb} and T_{rec} are the lower and upper temperature limits of the Carnot engine.

$$\eta_{Carnot} = 1 - \frac{T_{amb}}{T_{rec}} \quad I.3$$

$$\eta_{CSP\ ideal} = \left(\alpha - \frac{\varepsilon.\sigma_{rad}.({T_{rec}}^4 - {T_{amb}}^4)}{\eta_{opt}.C.DNI.}\right).(1 - \frac{T_{amb}}{T_{rec}}) \quad I.4$$

For thermochemical applications, the primary goal is not to produce electricity, so the coupling with a thermodynamic cycle is generally not considered. The energy efficiency of the solar system is therefore limited only by the receiver efficiency.

The exergy efficiency of thermochemical processes is another interesting parameter to quantify because it gives an indication on how well solar energy is converted into chemical energy. It is defined as the ratio of the maximum work that may be extracted from output products to the solar power input that drives the process. By applying the second principle of thermodynamics, the exergy efficiency of a solar thermochemical process can be expressed by Eq.I.4, which is similar to Eq.I.4 (Steinfeld and Meier, 2004).

Figure I. 4 shows the absorption, the ideal CSP and the Carnot efficiencies of a black body receiver operating at different temperatures and concentration ratios. It can be seen that higher concentration ratios increase the absorption efficiency. Moreover, for a given concentration ratio, the absorption efficiency decreases drastically with temperature. Indeed, the thermal

radiative losses evolve with temperature to the power 4. Furthermore, the exergy efficiency curves show that there is an optimum temperature at each concentration ratio that maximizes the conversion efficiency. Above this temperature, re-radiation losses become higher.

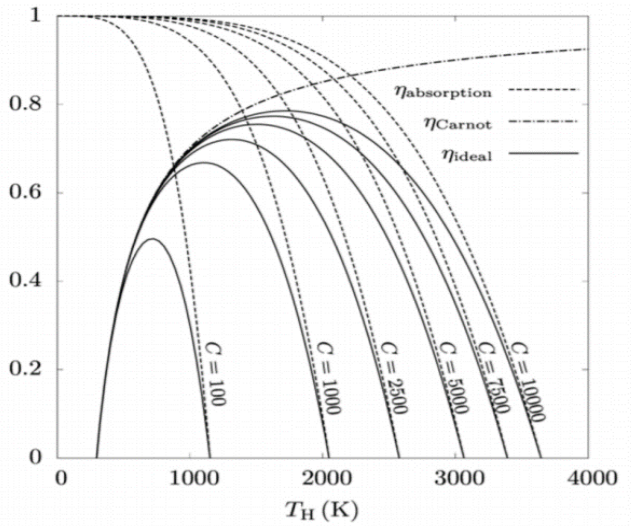

Figure I.4 Absorption, ideal CSP and Carnot efficiencies of a blackbody receiver (assuming η_{opt}=1.0) at different temperatures and concentration ratios (Fletcher and Moen, 1977)

I.3 Solar gasification

Various innovative concepts were developed to take advantage of solar energy and convert it into added-value chemical products. Powered either by solar electricity, solar photons or solar heat, these concepts were classified in three groups (Steinfeld and Meier, 2004): the electrochemical group converts electric power into chemicals using an electrolytic process; the photochemical and photobiological group uses the solar photons for photochemical and biological processes; the thermochemical group uses high temperature solar heat to drive endothermic chemical reactions. The latter is of particular interest as it offers thermodynamic advantages. In this regard, a number of pioneering processes using either water, carbon dioxide or carbonaceous resources or any combination of the three as a primary feedstock for hydrogen and syngas (i.e. mixture of CO and H_2) generation were investigated (Yadav and Banerjee, 2016). Within this scope, the gasification process has shown great promise and has been the subject of several research studies across the globe (Loutzenhiser and Muroyama, 2017; Puig-Arnavat et al., 2013).

Gasification is an endothermic process, which converts biomass into a spectrum of added value and marketable products. In line with the use of solar energy, solar gasification is considered to ensure the complete thermochemical conversion of biomass into syngas. In that respect, solar energy can be stored in the form of gaseous products composed mainly of hydrogen and carbon monoxide. The overall theoretical gasification process either with steam or CO_2 can be written as follow:

$$C_xH_yO_z+(x-z)H_2O_{(v)}\rightarrow xCO+(x-z+y/2)H_2 \quad I.5$$

$$C_xH_yO_z+(x-z)CO_2\rightarrow(2.x-z)CO+y/2H_2 \quad I.6$$

The actual process is more complex and involves three major steps. First, the pyrolysis consists of a thermal decomposition of wood at high temperature (300 to 1000°C) mainly producing incondensable gases, tars and chars. Then the remaining char is gasified (second step) with the help of an oxidizing agent. Gas phase reactions, such as the reforming reaction or the Boudouard reaction, occur in a third step. In conventional autothermal gasification reactors, the required heat is provided by burning at least 30% of the initial feedstock. The use of concentrated solar energy to drive the endothermal reactions results in saving biomass resources and producing more syngas with a higher gas quality.

I.3.1 Reactor designs

Experimental research at laboratory scale gave preference to cavity-type solar reactors where the solar cavity is at the same time the receiver and the reactor. This configuration ensures the highest temperatures, avoids the use of a heat transfer fluid (flowing between the solar receiver and the chemical reactor) and limits the heat losses. Cavity-type solar reactors can generally be classified depending on the method of heating the reactants i.e. directly or indirectly (Figure I.5).

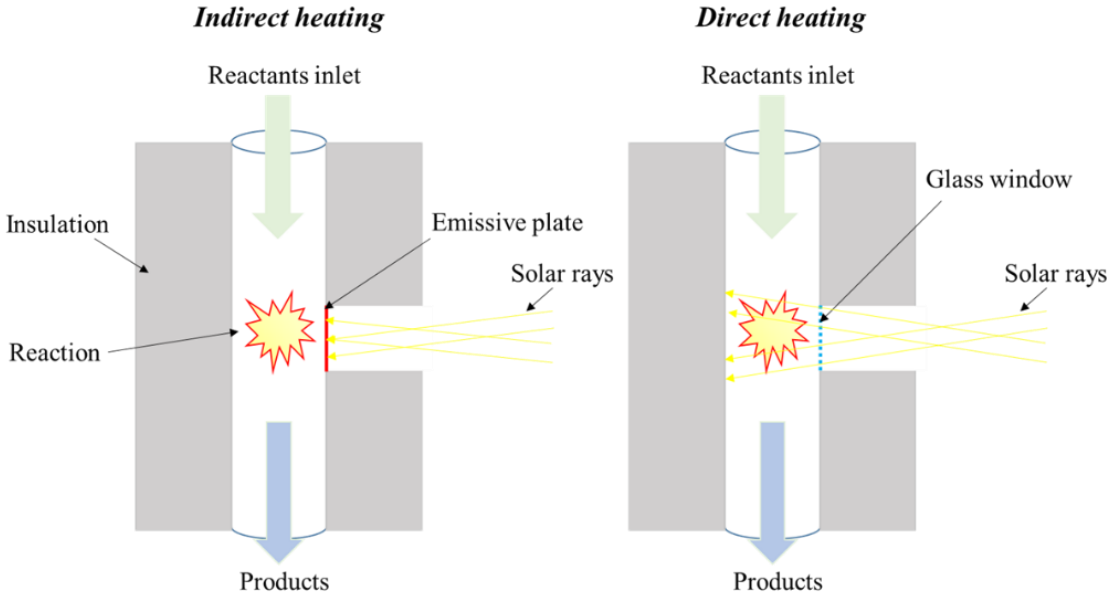

Figure I.5 Schematic of indirectly and directly heated reactors

Directly irradiated solar gasifiers generally make use of a transparent window that allows the concentrated sunlight to enter directly the reaction chamber. In such configuration, efficient solar absorption is achieved and heat losses are lowered, which enables to reach and maintain high temperatures (1000–1500°C). However, the transparent window mechanical resistance and cleanness are restraining factors due to inherent limitations regarding pressure and particles/smoke soiling/deposition. Alternatively, indirectly irradiated solar reactors use an opaque heat transfer wall to capture the highly concentrated solar flux and then transfer it to the reaction zone, thus avoiding the need for a transparent window. The type of material selected for the emissive wall should be constrained by its resistance to thermal shocks and maximum operating temperature, while it should offer chemical inertness, radiative absorbance, high thermal conductivity, and suitability for transient operation.

Different performance metrics were used in the literature to assess the performance of the solar conversion. The main performance indicators are recalled here: (i) the Carbon Conversion Efficiency (CCE, Eq.I.7) (ii) the Cold Gas Efficiency (CGE, Eq.I.8) and (iii) the Solar-to-Fuel Efficiency (SFE, I.9). The CCE quantifies the extent of biomass conversion inside the reactor. The CGE (also called upgrade factor) is the ratio between the calorific value of syngas and that of the initial feedstock. The SFE represents the ratio between the calorific value of syngas over the total thermal energy that enters the reactor including solar and biomass.

$$CCE = \frac{\mathrm{m}_{C\ in\ syngas}}{\mathrm{m}_{\ C\ in\ feedsotck}} \quad I.7$$

$$CGE = \frac{LHV_{syngas} \cdot \mathrm{m}_{\ syngas}}{LHV_{\ feedstock} \cdot \mathrm{m}_{\ feedstock}} \quad I.8$$

$$SFE = \frac{LHV_{syngas} \cdot \mathrm{m}_{\ syngas}}{Q_{solar} + LHV_{\ feedstock} \cdot \mathrm{m}_{\ feedstock}} \quad I.9$$

LHV of syngas/feedstock is the species Low Heating Value ($J.kg^{-1}$), m_i (kg) is the converted/produced feedstock/syngas mass. Q_{solar} (J) is the solar energy received by the reactor. Some authors expressed the SFE by another formulation, which is shown in Eq.I.10 (Kodama et al., 2002, 2010, 2010; Taylor et al., 1983). With $\Delta H_{reaction}$ the energy absorbed by the reaction.

$$SFE = \frac{\Delta Hreaction}{Qsolar} \quad I.10$$

The first solar gasifier (Gregg et al., 1980) was a directly irradiated L-shaped continuous fixed bed reactor (Table I.1-a). It was successful to convert different carbonaceous materials into syngas with more than 20% of the incoming sunlight effectively stored as fuel value in the product gas. Taylor et al., (Taylor et al., 1983a) studied few years later a directly irradiated fixed bed reactor for charcoal, wood and paper gasification (Table I.1-b, left). This reactor was irradiated from the top and the charge was pushed upwards the focal point using a piston as the gasification progressed. The obtained performance was compared to that of a directly irradiated fluidized bed reactor for CO_2 charcoal gasification. Compared to its fixed bed equivalent (Table I.1-b, right), which has a SFE (Eq.I.10) of 40%, the fluidized bed reactor reached only 10% efficiency at 950°C because of the more pronounced radiation losses on the upper part of the reactor and additional sensible losses in the exit gas. Piatkowski et al. (Piatkowski et al., 2009) studied another fixed bed reactor with batch mode operation (Table I.1-c). This reactor was composed of two cavities to minimize the heat losses; the upper one receives the solar radiation and heats the emissive plate, the lower one gets heated by the hot emitter to drive the thermochemical gasification reactions. The reactor was used to convert a wide variety of carbonaceous waste feedstocks such as charcoal, scrap tire powder, industrial sludge and sewage sludge. Its main drawbacks were the very low conductive heat transfer rate throughout the bed that entailed significant temperature gradients and build-up that leads to slagging and sintering inside the reactor. CGE and SFE (Eq.I.9) maximum values were 1.30 and 0.29 respectively and were achieved with beech charcoal feedsotck. Kodama et al. (Kodama et al., 2002) gasified bituminous coal with CO_2 in a small-scale fluidized bed reactor directly irradiated by a Xe lamp from the side (Table I.1-d, left). The fluidized coal particles were in direct contact with the quartz window, which was detrimental to its cleanliness and mechanical integrity. Therefore, in another study, the concept was improved by developing a new solar fluidized bed reactor irradiated from the top to insure a gap between the window area and the

reacting particles (Kodama et al., 2010) (Table I.1-d, middle) a maximum SFE value of 14% (expressed by Eq.I.11 and not considering the CO_2 term) was achieved at optimal conditions. This fluidized bed reactor was further improved (Gokon et al., 2012) by adding a draft tube in the center of the reactor, which allowed homogenizing the temperature throughout the bed (Table I.1-d, right) and enhance the stirring. CCE values of up to 73% were achieved. Entrained and vortex flow reactors were also solarized, and tested under both direct and indirect heating modes. Z' Graggen et al., (Z'Graggen et al., 2006) studied directly irradiated petroleum coke steam-gasification (Table I.1-e). The vortex flow configuration allowed achieving a CCE of up to 87% in a single pass of 1s residence time and a SFE (Eq.I.10) ranging between 5-9%. In the same vein, Müller et al. (Müller et al., 2017) gasified charcoal-water slurry in a windowless indirectly irradiated reactor at elevated pressure ranging from 1 to 6 bar (Table I.1-f). The radiations first heated a U-shaped SiC cavity, around which the gas-particle stream flows in the form of a vortex. A CCE of more than 94% was obtained in less than 5s with a CGE of 1.35 and a SFE (Eq.I.9) of 0.29. Other reactor designs were investigated such as two-zone drop tube/packed bed reactors (Bellouard et al., 2017b; Kruesi et al., 2013) where a porous material was placed in the hot region of the reactor to increase the particles residence time in the reaction zone, and molten salt reactors (Hathaway et al., 2014) in which molten salt was used as both heat transfer medium and catalyst for the reaction.

In short, the main studied reactor designs were packed-bed, fluidized bed, entrained and vortex flow reactors. Packed-bed reactors were operated in batch and continuous mode. These reactors accepted a wide variety of feedstocks with different shapes and sizes thanks to long residence times. However, they faced inherent issues related to high tars content, unreacted products and temperature gradients within the bed due to poor heat and mass transfer rates. Fluidized-bed solar reactors were developed and tested to achieve homogeneous temperature distribution. They required excess steam or inert carrier gas to achieve effective mixing, which reduced their net energetic performance. Entrained and vortex flow solar reactors offered excellent heat and mass transfer rates. Their drawback is the short residence time, and the need for finely ground particle (<1 mm) feed along with the gasifying agent.

Table I.1 Summary of main previous solar reactor designs

(a)-Gregg et al.,1980 : Packed bed reactor	(b)-Taylor et al.,1983 : Packed bed (left), fluidized bed (right)		(c)-Piatkowski et al., 2009 : Packed bed reactor
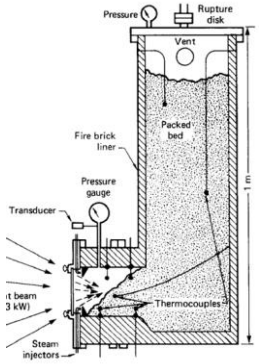	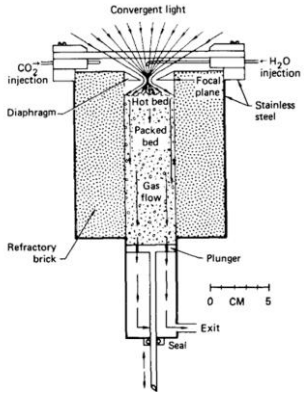	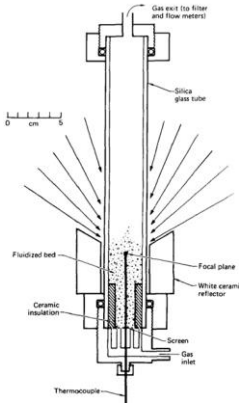	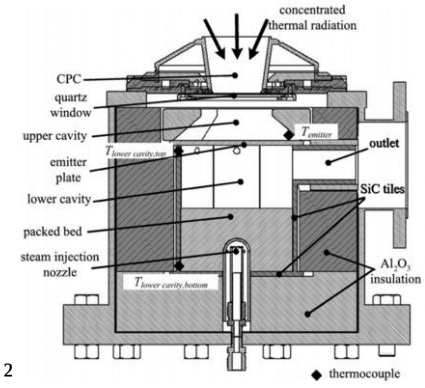
(d)-Kodama et al., 2002, (left); Kodama et al., 2010 (middle) ; Gokon et al., 2012 (right) : Fluidized bed			(e)-Z'Graggen et al., 2006 : Vortex flow reactor	(f)-Müller et al., 2017: Vortex flow reactor
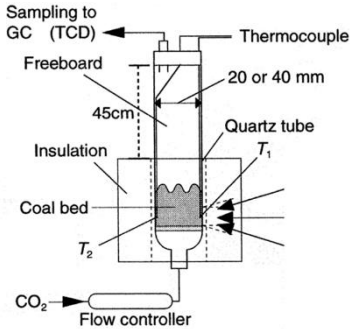	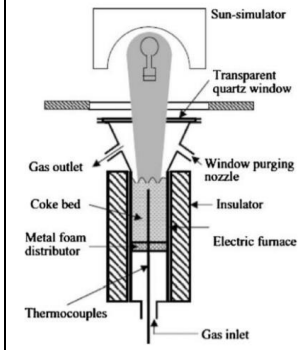	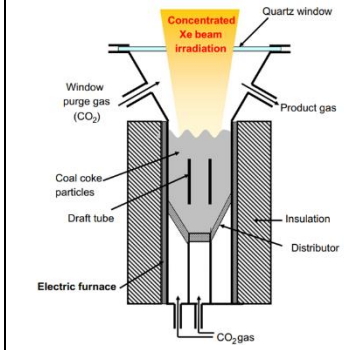	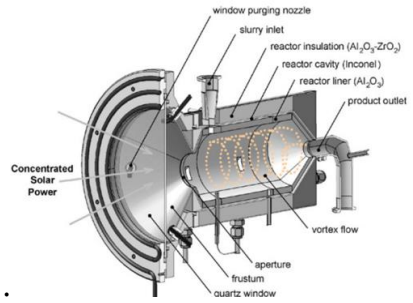	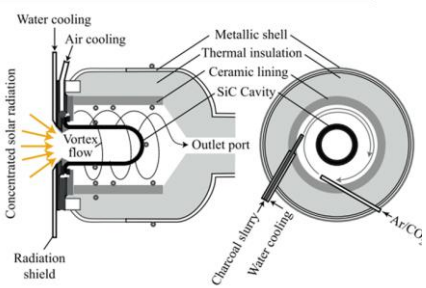

I.3.2 Management of intermittency

The significant interest and benefits of solar gasification raise the need to address the issue of solar energy intermittency to tackle varying input power and to ensure continuous operation. The continuous duty of solar gasification was pointed out very early. Bruckner (Bruckner, 1985) proposed a novel high temperature approach that increases the throughput, decreases the cost of solar driven gasification and deals with solar energy fluctuations. It consisted primarily of separating the reactor from the receiver. The receiver, placed at the top of a solar tower was filled with molten slag and was heated to temperatures up to 1800K. A thermal storage refractory vessel of molten slag was designed to insure the supply of energy to the gasifier during off-sun periods for up to 16 hours. The schematic of the process is shown in Figure I.6.

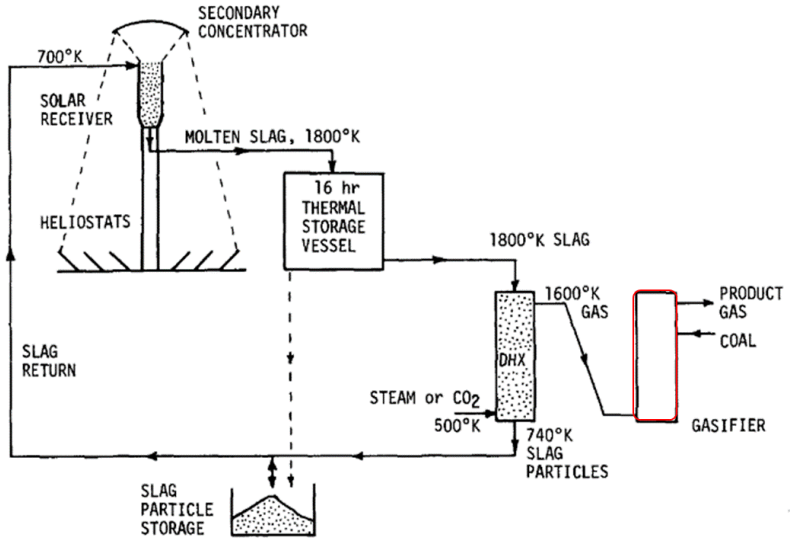

Figure I.6 Schematic of solar coal gasification system using molten slag as the heat transfer (Bruckner, 1985)

Since then, other innovative concepts were published to overcome the discontinuous solar flux. The work that comes closest to Bruckner's study considering concentrated solar energy and gasification distinctly is that of Xiao et al. (Xiao et al., 2013), Wu et al. (Wu et al., 2020) and Guo et al. (Guo et al., 2015). Xiao et al., 2013 studied experimentally a supercritical water gasification process heated by molten salt in a drop-tube helical heat exchanger/reactor (Table I.2-a). The reactor consisted of two concentric tubes where the molten salt and the supercritical water/biomass mixture flow separately. The molten salt was heated in a solar receiver represented by an electrical heater and flowed in closed circuit between the storage tank, the solar receiver, the reactor and the preheater (of biomass and water). In line with this, Wu et al., 2020 used parabolic dish collectors to generate high temperature steam, which was fed directly to a conventional gasification reactor (Table I.2-b). The high temperature steam served at the same time as the heat transfer fluid and the reactant of steam-pyrogasification. When the solar intensity was lower than the design point, air was injected in the gasifier to supply the reactor with the deficient process heat thanks to partial feedstock air-combustion. Guo et al., 2015 simulated a dual fluidized bed gasifier where the bed particles serve both as the heat storage media of high temperature solar heat and as bed materials for fluidization (Table I.2-c). In fact, the thermal energy required by steam-gasification was provided by the hot bed materials, which

were heated in a solar receiver. The bed materials described a complete loop between the warm tank, the solar receiver, the hot tank, the gasifier (which cools down the inert particles due to the endothermic nature of the reactions) and the combustor. The flow rate of the bed materials sent to the solar receiver, the hot materials storage tank level, and air injection in the combustor were controlled to deliver constant gas production rate and quality despite solar energy variability.

Table I.2 Examples of novel approaches to deal with solar energy transients thanks to the use of a HTF: receiver and chemical reactor separated)

(a)-Xiao et al., 2013: Molten salt	(b)-Wu et al., 2020 : Steam	(c)-Guo et al., 2015 : Bed particles
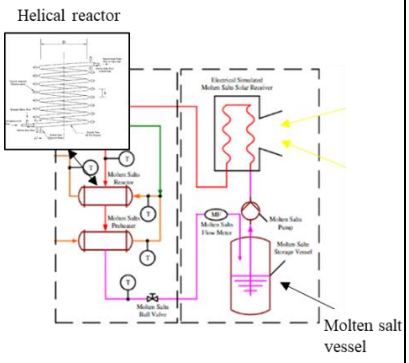	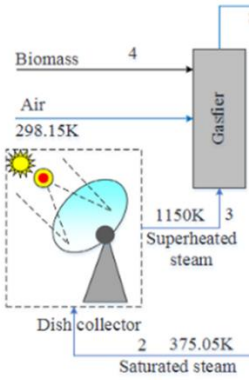	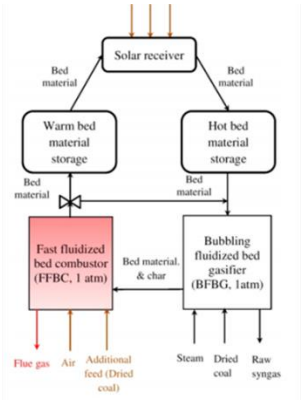

Besides, several studies concerning the management of solar intermittency were carried out on cavity-type reactors. This alleviates the complex interaction and control between the different systems components (including the HTF, piping, solar receiver, chemical reactor, storage units, heat exchangers, etc.) in addition to the significant energy and material savings that the configuration provides. Hathaway and Davidson (Hathaway and Davidson, 2017) proposed a novel solar reactor concept that makes use of molten salts acting as both reaction and heat storage media (Table I.3-a). Beyond the thermal benefits that molten salts provide concerning the stabilization of process temperature, molten salts were found to provide an effective catalytic effect on the gasification process, thereby improving the gas quality. Alternatively, a number of system-level simulation studies on biomass and coal continuous steam solar gasification considered in-situ injection of pure O_2 inside the solar cavity to overcome solar energy transients and elevate the reactor temperature (Kaniyal et al., 2013; Li et al., 2018; Sudiro and Bertucco, 2007). Muroyama et al. (Muroyama et al., 2018) were the first to demonstrate experimentally on an indirectly irradiated fluidized bed reactor the effectiveness of hybridization (i.e. combined solar gasification and oxy-combustion) to increase the reactor temperature (Table I.3-b).

Table I.3 Cavity-type solar reactors dealing with solar energy transients

(a)-Hathaway et al., 2017 : Molten salt reactor	(b)-Muroyama et al., 2018: Hybrid solar/combustion fluidized bed reactor
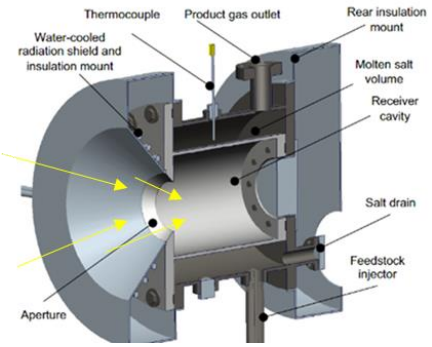	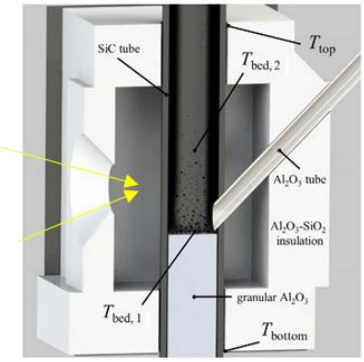

I.3.3 Scale up

I.3.3.1 Pilot scale projects

To date, only two pilot scale extrapolation projects were carried out. The Synpet project (Zacarías et al., 2010) concerned the study of a 500-kW solar cavity-type vortex flow reactor based on the work of Z'Graggen et al., 2006 and the Solsyn project (Wieckert et al., 2013) concerned the study of a 150-kW cavity-type packed bed reactor based on the work of Piatkowski et al., 2009 (Figure I.7). For the vortex flow reactor, a special unit based on pneumatic conveyor to supply the reactor with reacting petcoke particles from the ground was needed. In the packed bed configuration, the reaction chamber was filled with the feedstock prior to the experiments in batch mode operation. It involved six carbonaceous biomass and waste feedstocks with different morphologies and heterogeneous compositions. In the Synpet project, several defects and malfunctions (cracks, breaks etc.) were encountered during the commissioning phase. Furthermore, the reactor inner temperature during last tests could barely achieve 1050°C, against 1100-1300°C, which are the targeted values for ideal thermoconversion in the vortex flow reactor. Numerous points of improvement were highlighted to enhance the design, the durability and the robustness of the reactor. This first experience was valorized within the framework of the Solsyn project, which showed very positive outcomes with an upgrade of the feedstock calorific value by a factor of up to 1.3. The study demonstrated experimentally the technical feasibility of the process, its flexibility to handle several types of carbonaceous loads and its scalability.

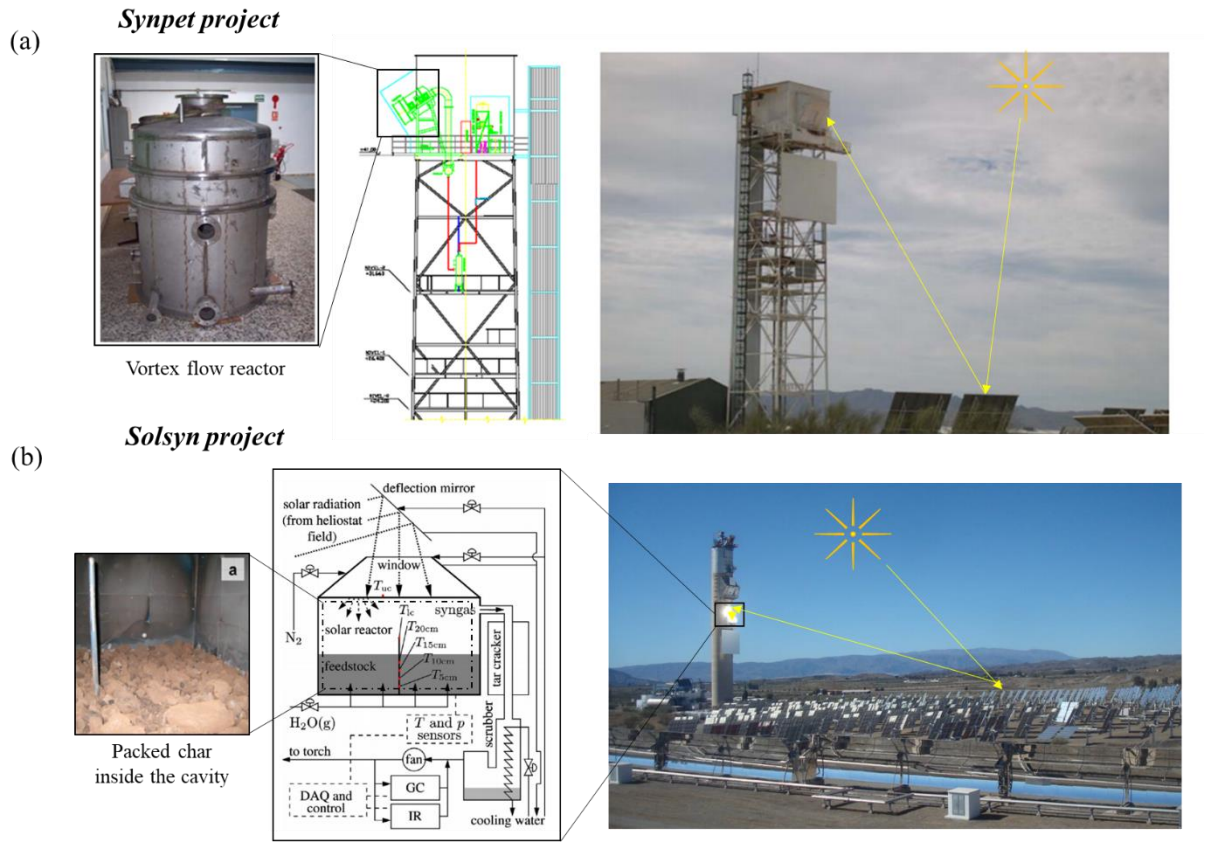

Figure I.7 Pilot scale projects: Synpet and Solsyn (Zacarías et al., 2010; Wieckert et al., 2013)

I.3.3.2 Simulation studies

Recent simulation studies on up-scaled solar reactors focused on liquid fuels, heat, cold and power generation. Globally, the published studies allowed quantifying the gains in materials and energy that can be achieved through solarization. The aim of this section is not to make an exhaustive inventory of research but rather, to show the main outlined integration pathways of solar gasification as well as the previously studied routes for solar-boosted syngas valorization. The most relevant studies covering the area are recalled here.

Kaniyal et al. (Kaniyal et al., 2013) studied the energetic and environmental performance of a Coal-To-Liquid (CTL) process integrated with a solar hybridized oxygen blown gasifier. The dynamic operation of the solar CTL system was modeled using MATLAB code that assumed steady-state operation at each time-step. The process incorporated an oxygen storage system to accommodate the variable solar flux through partial feedstock oxy-combustion and an upgraded syngas storage unit (H_2:CO~2.26) to reduce the syngas flow fluctuations due to solar energy variation and combustion. Different gasification temperature scenarios were studied. It was found that under equilibrium conditions at 1400°C and 1 bar, the total energetic output is improved by 21% on annual average with a reduction of 30% in greenhouse gas emissions as compared to a conventional non-solar process. Furthermore, the pressurized storage of oxygen was found to significantly reduce the capacity of the Air-Separation Unit (ASU) and the storage of the upgraded syngas allowed to operate within normal operational range. Thus, none of downstream chemical processes (especially the Fischer-Tropsch unit) required further development, except the solar gasifier.

In the same vein, Sudiro and Bertucco (Sudiro and Bertucco, 2007) studied simultaneous natural gas reforming and coal gasification. The complete process (including Fischer-Tropsch synthesis, hydrocracking reactor, and separation of products) from coal and methane to synthetic fuels was simulated using steady state conditions with Aspen Plus. The study showed that the solar process emits much less CO_2 (0.67 kg/kg fuel) than CTL and coupled GTL (Gas-To-Liquid) processes. Moreover, its CGE, defined as the ratio of the LHV of products (at the process outlet i.e. liquid fuels) over the LHV of feedstock in MW, is not far from 100% and much higher than that of a conventional carbon to liquid process.

Similarly, Li et al. (Li et al., 2018) studied an ICE-Combined Cooling Heating and Power (CCHP) system driven by the solar/autothermal hybrid gasifier (SAHG) with an indirectly irradiated two-cavity reactor. A simplified zero dimensional steady-state model was proposed to analyze the effects of the oxygen-to-feedstock and steam-to-feedstock ratios on gasification performance. Then, energy assessment of the SAHG-CCHP plant was conducted on a yearly basis assuming a period of operation from 7 a.m to 7 p.m each day. In this study, biomass, steam and oxygen flow-rates were controlled in order to maximize the syngas calorific value and minimize the amount of steam in the reactor. The study showed that the solar hybrid process achieves a yearly average increment of 14.2% in primary energy ratio under the solar radiation condition of Singapore. Moreover, increments in heat, power, and cooling of 19.5%, 23.8%, and 4.5%, were reached, respectively as compared to autothermal (non-solar) gasification.

Finally, Wang et al. (Wang et al., 2019) proposed a novel CCHP system based on solar-only thermal biomass gasification. The influence of key parameters such as the electric load ratio and the solar direct normal irradiance in the off-design work conditions on the thermodynamic performances was analyzed. The study showed that the solar thermal biomass gasification increased the heating value of product gas by 55.09% as compared to autothermal processes. The biomass saving ratios were approximately 9.22% and 2.02% in the cooling and heating modes respectively.

Large-scale system-level studies thus confirmed the promising interest in solar gasification. The coupling possibilities are numerous and cover a wide range of applications from the production of thermal energy and electricity to liquid fuel synthesis. The published studies showed that materials, energy and environmental benefits are substantial.

In the following, a focus on spouted bed reactors is made. This type of reactor technology constitutes the heart of the present study. Thus, their operation, design features and variants as well as the previously developed spouted bed gasifiers are presented.

I.4 Spouted bed reactors

I.4.1 Hydrodynamics

I.4.1.1 Flow regimes

With a conical-cylindrical geometry, the hydrodynamics of conventional spouted bed reactors is characterized by a cyclic motion of the solid particles (Figure I.8). Indeed, at the reactor inlet, a gas jet entrains the solid particles from the bottom through the central zone to the bed peripheral surface in the form of a fountain; the particles then reach the annular zone between

the inner walls and the central jet under the effect of gravity. The particles move back down towards the inlet and get re-entrained cyclically. In contrast to fluidized beds, conventional spouted bed reactors are distinguished with two zones of varying particles concentration, the dilute central zone in which the gas jet transports the particles in co-current, and the dense annular zone in which part of the jet flows in counter-current.

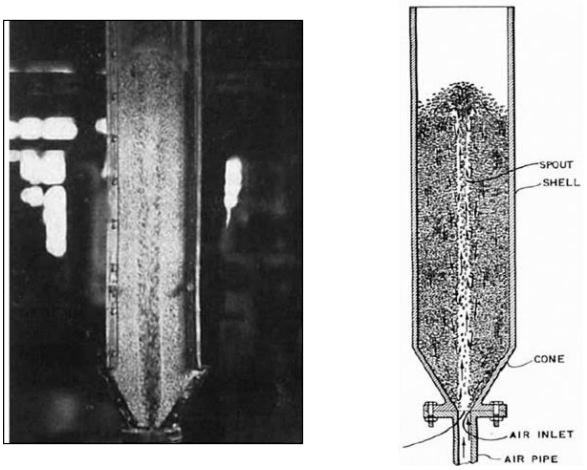

Figure I.8 Photography and scheme of a conventional spouted bed reactor (Mathur and Gishler, 1955)

For a given reactor geometry, bed height, and gas jet velocity, hydrodynamics in spouted beds can vary, affecting heat and mass transfer. Basically, three flow regimes are generally observed, the spouting, the incoherent spouting and the slugging regimes. The stable spouting occurs beyond a minimum inlet gas velocity (U_{ms}: minimum spouting velocity in $m.s^{-1}$). The incoherent spouting occurs when the inlet gas jet velocity is very high, which alters the cyclic operation and destabilizes the coherent mixing. Slugging takes place when the jet velocity is further higher such that the central jet disappears and gas bubbles form (Mathur and Gishler, 1955).

Marowski and Kaminski (Markowski and Kaminski, 1983) mentioned the possibility of operating at high speeds while maintaining a very stable cyclic flow thanks to the jet-spouting regime in dilute conical jet spouted beds (i.e. average void fraction > 0.75 and a shallow bed thickness ~2 or 3 times the reactor upper diameter, Figure I.9). Conical spouted bed reactors are characterized by a different bed structure and hydrodynamics. In contrast to the conventional spouted beds, conical spouted beds operate with a bed of particles, which is essentially distributed in the conical zone, and the upper cylindrical zone is reduced. In the jet spouting regime (diluted regime), the cycle time is about 0.5 s compared to 100 s in conventional spouted beds. Furthermore, in contrast to conventional spouted beds in which a velocity increase alters the flow stability, higher inlet gas speed favors access to the jet spouting regime in conical spouted beds.

Flow regime maps for both technologies giving the possible flow regimes at a fixed initial bed height, particles properties, inlet velocity and reactor geometry (i.e. cone angle, gas inlet diameter, cylinder diameter etc.) were previously published (Markowski and Kaminski, 1983; Olazar et al., 1992)

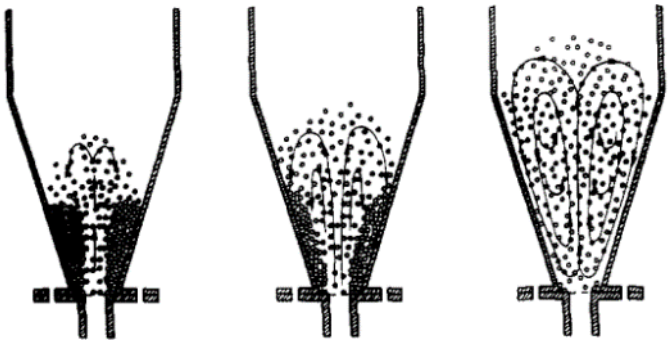

Figure I.9 Transition from spouting to jet spouting/fast spouting regime (Markowski and Kaminski, 1983; Olazar et al., 1992)

I.4.1.2 Segregation

Unlike fluidized bed reactors, conical spouted bed reactors handle very well uniform particles distributions, coarse particles, those of different natures (different densities) and also of non-regular texture and distributions. Indeed, low particle segregation was observed (Bacelos and Freire, 2008; Olazar et al., 1993; San Jose et al., 1994). San Jose et al., 1994 conducted a series of experiments on a conical reactor to study the distribution of spherical glass particles in the reactor. For this purpose, two diameters of 1 mm and 7 mm were used with a proportion of 50 wt.% of each. A peak particle concentration of 7 mm was observed at the annular zone with longitudinal segregation of the particles, which was explained by the fact that the larger particles have shorter trajectories and reach the central zone much earlier than the finer particles. Olazar et al. (Olazar et al., 1992) observed that the cone angle plays a crucial role in the treatment of large particle distributions; it was concluded that the ability of the reactor to treat particles of different sizes and textures decreases as the angle increases. Compared to conventional spouted bed reactors, conical reactors have demonstrated lower segregation, which allows them to treat sticky particles with different textures and size distribution (Altzibar et al., 2017).

I.4.1.3 Variants

Other reactor variants were investigated. The so-called spout-fluid bed reactors have the virtue of combining the principle of spouted beds with that of fluidized beds (Table I.4-a). This kind of reactor is characterized by very good wall-to-bed heat exchange coefficients that are higher than those of the fluidized bed and conventional spouted bed reactors (Zhong et al., 2006). An auxiliary gas flow is introduced through a porous distributor at the periphery of the inlet orifice. This flow ensures a better solid/gas contact and mixing especially in the dense annular region; moreover, it avoids possible bed agglomeration and dead zones. Furthermore, it minimizes particle sticking at the base of the cone and defluidization problems. This variant is interesting for sticky solid particles to avoid the formation of packed parcels in the annular zone and to extract a maximum of heat from the walls in case of wall-heated reactors.

Another variant consists in using a draft (Table I.4-b), which allows a better control of the gas residence time and the duration of particles cycle thanks to its size, its distance from the inlet and its geometry. Altzibar et al. (Altzibar et al., 2014) reported that the use of a draft increases

bed stability, decreases pressure drop, and peak pressure drop during the start-up. In addition, it was reported (Makibar et al., 2011; Nagashima et al., 2009) that these reactors operate at lower gas flow rates than conventional ones (without a draft), thus higher gas residence times can be achieved. In addition, the drafts can be porous, the porosity increases the gas flow in the annular zone.

Conventional conical spouted bed reactors are characterized by their short residence times, which is an excellent feature for minimizing pyrolysis side reactions in a process aiming at producing bio-oil. However, these short residence times (~1 ms) (Olazar et al., 2009) represent a major drawback for gasification since a short gas residence time is not favorable for tar cracking and reforming reactions. In gasification, it is necessary to maximize the gas residence time and increase the direct contact with high temperature surfaces. To overcome this problem, Lopez et al. (Lopez et al., 2017) proposed a new conical spouted bed reactor geometry that both increases the residence time of the gases and the gas/solid contact surface (inert bed or catalyst) (Table I.4-c). This geometry makes use of a non-porous draft, which minimizes the amount of gas flowing into the annular zone and facilitates access to spouting, and a confiner that confines the bed fountain. Altzibar et al. (Altzibar et al., 2017) first used this system in their study on ultrafine powders; the new reactor configuration allowed confining the fountain and reducing the particles entrainment through the exit by up to 70% while enlarging the spouting stability zone. This new reactor variant makes it possible to operate with finer catalyst particles for example in gasification, which increases the absorption surface and reduces the minimum spouting velocity (because of smaller particle sizes). As a result, the minimum spouting speed is lower, gas residence time is longer and the gas phase swept volume is greater.

Table I.4 Spouted bed variants

(a)- Zhong et al., 2006: Spout-fluid bed	(b)- Altzibar et al., 2014: Spouted bed with draft tube	(c)- Lopez et al., 2017: Conical spouted bed with confiner and draft tube
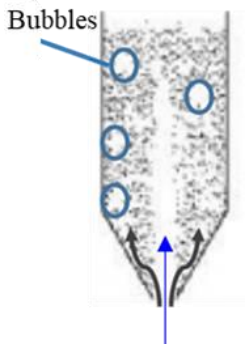	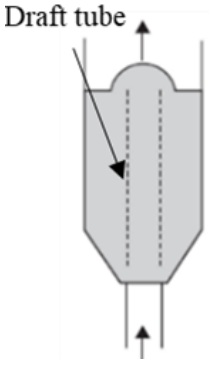	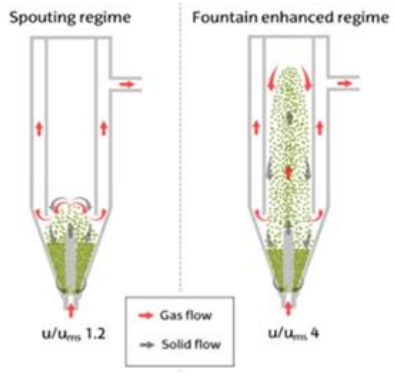

I.4.2 Design

A summary of the main outlined design rules/recommendations for a proper spouted bed operation is provided in this section. To facilitate reading, Figure I.10-left recaps the main characteristic dimensions of a spouted bed reactor.

Bilbao et al. (Bilbao et al., 1987) and San Jose et al. (San Jose et al., 1991) observed that the design of the gas inlet has a great influence on the stability of the bed. Thus, Olazar et al. (Olazar et al., 1992) tested and analyzed the hydrodynamics of the jet for several types of inlet (Figure I.10-right). It was observed that the flow in the reactor for inlet (a) (Figure I.10-right) is very unstable, especially for particles with diameters less than 6 mm: the jet rotates and changes position constantly. In inlets (b) and (c), the tip of the injection tube protruded beyond the conical base. An accumulation of particles at the gas inlet was observed for inlet (b) although the flow was more stable compared to (a). For inlet (c) (just as (b), the injection tube protruded from the conical base), it was observed that the converging geometry of the inlet pipe does not change much to the flow stability. Inlet (d) had fixed blades, these blades led to a very small improvement in the solid/gas mixture while inlet (e) showed a much better stability without limitation with respect to particle diameter. Finally, it was reported that the length of the gas injection tube is an important parameter to stabilize the flow. A minimum length of $5.D_o$ was this way recommended.

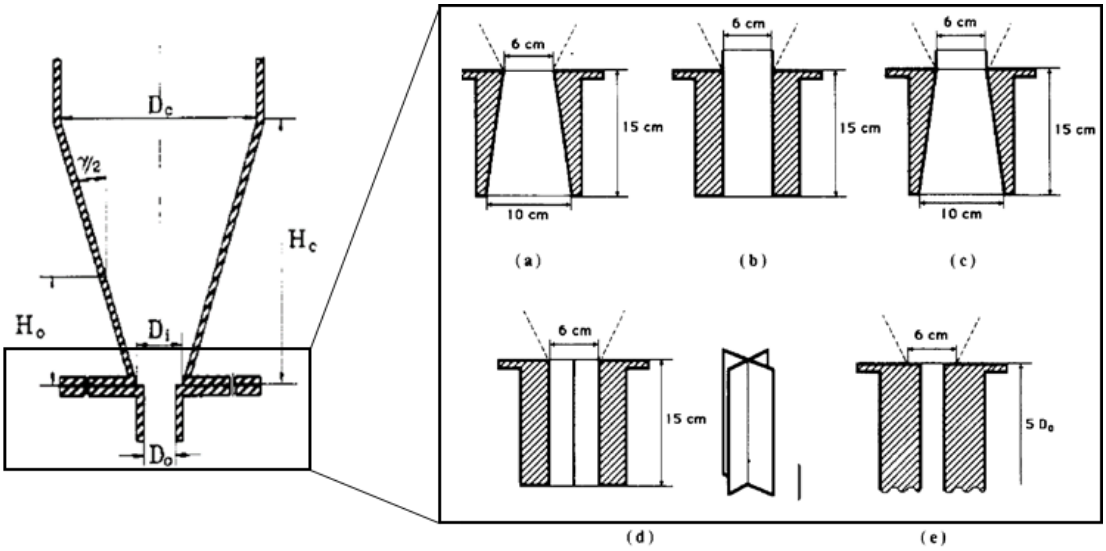

Figure I.10 Key dimensions in a spouted bed reactor (Olazar et al., 1992)

Three other geometrical parameters influence the spouting in spouted beds: D_o/D_i, γ, D_o/d_p. According to Olazar et al., 1992 , the D_o/D_i ratio must range between 1/2 and 5/6. The minimum value is due to the occurrence of dead zones at the bottom of the reactor, which have a direct effect on the mixing. The maximum value is due to observed instabilities resulting from jet distortion. The cone angle γ should range between 28° and 45° for a suitable operation and a proper stability region. When the angle γ is less than 28°, the cyclic motion is more difficult to reach. When γ is greater than 45°, the jet is altered and distorted, especially for small particle sizes. Romankov and Rashkovskaya (Romankov and Rashkovskaya, 1979) in their studies on the drying of suspended particles, recommended a cone angle of about 37°. Markowski and Kaminski (Markowski and Kaminski, 1983) used this angle value to study a small-scale conical spouted bed reactor; the small-scale reactor was successfully extrapolated to industrial scale for drying applications. Furthermore, Mathur and Gishler (Mathur and Gishler, 1955) established that the D_o/d_p ratio should be in the order of 30 for conventional spouted beds; however, this limitation was not valid in conical reactors. Experimentally, Olazar et al., 1992 did not observe

any limitation for this ratio; however, they recommended a value between 1 and 80 if jet-spouting operation is targeted and between 2 and 60 for standard spouting.

Finally, several studies on spouted beds showed that the minimum spouting velocity (generally denoted U_{ms}) increases with γ, d_p, D_o and H_o (loose static bed height). Empirical and semi-empirical correlations were proposed to predict U_{ms} for a given reactor geometry (Cui and Grace, 2008). These correlations involve geometric dimensionless parameters as well as the Reynolds number (Re) and the Archimedes number (Ar). They were determined for wide range of experimental conditions including particle size/density, reactor geometry, etc. and generally at room temperature solely. The suitability of these equations to higher temperatures is not straightforward. In fact, Ye et al. (Ye et al., 1992) and Olazar et al. (Olazar et al., 2009) showed that temperature is a sensitive factor affecting the hydrodynamics in spouted beds and generally reduces the minimum spouting gas speed. The correlation provided in (Olazar et al., 2009) for conical spouted beds was derived from a set of experiments carried out at temperatures up to 600°C. However, the aforementioned correlation can also be used at higher temperatures as the authors observed a quasi-asymptotic behavior of the velocity around 600°C.

I.4.3 Pyrogasification reactors

A number of spouted bed reactors were tested for pyrogasification. Sue-A-Quan et al. (Sue-A-Quan et al., 1995) studied the performance of a pressurized conventional air/steam spouted bed gasifier. Conversion characteristics for five different coals were studied based on the O_2/coal ratio. The experiments were carried out over a temperature range from 620°C to 900°C (below the ash melting point). The dry ash was removed and filtered from the synthesis gas. The operating pressure was varied from 500 to 144 kPa. Generally, for subbituminous coals, the spouted bed allowed to reach excellent performance with a syngas yield approaching that of thermodynamic equilibrium. The high volatile coals entailed nevertheless some difficulties in processing and the throughput was affected. The authors concluded that if appropriate measures are taken by for example injecting coal into the combustion zone or using hot circulating inert bed materials to improve the gasification operation, the spouted bed can be relevant to convert the different coals.

In a similar vein, a series of tests was carried out by Paterson et al. (Paterson et al., 2002) on an air spouted bed gasifier using a mixture of coal and sewage sludge pellets. Compared to a coal-only operation, the sewage sludge/coal co-gasification reactor showed enhanced performance. In fact, an increase in the calorific value of the synthesis gas was observed as well as a greater conversion of the raw material. It was thus concluded that sewage-based materials can be used in the spouted bed to improve the air-gasification process.

More recently, in 2015, the process of steam co-gasification of biomass and high density plastic (HDPE: High density polyethylene) was studied by Lopez et al. (Lopez et al., 2015) in a conical spouted bed (Figure I.11).

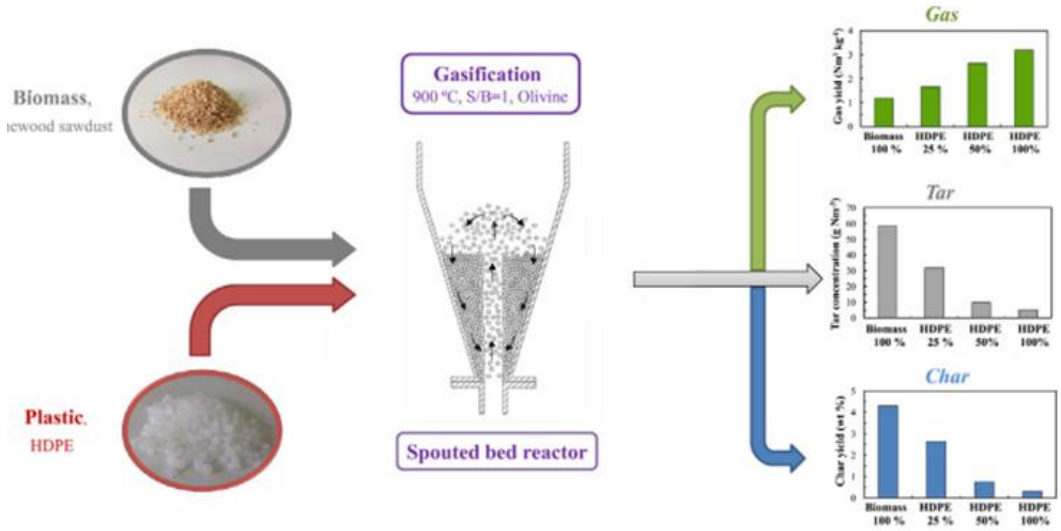

Figure I.11 Effect of biomass and plastic co-gasification on conversion (Lopez et al., 2015)

In this study, the reactor was placed inside a radiant oven of 1250 W. Olivine was used as bed material to reduce the amount of tar produced by gasification (at T~900°C). It was observed that the methane concentration was significantly reduced by biomass/plastic co-feeding while the CO and CO_2 concentrations only slightly varied. In addition, the study showed that to achieve a significant effect on the composition of the synthesis gas, a relative quantity of plastic greater than 50 wt. % is required. A more in-depth study on the plastic (Polyethylene PE) gasification in the same reactor was carried out by Erkiaga et al. (Erkiaga et al., 2013) with three bed materials (calcined olivine, γ-alumina and sand). The steps of plastic gasification in the spouted bed reactor were described as follows (Figure I.12):

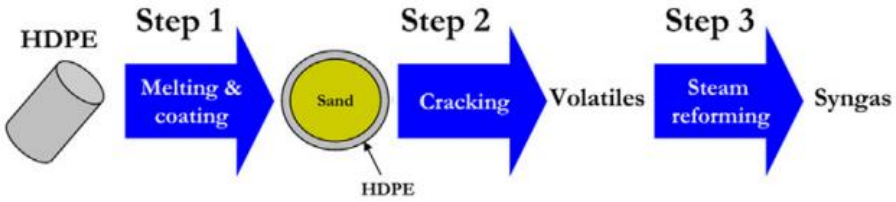

Figure I.12 Steps in the gasification of plastics in a conical jet reactor (Erkiaga et al., 2013)

It was reported that the unique hydrodynamics of the conical spouted bed reactors prevents particle bed agglomeration and defluidization problems, which are often encountered in conventional fluidized beds. In addition, heat transfer occurs immediately so that the PE particles melt and coat the solid particles rapidly. Promising performance was achieved with a H_2:CO ratio of 2.2, a very low methane and ethylene content and a molar fraction of tars (composed mainly of benzene) of less than 6 vol. %. Olivine was the material with the greatest effect on the reduction of tars.

Cortazar et al. (Cortazar et al., 2018a) improved the previous design by adding a non-porous draft and a confiner to study steam gasification of biomass using olivine as a primary in-bed catalyst (Figure I.13)

The experiments were conducted at 850°C and S/B (Steam-to-Biomass) mass ratio of two. Two bed particle diameters ranging from 250 to 333 µm and from 90 to 150 µm were compared

under the same experimental conditions. While the coarser particles barely reached a standard spouting regime, the finer ones were more severely carried upwards cyclically. The results showed that the use of a confiner remarkably increases the H_2 content and the carbon conversion rate. In addition, the fountain system plays an important role in minimizing the quantity of tars in the synthesis gas, in particular thanks to the increase in the olivine/gas contact surface and turbulence within the bed. The amount of tar decreased from 49.2 $g.Nm^{-3}$ to 34.6 $g.Nm^{-3}$ thanks to the use of the confiner, and declined from 34.6 $g.Nm^{-3}$ to 20.6 $g.Nm^{-3}$ by decreasing the size of the bed particles.

In the continuity of these first pioneering results, the effects of temperature on the composition of the syngas in the same reactor (Figure I.13) were investigated in another work of Cortazar et al. (Cortazar et al., 2018b). A temperature increase was found to positively impact the reactor throughput with a carbon conversion of more than 93% at 900°C, against around 78% at 800°C. The H_2 mass fraction was increased from 2.91% at 800°C to 7.21% at 900°C and the tar fraction was reduced by 88%.

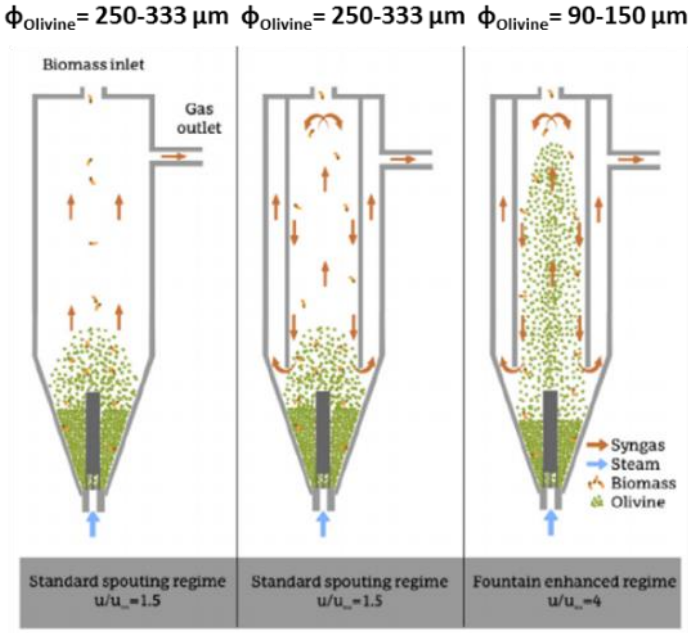

Figure I.13 Operating regimes (Cortazar et al., 2018a)

All spouted bed gasifiers found in the literature operate at temperatures below the ash softening point. Ash is usually simply filtered from the synthesis gas by cyclones and filters. Kikuchi et al. (Kikuchi et al., 1985) were the only ones to develop a spouted bed reactor that can naturally evacuate high-ash agglomerates with no simultaneous loss of coal. The reactor operates at atmospheric pressure in a temperature range of 1050-1170°C. The interest in operating at high temperatures lies in maximizing the yield of useful gases, i.e. H_2+CO, as well as improving the conversion of carbonaceous materials. The spouted bed was found to prevent clinkering thanks to its ash-agglomerating function that converts sticky ash into ash spherical agglomerates. These agglomerates get continuously expelled through the bottom of the reactor from the gas jet inlet (Figure I.14). The study showed that the amount of ash recovered depends on the H_2O:O_2 ratio. The higher the ratio, the less the amount of agglomerate is recovered and the lower is the yield of synthesis gas. The authors thus demonstrated the benefits of operating at

higher temperatures in spouted beds and paved the way for the possibility of operating at high temperatures.

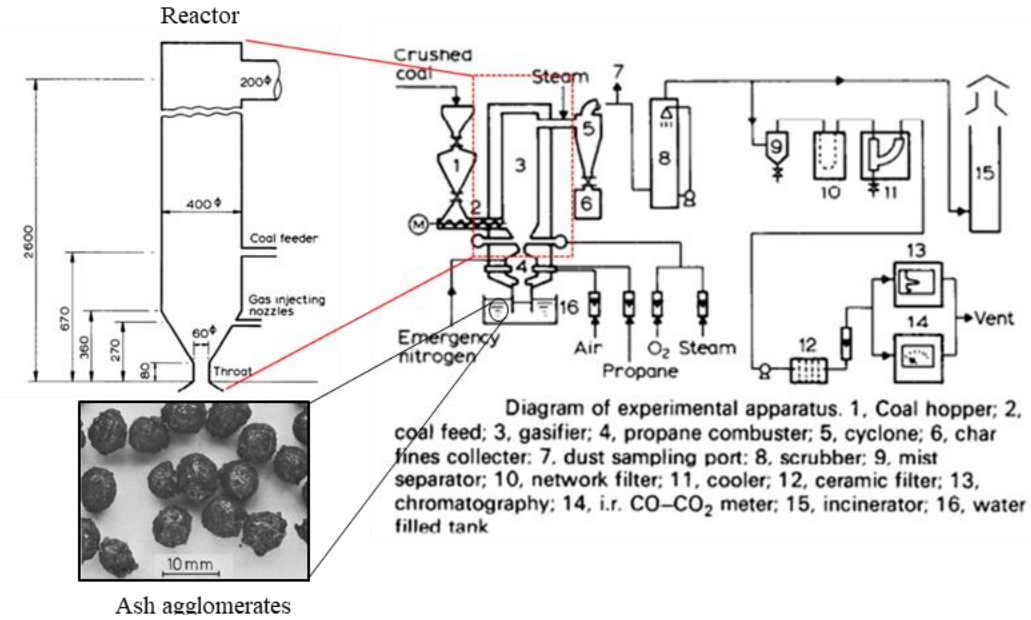

Figure I.14 Experimental bench of an agglomerating ash jet reactor (Kikuchi et al., 1985)

A novel solar conical spouted bed reactor was conceived and experimentally studied for the first time during the thesis of (Bellouard, 2017). Experiments were performed with either CO_2 or H_2O as oxidizing agents at temperatures up to 1400°C. Different types of wood particles with different diameters were investigated ranging from 0.3 mm to 5 mm. The reliable operation of the solar reactor based on this new design was achieved under real concentrated radiation using a parabolic dish solar concentrator.

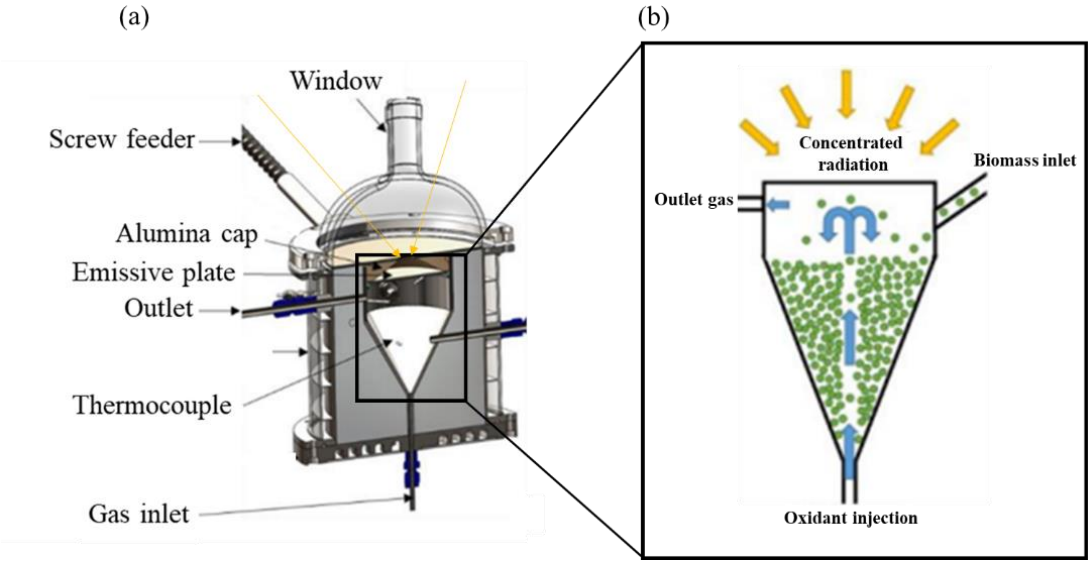

Figure I.15 (a) Detailed view of the solar reactor; (b) Scheme of the solar reactor operation

During the experiments, to prevent the injection tube from solid and liquid residues, a 1.5 cm height bed of packed SiC particles (2-3 mm size) was set initially inside the reactor. This however might have affected to a certain extent the spouting and the overall reactor

hydrodynamics. A comprehensive parametric study on the main gasification factors was carried out including temperature, reactants stoichiometry, heating method (direct or indirect), oxidant and biomass feeding rates. Delayed oxidant injection (i.e. after solar pyrolysis of feedstock) experiments were also performed to assess its impact on the products yield during the gasification phase. Very high conversion efficiencies were achieved with a CCE over 94% and a CGE of more than 1.21 thanks to solar heating. The rise of temperature and the injection the oxidizing agents in overstoichiometric proportion were found to improve the syngas yields. A comparison between the developed solar reactor design features (injection diameter/design, cone angle, spouted particles, etc.) and the presented literature recommendations is performed, it is provided in ANNEX 1.

In order to better grasp the operation of this new reactor, the current thesis proposes to study by CFD modeling the flow of particles and gases coupled with radiation and chemical reactions in the solar cavity. Several steps are involved in the decomposition of the reactive particles and several models exist to take into account the chemical reactions of pyrogasification. Section I.5 aims at providing a clear outlook on the existing models and the different approaches used in reactor modelling with CFD.

I.5 Pyrogasification: modelling and simulation

First, this part describes briefly the main conversion steps of biomass, including drying, pyrolysis and gasification. Second, it emphasizes the major kinetic approaches used in CFD modelling of gasifiers.

I.5.1 Drying

I.5.1.1 Description

The typical moisture content of freshly cut wood varies from 30 to 60% and can reach up to 90%, this moisture can be found in wood in two forms: external (outside the cell walls) and inherent (within the cell walls) (Basu, 2010). At room temperature, water can escape from the porous matrix of the wood by diffusion (evaporation). Near atmospheric pressure, and at 100°C, a pressure gradient induced by the boiling of liquid water controls the vaporization. As heating takes place, water separates from the solid and evaporates.

I.5.1.2 Modelling

Two approaches were widely used in gasifiers CFD modelling. The simplest method, proposed by Chan et al. (Chan et al., 1985) consists in modeling the process as a first order chemical reaction (Eq.I.11) described by an Arrhenius law characterized by a specific frequency factor and activation energy as shown in Eq.I.12. This approach has the advantage of being simple to implement, but it does not describe the actual process. The coefficients may vary with the wood type and thermodynamic and heating conditions.

$$H_2O_{\ liq} \rightarrow H_2O_{\ gas} \qquad \text{I.11}$$

$$\frac{dm_{water}}{dt} = A.e^{\frac{-E_a}{R.T}}.m_{water} \qquad \text{I.12}$$

The second method, named the droplet approach, uses a simple diffusion law to describe the evaporation of water for $T < T_{boiling}$ (Eq.I.13) (Janajreh and Al Shrah, 2013; Ku et al., 2015, 2014).

$$N_{water} = k_c\left(C_{water,p} - C_{water,g}\right) \quad I.13$$

Where N_{water} is the water flux ($mol.s^{-1}.m^{-2}$), the indices p and g denote the particle and the bulk gas surrounding the particle and $C_{water,p}$ ($mol.m^{-3}$) is deduced from the ideal gas law assuming the partial pressure of water is equal to the saturation pressure at the particle temperature T_p. k_c ($m.s^{-1}$) is the convective mass transfer coefficient, deduced from the Sherwood number correlation (Ranz and Marshsal, 1952).

At high Reynolds numbers, the flow of H_2O that escapes from the particle to the outside becomes more and more important (Stefan flow). An alternative formula (Eq.I.14) used in (Nakod, 2013) for modelling an air-fired entrained flow coal gasifier, and proposed by Miller et al. (Miller et al., 1998) and Sazhin (Sazhin, 2006) is more accurate.

$$\frac{dm_p}{dt} = k_c.A_p.\rho_g.ln(1 + b_m) \quad I.14$$

Where ρ_p and A_p are the particle density and surface, and b_m is the Spalding number. It is expressed by Eq.I.15 with $Y_{water,i}$ the mass fraction of water.

$$b_m = \frac{Y_{water,p} - Y_{water,g}}{1 - Y_{water,p}} \quad I.15$$

At $T = T_{boiling}$ Eq.I.16 is applied. This law predicts the mass loss as a function of the particle's Reynolds number. It is derived from the energy conservation applied to the particle. However, it translates the mass loss into shrinkage during drying.

$$\frac{d(d_p)}{dt} = -\frac{2}{\rho_p Lv(T)}\left[\frac{2.\lambda_g\left(1 + 0.23\sqrt{Re_p}\right)}{d_p}\left(T_g - T_p\right) + \varepsilon_p.\sigma_{rad}\left({\theta_R}^4 - {T_p}^4\right)\right] \quad I.16$$

With Lv the latent enthalpy of vaporization ($J.kg^{-1}$), λ_g the bulk gas thermal conductivity ($W.m^{-1}.°C^{-1}$), ε_p the particle emissivity, Re_p the particle Reynolds number (Eq.I.17), θ_R (K) is the radiative temperature (Eq.I.18) expressed as function of I ($W.m^{-2}.sr^{-1}$), the intensity of radiation.

$$Re_k = \frac{\rho_g V_g d_p}{\mu_g} \quad I.17$$

$$\theta_R = \left(\frac{\int_0^{4\pi} I.d\omega}{\sigma_{rad}}\right)^{1/4} \quad I.18$$

Other drying approaches were proposed such as diffusion models (Kucuk et al., 2014) and continuum models (Whitaker, 1977); they are recalled in detail in the review of Kharaghani et al. (Kharaghani et al., 2019).

I.5.2 Pyrolysis

I.5.2.1 Description

Pyrolysis takes place at temperatures between 200 and 800°C. During this stage, the biomass is thermally degraded, and volatile species consisting of light gases, water and primary tars are released. The remaining solid is called char and is mainly composed of C atoms with a small proportion of minerals (ash).

I.5.2.1.1 Char

The amount of char produced, its reactivity and morphology depend strongly on the final temperature and the heating rate of the particles. Indeed, the higher the heating rate and temperature, the lower is the amount of char (Iwasaki et al., 2014; Vigouroux, 2001). Some researchers (Dall'Ora et al., 2008; Keown et al., 2005; Williams and Besler, 1996) associated this phenomenon by the self-gasification of char with highly reactive volatile pyrolysis products. Furthermore, while Septien et al. (Septien et al., 2018) observed that the char reactivity increases with the heating rate due to a more damaged structure, van Heek and Mühlen (van Heek and Mühlen, 1991) observed that a temperature increase adversely affects the char reactivity due to a reduced number of active sites and of edge atoms. The size of particles is also a very important parameter that affects the formation of char, particularly due to higher heat transfer limitations (i.e. lower heating rates and temperature at the core of the particle) (Van der Drift et al., 2004) and longer volatiles residence time inside the pyrolyzing solid matrix, resulting in more pronounced secondary reactions (Bamford et al., 1946). Other factors such as the material physico-chemical properties, its structural characteristics and its moisture content have also an influence on the pyrolysis process and may strongly affect the yield of char and volatiles.

I.5.2.1.2 Volatiles

Light gases are mainly composed of H_2, CO, CO_2, CH_4, C_2H_2, C_2H_4, C_2H_6 and C_6H_6. Primary tars are composed of hundreds of molecular species produced by the thermal decomposition of biomass macromolecules, and are compounds derived from cellulose, hemicellulose or lignin. Secondary reactions of the primary tars (from 400°C to 600°C) can take place both inside the biomass particle and outside. These reactions produce secondary (600°C to 800°C) and tertiary (800°C to 1000°C) tars. Secondary tars are composed of phenols and alkenes. Tertiary products are characterized by aromatic compounds without oxygen substituents (Milne and Evans, 1998). The increase in the severity conditions (i.e. temperature x gas residence time) leads to two types of transformations for tars (Delgado et al., 1996; Milne et al., 1998; Nowakowska, 2014; Xiao et al., 2017)

1- The appearance of heavier and more stable molecules (Polycyclic Aromatic Hydrocarbons: PAH) such as naphthalene and anthracene

2- The decomposition into lighter species by various mechanisms such as partial oxidation mechanisms (if O_2 is present), thermal cracking (>1100°C), steam reforming, dry reforming or hydrogenation.

I.5.2.2 Modelling

I.5.2.2.1 Major features

To simulate the pyrolysis step, a model representative of the aforementioned phenomena is needed. Yet, there is no model that is valid over a wide range of operating conditions, and most models are often based on experimental data developed for a specific biomass sample under well-defined conditions (Elfasakhany et al., 2008). A low temperature model is therefore difficult to extrapolate to higher operating temperatures.

Different classes of kinetic models were proposed for the pyrolysis of wood and other lignocellulosic materials (Di Blasi, 1993): one-stage global single reaction, one-stage multi-reactions and two-stage semi-global. The third class considers pyrolysis as a two-stage reaction: the products of the first reaction (volatiles and gases) react to produce other species. Multi-component degradation mechanisms were also proposed. They come closer to reality but require proper biomass characterization and rigorous determination of kinetic parameters for each of these components. It is generally assumed that there are no interactions between these components. In addition, these models include an intermediate activation step that forms an active biomass component with the same chemical properties as the starting biomass but with modified physical properties such as porosity (Di Blasi, 1997).

Even with progress of science and the multitude of approaches proposed for the pyrolysis process, there is still no prominent method capable of predicting char and volatile yields since these data are highly dependent on particles type, composition, size and operating conditions. Often, model unknowns are inferred from experiments conducted at very low residence times to minimize secondary pyrolysis reactions.

In the following, a focus on the modeling of tars and char conversion in gasifiers is made. Light volatiles (i.e. H_2, CO, CO_2, CH_4) conversion is generally described by global chemical reactions modelled by Arrhenius laws (Mularski et al., 2020).

I.5.2.2.2 Tars

The condensable phase of the pyrolysis gases is made up of a very complex mixture of chemical species, the consideration and the complete identification of the compounds constituting the tars as well as their kinetic modelling would require very large calculation times. The use of model compounds to describe their behavior can be interesting (Baumlin, 2006). However, the choice of the model compound is not always obvious. This choice can be made either on the most abundant compound in the vapors, or representing the major chemical family, or on the compound with the most limiting cracking kinetics, or on the compound with a cracking rate closer to that of real biomass vapors (Nowakowska, 2014).

Because of the complexity of the problem, several CFD studies on gasification reactors did not take into account tars (Ibrahimoglu et al., 2017; Ku et al., 2015; Liu et al., 2014; Myöhänen et al., 2018). This is often related to their low concentration in the synthesis gas due to the severity of the operating conditions of the reactor. This hypothesis must systematically be verified by experimental measurements. Thus, these models assumed that all the tars were transformed into non-condensable and/or char species. A number of authors took into account the tars thanks to a model molecule called 'tar'. Some considered that the tar species are inert and do not undergo any transformation (Gao et al., 2018; Singh et al., 2013). Others took into account only the cracking reaction to produce light hydrocarbons (Grønli and Melaaen, 2000) while others integrated a heterogeneous cracking reaction to produce secondary char (Ismail et al., 2018). More elaborate models were also used to consider refractory tars additionally in the mixture (Xue and Fox, 2014). All these authors did not provide any information on the physico-chemical properties (molar mass, viscosity, thermal conductivity, etc.) of the tar molecules. Some

researchers such as (Yu et al., 2007) modelled tars by a well-defined heavy molecule, which is expected to be largely present in the mixture during pyrolysis.

I.5.2.2.3 Char

With regard to the thermal degradation kinetics of wood, two models were mainly used. The simplest model is the one in which the mass loss of a particle follows a first-order reaction rate (Manyà et al., 2003). This approach assumes that there is a critical step with a higher activation energy representative of the complex pyrolysis mechanism (Eq.I.19). This model has been widely used in CFD modelling of gasification reactors and practical engineering applications (Basu, 2010).

$$\frac{dm_p}{dt} = k.m_p \qquad I.19$$

The Kobayashi model is another famous model that was extensively used for coal pyrolysis simulation. In this model, the mass loss is governed by two parallel competing first-order reactions with different activation energies: one plays a dominant role at low temperatures and the other dominates the reaction at high temperatures (Luan et al., 2013; Silaen and Wang, 2010, 2010). Other models such as the DAEMs (Distributed Activation Energy Models) have shown high accuracy although less used in CFD simulation of gasifiers. Contrary to the previously presented kinetic models, the DAEMs assume that the activation energy of the pyrolysis reactions follows a probability density function f(E_a) (Xiong et al., 2016).

I.5.3 Gasification

I.5.3.1 Description

Two types of chemical reactions are involved in gasification: heterogeneous reactions (solid-gas) and homogeneous reactions (gas-gas). Heterogeneous reactions convert char (solid carbon) into gas (H_2, CO and CO_2) under the action of an oxidant (O_2, H_2O and/or CO_2). The three main reactions are:

Steam gasification:

$$C + H_2O \rightarrow H_2 + CO \quad \Delta H^{T=25°C}=131.2 \text{ kJ.mol}^{-1} \qquad I.20$$

Boudouard reaction:

$$C + CO_2 \rightarrow 2CO \qquad \Delta H^{T=25°C}=172.5 \text{ kJ.mol}^{-1} \qquad I.21$$

Char oxy-combustion:

$$\beta C + O_2 \rightarrow (2-\beta)CO_2 + 2(\beta-1)CO \quad \Delta H^{T=25°C}<0 \qquad I.22$$

The oxidation reaction (Eq.I.22) with oxygen is the fastest. Oxidation of carbon by water vapor (Eq.I.20) is 50 times slower, and oxidation of carbon by CO_2 (Eq.I.21) 150 times slower. Homogeneous reactions (Eqs.I.23-I.25) are very fast and can be considered practically instantaneous at high temperatures (>1000°C) (Boudet et al., 2009)

The combustion of H_2, CO and CH_4 is given by:

$$H_2 + \frac{1}{2}O_2 \rightarrow H_2O \qquad \Delta H^{T=25°C} = -241.09 \text{ kJ.mol}^{-1} \qquad I.23$$

$CO + \frac{1}{2}O_2 \rightarrow CO_2$ $\Delta H^{T=25°C}$ =-283.01 kJ.mol^{-1} *I.24*

$CH_4 + 2O_2 \rightarrow CO_2 + 2H_2O$ $\Delta H^{T=25°C}$ =- 802.22 kJ.mol^{-1}

or *I.25*

$CH_4 + 1.5O_2 \rightarrow CO + 2H_2O$ $\Delta H^{T=25°C}$ =-519.28 kJ.mol^{-1}

The water-gas shift reaction can be written as follows:

$H_2O + CO \leftrightarrow H_2 + CO_2$ $\Delta H^{T=25°C}$ = -41.18 kJ.mol^{-1} *I.26*

Methane reforming reactions (Eqs.I.27-I.28) require longer residence times, higher temperatures and very often the presence of catalysts. These reactions are important if a synthesis gas composed only of H_2 and CO is targeted.

$CH_4 + H_2O \rightarrow 3H_2 + CO$ *I.27*

$CH_4 + CO_2 \rightarrow 2H_2 + 2CO$ *I.28*

By considering various physico-chemical limitations (chemical kinetics and diffusion phenomena), the sizing of commercial gasifiers should provide sufficient residence time for the reactants to either disappear (except for a small amount of soot at the reactor outlet), or to reach thermodynamic equilibrium in case of balanced reactions.

I.5.3.2 Modelling

There are several kinetic models to simulate the gasification step. Each model describes the gasification rate by a different expression. The conversion rate is often expressed by Eq.I.29 (Ahn et al., 2001; Mahinpey and Gomez, 2016):

$$\frac{dX}{dt} = k.F(X).(1-X) \quad \textit{I.29}$$

With X the extent of char conversion (1-m_{char}/ $m_{initial\ char}$), and k the rate constant. It varies with temperature and oxidant partial pressure (P_j) and it is generally expressed by Eq.I.30:

$$k = A.exp\left(\frac{-E_a}{R.T}\right).P_j^{\,n} \quad \textit{I.30}$$

More elaborated models include multiple rate constants to provide a more mechanistic representation of the chemical process as in the Langmuir-Hinshelwood (LH) (Gadsby et al., 1946) and the Blackwood and McGrory (Mühlen et al., 1985) models. These models are based on adsorption/desorption theories. They account for various chemical mechanisms such as the inhibition effects related to simultaneous CO_2 and H_2O gasification or to the presence of H_2 (even in low concentrations) (Barrio and Hustad, 2008; Fushimi et al., 2011; Roberts and Harris, 2007).

F(X) in Eq.I.29 is the surface function, and its formulation depends on the selected physical conversion model; the best-known models are presented in detail in the review of Gómez-Barea and Leckner (Gómez-Barea and Leckner, 2010) and are recapped in this report.

The first model is the Volumetric Model (VM) (Eq.I.31), it assumes that the reaction takes place throughout the particle in a homogeneous manner, and the internal fields of species concentration and temperature are uniform throughout the conversion process. If the external resistance is small (small particles, porous morphology etc.), this model can be applied and the

gasification rate of a particle is equal to the intrinsic chemical conversion rate of the particle (rather valid for low temperatures). Guizani et al. (Guizani et al., 2015) found that for 0.2 mm wood char particles, the conversion will take place under the chemical regime (intrinsic to the particle) up to the temperature of 800°C, and the limitations by diffusion start appearing from 900°C.

$$\frac{dX}{dt} = k_{VM}(1 - X) \qquad I.31$$

Other surface models were proposed, they are more suitable for non-porous char particles. They consider that the reaction is very fast and takes place as soon as the reactants reach the outer surface of the particle. The reaction surface is either identical to the outer surface of the particle, or to its shrinking core when the biomass contains lots of ash. In these models, the conversion rate is proportional to the external surface area of the shrinking particle/core (Eq.I.32 was established for spherical particles):

$$\frac{dX}{dt} = k_{sc}(1 - X)^{2/3} \qquad I.32$$

As described in section I.5.2, char has different properties depending on the pyrolysis conditions. This has a direct impact on the course of the gasification reactions. At the start of the conversion, the pores become larger and more open. Later, when the pores meet, a decrease in the exchange surface of the particle occurs. To account for the particle structure change, the random pore model, for which the reaction rate is expressed in Eq.I.33, was proposed.

$$\frac{dX}{dt} = k_{RPM}(1 - X)\sqrt{1 - \Psi ln(1 - X)} \qquad I.33$$

Ψ is a structural dimensionless parameter related to the initial pore structure. It is often determined experimentally with the kinetic constants (A, E_a) (Gao et al., 2018; Mahinpey and Gomez, 2016; Tomaszewicz et al., 2017).

This model can be further complexified to gain in precision as in reality; the surface reactivity is proportional to the number of active sites available rather than the surface area of the particle (Bell et al., 2011).

Finally, because of the complexity of the physico-chemical modelling, especially regarding the evolution of the particle's structure and morphology, other researchers determined empirical expressions for the apparent kinetics of the char samples from detailed experimentation and validation. Polynomial regressions were usually used for this purpose (Tagutchou, 2008; Teixeira, 2012; Van de steene et al., 2011).

I.6 Conclusion and methodology

This chapter introduced the subject of the thesis, recalled earlier studies covering the topic and provided the main technical and scientific information to conduct the work. The following conclusions can be drawn:

- Today solar technologies have reached a high degree of maturity and their coupling with high temperature thermochemical processes such as gasification is auspicious.

- Different laboratory-scale solar reactors were designed and tested. Each design has its distinctive features. The ultimate goal is to make the best use of the solar resource thanks

to optimized solar heating, minimum heat losses and proper gas/solid contacting systems that insure bed isothermicity.

- Solar reactors need to be easily scalable with minimal issues and concerns during operation at large scale. Besides, they should be robust and able to withstand the highly concentrated and variable solar flux.

- Solar intermittency is a major issue in solar gasification. For cavity-type reactors, two main solutions were proposed, the first one consists in using a heat storage medium placed inside the solar cavity to maintain the reactor temperature even in the absence of solar energy and the second one consists in using an internal injection of O_2 to increase the reactor temperature by partial oxy-combustion of the feedstock during low DNI periods.

- Among the different designs of gasifiers, spouted beds. These have shown attractive hydrodynamic and thermochemical characteristics. Generally they operate below 900°C. They were tested for biomass, waste and plastics air and steam gasification. High conversion efficiencies were achieved by spouted beds, which was associated to their very specific gas-particles flow recirculations.

- Spouted beds operate generally at low gas residence time. However, conversion can chiefly be improved through the use of in-bed catalysts to enhance the gasification kinetics. The use of draft tubes and/or confiners can increase the volume swept by gas as well as the contact surface between gas, solids and walls. Besides, low cone angles with low inlet tube diameters and fine bed particles can significantly reduce the minimum spouting velocity, which improves gas residence time.

- The operation of these reactors at higher temperatures is interesting because it improves gas quality even further. This can be achieved only through a proper management of agglomerating ashes during conversion.

This thesis aims to study a novel solar gasifier concept from laboratory to industrial scale. It is the continuation of the thesis of (Bellouard, 2017) during which a solar spouted bed reactor was conceived. First experiments showed promising results that confirm the merits and the value of the technology. However, there remains number of scientific locks and obstacles to be addressed. Questions concern the understanding of reactor operation including its hydrodynamics, heat transfer and chemistry, which would allow determining improvement strategies to achieve higher efficiencies. Other issues concern the management of the variable heat flux during both high and low DNI periods, the conversion of ashy feedstocks such as waste and finally, the MW scale reactor operation and the techno-economic feasibility of the process at large scale.

In order to answer all these questions, various simulation and experimentation tools were devised. The commercial CFD (Computational Fluid Dynamics) Fluent© code was used to

simulate the solar reactor in 2D and 3D. C++ User Defined Functions (UDFs) were developed and used as solver complements. The Python software was used to simulate the dynamic operation of the up-scaled reactor, and the DOE's H2A tool (NREL H2A, 2018) was used to analyze the process techno-economics. Besides, the experimental test bench of the solar reactor was used to validate the numerical approaches and perform complementary steady and dynamic experiments (solar-only or hybrid solar/combustion operating modes). A new transparent PMMA (PolyMethyl Methacrylate) cavity was also conceived to visualize at room temperature new flow configurations aiming at improving the previous reactor operation.

II. CHAPTER 2

Numerical and experimental study of a novel solar reactor for biomass gasification

II.1 Introduction

This chapter presents a numerical and experimental study of a novel solar reactor for biomass gasification. It is divided in three parts. The first one consists in studying, thanks to numerical simulation and experimental validation, the allothermal operation of a novel spouted bed solar reactor (Bellouard, 2017). The goal is to bring new understanding aiming at clarifying the functioning of the reactor to highlight its main hydrodynamic, thermal and chemical features and to identify areas of improvement. The second part examines for the first time, through numerical simulation and experimental tests on beech wood, a new hybrid operating mode that combines external solar heating with internal oxy-combustion to address the issue of solar energy intermittency. The third and last part focuses on solar and solar-hybrid waste gasification thanks to high temperature on-sun experimentation. An exploratory study was conducted to provide insights into the solar conversion of ashy and heterogeneous waste feedstocks in the novel solar reactor.

II.2 Allothermal operation

II.2.1 Principle and objectives

This section provides a detailed understanding of the operation of a novel lab-scale solar gasifier based on the principle of conical jet spouted (diluted) beds. CFD (Computational Fluid Dynamics) modelling comes up as a key tool to thoroughly investigate critical parameters such as heat and mass transfer rates, gas and solid residence times, fluid flow and recirculation patterns, temperature and species distribution etc. in the solar-radiated cavity. CFD solves in this way the fundamental coupled equations of physics and chemistry to predict the gasifier behavior under specific boundary and thermodynamic conditions.

Quite a few autothermal non-solar industrial and bench-scale gasifiers were studied using CFD. Lu et al. (Lu et al., 2018) presented a two-dimensional computational model of a fixed bed reactor for carbonized woody briquettes gasification based on an Euler-Euler approach. They showed that the equivalence ratio (ER) and the fuel particles size have a major influence on the product gas composition and temperature distribution within the gasifier. Ku et al. (Ku et al., 2014) studied biomass steam gasification in a fluidized bed reactor using a coupled CFD-DEM (Discrete Element Modelling) approach to account for particulate collisions. Results in terms of particle flow pattern, particle mixing and entrainment as well as product gas composition and carbon conversion were qualitatively and quantitatively analyzed. Jeong et al. (Jeong et al., 2014) studied the effect of coal particle size on the gasification process in a two-stage commercial entrained-bed gasifier based on an Euler-Lagrange method. The study showed that the carbon conversion efficiency and cold gas efficiency were maximized with a coal particle size of 100 mm. The two-stage commercial entrained-bed reactor was also investigated by Luan et al. (Luan et al., 2013). A parametric study of the 3D cross-type gasifier was conducted. The study showed that the CFD model could adequately capture the gasification behavior and explain the reactor performance. Kumar et al. (Kumar et al., 2017) used the Discrete Phase Modelling (DPM) method with a volatile break-up approach to simulate biomass gasification in a downdraft gasifier. The

volatile break-up approach[1] models the pyrolysis gases formed during the devolatilization by a pseudo-chemical species that in turn breaks up in the gas phase into different molecules (H_2, CO, CO_2, CH_4 and H_2O). The only work that deals with CFD modelling of gasification in spouted beds is that of Deng et al. (Deng et al., 2008). The authors studied coal gasification in a pressurized spout-fluid bed with an air-steam supply. The model was validated against experimental data for a 0.1 MW gasification unit operating at elevated pressure. Besides, very little research has been done concerning CFD modelling of solar gasification reactors. Bellan et al. (Bellan et al., 2018a, 2018b) were the first to investigate the thermal performance of a 30 kW fluidized bed reactor. However, chemical reactions were not taken into account and only inert bed materials were considered. Recently, Dai et al. (Dai et al., 2019) used the DPM approach to simulate a 10 kW_{th} directly irradiated vortex flow reactor for solar CO_2 coal gasification.

In this work, a 3D CFD model of the new spouted bed solar reactor was developed. Prior to CFD multiphysic simulations, a time scale analysis of the different physico-chemical phenomena taking place inside the reactor was performed. Thereafter, the reactor was simulated to capture its thermal, chemical and two-phase (gas-particle) flow features. Results in terms of temperature and species distribution, particle-flow patterns and residence time were analyzed. Experimental validation tests were conducted under real concentrated solar flux at the CNRS-PROMES solar furnace in Odeillo. Finally, process improvement strategies were identified and discussed in light of the numerical simulation results.

The results presented in this section were published in the *International Journal of Heat and Mass Transfer* (IJHMT) (Boujjat et al., 2019a).

II.2.2 Experimental test bench

II.2.2.1 Solar reactor

Spouted bed reactors were studied for many applications such as drying (Markowski and Kaminski, 1983), pyrolysis (Makibar et al., 2011) and autothermal (non-solar) gasification (Lopez et al., 2017). In this work, a novel 1.5 kW_{th} solar conical spouted bed reactor was simulated and tested under real concentrated high-flux solar energy for continuous steam gasification of beech wood particles (Figure II.1). Unlike fluidized beds in which a fluid flows through a uniform distributor plate to float the particles randomly, conical spouted beds are characterized by a small centrally located opening at the conical base of the reactor. Clearly, the gas flow rate and pressure drop are such that the resulting high-velocity jet causes particles to rise rapidly in a hollowed central core and then revert to the annular region between the central spout and the cavity walls. The vigorous cyclic flow in spouted beds allows handling solid particles of irregular texture/shape and leads to less segregation than fluidization. Hence, conical spouted beds are best suited for physical and chemical operations that require the handling of solids of wide size distribution, with sticky or cohesive nature, as it is the case for thermochemical processes such as pyrolysis, gasification

[1] Default approach of Fluent©

and combustion. Different flow patterns are possible depending on the bed height, particles properties and inlet jet velocity (Mathur and Gishler, 1955). Spouted and jet spouted/fast spouting regimes are among the best possible contacting regimes to increase heat and mass transfer rates (Olazar et al., 1992). The jet spouted regime is characterized by an inlet speed much greater than the minimum spouting velocity (U_{ms}). This regime is accessible for shallow and dilute beds (Markowski and Kaminski, 1983). Different empirical and semi-empirical mathematical formulations are available in the literature to estimate U_{ms} for conical spouted beds. The correlation of Olazar et al. (Olazar et al., 2009) is the only one established and validated up to temperatures of 600°C that correspond to pyrolysis conditions.

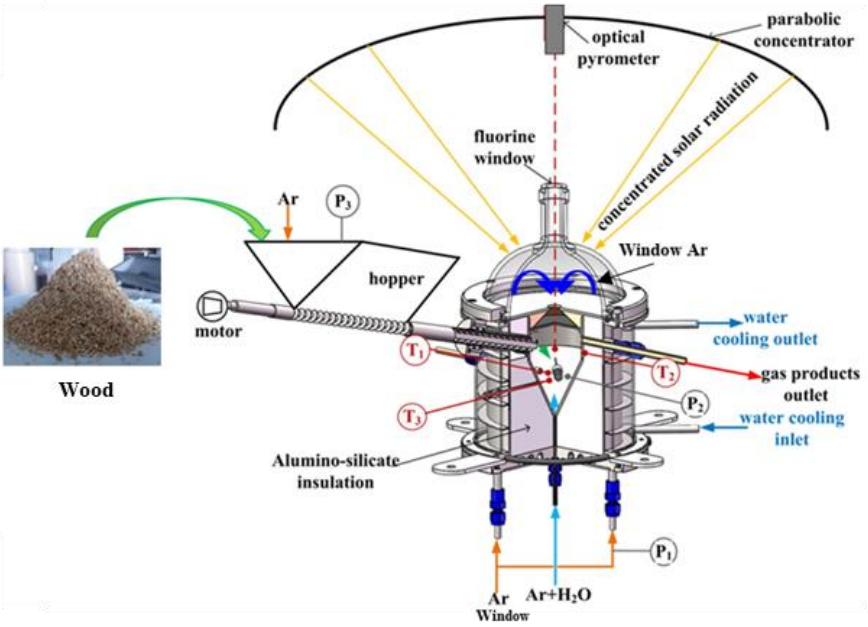

Figure II.1 Scheme of the solar reactor for biomass gasification

The 60° angle conical spouted bed reactor is made of a cavity machined in a high-temperature resistant metallic FeCrAl alloy (density (ρ): 7.1 g.cm^{-3}, thermal conductivity (λ): 35 W.m^{-1}.K^{-1} at 1400°C, heat capacity (c_p): 0.8 kJ.kg^{-1}.K^{-1} at 1400°C, emissivity (ε): 0.7). The cavity is composed of a vertical cylindrical receiver of 0.078 m inner diameter with a conical bottom (total height: 115 mm). The cavity is pierced at the bottom to allow the passage of an alumina inlet tube of 2 mm inside diameter from which the oxidizing agent is injected. The whole cavity is insulated by a 30 mm-thick layer of porous ceramic fiber made of SiO_2 and Al_2O_3 (65% Al_2O_3-35% SiO_2, ρ=400 kg.m^{-3}, λ= 0.22 W.m^{-1}.K^{-1} at 1200°C). The top of the metallic cavity is lined with an alumina cap (20 mm diameter aperture) to reduce heat losses (ρ=3900 kg.m^{-3}, λ=9.1 W.m^{-1}.K^{-1} at 1000°C, c_p=0.95 kJ.kg^{-1}.K^{-1} at 100°C). To protect the alumina cap from the direct high-flux solar radiation and minimize radiation losses, a 2 mm layer of zirconia felt and a protective graphite plate (ρ=5700 kg.m^{-3}, λ=2.2 W.m^{-1}.K^{-1} at 25°C, c_p=0.5 kJ.kg^{-1}.K^{-1} at 25°C) are placed above. A screw feeder driven by a motor is fixed to the hopper made of stainless steel (ρ=7900 kg.m^{-3}, λ=16.3 W.m^{-1}.K^{-1}, c_p=0.5 kJ.kg^{-1}.K^{-1} at 800°C, ε= 0.85) and transports the feedstock. The whole feeding system

is hermetically fixed to the reactor shell that is water-cooled. This reactor can operate in direct or indirect heating configurations. To do so, a 2 mm thick removable emitter plate can be placed below the alumina cap; this plate is made out of graphite and is covered by a SiC coating to withstand oxidation conditions. Table II.1 summarizes the main reactor materials and their physical properties.

Table II.1 Solar reactor materials (at 1400°C, otherwise specified)

Component	ρ (kg.m^{-3})	c_p (J.kg^{-1}.°C^{-1})	λ (W.m^{-1}.°C^{-1})	ε
Alumina cap	4000	795	7	0.80
FerCrAl cavity	7100	800	35	0.70
Insulation	400	800	0.22	0.20
Zirconia	5700	500 (25°C)	2.2 (20°C)	-
Graphite	1400	710 (25°C)	25 (25°C)	0.98
SiC	3100	750 (25°C)	120 (25°C)	0.96

The reactor was positioned at the focus of a 2 m-parabolic solar furnace at CNRS-PROMES. The concentrated solar power entered the cavity through the aperture positioned at the focal point of the solar concentrator (Figure II.2).

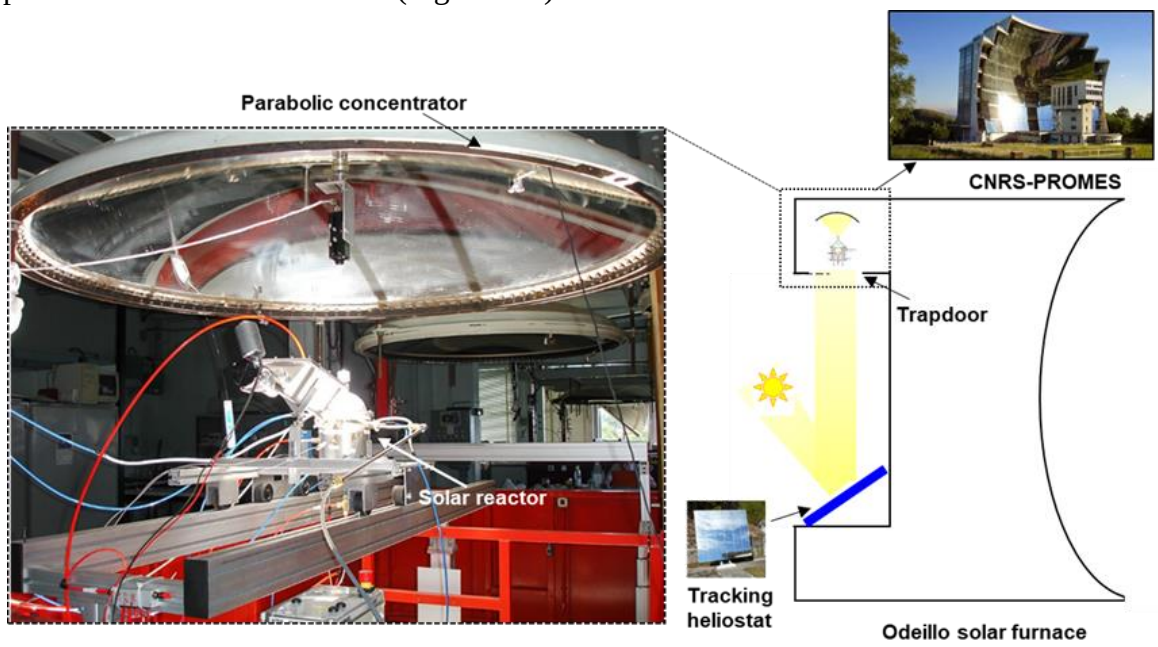

Figure II.2 Reactor coupling with CNRS vertical axis solar facility and photography of the experimental test bench

The feedstock was stored in a hopper (1.15 L capacity) and was continuously transported by a screw feeder to fall into the hot cavity by gravity until complete injection. Table II.2 summarizes the properties of the gasified beech wood particles.

An Ar flow (0.5 NL.min^{-1}) was continuously injected in the hopper and then flowed via the screw path so that the hot gas from the cavity could not interact with the feedstock. Moreover, a flow of Ar (2.0 NL.min^{-1}) was also injected below the window to prevent the hot gas and the particles from entering the window area and soiling it.

Table II.2 Beech wood particles characteristics

Chemical composition	C (wt. %)	48.3
	H (wt. %)	6.7
	O (wt. %)	44.4
	N (wt. %)	0.1
	S (wt. %)	<0.1
	Ash (wt. %)	0.46
	Hum. (wt .%)	8.9
Physical properties	$\rho_{Biomass}$ ($kg.m^{-3}$)	650
	$c_{pBiomass}$ ($J.kg^{-1}.°C^{-1}$)	1500
	$LHV_{Biomass}$ ($MJ.kg^{-1}$)	16.83

The jet gases were injected from the bottom alumina tube to spout the particles. They were composed of 0.2 $NL.min^{-1}$ of Ar and 0.2 $g.min^{-1}$ of steam, thus providing a slightly over-stoichiometric Steam/Biomass (S/B) ratio of 1.24 based on the global steam gasification reaction depicted in Eq.II.1 (where S denotes steam mass flow rate including both inlet steam and moisture contained in biomass, and B denotes dry mass feeding rate of biomass).

$$C_{6.0}H_{10.0}O_{4.1}+1.9H_2O_{(v)}\rightarrow 6.0CO+6.9H_2 \quad \Delta H°_{gasification} = 0.86\ MJ.mol^{-1} \qquad II.1$$

The produced gases flowed through a gas cleaning unit composed of a bubbler and two cartridge filters to remove excess steam and outlet char/soot particles. The synthesis gas molar composition was then analyzed continuously using an on-line gas analyzer every 3s. The mole fractions of the CO, CO_2, CH_4 and C_nH_m (mainly C_2H_2, C_2H_4, C_2H_6) were measured by non-dispersive infrared (NDIR) detectors. The concentration of H_2 was measured by a thermal conductivity detector (TCD) (the accuracy of the measuring cells is ±2 % of full scale, ranges: 0-20 % for H_2 and CO, 0-10 % for CO_2 and CH_4, calibrated with standard gases). These measurements were verified using a gas chromatograph (GC) equipped with two columns using argon as carrier gas. In particular, the GC provides more accurate data for light hydrocarbons (C_2H_m). Given the targeted high temperatures, tars were not experimentally measured and only light gaseous hydrocarbons (mainly C_2H_2 and C_2H_4) were quantified. The argon injections were carried out using three mass flow meters (Brooks SLA5850S, scale: 0-5 $NL.min^{-1}$, accuracy: ± 0.2% of full scale). Water was injected into a capillary tube positioned inside the alumina tube by means of a mass flow meter (scale: 0-30 $g.h^{-1}$, accuracy: ± 1% of full scale). As shown in Figure II.1, two thermocouples (T) directly measured the internal temperature of the cavity (T3 near the bottom of the cavity in the conical region and T1 in the center of the cavity) and one thermocouple (T2) measured the temperature at the external wall of the cavity. To protect the thermocouples from reactive gases, their tips were covered with an alumina protection tube. In addition, an optical pyrometer (Impac, operating at 4.8-5.2 μm in an absorption band of H_2O) was used and placed at the center of the parabolic mirror. Three pressure measurements were set in the window area (P1), cavity (P2), and hopper (P3). A Venturi vacuum pump was placed at the exit of the outlet tube to control and maintain the reactor pressure below 1 bar (atmospheric pressure of ~0.86 bar at site elevation). All obtained data were controlled and collected by

an automated data acquisition system (BECKHOFF). Finally, the DNI (Direct Normal Irradiance) was measured every 0.8 s using a pyrheliometer throughout the experiments.

II.2.3 Time scales analysis

A time scale analysis was carried out prior to detailed CFD simulation, which allowed quantifying the importance of some phenomena in comparison to others, thus justifying the choice of certain models and pointing out limits and possible improvements of the proposed model. It is described in ANNEX 1.

II.2.4 Model development

The developed 3D model simulated the reactive two-phase flow (biomass/gases) inside the solar reactor. The kinetics of pyrolysis and char gasification, and the particles behavior when undergoing solid-gas chemical reactions (i.e. shrinking model accounting for change in particle size), porosity and density, were hooked to the Fluent© solver thanks to User-Defined C++ Functions (UDFs). The model is described in detail in the following sections.

II.2.4.1 Geometry, mesh and boundary conditions

The 3D geometry was created to represent as close as possible the reactor design. The main mechanical components of the reactor were reproduced (Figure II.3).

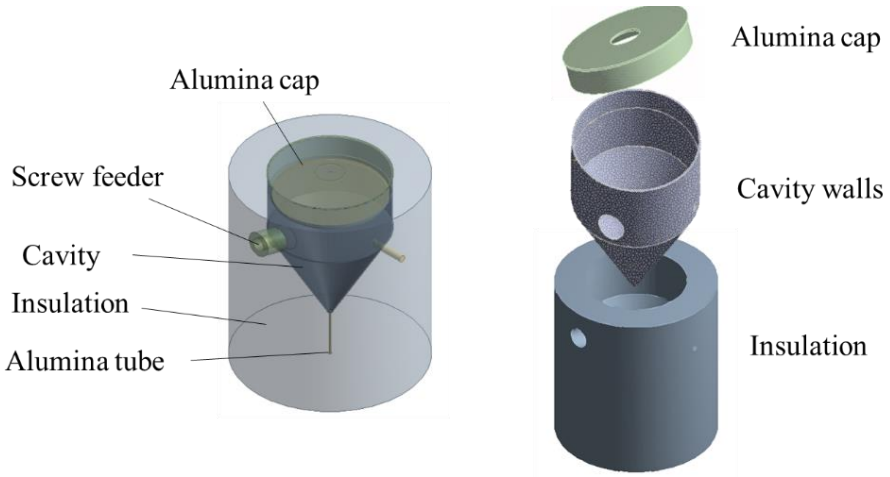

Figure II.3 3D geometry for CFD simulations

In order to avoid skewed and low quality meshes, the wall thermal resistance associated with the zirconia and graphite layers at the top of the alumina cap was taken into account by solving a 1D energy equation artificially through the thickness of the layer (assuming normal flux only). The same was applied for the screw feeder. Radiative heat losses from the reactor alumina cap and upper insulation were integrated into the model. It was assumed that these components exchange thermal energy by radiation with an external black body at 25°C ($Q_{loss}=A.\varepsilon.\sigma_{rad}(T^4-T^4_{ex})$). The reactor external borders were continuously water-cooled and thus a boundary temperature of 25°C was set. The radiative source that represents the incoming concentrated solar power was simulated by a semi-transparent surface allowing re-radiation outside of the reactor. On a geometrical point of view, the boundary condition

for the radiative source was a circle arc subtending a 120° angle, thus accurately representing the way that the concentrated solar flux enters the reactor in the current configuration. The solar power was specified in terms of an incident radiant heat flux density ($W.m^{-2}$) and was assumed specular. The internal walls of the reactor were assumed gray and opaque, they were characterized by an emissivity ε ($\varepsilon_{alumina}$=0.80, ε_{cavity}=0.70, $\varepsilon_{screw\ feeder}$ =0.85) and a diffusion fraction f_d. The latter was taken as 1 meaning that the reflected radiations are diffuse and therefore the specular component is equal to zero. The developed model assumed for the sake of simplification that the global emissivity is equal to the global absorptivity. The three reactor gas inlets (window, screw feeder and bottom gas jet inlet) were modelled with an inlet temperature of 25°C. The reactor operating pressure was fixed to 860 hPa corresponding to experimental site elevation.

A thermal/hydrodynamic study of the reactor allowed choosing the optimal cell size to accurately solve the gradients in the spout (central) region of the reactor where rapid changes in terms of velocity, temperature and species molar fraction are expected. Mesh sensitivity study was performed. Figure II.4-a shows the axial gas velocity and temperature profiles in the inlet bottom alumina tube and inside the cavity as a function of grid size.

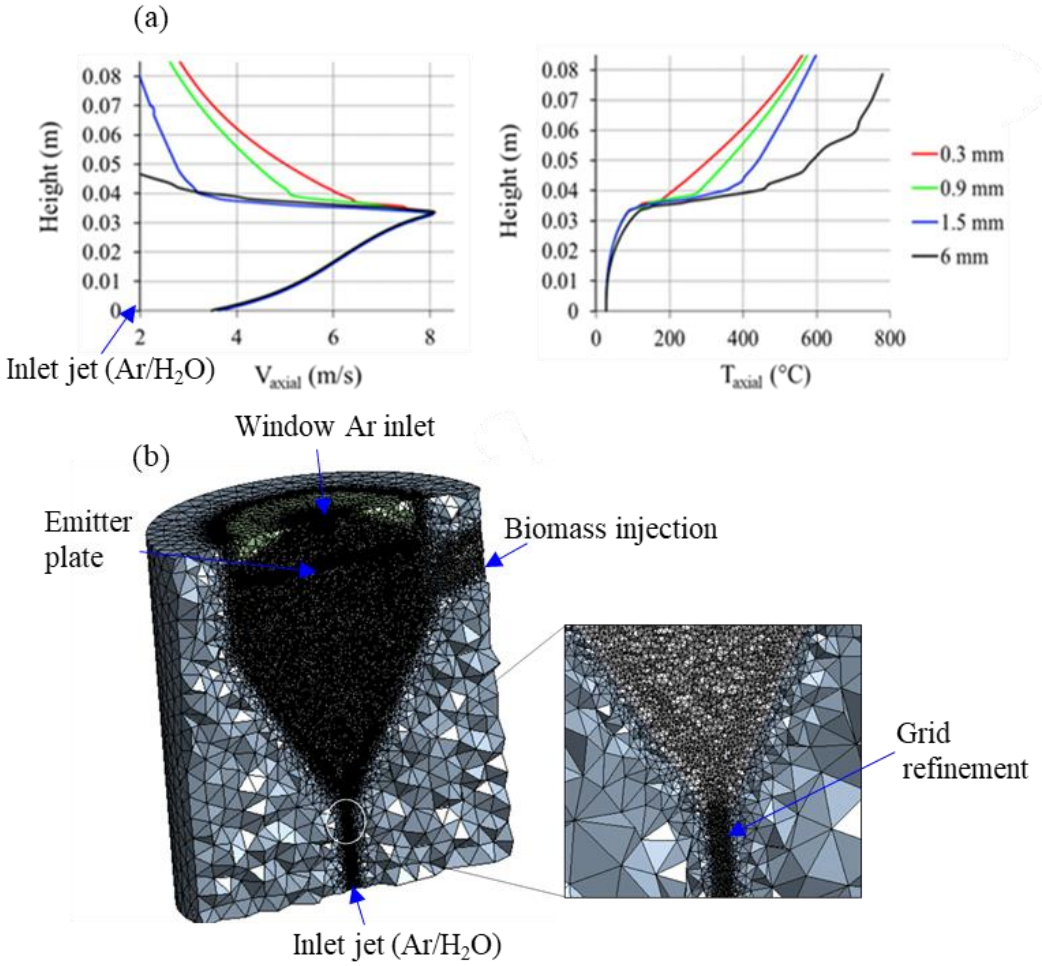

Figure II.4 (a) Sensitivity of jet gases velocity and temperature to grid size inside the conical cavity; (b) General overview of the generated 3D mesh boundary conditions

The cell sizes at the inlet/outlet tubes were set to 0.25 mm and were smoothly varied with a transition factor of 1.1 inside the conical and cylindrical part of the fluid phase region. The largest cell sizes in the cavity region shift the velocity to lower values whereas the gas temperature is increased. Larger mesh sizes promote numerical diffusion, thus the jet velocity at the central spout region is underestimated, while the central spout temperature is overestimated. An internal cell size of 0.9 mm offers the best compromise between precision and computational time. Therefore, the inlet/outlet tubes cell sizes were kept at 0.25 mm and the fluid domain (reaction zone) mesh size was fixed at 0.9 mm. Overall, a very fine mesh composed of 5 634 872 cells in the direct heating configuration and 6 369 271 cells in the indirect heating configuration (including emissive plate) was generated. The average orthogonal quality of the generated tetrahedral grid was 0.85 and the average skewness was 0.22 (Figure II.4-b).

II.2.4.2 Chemical modelling

As recalled by Di Blasi (Di Blasi, 2008), the kinetic models of lignocellulosic fuel pyrolysis are classified as: (i) one step global reaction, which assumes a constant ratio between volatiles and char; (ii) multi-reaction models, where several reactions are used to correlate specific experimental data; (iii) semi-global models, where the kinetic mechanisms include both primary and secondary reactions. There are also multi-component degradation mechanisms, which are closer to reality but require to properly characterize the biomass and to rigorously determine the kinetic parameters for each of the biomass components. Even if simpler, one-step models are extensively used especially in CFD for the formulation of engineering models in view of reactor design and optimization (Di Blasi, 1998; Ismail et al., 2018; Ku et al., 2015; Liu et al., 2014). In this study, biomass pyrolysis was represented by a one-step reaction as described in Eq.II.2:

$$Biomass \rightarrow \gamma_1 CO + \gamma_2 H_2 + \gamma_3 CO_2 + \gamma_4 CH_4 + \gamma_5 H_2O + \gamma_6 C_6H_5OH_{(g)} + \gamma_7 C_{(s)} \qquad II.2$$

To simulate the kinetics of the pyrolysis step, the model needs to take into account different physical and chemical phenomena. The amount of char produced, its reactivity and its morphology strongly depend on the pyrolysis temperature, the biomass particle size and the heating rate. To date, there is no model that is valid over a wide range of operating conditions and most models are often based on experimental data developed for a specific sample under given conditions (Elfasakhany et al., 2008). In this work, the kinetic of the pyrolysis reaction follows a first order Arrhenius law with $E_{a,pyrolysis}=7x10^7$ J.kmol^{-1} and $A_{pyrolysis}=7.4x10^3 s^{-1}$ taken from the work of Chen (Chen, 2009) and Billaud (Billaud, 2015). This law was successfully validated for high temperature (T>800°C) fast pyrolysis of millimetric beech wood in a 0.075 m internal diameter Drop Tube Reactor (DTR) at atmospheric pressure under inert atmosphere (N_2) (Billaud et al., 2016), thus approaching the pyrolysis conditions (wall temperature and pressure) encountered in the studied solar reactor. The produced char then reacts at elevated temperatures with steam. The allothermal thermochemical steam gasification of the millimetric beech char was simulated by Septien et al. (Septien et al., 2013) on the same DTR with wall temperatures varying from 1000°C to 1400°C. The Random Pore Model (RPM) was used because it incorporates the changes of char structure

related to pore growth and coalescence and its initial properties (Mahinpey and Gomez, 2016). In this case, the extent of char conversion is expressed by Eq.II.3:

$$\left.\frac{dX}{dt}\right|_{gasification} = k_{gasification}.(1-X).f(X) \quad \textit{II.3}$$

With $X = 1 - \frac{m_{char}}{m_{char\,(t_0)}}$ *II.4*

$$k_{gasification} = {P_{ox}}^{N}.A_{gasification}.exp\left(\frac{E_{a,gasification}}{RT_{fuel}}\right) \quad \textit{II.5}$$

$$f(X) = \sqrt{1-\Psi.ln(1-X)} \quad \textit{II.6}$$

Ψ was taken equal to 1, which is in the range of the values reported in the literature (Fermoso et al., 2009; Sangtong-ngam and Narasingha, 2008). The activation energy $E_{a,gasification}$=149 kJ.mol^{-1}, the frequency factor $A_{gasification}$=217893 s^{-1}bar$^{-0.7}$ and the order related to the oxidant N = 0.7 were used, which also corresponds to the reported data (Di Blasi, 2009).

Different approaches can be used to determine the stoichiometric coefficients of Eq.II.2. Some researchers calculated the coefficients from the proximate analysis of the biomass particle. The goal is to achieve the elemental mass balance (Deng et al., 2008; Liu et al., 2016; Yu et al., 2007). However, in proximate analysis, the liquid and the gas yields are often lumped together and the char yield is determined at standard operating conditions as specified in test codes. Actually, the amounts of condensable, incondensable and solid yields are strongly dependent on the operating conditions such as temperature, heating rate and residence time. Hence, another approach would be to determine these coefficients from experimental data while closing the mass and chemical element balance. Septien et al. (Septien et al., 2013) have conducted fast pyrolysis experiments under inert atmosphere of millimetric beech wood at 800°C. This corresponds to the operating conditions for pyrolysis in this study; thus the achieved results were collected and treated in order to close the elemental mass and chemical balance of the involved biomass.

Overall, the following coefficients were used (Table II.3).

Table II.3 Coefficients of the pyrolysis reaction

γ_1	γ_2	γ_3	γ_4	γ_5	γ_6	γ_7
2.76	2.71	0.35	0.45	0.44	0.32	0.53

C_nH_ms and tars were represented by phenol in gaseous form. Indeed, phenol is a major constituent of primary and secondary tars and can therefore, in a first approximation, serve as a model molecule (Morf et al., 2002). In addition, the boiling point of phenol is in the order of 180°C, which validates the hypothesis of a gaseous state. The degradation of phenol can be described by a semi-global mechanism (Eqs.II.7-II.9).

$$C_6H_5OH \rightarrow CO + C_5H_6 \quad \textit{II.7}$$

$$2C_5H_6 \rightarrow C_{10}H_8 + 2H_2 \quad \textit{II.8}$$

$$C_{10}H_8 + 10H_2O \rightarrow 14H_2 + 10CO \quad \textit{II.9}$$

The choice of cyclopentadiene (C_5H_6) as a reaction intermediate results from its important role in the decomposition of phenol (Brezinsky et al., 1998) and the formation of naphthalene (Marinov et al., 1998). Note that naphthalene ($C_{10}H_8$) is not only an important component of tertiary tars but also a polycyclic aromatic hydrocarbon, i.e. a precursor of soot. The kinetics of phenol pyrolysis was previously studied by Horn et al. (Horn et al., 1998) in the temperature range from 1450 to 1650K. It was concluded that the molecular mechanism that converts phenol to cyclopentadiene and carbon monoxide is the most dominating step of phenol conversion. Therefore, reactions (Eq.II.7) and (Eq.II.8) were selected to represent the decomposition process of primary and secondary tars. The thermal conversion of naphthalene was represented by Eq.II.9 and its kinetics was taken from the review of Li and Suzuki. (Li and Suzuki, 2009). Furthermore, several homogeneous chemical reactions take place. The forward WGS reaction produces H_2 at the expense of CO; this equilibrium reaction is of prime importance to balance the H_2:CO ratio (Eq.II.10). Additional methane reforming occurs, thus producing more H_2 and CO (Eq.I.11).

$$CO + H_2O \leftrightarrow CO_2 + H_2 \qquad II.10$$

$$CH_4 + H_2O \rightarrow 3H_2 + CO \qquad II.11$$

Table II.4 presents the kinetic data used in this study; the frequency factor A is given so that the rate of reaction r is expressed in kmol.m^{-3}.s^{-1} (Eqs.I.12-I.13). r_i is the rate of the reaction i, k_i the kinetic constant.

$$r_i = k_i \prod_j [C_{ij}]^{N_{ij}} \qquad II.12$$

$$k_i = A_i exp\left(^{-E_{a_i}}/_{R.T}\right) \qquad II.13$$

Table II.4 Chemical kinetic parameters

Reaction	N	*A*	E_a (J.mol^{-1})
7	N=1	7.00 10^{12}	60802.0
8	N=1	1.00 10^{9}	10010.0
9	$N_{C_{10}H_8}$=1.6	1.70 10^{14}	32400.0
10 (Forward WGS)	N_{H_2O}=1, N_{CO}=1	2.98 10^{8}	162607.0
10 (Backward WGS)	N_{CO_2}=1, N_{H_2}=1	1.26 10^{10}	196229.0
11	N_{CH_4}=1, N_{H_2O}=1	1.48 10^{11}	259700.0

II.2.4.3 Physical properties determination

The gas phase temperature varies from 25°C to more than 1300°C. This results in a non-negligible change in the physical properties of the fluid phase. The gas density was modeled by the ideal gas law and the kinetic theory was used to calculate intrinsic viscosities, thermal conductivities and mass diffusivities of each gas (Eqs.II.14-II.16).

$$\mu_i = 2.67\ 10^{-6}.\frac{\sqrt{M_{w,i}T}}{\sigma_i{}^2.\Omega_\mu\,(\bar{\varepsilon}_i/k_b)} \quad II.14$$

$$\lambda_i = \frac{15R.\mu}{4M_{w,i}}.\left(\frac{4c_{p,i}M_{w,i}}{15R}+\frac{1}{3}\right) \quad II.15$$

$$D_{ij} = 1.88\ 10^{-2}.\frac{\sqrt{T^3\left(\frac{1}{M_{w,i}}+\frac{1}{M_{w,j}}\right)}}{P.\left(\frac{\sigma_i+\sigma_j}{2}\right)^2.\Omega_D\left(\overline{\varepsilon_m}/k_b\right)} \quad II.16$$

$$\overline{\varepsilon_m}/k_b = \sqrt{\left(\bar{\varepsilon}/k_b\right)_i.\left(\bar{\varepsilon}/k_b\right)_j} \quad II.17$$

With R the gas constant, $M_{w,i}$ the molecular weight of the gas species 'i', σ_i (Å) and $\bar{\varepsilon}_i/k_b$ (K) the Lennard-Jones (L-J) parameters, which are tabulated (Hirschfelder et al., 1964) and integrated to Fluent© to determine Ω_μ and Ω_D. Then, gas mixture properties (used in the gas phase conservation equations i.e. Eqs.II.35, II.38, II.42) were deduced from Eqs.II.18-II.20 as function of the species intrinsic properties and volume fraction (x_i).

$$\mu = \sum_{j=1}^{n}\frac{x_j\mu_j}{\sum_{\substack{r=1\\r\neq j}}^{n}X_r\varphi_{jr}} \quad II.18$$

$$\lambda = \sum_{j=1}^{n}\frac{x_j\lambda_j}{\sum_{\substack{r=1\\r\neq j}}^{n}X_r\varphi_{jr}} \quad II.19$$

$$D_{i,m} = \frac{1-x_i}{\sum_{\substack{r=1\\r\neq j}}^{n}x_r D_{jr}} \quad II.20$$

$$\varphi_{ij} = \frac{\left\{1+\left(\frac{\mu_i}{\mu_j}\right)^{0,5}\left(\frac{M_{w,j}}{M_{w,i}}\right)^{0,25}\right\}^2}{\left\{8.\left(1+\left(\frac{M_{w,j}}{M_{w,i}}\right)\right)\right\}^{0.5}} \quad II.21$$

The reactor solid components (i.e. cavity walls, insulation, alumina cap, screw feeder, emitter plate etc.) properties are presented in Table II.1.

II.2.4.4 Discrete phase modelling

The particle size distribution of the biomass powder was characterized with a Camsizer XT (Retsch Company) by dynamic image analysis. The probability and the cumulative density functions are plotted in Figure II.5.

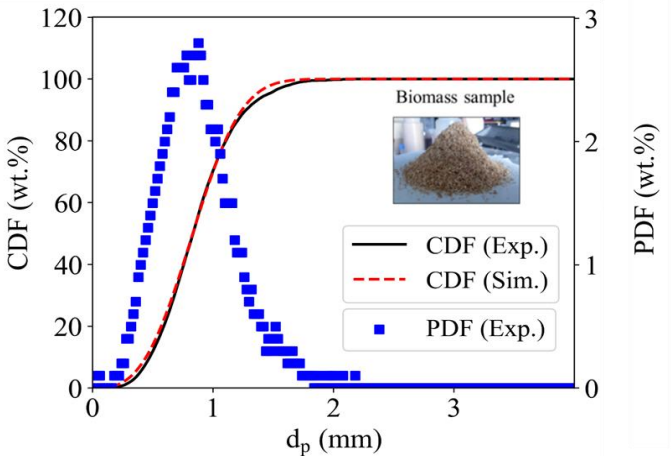

Figure II.5 Powder analysis and size dispersion modeling

Each millimetric reactive particle was modeled as a multicomponent particle called 'fuel'; at t=0s, the fuel particle is composed exclusively of 'biomass'. 'Char' forms on the particle's surface throughout the reaction. In the model, the fuel particles were injected uniformly from the outer annular surface surrouding the screw feeder (Figure II.3: annular region between the screew feeder and the injection tube). The particles initial velocity was set to 0 $m.s^{-1}$. Due to the entering argon flow rate (the one flowing from the hopper to the cavity through the screew feeder) and thanks to the inclined configuration of the screw feeder, the particles continuously dropped into the cavity.

The Rosin-Rammler distribution (Eq.II.22) was used to get a mathematical formulation that best describes the size dispersion of the particles. For the considered biomass, the Rosin-Rammler parameters ($\tilde{d}$, δ) were (0.94 mm, 3.0).

$$C = e^{\left(-{d_{fuel}}/{\tilde{d}}\right)^{\delta}} \qquad II.22$$

The particles were tracked in space in a Lagrangian reference frame while heat, mass and chemical reaction rates of pyro-gasification were computed. The calculated local sources and sinks were weighted by the Probability Density Function (*PDF*) (${dC}/{dd_p}$) before being added or subtracted from the gas phase mixture equations. In this study, the PDF was represented by 6 classes ranging from 0.2 mm to 2.0 mm. The discrete phase conservation are presented in the following sections.

II.2.4.4.1 Momentum conservation

The force balance was written for each fuel particle, it equated the particle inertia with the drag and the gravity force (Eq.II.23). The drag force was encountered by each moving particle during its trajectory. It is known to play a key role in mass, heat and momentum transfer and above all, it represents the most important parameter that governs the particle movement within a gas stream (Kelbaliyev, 2011).

$$\frac{dv_{fuel}}{dt} = F_D\left(v - v_{fuel}\right) + \frac{g.(\rho_{fuel}-\rho)}{\rho_{fuel}} \qquad II.23$$

The particle position (s vector) was deduced by integrating Eq.II.24.

$$\frac{ds_{fuel}}{dt} = v_{fuel} \qquad II.24$$

The fuel particle density was computed by Eq.II.25 (the fuel particle is composed of both biomass and char).

$$\rho_{fuel} = x_{Biomass} \cdot \rho_{Biomass} + (1 - x_{Biomass}) \cdot \rho_{char} \qquad II.25$$

With $x_{Biomass}$ the biomass volume fraction in the fuel particle. $F_D.(v\text{-}v_{fuel})$ the drag force per particle mass unit, v is the gas phase velocity and v_{fuel} is the particle velocity ($m.s^{-1}$), ρ and ρ_{fuel} are the corresponding densities. F_D is calculated as a function of the drag coefficient C_D (Eq.II.26), which in turn is deduced from the correlation proposed in the work of Morsi and Alexander (Morsi and Alexander, 1972) for discrete spherical particles.

$$F_D = \frac{18\mu C_D Re}{24\rho_{fuel}{d_{fuel}}^2} \qquad II.26$$

With $Re = \frac{\rho d_{fuel}|v - v_{fuel}|}{\mu}$ *II.27*

And $d_{fuel} = (\frac{6m_{fuel}}{\pi \rho_{fuel}})^{\frac{1}{3}}$ *II.28*

II.2.4.4.2 Mass conservation

Given the time spent by the particles in the screw feeder and the low moisture content of the studied biomass (Table II.2), the particles were assumed to enter the reactor in a dry state. In order to insure the same amount of steam in simulation and experimentation, steam from moisture was directly introduced through the biomass injection tube external face to the reactor. Then, both pyrolysis and gasification take place. The mass of each fuel particle as function of time was calculated by integrating Eq.II.29:

$$r_{fuel} = \frac{dm_{fuel}}{dt} = \frac{dm_{fuel}}{dt}\}_{pyrolysis} + \frac{dm_{fuel}}{dt}\}_{gasification} \quad \textit{II.29}$$

II.2.4.4.3 Energy conservation

Each particle exchanges energy with the outer environment by convection and radiation[2], as described by Eq.II.30 (ε_{fuel} is the surface emissivity of char, assumed equal to 0.9) (Pozzobon et al., 2014; Qi et al., 2019).

$$m_{fuel} c_{p,fuel} \frac{dT_{fuel}}{dt} = h_{fuel} A_{fuel} (T_\infty - T_{fuel}) + \sigma_{rad} A_{fuel} \varepsilon_{fuel} ({\theta_R}^4 - {T_{fuel}}^4) + H_{rxn} \quad \textit{II.30}$$

With

$$\begin{cases} c_{p,fuel} = Y_{Biomass}\, c_{p,Biomass} + (1 - Y_{Biomass}).\, c_{p,char} & \textit{II.31} \\ H_{rxn} = r_{fuel,pyrolysis}.\,(h_{f,pyrolysis\ products} - h_{f,Biomass}) + r_{fuel,gasification}.\,(h_{f,CO} - h_{f,H_2O} - h_{f,Biomass}) & \textit{II.32} \end{cases}$$

The particle temperature was assumed uniform (no temperature gradient between surface and core), which constitutes an important hypothesis of the model especially for the largest freshly injected woody particles[3]. This however simplifies and lightens significantly the complex gas-particle flow 3D simulation given that the particles are not meshed. They are rather characterized by an effective temperature that drives their overall apparent conversion kinetics. In addition, heat transfer by particle/particle and wall/particle interactions was neglected because the particle volume fraction is less than 1%. Furthermore, given the low ash content of the considered biomass (below 0.5 wt. %), its contribution to heat transfer was also neglected. $Y_{Biomass}$ is the mass fraction of biomass in the fuel particle. The enthalpy of formation of the considered biomass ($h_{f,Biomass}$ in J.kg^{-1}) was calculated from Eq., where a_{CO2} and a_{H2O} are the stoichiometric coefficients of the complete oxy-combustion reaction.

$$h_{f,Biomass}(298K) = a_{CO_2} h_{f,CO_2}(298K) + a_{H_2O} h_{f,H_2O}(298K) - LHV_{Biomass}.\, M_{w,Biomass} \quad \textit{II.33}$$

[2] Boltzmann number (convection/radiation) ~ 0.4-5; both heat transfer modes are present intensely, cf. ANNEX 1

[3] Expected Biot number ~1; thermal gradients can occur, cf. ANNEX 1

h_{fuel} is expressed as a function of the particles' Reynolds number and the gas phase Prandtl number, according to Ranz and Marshall (Ranz and Marshsal, 1952). θ_R is the radiation temperature and it is calculated by Eq.II.34. With I the intensity of radiation ($W.m^{-2}.sr^{-1}$).

$$\theta_R = \left(\frac{\int_0^{4\pi} I.d\omega}{\sigma_{rad}}\right)^{1/4} \quad \textit{II.34}$$

II.2.4.5 Gas and solid components modelling

For the gas phase, the calculated Re values range between 100 in the central spout down to ~10 in the annular region[4], these values were well below 2300, which is the critical Re number in pipes, and below 300-450, which is the critical Re number in confined coaxial jets (Gore and Crowe, 2012). Therefore, a laminar solver was chosen to solve the conservation equations. Steady state calculations were performed for the fluid flow and the solid components (i.e. cavity walls, insulation, cap etc.) of the reactor expressed by systems of PDEs (Partial Differential Equations), while time-dependent ODE (Ordinary Differential Equations) were solved for the discrete phase, i.e. fuel particles.

II.2.4.5.1 Momentum conservation

The steady-state Navier-Stokes equation (Eq.II.35) was solved.

$$\nabla.\left(v(v)\right) = -\nabla.p + \nabla.(\bar{\bar{\tau}}) + \rho g + F_{fluid-particle} \quad \textit{II.35}$$

$$\text{With } \bar{\bar{\tau}} = \mu.[(\nabla.v + \nabla v^T)] - \frac{2}{3}\nabla v.\bar{\bar{I}} \quad \textit{II.36}$$

With $\bar{\bar{I}}$ the unity matrix, g ($m.s^{-2}$), the acceleration due to gravity, P (Pa), the fluid pressure, $F_{fluid\text{-}particle}$ ($kg.m^{-2}.s^{-2}$ or $N.m^{-3}$) the momentum exchange between the fluid phase and the particulate phase; it was calculated by Eq.II.37 at each control volume as the sum of the contribution of each parcel (representing many physical particles with the same diameter and trajectory) crossing the cell.

$$F_{fluid-particle} = \sum \frac{18\mu.C_D.Re}{24.\rho_{fuel}.{d_{fuel}}^2}.\left(v_{fuel} - v\right).\dot{m}_{fuel}.\Delta t \quad \textit{II.37}$$

Where Δt is the time step used to solve Eqs.II.23,II.29,II.30. $\dot{m}_{fuel}$ is the mass flow rate of a given parcel at a specific cell.

II.2.4.5.2 Mass conservation

The local mass fraction (Y_k) of each species was calculated by solving the following convection-diffusion equation (Eq.II.38):

$$\nabla.(\rho v Y_k) = -\nabla.J_k + S_k + R_k \quad \textit{II.38}$$

$$\text{With } J_k = -\rho D_{k,m}\nabla Y_k \quad \textit{II.39}$$

[4] Lower velocities and higher temperatures expected in the annulus decrease the Re number, cf. ANNEX 1

S_k (kg.s^{-1}.m^{-3}) is the rate of production/consumption of the species k, it is expressed by Eq.II.40

$$\text{And } S_k = M_{w,k} \sum_{r=1}^{N_r} \left(\nu'_{k,r} - \nu_{k,r} \right). k_{k,r} \prod_j [C_{kj,r}]^{N_{kj,r}} \quad \textit{II.40}$$

Where $\nu_{k,r}$ and $\nu'_{k,r}$ are respectively the stoichiometric coefficients of the reactants and products in the reaction r. N_r is the total number of chemical reactions. R_k is the generation rate by addition or subtraction from the dispersed phase. It was calculated for each cell of the fluid volume by Eq.II.41.

$$R_k = \frac{\dot{m}_{fuel,cell\_inlet} - \dot{m}_{fuel,cell\_outlet}}{V_{cell}} \quad \textit{II.41}$$

Where $\dot{m}_{fuel,cell\_inlet}$ and $\dot{m}_{fuel,cell\_outlet}$ are respectively the mass flow rates of the particles entering and leaving the cell.

II.2.4.5.3 Energy conservation

The energy conservation (Eq.II.42) was also solved for the fluid phase; it takes into account heat transfer by convection, conduction and the transfer of enthalpy due to species diffusion.

$$\nabla.\left(v(\rho E + p)\right) = \nabla.\left(\lambda \nabla T - \sum h_j j_j\right) + S_{h,rad} + S_{h,rxn} + S_{h,fuel} \quad \textit{II.42}$$

$$E = \sum_j Y_j h_j - \frac{p}{\rho} + \frac{v^2}{2} \quad \textit{II.43}$$

$$h_j = \int_{298.15\ K}^{T} c_{p,j}\, dT \quad \textit{II.44}$$

With $c_{p,i}$ (J.kg^{-1}.°C^{-1}), the gas species heat capacity, h_j the species sensible enthalpy. S_h terms include the sensible heat transferred from fuel particles to the gas phase, the absorbed/emitted radiations by the gas phase ($S_{h,rad}$), and enthalpies of homogeneous and heterogeneous reactions ($S_{h,rxn}$).

Furthermore, the local temperature of the solid components of the reactor (alumina cap, cavity walls, insulation, and screw feeder) was predicted by solving Eq.II.45 II.45

$$\nabla.\left(\lambda_{solid,i}\, \nabla T\right) = 0 \quad \textit{II.45}$$

Where $\lambda_{solid,i}$ stands for the thermal conductivity of each solid component.

II.2.4.5.4 Radiative transfer

The discrete ordinates model was used to simulate radiation; the model transforms the radiative heat transfer equation (RTE – Eq.II.46) into a transport equation for radiation intensity in the spatial coordinates. Then, the transport equation is solved for a fixed number of directions $\vec{l}$. Here, the number of control angles used to discretize each octant of the angular space is 128 solid angles. The equation takes into account the particulate absorption/emission and radiation scattering, the gas phase is assumed to be semi-transparent, non-scattering and the absorption coefficient is computed using the weighted-

sum-of-gray-gases model (WSGGM) domain-based of Fluent©. It calculates the absorptivity 'a' locally as a function of the mass fraction of water vapor and carbon dioxide. In fact, these gases are the most absorbing/emitting gases in the mixture and are considered to represent the overall radiation/gas phase interaction.

$$\nabla.(I.s) + (a + a_{fuel})I(s,l) = a.\frac{\sigma_{rad}T^4}{\pi} + E_{fuel} + \frac{\sigma_{fuel}}{4\pi}\int_0^{4\pi} I(s,l).\varphi(l,l')d\omega \qquad \textit{II.46}$$

Eqs.II.47-II.49 are the definitions of the equivalent emission, absorption and scattering coefficients; their calculation is done in each control volume and accounts for the sum of all particles in the control volume. The scattering factor $f_{d,fuel}$ was assumed equal to 0.9.

$$\begin{cases} E_{fuel} = \lim_{V\to 0}\sum \varepsilon_{fuel,i}.\frac{\sigma_{rad}.A_{fuel,i}.{T_{fuel,i}}^4}{\pi V} & \textit{II.47} \\ a_{fuel} = \lim_{V\to 0}\sum \varepsilon_{fuel,i}.\frac{A_{fuel,i}}{V} & \textit{II.48} \\ \sigma_{fuel} = \lim_{V\to 0}\sum (1-\varepsilon_{fuel,i})(1-f_{d\ fuel,i})\frac{A_{fuel,i}}{V} & \textit{II.49} \end{cases}$$

II.2.4.6 Numerical methods

The Finite-Volume Method (FVM) was adopted for the gas and solid components of the reactor. Integral balance equations were formulated for each control volume. The governing equations were then solved sequentially according to a pressure-based segregated algorithm until complete convergence. Convergence was checked by verifying the overall mass and energy balances (1% maximum error) while the outlet gas exit temperature and syngas composition reach constant values. First order discretization schemes were used during the first iterations of the calculation. Once residuals stabilized, second order space discretization schemes were set for the flow equations. Concerning the pressure equation, the body force weighted spatial interpolation scheme was used. DPM injections were computed every 20 iterations (of the fluid flow) until complete convergence. To integrate the equations of motion for the wood particles, the Fluent© automated Tracking Scheme was used. This scheme provides a mechanism to switch in an automated fashion between numerically stable lower order schemes and higher order schemes depending on the distance to hydrodynamic equilibrium. The calculations were performed in parallel computing mode on 20 cores. The required time of complete convergence for a single run ranges between 4 to 5 days, it may be longer and require more computational time (4 to 5 more days) if combustion reactions are also considered[5] (section II.3).

II.2.5 Experimental tests

In this section, experimental tests were conducted to validate the numerical model. The aim of the experimental work is not to perform an exhaustive parametric study of the reactor as previously presented in (Bellouard, 2017), but to support the numerical approach thanks to

[5] The very fast kinetics and the highly exothermic reactions destabilize convergence, thus, the numerical solution was under relaxed to insure stability and proper convergence at the expense of a greater computational time.

specific experimental points. Accordingly, simulations were performed to get a clearer understanding of the reactor operation. Experiments were realized under real concentrated solar flux with two biomass feeding rates (1.2 g.min^{-1} and 2 g.min^{-1}). The total mass injected into the reactor was 30 g and the total duration of one experiment was around 30 min. For the current reactor configuration, no bed material was used. The cavity was initially empty and the injected wood particles were the only spouted particles inside the reactor. Table II.5 summarizes the operating conditions used to study the solar jet spouted bed reactor.

Table II.5 Experimental conditions of the solar reactor

Heating mode	Indirect		Direct	
T3	1200°C		1200°C	
Run #	1	2	3	4
Biomass flow rate (g.min^{-1})	1.2	2	1.2	2
Steam flow rate (g.min^{-1})	0.2	0.35	0.2	0.35

For each gas species, the time-dependent production rate (F_i) was calculated from the known inlet flow rate of inert gas (F_{Ar}) and the measured species outlet mole fractions (x_i) following Eq.II.50.

$$F_i(t) = F_{Ar}(t).x_i(t)/x_{Ar}(t) \qquad \textit{II.50}$$

The instantaneous production rates of the main gas species contained in the syngas for a biomass feeding rate of 1.2 g.min^{-1} and an over-stoichiometric water flow rate of 0.2 g.min^{-1} are shown in Figure II.6 (Run #1, indirect heating).

The available DNI was stable during the experiment with a global variation less than 1% from 1007.6 W.m^{-2} to 1021.6 W.m^{-2} (Figure II.6-a). The entering solar power was adjusted throughout the experiment by partially closing or opening a trap door below the reactor frame to stabilize the reactor temperature. All the biomass feedstock was this way converted at 1200°C with no remaining char inside the cavity after the test. The reactive feedstock load was indirectly subjected to the incident solar flux. The absorbing heat transfer plate was placed below the alumina cap. The mean plate temperature was 1370°C at its center with a standard deviation of 26°C.

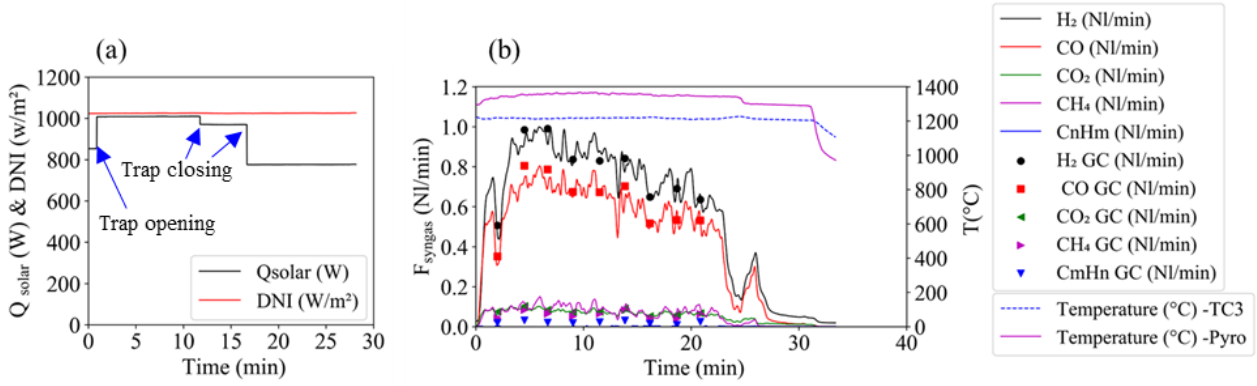

Figure II.6 (a) DNI and reactor solar power input; (b) Evolution of the syngas production rates and temperatures as a function of time (Run#1)

This plate absorbed the highly concentrated solar power and transmitted it by radiation to the bed of particles. It can be observed that the produced gas was mainly composed of H_2 and CO (Figure II.6-b). The high temperature reached by the reactor (1200°C) favored the production of H_2 and CO at the expense of CO_2, CH_4 and C_nH_m. The C_nH_ms total yield was very low and was predominantly composed of C_2H_2 and C_2H_4. Some traces of C_2H_6 were also measured. Tars were however not quantified during the experiments. The observed small variations in the gas production rates were due to the screw feeder outlet that could not be directly inserted in the hot zone of the reactor, thus the biomass particles were pushed by preceding particles and fell into the cavity in the form of small parcels by gravity. For the same set point temperature, oxidant and carrier gas flow rates, experiments were conducted without the emitter plate to expose the bed of particles directly to the concentrated solar radiation.

The average syngas molar composition was evaluated thanks to the time integration of the gas production rates over the total duration of the experiment (t_f) following Eq.II.51.

$$\bar{x}_i = \frac{\int_{t=0}^{t=t_f} F_i.dt}{\sum_k \int_{t=0}^{t=t_f} F_k.dt} \qquad \textit{II.51}$$

Cleaning and maintenance operations were carried out between the experimental runs. The material mass balance was checked by comparing the initial mass of fed reactants (biomass and water) with the mass of products outputs (syngas components, entrained char/soots and excess water trapped in bubbler and filters). After experiments, no char remained inside the cavity thus denoting complete biomass conversion. Char/soots were only recovered in the outlet components and quantified by weighting. The mass balance closure was higher than 90% for all the experimental runs. The achieved gas composition, CCE (Eq.I.7) and CGE (Eq.I.8) for the four runs are summarized in Table II.6. The experimental results reliability and consistency regarding data reproducibility being described and validated before in previous work (Bellouard, 2017).

Table II.6 Average outlet gas composition (on volume basis) and CCE (accuracy of measuring cells: ±2 % of full scale)

	Run#			
	1	2	3	4
H_2	50.0%	47.9%	51.6%	48.4%
CO	38.5%	38.1%	38.3%	40.7%
CH_4	5.5%	6.6%	4.2%	4.4%
CO_2	4.9%	6.0%	4.5%	4.5%
C_nH_m	1.1%	1.4%	1.4	2.0%
CCE	77.7%	82.4%	79.3%	85.0%
CGE	106.3%	111.0%	110.6%	117.7%

The reactor performances showed good syngas quality and conversion efficiency. The H_2:CO molar ratio reached 1.35 in Run#3 and CCE reached 85.0% in Run#4. Increasing the biomass feeding rate led to a slight increase in the CCE for both heating configurations (indirect: 77.7%-82.4%, direct: 79.3%-85.0%) whereas the H_2 molar fraction declined (by

4.2% for indirect heating and by 6.2% for direct heating). In addition, it promoted the formation of CH_4, CO_2 and C_nH_m. Globally, directly heating the reactor resulted in slightly higher H_2 concentration especially for lower biomass feeding rates. Compared with Run#1, exposing the bed to direct radiations (Run#3) resulted in the H_2 molar fraction increase by 3.2% and the CH_4 molar fraction decline by over 23.6%. Additionally, directly heating the reactor increased somewhat the CCE by 2.0% at 1.2 $g.min^{-1}$ and by 3.1% at 2 $g.min^{-1}$. The impact of the heating mode and feeding rate was also noted in the CGE, which followed a similar pattern as the CCE. In fact, wood feeding rate increase, improved the CGE by 4.4% and 6.4% for the indirect and direct heating modes respectively thanks to the more pronounced biomass conversion. Moreover, at fixed biomass flow rate, the direct mode showed higher CGE values (by 4.0% and 6.0% at 1.2 $g.min^{-1}$ and 2 $g.min^{-1}$) thanks to improved CCE and hydrogen yield.

II.2.6 Numerical study

Numerical reactor modelling aims to provide a better understanding of the biomass thermal conversion process. In this study, both the particulate and the gas flows inside the cavity of the solar jet spouted bed reactor were investigated. Thermal, hydrodynamic and chemical aspects of the solar reactor were analyzed in the conditions of the runs described in Table II.5. Numerical calculations were conducted with Q_{solar} ($F_{raw\ biomass}$ = 1.2 $g.min^{-1}$) = 0.9 kW_{th} and Q_{solar} ($F_{raw\ biomass}$ = 2 $g.min^{-1}$) = 1 kW_{th}, which corresponds to the mean solar power inputs that entered the reactor during the experimental runs.

II.2.6.1 Particulate phase

Each injected biomass particle in the 3D domain is tracked while heat, mass and momentum exchange rates are computed. Three different diameter variations for three injected particle streams are plotted in Figure II.7.

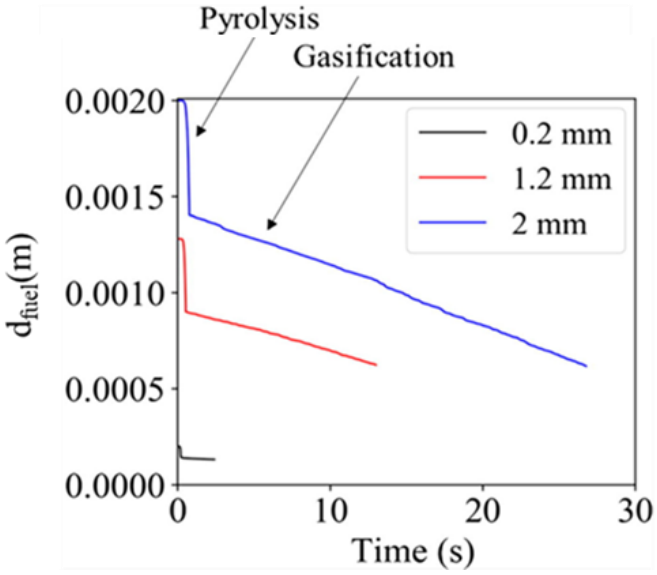

Figure II.7 Particles diameter as function of residence time for three initial diameters (0.2, 1.2, 2 mm) (Run#1)

The diameter of each particle decreases as a function of time. The particle shrinkage during the pyrolysis step is controlled by the shrinkage factor (equal to 0.7 that corresponds to the reported values for high-temperature fast pyrolysis of millimetric beech wood particles (Chen, 2009; Guizani et al., 2017)). Additional shrinking is calculated by the model as a result of particle consumption (mass loss) during the gasification step. The particle size variation is a key asset for the reactor operation, as the particles entrainment in spouted bed is highly sensitive to the particles diameter (Olazar et al., 1992).

During their lifetime inside the reactor, the moving particles describe a number of cycles in which they are pyrolyzed and gasified. The desired vigorous cyclic flow in the studied reactor is well confirmed by the model (Figure II.8-particles pathlines). The high-velocity jet at the bottom inlet causes the particles to rise rapidly in the central core to reach velocities in the order of 2 $m.s^{-1}$ in the spout region. Due to gravity, the particles revert to the annular zone between the central spout and the cavity walls at a speed in the order of 0.1 $m.s^{-1}$. Hence, the main objective of retaining the particles in the reaction zone through cyclic patterns is largely achieved. The model also points out that the very light 0.2 mm diameter particles exit the reactor as soon as they pyrolyze, whereas the bigger particles stay longer in the cavity. The entrainment phenomenon is thus clearly emphasized by the model. It is due to the fact that the shrinking particles get increasingly smaller and lighter throughout their trajectories to reach a point where the gas velocities inside the cavity are high enough to entrain particles towards the outlet, which determines their residence time in the cavity.

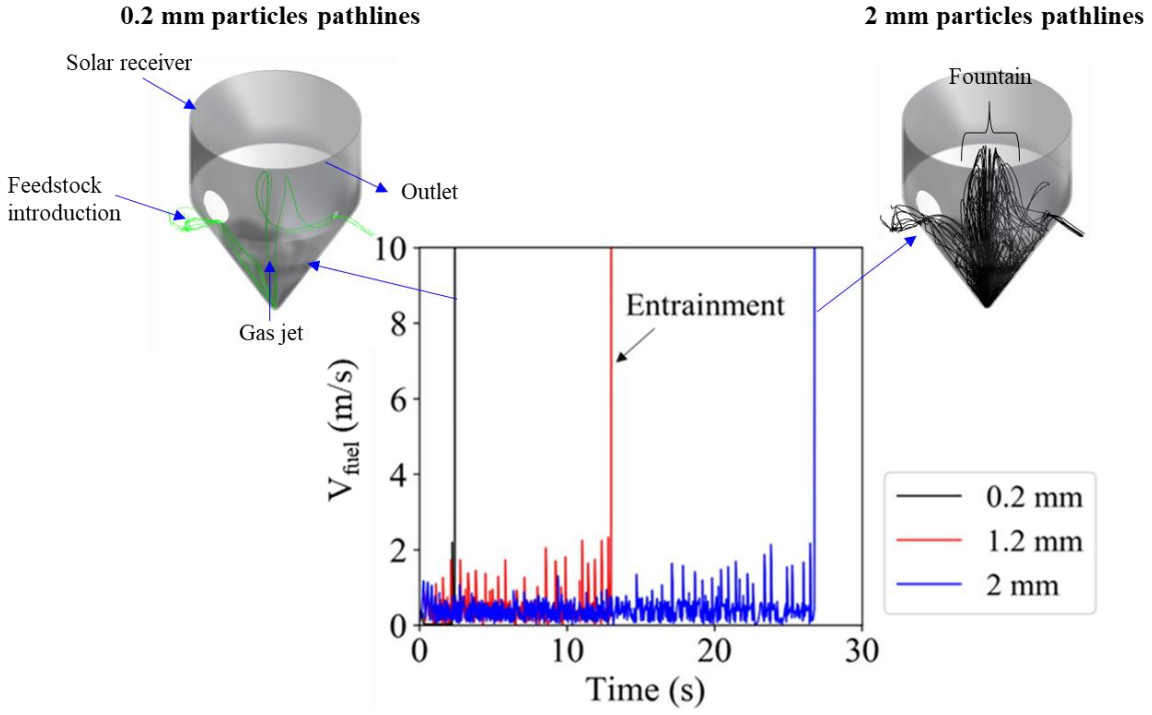

Figure II.8 Particles velocity magnitude as function of time and pathlines of 0.2 and 2 mm particles (Run#1)

The evolution of the biomass particles composition as a function of residence time is depicted in Figure II.9-a. The lightest 0.2 mm particles start to pyrolyze at around t = 0.15 s

while the biggest 2 mm particles get decomposed some time after at around t = 0.60 s. During the pyrolysis step, char is formed continuously at the outer surface of each particle until complete devolatilization, as shown in Figure II.9-b.

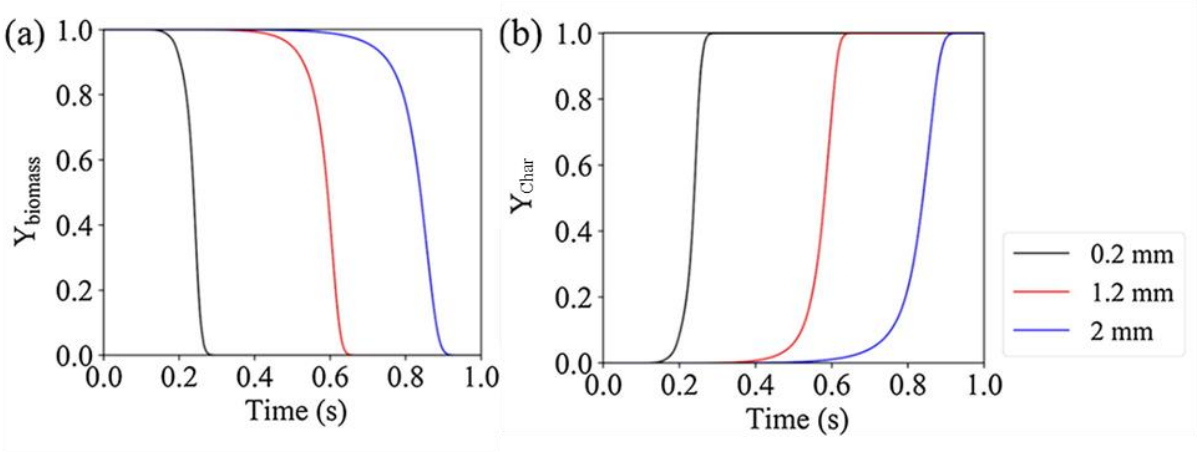

Figure II.9 Biomass and char mass fractions as function of time (Run#1)

Owing to the intense solar heating, the particles temperature rises rapidly to reach values above 1000°C during the first instants of operation just after injection. Figure II.10 shows the evolution of the particles temperature as a function of residence time and the particles trajectories. The simulations predict a fluctuating temperature pattern depending on the location of the particles in the reaction zone. The inlet gases are injected at ambient temperature, which cools down the bottom area of the cavity. When entrained towards the top of the cavity, the particles are heated up continuously to achieve values above 1200°C in the indirect heating mode. Then, the flow of particles is cooled on the way back to the bottom of the reactor and gets entrained cyclically.

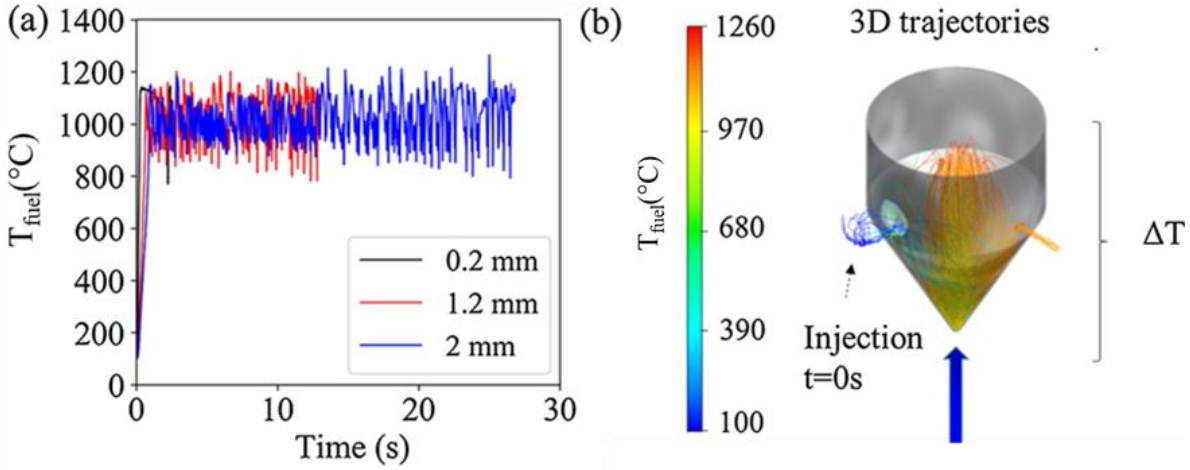

Figure II.10 (a) Fuel particles temperature as function of residence time; (b) Trajectories of the 2 mm particles colored by their temperature (Run#1)

Moreover, Figure II.11-a shows that the temperature variation (T_{max}-T_{min}) for the 1.2 mm particles is higher than the one encountered by the 2 mm particles, which is related to the lower thermal inertia ($c_{p,fuel}.m_{fuel}$) of the lightest particles. Furthermore, Figure II.11-b

reveals that the difference (T_{max}-T_{min}) increases during the conversion, which is caused again by the decrease of thermal inertia related to the mass loss.

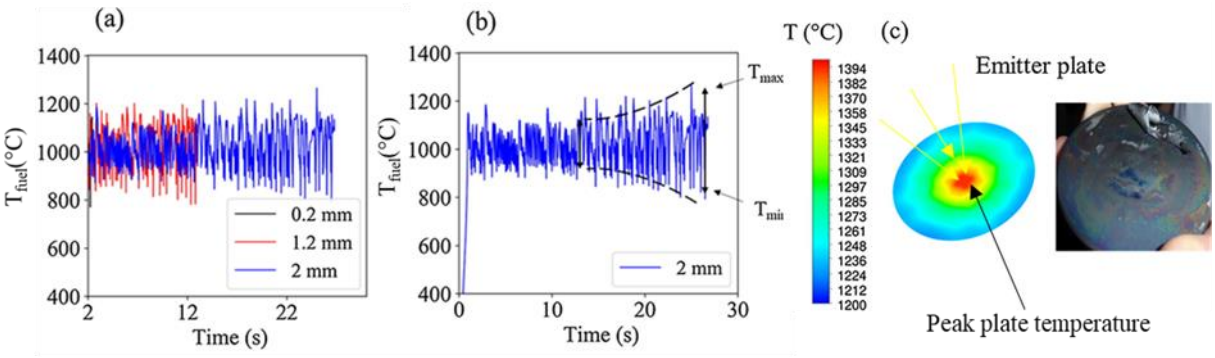

Figure II.11 Particles temperature as a function of residence time (Run# 1) during indirect heating along with emitter plate temperature.

Overall, the major highlighted differences with the direct heating mode concern the evolution of particles temperature inside the reactor (Figure II.12)

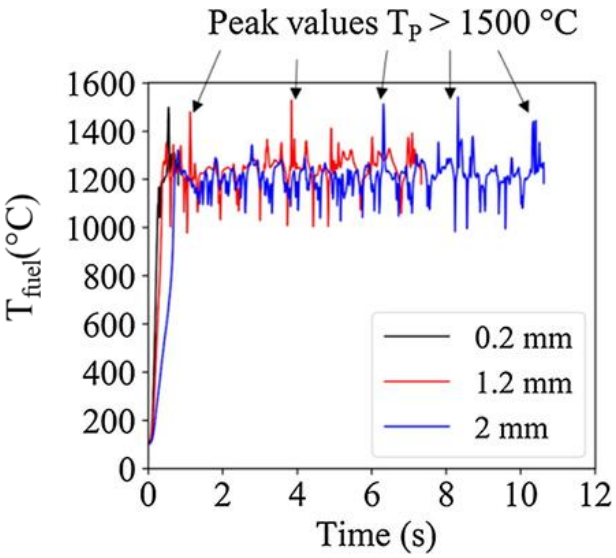

Figure II.12 Particles temperature as function of residence time (Run#3) during direct heating

The maximum attainable particle temperature in the indirect mode cannot exceed the emitter plate temperature (Figure II.11-c), which shows a Gaussian temperature profile with peak values at the center due the concentrated radiation. In return, directly heating the reactor leads to particle maximum temperatures as high as 1500°C in the upper fountain thanks to the direct and intense irradiation. This entails a particle temperature variation of about 500°C during each of the cycles described by the reacting particles.

II.2.6.2 Fluid phase

II.2.6.2.1 Thermal analysis and validation

The model was applied to study the temperature distribution for both the gas mixture and the solid reactor components (Figure II.13). Simulations predict a cavity wall temperature of around 1200°C for the four operating configurations (Figure II.13-b), which is in line with

experimentally measured cavity temperatures (Figure II.13-a). For the indirect heating mode, the plate temperature at its center was measured all along the experiments with a pyrometer (Figure II.6-b).

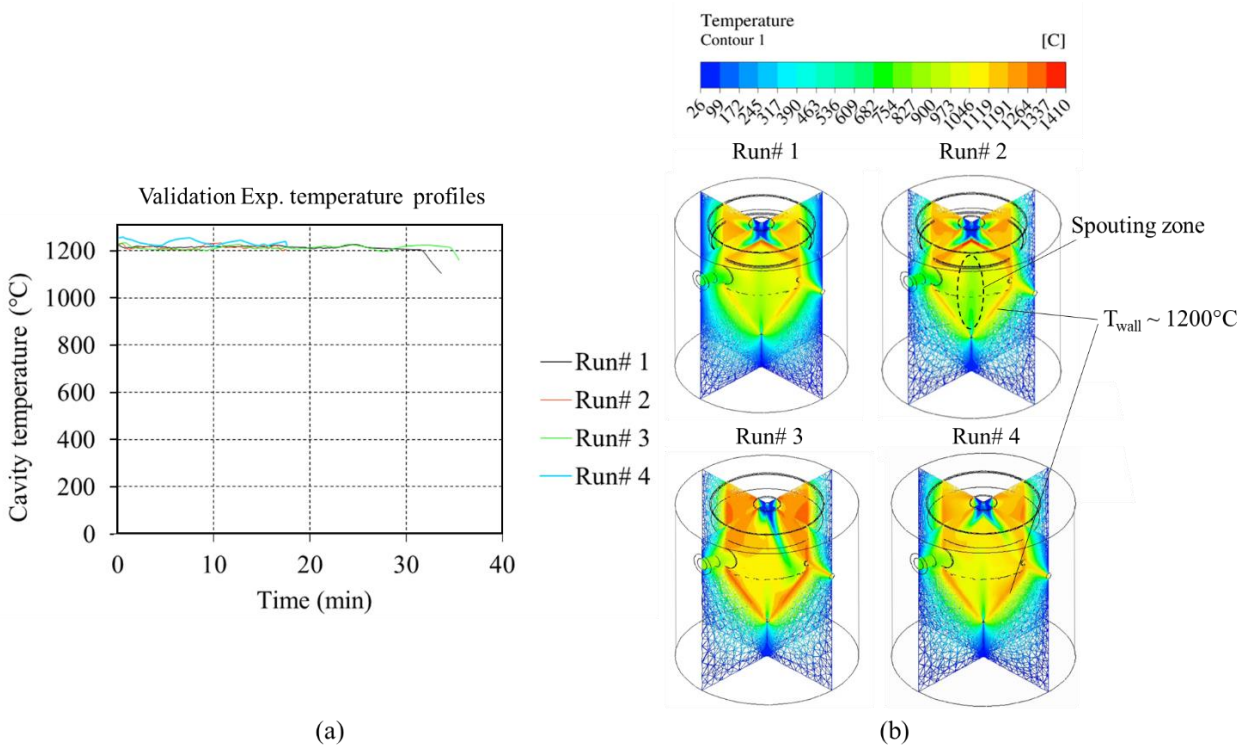

Figure II.13 (a) Experimental reactor cavity temperature (T3) as a function of time; (b) Predicted temperature distribution from simulations

The simulations predict a plate temperature of 1369°C for Run# 1 and 1410°C for Run#2. The discrepancy with the measured mean temperatures is 29°C for Run# 1 and 33°C for Run# 2, which thus represents a relative difference of less than 2.5%. In addition, the simulations also show that the spouting zone temperature is consistently lower than that of the annular zone especially for the indirect heating mode. Indeed, for Run#1 and Run#2 (indirect heating), the spouting zone temperature is about 900°C (and even lower) while the nearby walls temperature exceeds 1046°C. For Run#3 and Run#4 (direct heating), the spouting zone rapidly reaches higher temperatures approaching 1050°C. Moreover, the temperature appears to be more homogeneously distributed. Globally, the simulations reveal that the reaction zone for the direct heating configuration achieves higher temperatures with an estimated temperature discrepancy of 100°C between direct and indirect heating configurations. This can be explained by the direct exposure of the reactor cavity to the incoming radiations, which in turn results in better particle radiation absorption. Therefore, the biomass particles reach more elevated temperatures (more than 100°C difference) when directly heated (Figure II.12), and subsequently the particles transfer more heat to the gas phase by radiation and thermal convection.

II.2.6.2.2 Chemical analysis and validation

The model was also used to calculate the gas species concentrations at the reactor outlet. The gas molar fraction of the product 'i' at the reactor outlet is calculated by dividing the summation of its molar fraction at each cell and its facet area by the total area of the outlet surface Eq.II.52.

$$\tilde{x}_i = \frac{1}{A_{outlet}} \int x_i dA \qquad \textit{II.52}$$

The obtained results are summarized in Figure II.14. The predicted outlet gas composition is in agreement with the experimental measurements for the main gases including H_2, CO, CH_4, and CO_2 (discrepancy remains within a narrow range of 8–10%). Simulations reveal that exposing the reactor to direct radiation increases slightly the yield of H_2 at the expense of CH_4, which is in line with the experimental results and can be explained by the higher reaction zone temperature. However, the model somewhat over-estimates the yield of CO compared to other gases. This point can be related to different reasons among which the forward water-gas shift reaction taking place at lower temperatures in downstream tubes prior to syngas sampling which is not modelled here, and the simplified mechanism used for modelling the thermal degradation of tars. In fact, gas phase reactions can be modelled more accurately with detailed kinetic mechanisms such as the Skjøth-Rasmussen scheme (Skjøth-Rasmussen et al., 2004) (involving 159 species and 773 chemical reactions). The use of such a scheme for 3D modelling of the solar reactor would increase significantly the computational cost, which constitutes a strong limitation.

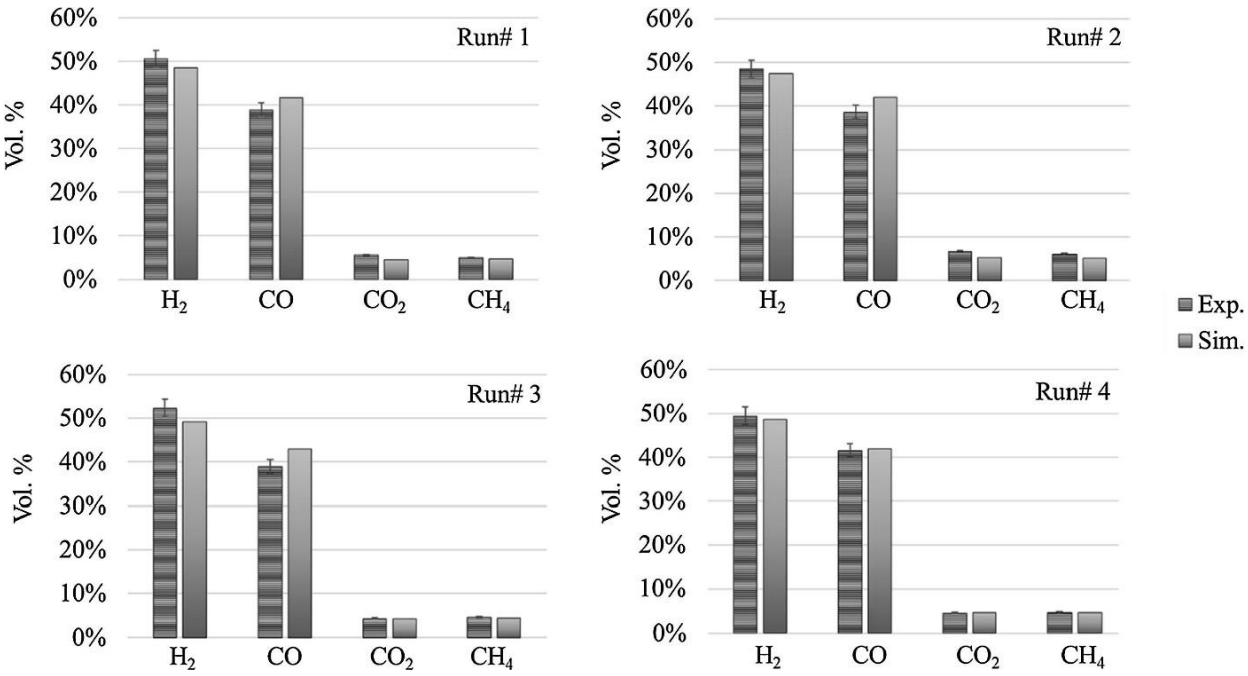

Figure II.14 Comparison between experimental and calculated data for syngas composition

The extent of the particles conversion expressed by the CCE (Eq.I.7) inside the reactor was compared with the experimental one. It is presented in Figure II.15. The simulation shows that directly heating the reactor leads to an increase of CCE thanks to improved gasification

kinetics resulting from higher particles temperature when directly irradiated. Moreover, slightly better conversion was achieved at higher biomass feeding rates, which is due to the higher steam partial pressure inside the cavity, especially in the spout region. Indeed, $(S/B)/(S/B)_{st,1.2g/min}$= 1.24 while$(S/B)/(S/B)_{st,2g/min}$= 1.28. Thus, the global experimental trends are well reproduced by the model; however, simulations overestimate CCE for the direct heating mode with an absolute discrepancy of around 10%.

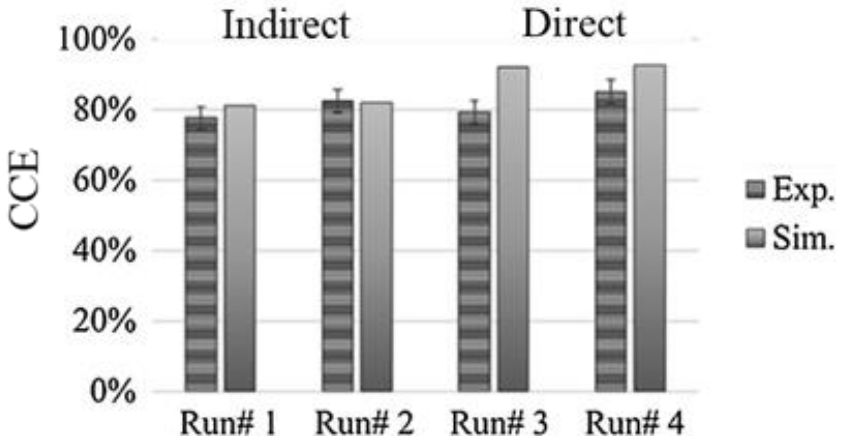

Figure II.15 Simulated and experimental Carbon Conversion Efficiency

This can be related to the very specific physical conditions that the particles undergo within the studied reactor (temperature gradient ~500°C with a solar heating rate of 2000°C.s^{-1}), which may affect the mechanical structure of the reacting char particles and also their overall reactivity giving rise to deviations from the experimental observations. As explained in Section II.1.4.2, the kinetic law used to simulate gasification was developed and validated on a simple 1D isothermal drop tube reactor operating at a maximum temperature of 1400°C (Septien et al., 2013), which differs somewhat from real test conditions in the jet spouted bed, especially in the direct heating mode. Besides, for a better prediction of the conversion process, a more complex simulation of tars and light hydrocarbons using additional model molecules may be appropriate. In addition, soots were not considered in this model; however, their amount at the reactor temperature is not negligible due to the decomposition of heavy molecules. Soot modelling that integrates their formation, steam-gasification (which has much slower kinetics than that of char gasification (Septien et al., 2014; Vander Wal and Tomasek, 2004), transport and interaction with radiation can definitely improve the accuracy of the model.

In spite of the complexity of the multiphysics two-phase flow modelling, the simulations showed a fairly good agreement with experiments in terms of outlet gas composition, temperatures and carbon conversion. To further analyze the reactor, the distributions of the water steam and gas products inside the reactor were investigated. For this purpose, the steam mass fraction is plotted in Figure II.16. The spouting central region exhibits the highest steam concentration while the annular zone is H_2O diluted. This should favor the gasification reaction kinetics in the spouting region. According to Spreutels et al. (Spreutels et al., 2016), heat and mass transfer rates at the spouting zone are much higher than those in the annular

zone, which makes this region particularly important for the reaction. However, in the studied configuration, the spouting zone is also characterized by lower temperatures, which adversely affects the progress of the reactions.

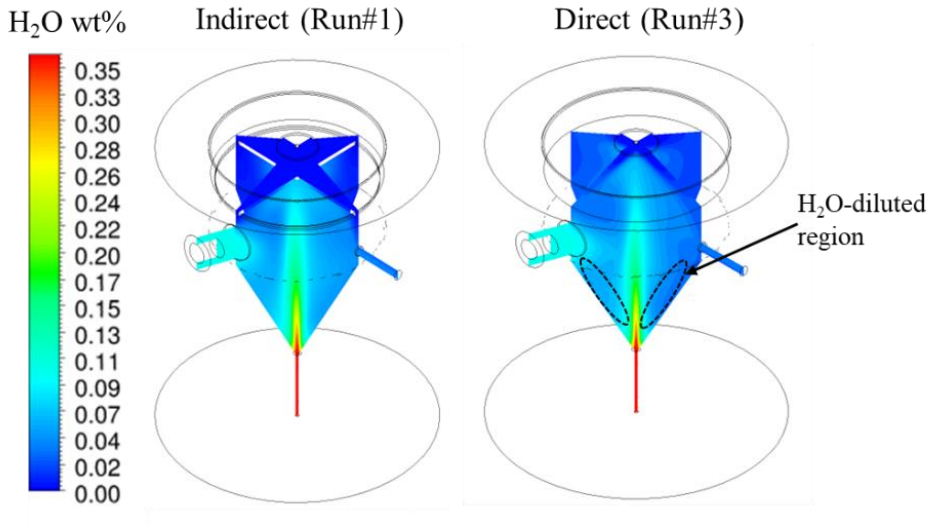

Figure II.16 Steam mass fraction contour: indirect (Run#1) vs. direct (Run#3)

Regarding product gases, the H_2 mass fraction contour is plotted in Figure II.17 according to the vertical section where the biomass is injected and in Figure II.18 at a cross (p) section for each of the other syngas components. The release of the pyrolysis gases occurs gradually in the 3D domain, which affects strongly the syngas composition and the species distribution. In fact, pyrolysis gases start to be formed early in the injection tube as a result of the fast pyrolysis of the smallest particles. Moreover, a high gas concentration region is identified at the corner below the injection tube (Figure II.17-a). As shown in Figure II.17-b, the high velocity of the inlet gas jet repels the entering non-reacted particles to the border of the cone till the particles mass gets sufficiently low for being entrained and joining the central spout. This explains the gradient in product gases concentration inside the cavity.

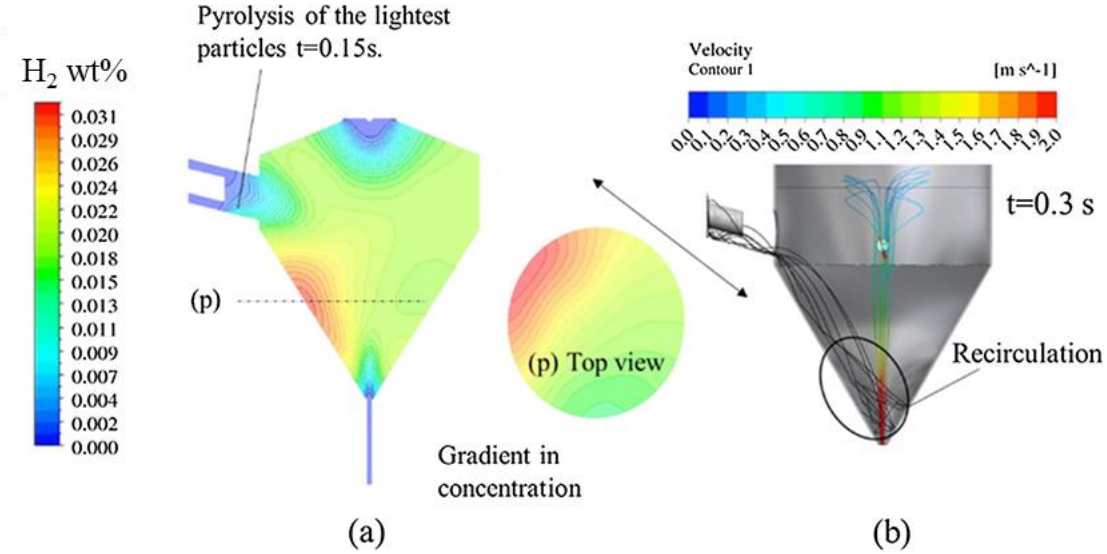

Figure II.17 (a) H_2 mass fraction distribution inside the reactor, (b) Particle trajectories colored in black and spout gases velocity streamlines (Run# 3).

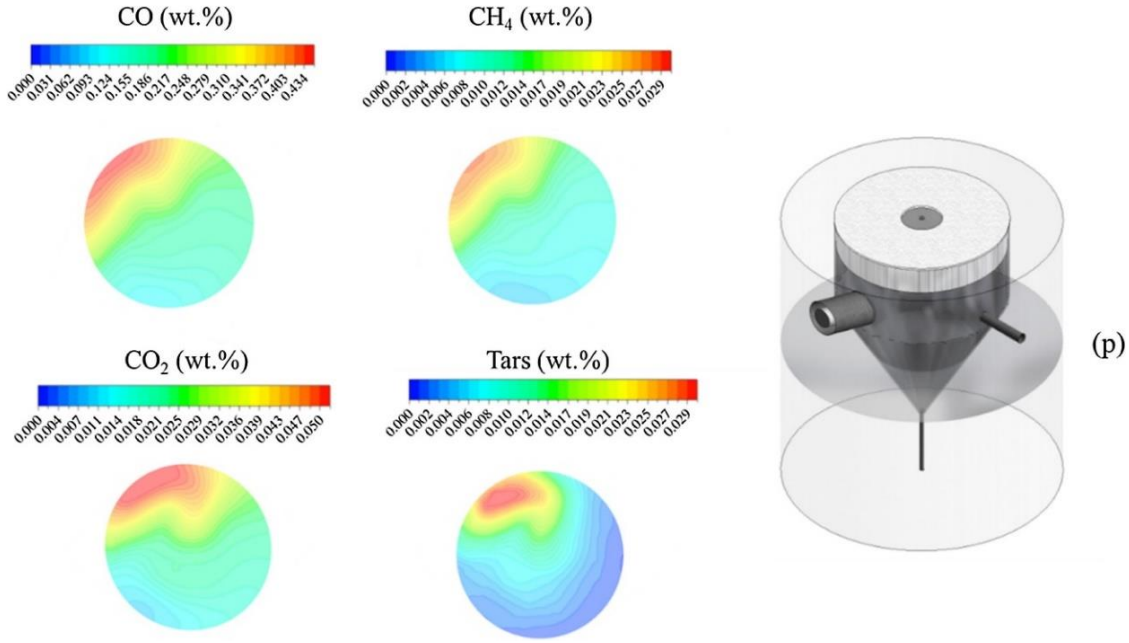

Figure II.18 Syngas mass fraction inside the reactor over a cross section (p)

The volumetric loading of the reactor is shown in Figure II.19. The cavity is globally empty and the gases occupy almost all the space. Particles concentration, under the effect of gravity and the gas jet, is the highest at the bottom of the cone and in the proximity of the walls.

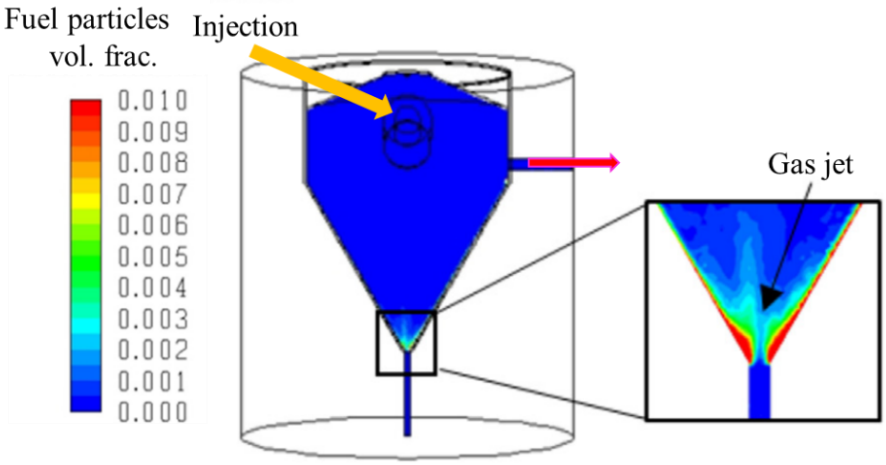

Figure II.19 Predicted volumetric load of the reactor during Run#3

The interaction between the particles and the wall in this model was considered elastic (i.e. restitution coefficient of 1) for the sake of simplicity, however, in reality considerable kinetic energy losses can occur after collision. The resulting change in momentum and trajectory depends on number of parameters such as the particles size, shape, physical properties (density, diameter, electromagnetic forces etc.), the angle of incidence and the wall roughness. A more in-depth study on the reacting particles/wall interaction can help improving the hydrodynamic predictions thanks to more realistic and precise tangential and normal restitution coefficients.

II.2.6.3 Improvement strategies

These results provide insights into possible improvements of the solar reactor geometry to enhance the mixing, residence time and temperature distribution homogenization. Lopez et al. (Lopez et al., 2017) mentioned the possibility of confining the particles in conical spouted beds thanks to a tube welded to the lid of the reactor. This confiner aims to confine the jet and gasification gases and to avoid the entrainment of the lightest particles. Baffles fixed on the confiner and on the cavity walls may also retain the small particles longer in the reaction zone and increase the surface exchange area between the hot surfaces and the gas phase. In addition, to overcome the issue raised by the H_2O-diluted hot annular zone and the local concentration of the pyrolysis gases at the corner of the reactor, an auxiliary steam flow could be introduced directly towards the annular zone through lateral injections. This would bring the advantage of increasing the steam oxidant concentration at the annular region, which in turn would dilute the pyrolysis gases with steam while providing a novel solution for controlling the central gas jet flow rate. A new work recently conducted by Wu et al. (F. Wu et al., 2020) examined this solution thanks to multiple small gas injections at the reactor conical wall to directly fluidize the annular region. Besides, to minimize the temperature gradient encountered by each particle when flowing between annular and spout zones (that penalizes the reaction kinetics), inlet gases should be preheated prior to their injection, for example, by recovering heat from the outlet syngas. The simulations also predicted a cavity wall temperature, which was hundred degrees higher than the inner reaction zone temperature because most of the incoming solar radiations were absorbed directly by the reactor cavity while the gases and biomass particles absorbed a smaller portion of the solar load. In order to address this issue, inert fine particles to be spouted with the woody feedstock by the gas flow inside the cavity can be used to absorb part of the entering solar radiations and to transfer heat to the reactants by convection, radiation and particle-to-particle interactions. Likewise, inert packed bed particles set at the bottom of the reactor can also decrease the central jet velocity and reduce the intensity of entrainment inside the reactor. A patent application has been filed thanks to 3D multiphysics simulations concerning heat transfer intensification in the jet spouted bed reactor. The new concept is described in ANNEX 1.

These results provided a clearer insight into the reactor operation at optimal heating conditions with beech wood particles. Two main points remain to be solved: (i) solar energy intermittency that presents severe constraints for the continuity of the solar process, (ii) the conversion of high-ash waste feedstocks that raises new difficulties and challenges to evaluate. These two issues are tackled in the following sections II.3-II.4.

II.3 Hybrid operation

II.3.1 Principle and objectives

The industrial deployment of solar processes such as solar gasification is strongly limited by the variability of solar energy that hinders a priori day and night continuous operation. The concept of hybrid solar gasifiers is thus proposed to couple autothermal gasification with

solar (allothermal) gasification so as to meet the requirement for stable and continuous operation under intermittent or fluctuating solar irradiation. Solar process hybridization through partial oxy-combustion of the feedstock appears to be crucial because thermochemical processes are very sensitive to small solar energy input variations, and require permanent control of thermodynamic conditions to ensure fuel production quality. Very little researches have been undertaken concerning mixed solar/combustion reactors. Most of the earlier works dealt with the simulation of hybrid solar gasification at a system scale based on equilibrium models (Kaniyal et al., 2013; Li et al., 2018; Sudiro and Bertucco, 2007). These models have definitely shown the interest of hybridization to promote process integration. Experimental validation tests under direct real concentrated solar power and detailed 3D numerical simulations of solar hybrid gasification have never been performed. Muroyama et al. (Muroyama et al., 2018) were the first to study an indirectly heated solar hybrid fluidized bed reactor for activated carbon gasification. In the continuity of this study, this section aims to investigate process hybridization in the studied spouted bed reactor for the first time via numerical simulations and experimentations under real direct concentrated solar flux. Prior to the experimental study, the operational feasibility of the process was first investigated using 3D/2D CFD simulations. Dynamic experiments were thereafter performed on beech wood to assess the dynamic behavior of the hybrid reactor and to validate its ability to elevate temperature and to continuously run the process (especially when the solar resource is low), while a controlled amount of O_2 was injected during hybrid allothermal/autothermal operation. Results in terms of temperature profiles, biomass conversion, syngas yields before and after hybridization are discussed.

The results presented in this section were published in *Energy* (Boujjat et al., 2019b)

II.3.2 Numerical study

II.3.2.1 3D steady state simulations

Hybrid solar-combustion simulations were performed on the directly irradiated reactor. Combustion reactions were added to the previously developed 3D model (section II.2.4). Char particles oxy-combustion was modelled by the following law (Eq.II.53) that includes the effects of both diffusion and kinetic rates:

$$r_{combustion} = \frac{dm_{char}}{dt}\}_{Combustion} = A_{fuel}.(1 - Y_{Biomass}).R_{KIN}(P_{O_2} - (r_{ccombustion}/D_0))^{0.65} \quad \textit{II.53}$$

$$R_{KIN} = A_{combustion} e^{-E_{a,combustion}/RT_{fuel}} \quad \textit{II.54}$$

$$D_0 = \frac{C_{dif}(T_{fuel} + T)^{0.75}}{2.d_{fuel}} \quad \textit{II.55}$$

C_{dif} is the diffusion rate constant, in most cases this coefficient is set to 5.10^{-12} s.$K^{-0.75}$. This value can be deduced assuming that the rate of diffusion of the oxidant to the surface of the particle is in equilibrium with the rate of consumption by reaction at the surface. The mass of each fuel particle as function of time is thus calculated by integrating Eq.II.56 that accounts for combustion:

$$r_{fuel} = \frac{dm_{fuel}}{dt} = r_{fuel,pyrolysis} + r_{fuel,gasification} + r_{fuel,combustion} \quad \textit{II.56}$$

Additional gas phase combustion reactions were integrated (Eqs.II.57-II.59). Their global kinetics were taken from the work of Nakod (Nakod, 2013) for modelling an oxy-fired and an air-fired entrained flow reactor.

$$CO + 0.5O_2 \rightarrow CO_2 \quad \textit{II.57}$$

$$H_2 + 0.5O_2 \rightarrow H_2O \quad \textit{II.58}$$

$$CH_4 + 1.5O_2 \rightarrow 2H_2O + CO \quad \textit{II.59}$$

From allothermal experimental conditions in Run#3 (direct heating configuration), oxygen (0.25 NL.min^{-1}) was added to the inlet spout gases (0.2 NL.min^{-1} of Ar and 0.2 g.min^{-1} of H_2O) and an extra-biomass injection of 0.2 g.min^{-1} was set corresponding to the fraction combusted with the added amount of O_2. The predicted temperature distribution inside the reactor (solid components and reaction zone) of the hybridized gasifier (with Q_{solar}=0.9 kW_{th}) is depicted in Figure II.20. The central spout region reaches very high temperatures (~1800°C at the central spout near the flame zone) while the annular zone seems to be less affected by the O_2 injection with a temperature increase of around 150-200 °C.

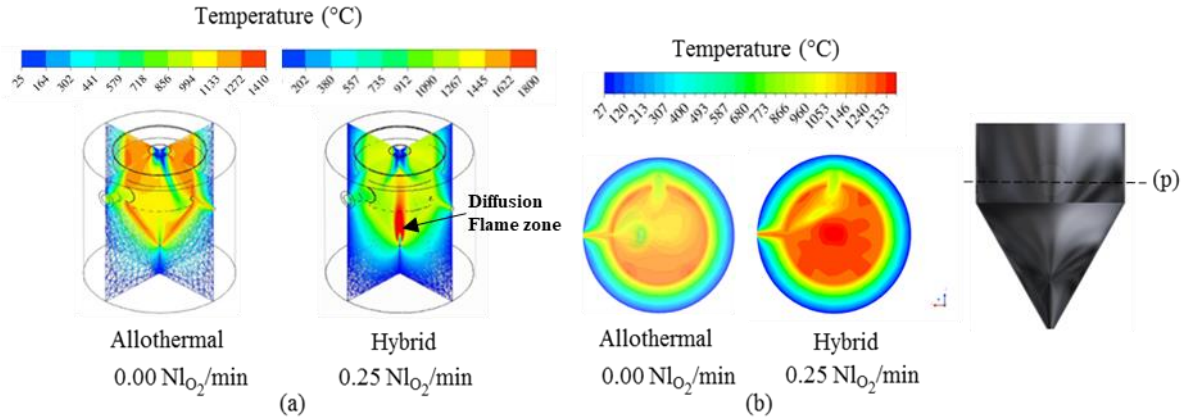

Figure II.20 Temperature distribution for allothermal and hybrid modes: (a) vertical cross-sections, (b) horizontal section

Ar, CO_2 and H_2O mass fraction distributions are plotted in Figure II.21. These gases appear to be effectively routed by the Ar protective flow towards the outlet (Figure II.21-a).

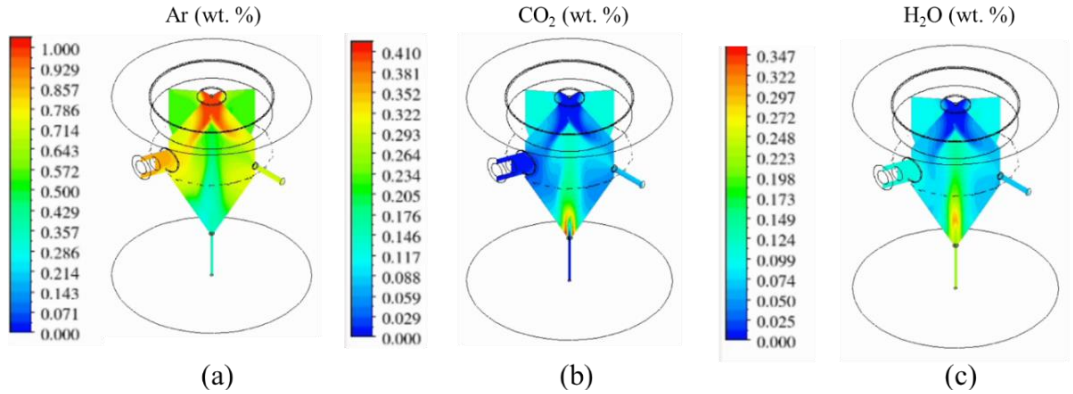

Figure *II.21 Mass fraction spatial distribution of Ar, CO_2, and H_2O at the core of the reactor*

This confirms that the current protective gas prevents well window soiling. The flame front can be identified by the highest CO_2 concentration region (as shown in Figure II.21-b) where a very thin ellipsoidal surface delimited by the highest gas concentration at the bottom of the conical cavity is observed. It is also found that the highest steam concentration is not at the injection tube (where steam is initially fed) but rather, is at the bottom of the cone in the central region where combustion reactions take place and locally generate more steam that gets mixed with the inlet gas jet (Figure II.21-c).

To ascertain the functioning principle of the hybrid solar gasification process in the solar-combustion jet spouted bed, representative 1.2 mm diameter (present in large amount according to the biomass size dispersion) fuel particle stream was tracked all along its lifetime inside the reactor. Just as in the allothermal operation (Figure II.8), Figure II.22-a shows the fuel particle velocity as a function of its residence time in the cavity. It can be seen that the particle describes a number of cycles (from the spout to the annular region of the bed as evidenced by the successive velocity peaks) during which it pyrolyses, gasifies and burns before being expelled from the reactor at the end of the stay. Figure II.22-b shows the fuel particle temperature and the trajectory that it follows. It reveals that peak temperature values are reached when the particle moves over the spout region between the very hot combustion zone (flame zone) at the bottom area and the fountain zone near the radiation entrance where the particle/radiation entrance view factor is maximum. Figure II.22-c shows the conversion of the particle as a function of time. Two regions with two different slopes can be observed. The sharp decrease in the particle mass (and diameter from Eq.II.28) during the first instants of injection is due to the fast pyrolysis of the particle. Char gasification subsequently occurs and constitutes the slowest step of the conversion process. A more detailed view of the conversion during gasification is also provided to properly differentiate the reaction rates of both oxy-combustion and steam gasification at the spout region and elsewhere. Steps correspond to mass losses due to particle combustion in the spout region, while gasification occurs continuously during the low declining slope (slower process).

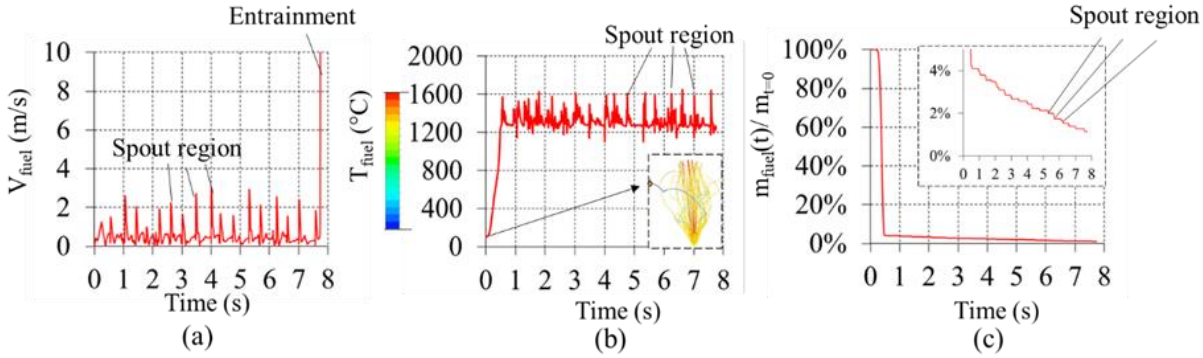

Figure *II.22 Fuel particle velocity, temperature and extent of particle conversion (for 1.2 mm initial particle size)*

Still regarding the discrete phase flow analysis, the simulations reveal that the lightest injected wood particles behave quite differently as their solid residence time is very low (< 1 s). In Figure II.23, a particle with 0.2 mm initial size is tracked.

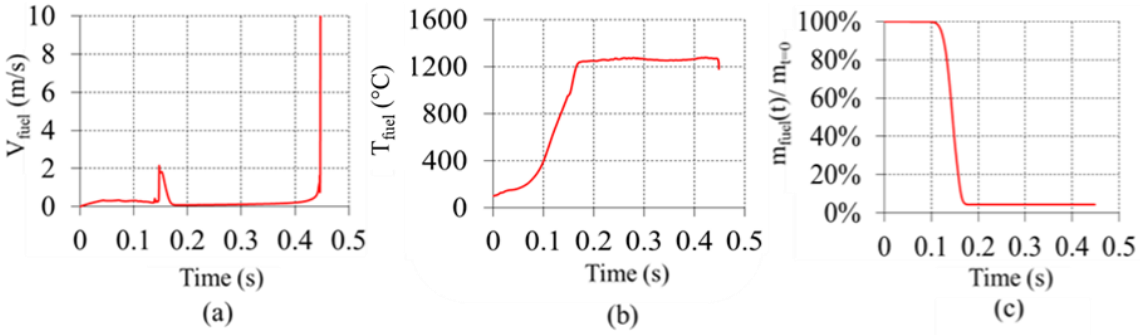

Figure *II.23 Fuel particle velocity, temperature and extent of particle conversion (0.2 mm initial size)*

The peak velocity and temperature values are no longer observed, which means that light particles spouting is not actually established in the conical cavity. The fuel particle is heated up to 1300°C, and during this period, it pyrolyses and gets entrained by the high velocity jet to the exit. The inlet gas flow rate appears to be a crucial parameter for the solar spouted bed that should be optimized to maximize the particles conversion, the phase mixing, and the exposure to direct solar radiation such that high particle crest temperatures can be reached. The effects of different O_2 flow rates, i.e Equivalence Ratios (ER) $(B/O)/(B/O)_{st}$, (where B corresponds to the dry feeding rate of biomass (Table II.7) on biomass conversion, gas quality, gas composition and cavity wall temperature were studied in Figure II.24.

Table II.7 Operating conditions for the analysis of oxygen injection effects on the reactor output Q_{solar}=0.9 kW

Simulation #	F_{oxygen} ($NL.min^{-1}$)	$F_{biomass}$ ($g.min^{-1}$)	F_{steam} ($g.min^{-1}$)	ER $(B/O)/(B/O)_{st}$
1	0.00	1.2	0.2	-
2	0.18	1.3	0.2	6.38
3	0.25	1.4	0.2	4.95
4	0.38	1.6	0.2	3.72

The simulations reveal that the syngas composition is considerably affected, especially H_2 and CO_2 concentrations. In fact, with respect to the allothermal operation, H_2 volume fraction decreased by around 30% at 0.38 $NLO_2.min^{-1}$ while CO_2 increased sharply by 415% and CO decreased by 9%. CH_4 slightly declined and C_nH_m increased marginally (Figure II.24-c). The H_2:CO ratio constantly decreased to reach values as low as 0.8 at 0.38 $NLO_2.min^{-1}$. Moreover, Figure II.24-e shows that the more the oxygen flow rate is increased, the more pronounced is the decrease in the H_2:CO ratio. The opposite is also true for the cavity wall average temperature that consistently increased up to 1305 °C in a non-linear fashion. To study the effects of oxygen injection on the extent of biomass conversion inside the reactor, the Carbon Conversion Efficiency (CCE) was calculated (Figure II.24-a). The CCE represents the mass flow rate ratio of C atoms in the produced syngas over C atoms in the inlet biomass. The CCE is found to increase as the O_2 flow rate increases (the maximum

value of 95% is attained for 0.25 $NLO_2.min^{-1}$). At 0.38 $NLO_2.min^{-1}$, the CCE decreases slightly to 94%. The conversion of biomass inside the reactor is the result of two opposite physical phenomena. On the one hand, increasing O_2 promotes the kinetically rapid combustion reactions and favors the carbon conversion, but on the other hand, higher inlet jet gases flow rates facilitate the entrainment of the lightest reacting particles and thus limit the conversion. To maintain optimal spouting conditions that increase both the gas and solid phases residence time, the inlet carrier gas flow rate needs to be continually controlled during the hybrid process.

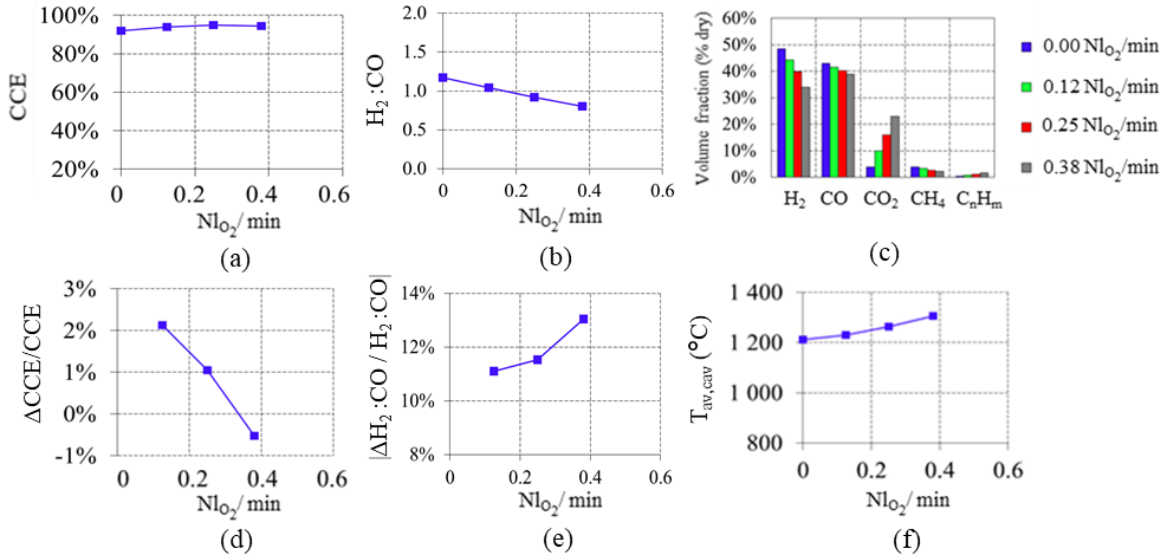

Figure II.24 Effects of O_2 injection on the conversion of biomass with highlights on (a) CCE; (b) H_2:CO; (c) gas composition; (d) CCE variation; (e) H_2:CO variation; (f) Reactor cavity temperature

Overall, the model confirms the operational feasibility of process hybridization and opens the way for further hybrid solar/combustion experiments. Nevertheless, the dynamic behavior of the reactor during the hybrid phase is still unclear and not predicted by the 3D steady state model. For this reason, prior to the experimental study, transient simulations were performed thanks to a simplified dynamic 2D model of the reactor, which allows to get insights into its dynamic response. The developed dynamic model and the results are presented in the following section.

II.3.2.2 2D Transient simulations

A thermal transient 2D hybrid solar/combustion CFD model was developed in order to visualize the time evolution of the reactor cavity temperature for different wood feeding rates when switching from a solar-only heating mode to a hybrid solar-combustion mode. Such transient simulation was not applicable to the complete 3D model due to excessive computational time. According to previous work on the solar reactor (Bellouard, 2017; Bellouard et al., 2018, 2017a), the solar reactor temperature needs to be above 1200°C (i.e. Q_{solar} >0.9 kW_{th}) for a proper operation (good syngas quality, no smoke formation and high performance). Thus, the transient simulations started at t=0 min from an initial stationary

temperature field obtained in allothermal mode with Q_{solar}=0.8 kW_{th}. The resulting cavity wall average temperature was around 1160°C (Figure II.25-a). In this simplified model, only the energy and the radiative heat transfer equations were solved for the axisymmetric domain. The transient simulations were conducted assuming that a constant amount of biomass (1.2 $g.min^{-1}$) is gasified, while combusting an extra-amount (0.2, 0.4 or 0.6 $g.min^{-1}$) aims to supply additional process heat to maintain the wall temperature at around 1200°C with Q_{solar}=0.8 kW_{th}. In this model, no particle injection was considered but instead, a volumetric heat sink from steam gasification (based on Eq.II.1) and heat source from wood combustion ($C_{6.0}H_{10.0}O_{4.1}+6.42O_2 \rightarrow 6.00CO_2+4.98H_2O$) were applied directly to the cavity wall (1 mm thick) as depicted in Eq.II.60.

$$\frac{\partial(\rho.cp_{cavity\ wall}T)}{\partial t} = \nabla.\left(\lambda_{cavity\ wall}\nabla T\right) - \left(\dot{m}_{biomass}.\Delta H_{gasification} + \dot{m}_{extra-biomass}.\Delta H_{combustion}\right)/V_{cavity\ wall} \qquad \textit{II.60}$$

Temperature control of solar hybrid reactors is a relevant issue requiring the design of feeding strategies that precisely control the biomass, steam and oxygen flow rates based on the reactor temperature and syngas demand. In this work, a simple C++ on/off control algorithm (for extra-wood supply and combustion) was coupled to the CFD thermal simulation to maintain the cavity wall average temperature at around 1200°C (Figure II.25-b).

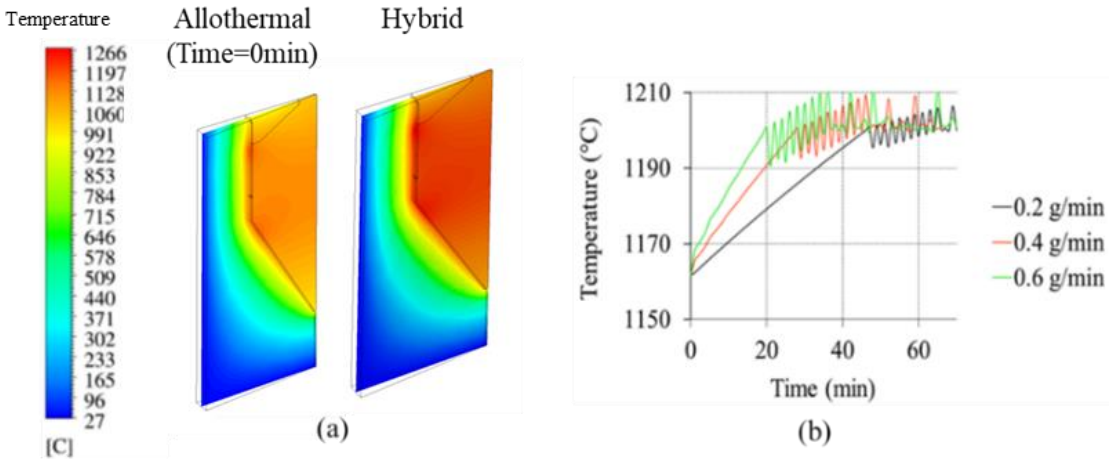

Figure II.25 (a) Stationary temperature contours for the hybrid (with extra-wood injection) and allothermal (before extra-wood injection, initial condition at t=0) modes, (b) Time evolution of the averaged cavity wall temperature during the hybrid operation

The combustion of 0.2 $g.min^{-1}$ (representing 14% of the total feedstock rate) enabled to reach the reactor cavity wall temperature of 1200°C after approximately 45 min. The increase of the extra-injected biomass particles to 33% (0.6 $g.min^{-1}$) diminished significantly the system response/stabilization time to less than 20 min. In practice, O_2 injection increases the reaction zone temperature (fluid phase) nearly instantly thanks to internal homogeneous and heterogeneous oxy-combustion reactions (corresponding to the flame located in the hollowed central core, Figure II.20). However, the stabilization of the reactor wall temperature can take much longer time (i.e. several tens of minutes) after oxygen injection.

Given the promising models outcomes, hybrid directly and indirectly irradiated experiments were performed at CNRS-PROMES on the solar reactor. The obtained results are discussed in the following sections.

II.3.3 Experimental study

A first hybrid solar-combustion experiment was performed in indirect heating mode (Run#5) with an initial feedstock of 30g and a biomass injection flow rate of 1.2 $g.min^{-1}$. During this run, no steam was fed into the reactor and oxygen was the only oxidizing agent injected from the bottom alumina tube[6]. The DNI was very stable (variation of 1.7%) and the average solar power input was 0.77 kW_{th}. The goal was to assess the impact of different oxygen flow rates on the reactor temperature. Oxygen injection was controlled by a CO_2 flow meter (Brooks SLA5850S, scale: 0-5 $NL.min^{-1}$, precision: ± 0.2% full scale) thanks to a correction factor of 1.25 to get the real O_2 flow rate. Five separate oxygen/wood injections (inj#1-5) with 0.25-0.38-0.10-0.25-0.38 $NL.min^{-1}$ of O_2 were carried out consecutively. The total duration of the experiment was about 44 min and the reactants flow rates are shown in Figure II.26. Inlet oxygen flow rate and outlet oxygen molar fraction are plotted. It can be observed that O_2 was fully consumed by the reaction during the wood injection phases and its molar fraction increased progressively when wood injection was stopped due to residual char particles oxidation. Table II.8 shows in detail the overall material mass balance of the experiment (Run#5) which is also representative of the different runs.

Table II.8 Overview of the mass balance of the solar combustion experiment (Run#5, closure >96%)

Input		Output			
Water	0.00g	Syngas		Solid deposit+unconverted water	
Oxygen	12.53g	CO	13.24g	Tubes	3.10g
		CO_2	12.43g	Bubbler	8.50g
		CH_4	0.86g	Filter	0.50g
		C_nH_m	0.80g		
Biomass	28.87g	H_2	0.54g		
		Total gas:	27.87g	Total deposit:	12.10g
Total input:	41.40g	Total output: 39.98g			

The biomass feedstock was successfully converted thanks to solar heating and oxy-combustion with a CCE of 82.9%. 1.13g of biomass remained however at the end of the experiment in the hopper as wood injection was stopped few minutes before the end due to the formation of smoke in the window area. Smoke formation was attributed to the very low oxidant concentration (ER=2.80 during inj#5) and the low solar input.

[6] Around 110 mg/min was continuously- supplied through feedstock injection tube due to biomass moisture (8.9 wt.%, Table II.2)

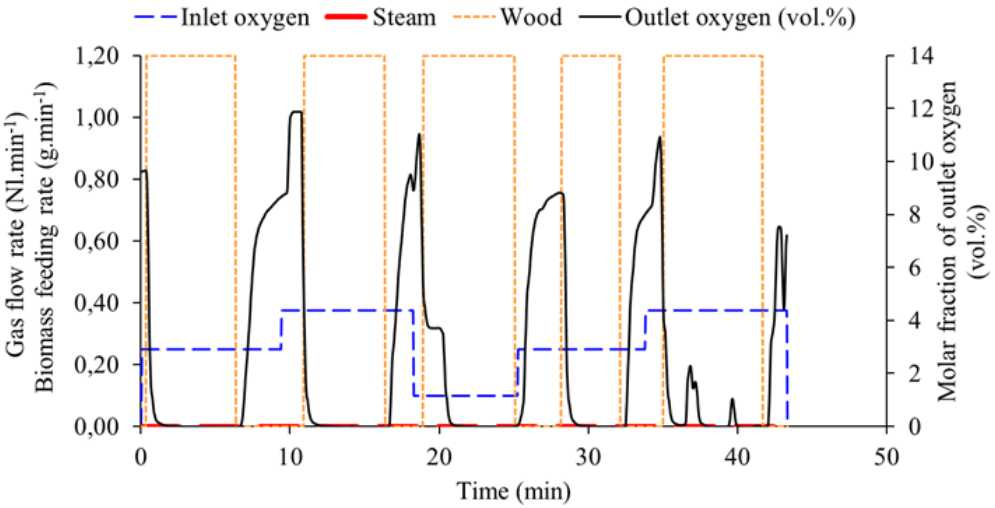

Figure II.26 Reactant flow rates in Run#5 (solar-combustion, indirect)

At time=0 min, the reactor was solar heated (i.e. no combustion) to a temperature (T3) of around 1189 °C. Figure II.27-left shows the reactor temperature as measured by T3 (inserted inside the reaction zone), T2 (positioned at the external cavity wall temperature, in the upper cylindrical region) and Tpyro (pointing directly at the emissive plate center) (Figure II.1). Figure II.27-right shows the resulting outlet gas flow rates.

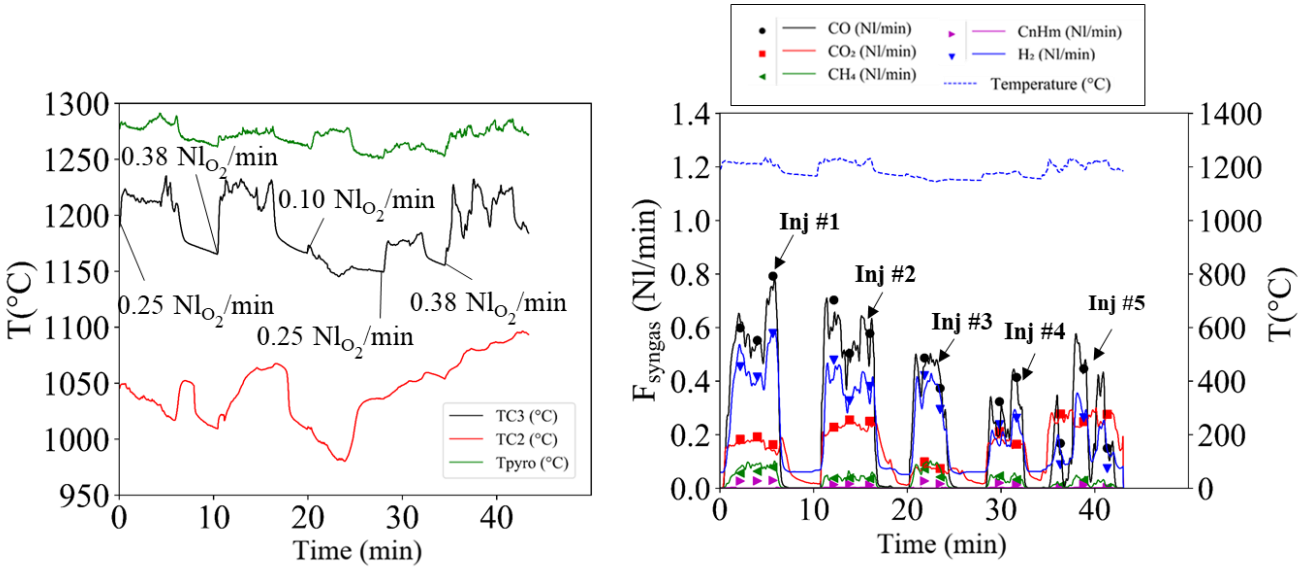

Figure II.27 Impact of different oxygen flow rates on the reactor temperature (T3, T2 and Tpyro) and on syngas flow rates injections #1-5

The injection of 0.25 NL.min^{-1} of O_2 (inj#1) raised T3 temperature by around 41°C. The injection of 0.38 NL.min^{-1} of O_2 (inj#2) led to T3 increase by 67°C (from 1165°C to a crest value of about 1232°C) while 0.10 NL.min^{-1} of O_2 in inj#3 did not affect the temperature significantly. In inj#4-5, 0.25 NL.min^{-1} and 0.38 NL.min^{-1} of O_2 was fed into the reactor once again to confirm inj#1-2 temperature rise, and comparable temperature variations were achieved. Tpyro measurements were less impacted by O_2 injection with a maximum temperature increase of 20°C. Its response time was very similar to that of T3. T2 showed greater thermal inertia and lower temperature fluctuations as its position was a little far from

the reaction zone. The gas was very rich in CO_2 due to combustion reactions with up to 41.2 vol. % during inj#5 and on average over the whole experiment, the CO_2 content was 24.4 vol. %. Hydrogen concentration was much lower than in previous allothermal steam gasification runs (Table II.6), the H_2:CO ratio was minimal during inj#5 (H_2:CO=0.48) and maximal inj#3 (H_2:CO=0.64). Finally, the overall CGE was about 65.9%, which is way below than that of allothermal steam gasification (Table II.6) that generally exceeds 100%.

This first run, confirmed experimentally the potential of hybridization to elevate the process temperature during the solar operation. Further hybrid solar-driven steam gasification experiments were thus performed in direct and indirect heating modes (Runs#5-10, Table II.9) under very stable solar conditions with DNI variation less than 4% (in Run#7). Complete biomass conversion was achieved with mass balance closure beyond 86% (in Run#9). Table II.9 recaps the operating conditions for each run. The carrier gas flow rates were kept constant just as in section II.2, i.e. 0.2 NL.min^{-1}, 0.5 NL.min^{-1} and 2.0 NL.min^{-1}of argon through the bottom alumina tube, the screw feeder and the window area respectively.

Table II.9 Operating conditions for studying the effects of hybridization on the solar operation

Run #	Mass (g)	Heating mode	Initial reactor temperature (T3 in °C)	$F_{biomass}$ (g.min^{-1})	F_{steam} (g.min^{-1})	F_{oxygen} (NL.min^{-1})	ER (hybrid phase) $(B/O)/(B/O)_{st}$
5	30g	Indirect	1200	1.2	0.0	0.10 -0.25-0.38	10.61-4.25-2.80
6	30g	Direct	1200	1.2	0.2	0.00-0.25	4.25
7	50g	Indirect	1300	1.2-1.4	0.2	0.00-0.25	4.95
8	50g	Direct	1300	1.2-1.4	0.2	0.00-0.25	4.95
9	30g	Indirect	1300	1.2-1.4	0.2	0.00-0.25	4.95
10	30g	Direct	1300	1.2-1.4	0.2	0.00-0.25	4.95

In all the runs, a thin layer of SiC particles was set at the bottom of the reactor to protect the gas jet injection and water capillary tubes from ash residues. Figure II.28-a shows the measurements of outlet gas production rate evolution realized for Run#6. In this run, the reactor was directly irradiated. Only steam and biomass were injected at the beginning of the experiment with an entering solar power of around 0.75 kW_{th}. Temperature as measured by T3 is plotted (Figure II.28-a). It can be observed that the highly endothermal gasification reactions lead to a temperature drop from 1197°C (time=0 min) to 1145°C (Time=6 min while the gas production rates increased continuously. During this period, fumes impinged upon the window (Figure II.28-b) due to low solar input and gasification temperatures. Wood injection was thus stopped until the tangential upper Ar flow blows the smoke and cleans the window area. Then, a supplementary O_2 flow (0.25 NL.min^{-1}) was injected with the inlet jet gases (Ar and H_2O). As a result, the gas production rates rose and the reactor temperature increased constantly to around 1200°C at the end of the experiment.

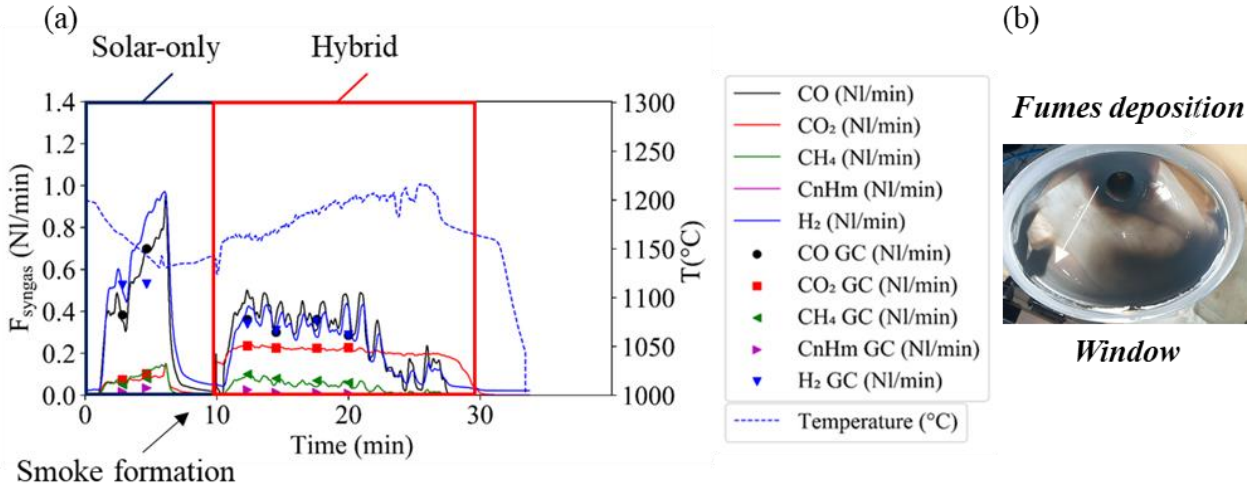

Figure II.28 (a) Syngas production rates and reactor temperature (T3) as a function of time: allothermal mode (1.2 g.min^{-1} of wood, 200 mg.min^{-1} of steam); hybrid mode (1.2 g.min^{-1} of wood, 200 mg.min^{-1} of steam, 0.25 NL.min^{-1} of oxygen); (b) smoke deposition on the window Run#6

The strongly exothermic oxy-combustion reactions were successful to meet the need of continuous process operation until complete biomass conversion. Nevertheless, as expected from the CFD simulations, the H_2 content decreased substantially while CO_2 significantly increased when compared with allothermal operation. The time-averaged molar fractions (on dry basis) of the produced syngas were calculated: CO (35%), H_2 (30%), CO_2 (30%), CH_4 (5%) and C_nH_m (<1%). The H_2:CO ratio reached values below 1 in agreement with numerical predictions. The overall CCE was 84.0%. The CGE was improved in comparison with Run#5 thanks to steam supply and reached 80.0%.

To further analyze the effect of the reactor temperature on the hybrid process, the same reactants and carrier gas flow rates were injected at a higher solar power input in indirect and direct heating mode (Runs#7-8, Figure II.29). The average solar power in these two runs was estimated at 1.15 kW_{th} and 1.13 kW_{th} respectively. Just as in Run#6, during the first 16 minutes (Run#7) and 20 minutes (Run# 8) of allothermal operation, temperature decreased steadily because of feedstock steam gasification, i.e. from 1307°C to 1215°C in Run#7 and from 1316°C to 1245°C in Run#8. Then, the wood feeding rate was increased from 1.2 to 1.4 g.min^{-1} and the O_2 feeding rate was fixed to 0.25 NL.min^{-1}. An increase in the reactor temperature by up to 135°C in Run#7 and 105°C in Run#8 was achieved. The reactor temperature as measured by T3, T2 and Tpyro is plotted in Figure II.30. The pyrometer for the indirect heating mode measured the emitter plate central temperature. For the direct heating mode, it directly pointed at the core of the conical cavity. T2 indicated lower temperatures that were about 100°C to 150°C below T3 as a result of internal thermal resistance of the metallic cavity wall.

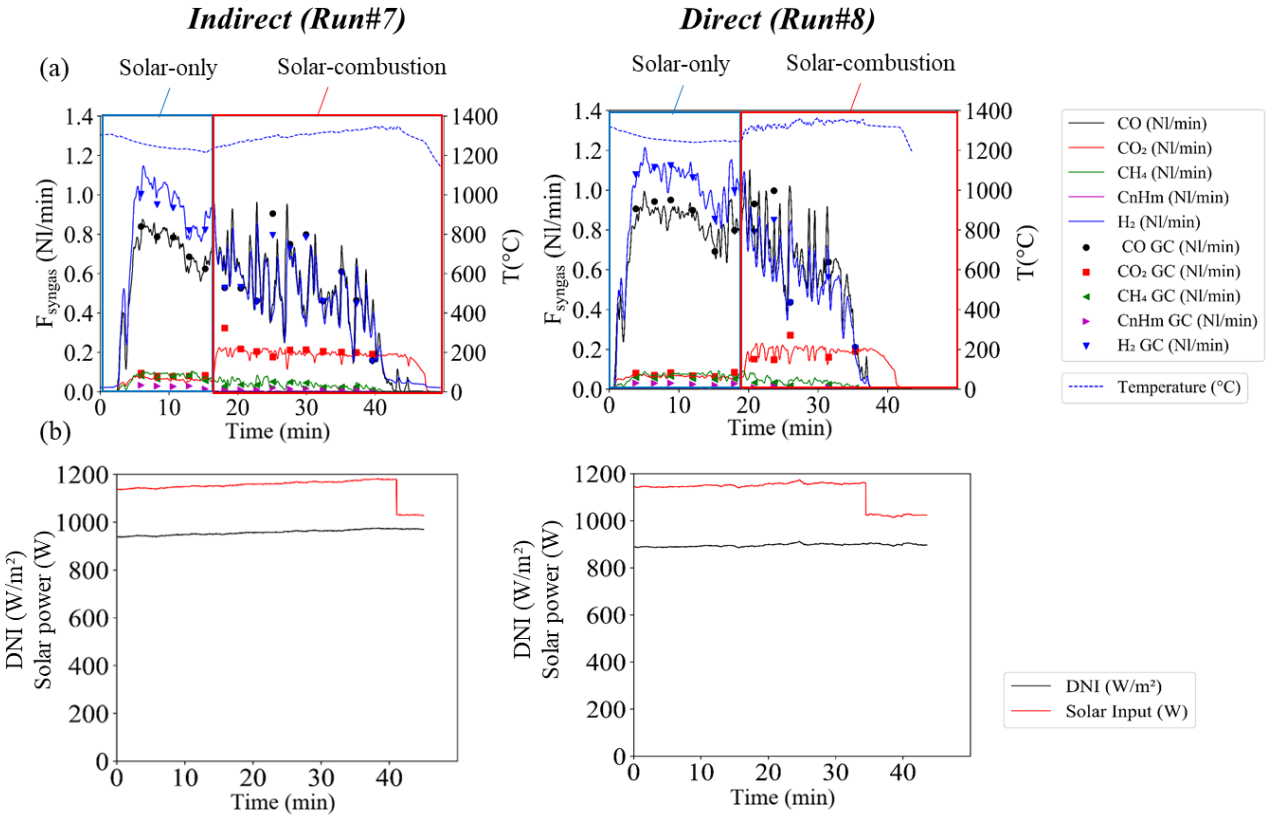

Figure II.29 (a) Syngas gas yield and reactor temperature (T3) as function of time: allothermal mode (1.2 g.min^{-1} of wood, 200 mg.min^{-1} of steam); hybrid mode (1.4 g.min^{-1} of wood, 200 mg.min^{-1} of steam,0.25 NL.min^{-1} of oxygen) - Runs#7-8-indirect vs. direct heating configuration (b) Solar load Runs#7-8

In line with Run#5, the emissive plate temperature was only slightly affected by oxygen injection according to pyrometer measurements. In contrast, Tpyro showed for the direct heating mode (Run#8) a sharp increase in temperature and strong fluctuations. The latter were due to optical disturbances caused by the spouted char particles as well as by the injected raw (unreacted) biomass particles that fall by gravity to the bottom of the cone in the form of small parcels. These particles were subjected to temperature variations when being spouted, which is clearly evidenced by the pyrometer measurements. Moreover, T3 took several tens of minutes to stabilize in Runs#6-7 while in Runs#5,8, T3 increased rapidly (~1-2 minutes). This difference in response is not related to the method of heating nor to the solar power input that remained almost constant during the experiments, given that Run#5 (rapid increase in temperature) and Run#7 (slow increase in temperature) were both performed in indirect heating mode. It is more likely due to hydrodynamic factors affecting the flame location relative to that of T3. In fact, the presence of SiC/char particles at the cone base can deflect the central jet/flame zone further from T3 and delay the measurements. Consistently with the transient simulations, the complete stabilization of the wall temperature (T2) is achieved only after several tens of minutes.

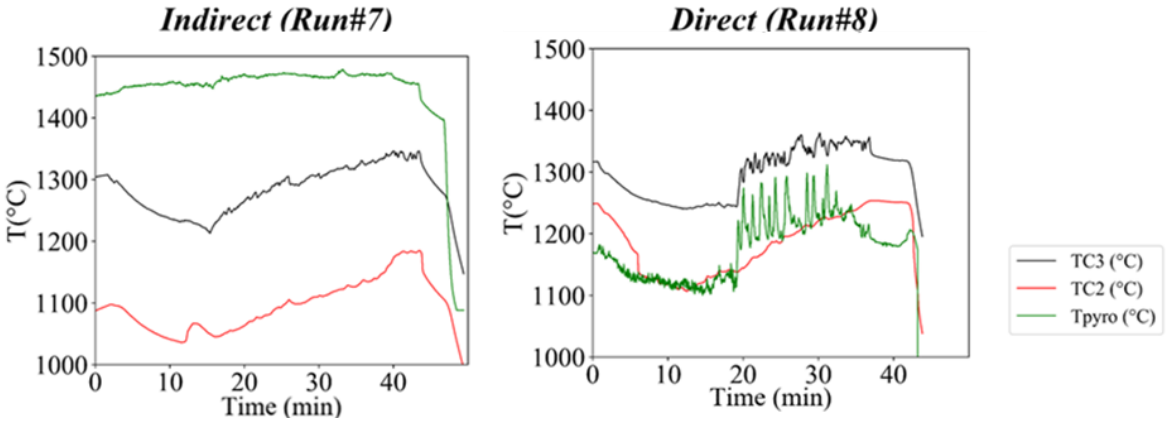

Figure II.30 Reactor temperature measured by T3, T2 and pyrometer (Tpyro) in (°C) (Runs#7-8)

The increase of cavity temperature was accompanied by an almost instantaneous decline in H_2 and CO production rates and a strong increase of CO_2. H_2 and CO_2 were the most impacted gases in the mixture. This affected the syngas quality in terms of H_2:CO ratio and syngas energy content. Figure II.31 shows the time evolution of the H_2:CO and LHV before and after O_2 injection for the indirectly and directly solar heated reactor. It can be seen that the H_2:CO ratio declined from around 1.3 for the two modes to reach values approaching 0.9 after hybridization. The syngas thermal energy content also decreased significantly from 355 W for Run#7 and 430 W for Run#8 to 236 W and 301 W, respectively. Globally, the two heating modes showed very similar behavior, with a slightly higher gas production rates for the direct configuration especially during the allothermal phase of the experiments.

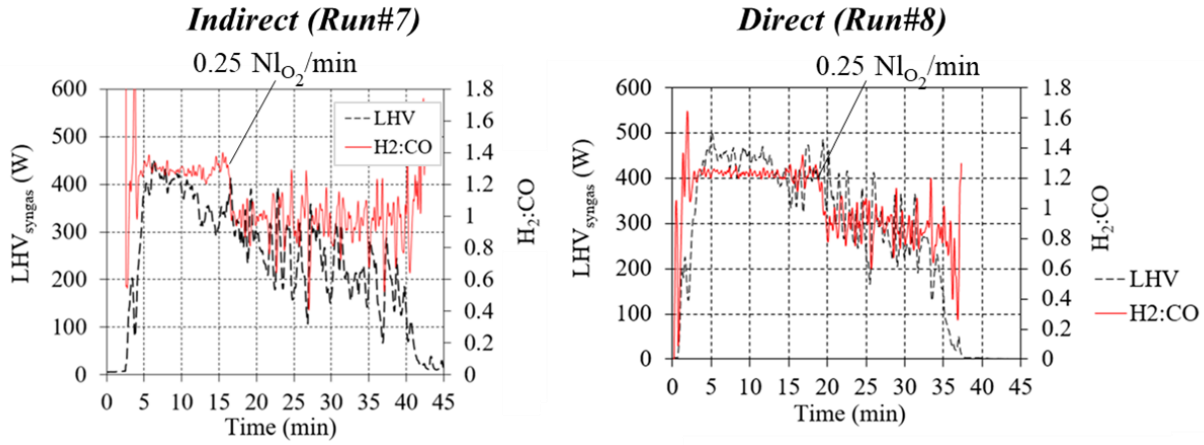

Figure II.31 LHV and H_2:CO ratio as a function of time (Runs#7-8)

Regarding the gradual decrease in the gas production rates (Figure II.29) and LHV (particularly from 20 min) with time, it may presumably be associated to a feeding rate decrease over time due to a more difficult transport of the millimetric particles by the screw feeder as the hopper gets empty. Gas composition during allothermal and hybrid phases for the two runs is shown in Figure II.32. H_2 declined from 50.9% to 38.4% and from 49.3% to 36% for the direct and indirect heating modes respectively. Likewise, CO_2 increased substantially from 3.0% to 15.40% and from 4.4% to 19.0% in the direct and indirect heating modes.

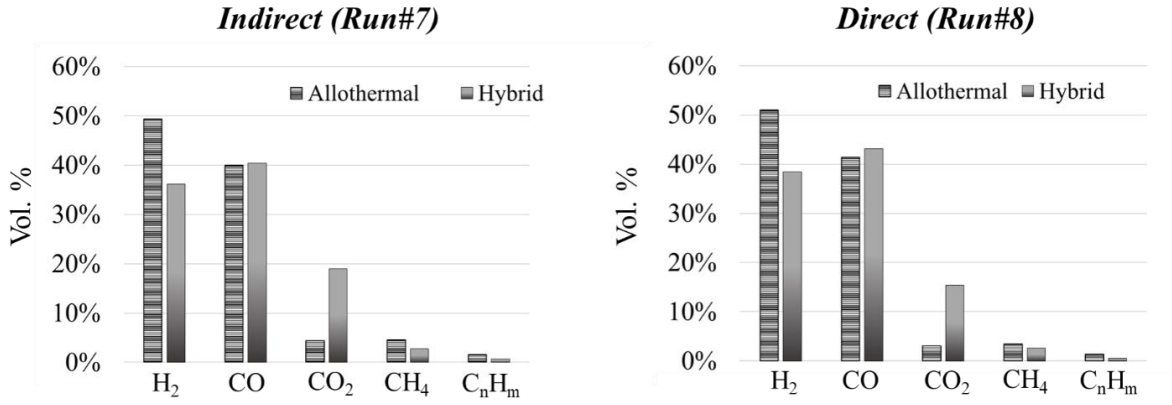

Figure II.32 Gas composition (Runs#7-8)

The overall CCE of the two experiments was 81.8% in Run#7 and 82.8% in Run#8 denoting a suitable biomass conversion during both allothermal and hybrid phases. Accordingly, the strong decline in gas production rates after O_2 injection (especially for H_2 and CO depicted in Figure II.29) from around 1.1 NL.min^{-1} (indirect, Run#7) and 1.2 NL.min^{-1} (direct, Run#8) to 0.6-0.4 NL.min^{-1} is not related to poorer wood particles conversion or higher particles entrainment, but to combustion reactions. Moreover, as the syngas thermal power (Figure II.31) declined importantly after hybridization, the overall CGE of the two experiments was lower than 100%. Besides, the shorter allothermal period in Run#7 led to a lower CGE value that barely reached 86.7% against 97.0% in Run#8.

Runs#9 (indirect)-10 (direct) represent the first attempt to control the reactor temperature under variable solar input. To do so, the same injection strategy of Runs#7-8 was adopted, i.e. allothermal gasification of 1.2 g.min^{-1} of wood by 0.2 g.min^{-1} of steam + injection of additional 0.2 g.min^{-1} of wood and 0.25 NL.min^{-1} of O_2 during the hybrid phase. In these two runs, the passage of clouds was simulated by shading part of the 2 m diameter parabola via partly closing the shutter (Figure II.33-a). Process hybridization (i.e. extra-wood supply and O_2 injection) aimed at maintaining the reactor temperature constant despite drop of solar energy input. The biomass was first steam-gasified at Q_{solar}=1.20 kW_{th} in Run#9 and at Q_{solar}=1.25 kW_{th} in Run#10. Reactor temperature during biomass/steam injection time based on T3 was respectively equal to 1327°C and 1350°C (Figure II.33 b). During the allothermal phase of the process (until time=11 min in Run#9 and time=12 min in Run#10), 1.2 g min^{-1} of wood was solar gasified by 0.2 g.min^{-1} of steam. This rapidly increased the gas production rates to reach 1.43 NL.min^{-1} in Run#9 and 1.48 NL.min^{-1} in Run#10 for H_2 (Figure II.34). The sharp decline in the solar power input to respectively 0.68 kW_{th} and 0.65 kW_{th} decreased temperature markedly by 53°C (Run#9) and 82°C (Run#10). As a result, gas production rates declined progressively due to slower gasification kinetics. The impact on hydrogen flow rate was the highest and dropped by up to 0.39 NL.min^{-1} (Run#9) and 0.48 NL.min^{-1} (Run#10). The injection of oxygen increased the reactor T3 temperature to a peak value of 1366°C in Run#9 and 1399°C in Run#10. Due to the low solar input, temperature T3 kept decreasing during the hybrid phase gradually and less markedly to reach around 1323°C in both runs at the end of the experiment. Solar power sharp decrease greatly affected T2 temperature with a total drop by 227°C in Run#9 and by 180°C in Run#10. While

oxycombustion raised T3 temperature markedly, it hardly influenced T2 measurements. A very slight temperature increase was nonetheless observed at the end of the experiments (areas surrounded by two blue circles in Figure II.33-b, right) and this probably was due to combustion reactions.

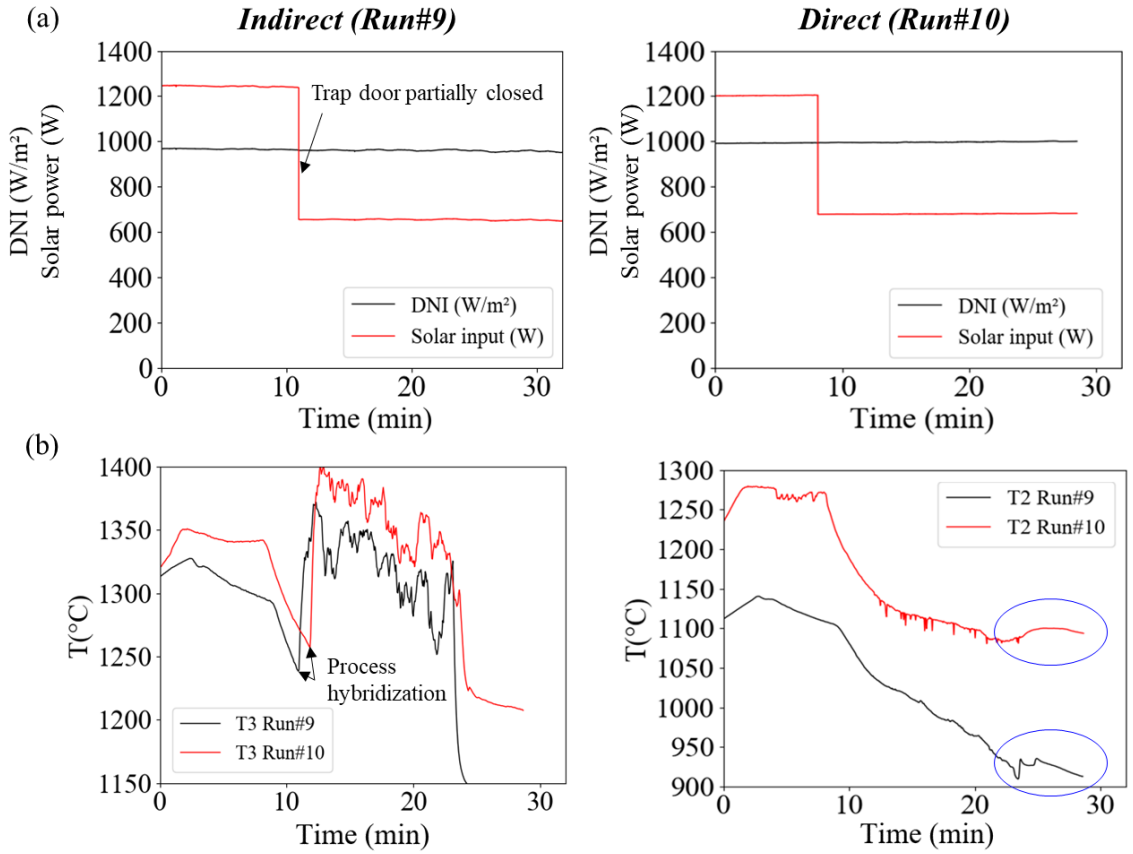

Figure II.33 (a) Solar power input simulating the passage of clouds; (b) Reactor temperature as measured by T3 and T2 in Runs#9-10

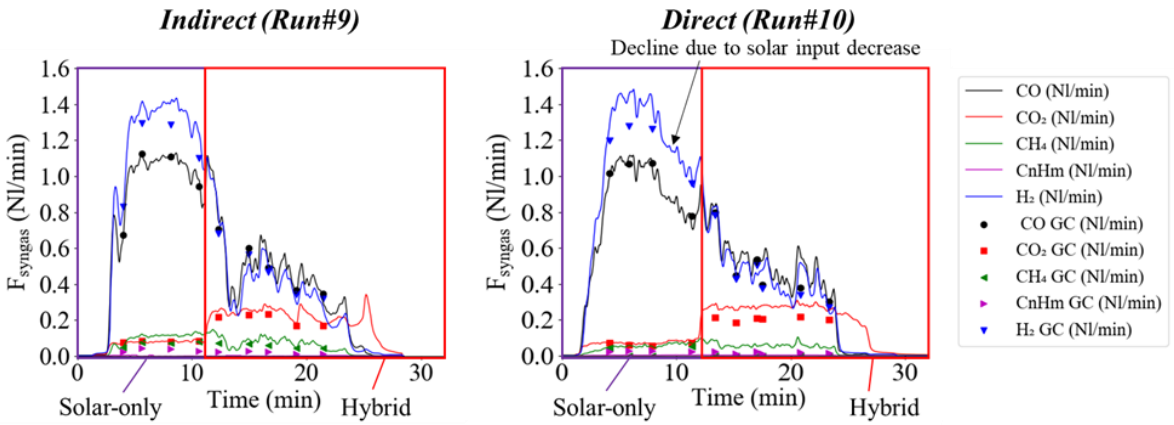

Figure II.34 Syngas production rates during Runs#9-10

A more in-depth study on the reactor dynamics would improve understanding and help determine more optimized control strategies for wood/oxygen/steam supply to insure syngas quality while meeting the continuous syngas demand.

II.4 Waste solar gasification

II.4.1 Principle and objectives

Solar and solar hybrid gasification of beech wood was successfully achieved in the solar spouted bed reactor. However, questions persist about its ability to treat more varied loads such as waste and plastic feedstocks. Although essential for scale up as it offers an attractive way for improving the economical balance, the use of Municipal Solid Waste (MSW) and industrial waste (IW) as a primary feedstock was barely discussed. Due to the complex nature of waste and its high content of ash, its efficient solar conversion in the solar spouted bed reactor needs to be carefully examined. Often, the recovery of material and energy from MSW and IW is carried out through the production of Solid Recovered Fuels (SRF). Prepared from plastic wastes, food packaging wastes including plastic, paper, aluminum, glass etc., SRF present several advantages over unprocessed waste as they are easier to handle with fairly constant physico-chemical properties and a low chlorine content (generally below 1.5%) (ADEME REPORT, 2012). Within this framework, and with the purpose of recycling waste with natural sunlight, solar and solar hybrid gasification of waste particles in the form of SRF was explored in the directly irradiated conical cavity-type solar reactor. The goal was to assess the ability of the reactor to convert the millimetric waste particles, quantify the gas products and identify the potential technical issues to be tackled for improving the reliability of the solar process.

II.4.2 Experimental study

Two experiments were performed under direct solar heating conditions. The experimental conditions are recapped in Table II.10

Table II.10 Operating conditions for SRF particles solar gasification

	Run# 1	Run# 2	
$T_{operating}$	1300°C	1300°C	
$m_{feedstock}$	20 g	20 g	
Operating mode	Allothermal	Allothermal	Hybrid
F_{SRF}	0.57 $g.min^{-1}$	0.58 $g.min^{-1}$	0.58 $g.min^{-1}$
F_{steam}	0.25 $g.min^{-1}$	0.20 $g.min^{-1}$	0.20 $g.min^{-1}$
F_{oxygen}	0 $NL.min^{-1}$	0 $NL.min^{-1}$	0.25 $Nl.min^{-1}$
Mass $(S/SRF)/(S/SRF)_{st}$	1.06	0.87	0.87

The millimetric SRF sample particles characteristics are summarized in Table II.11.

Table II.11 SRF characteristics

	C (wt.%)	H (wt.%)	O (wt.%)	N (wt.%)	S (wt.%)	Ash (wt.%)	Cl (wt.%)	Moisture (wt.%)	LHV ($MJ.kg^{-1}$)
SRF	48.6	5.7	25.8	2.9	0.9	15.0	1.1	8.9	20.6

The SRF sample, originally in the form of pellets, was crushed into particles with a diameter ranging from 0 to 5 mm (Figure II.35). The biggest particles were generally due to fragments of plastic and the smallest particles had a foam-like texture.

Figure II.35 SRF sample preparation

Due to the heterogeneity of the SRF particles, a repeatable and precise calibration of the volumetric screw feeder flow rate could not be achieved and therefore, in the following, the actual SRF feeding rate was calculated by dividing the initial feedstock mass over the experimental feeding duration. To protect the injection tube from liquid and solid residues, a layer of around 1.5 cm of 3 mm alumina particles was initially disposed at the cavity bottom inside the reactor initially.

The experiments were carried out under stable solar conditions (DNI variation less than 10%). The SRF particles were gasified with a slightly overstoichiometric steam flow rate $((S/SRF)/(S/SRF)_{st}=1.06)$. For Run#2, the particles were also partially burnt under oxygen-lean conditions. The calculated ER was 2.74. The global chemical reaction that describes the steam-only gasification of the studied SRF is presented in Eq.II.61; the oxy-combustion reaction is given in Eq.II.62:

$$C_6H_{8.4}O_{2.4}+3.6H_2O\ (v)\rightarrow 6CO+7.8H_2 \quad \Delta H°_{gasification} = 1.14\ MJ.mol^{-1} \qquad II.61$$

$$C_6H_{8.4}O_{2.4}+6.9O_2\rightarrow 6CO_2+4.2H_2O(v) \quad \Delta H°_{combustion} = -2.45\ MJ.mol^{-1} \qquad II.62$$

Figure II.36 shows the measurements of the outlet gas production rates.

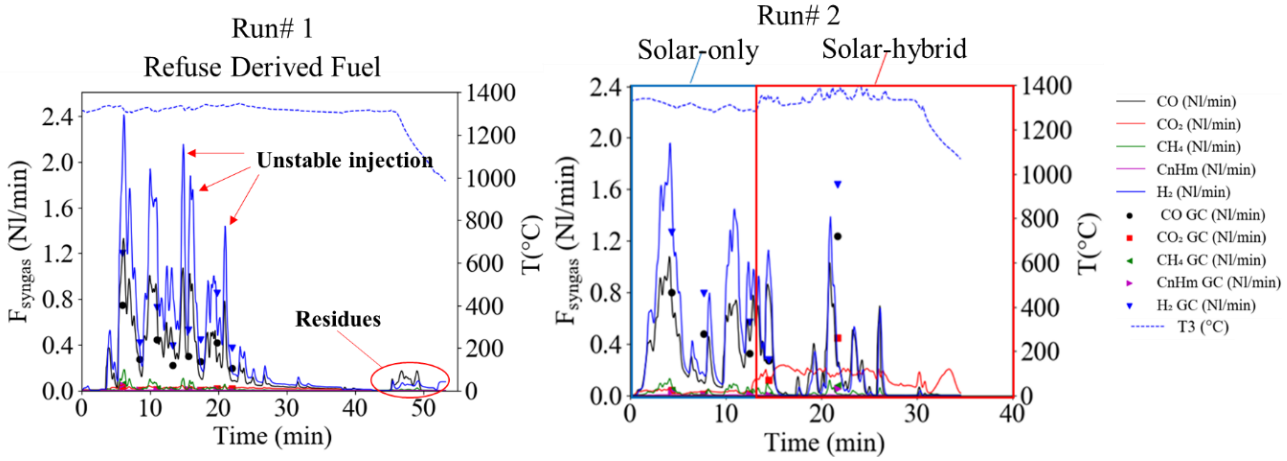

Figure II.36 Syngas flow rates and reactor temperature (T3 inside the cavity) for Runs#1-2

Noticeable fluctuations in the gas flow rates reflected by variable peaks and valleys all along the experiments were observed. They were due to the unstable injection of the particles caused by the heterogeneity of the sample and the possible melting of plastics and inorganics at the screw feeder and at the injection tube that affect the particles flowability. Moreover, it can be observed that the produced gas was composed predominantly of H_2 and CO. CO_2, whereas CH_4 and C_nH_m were produced in a lower amount. The C_nH_m were composed mainly of C_2H_2 and C_2H_4. Figure II.37 shows the GC measurements of the C_nH_m. The syngas composition during Run#1 was calculated by time integration of syngas production rates: H_2 (56.8%), CO (32.1%), CO_2 (7.3%), CH_4 (2.3%), C_nH_m (1.5%). The achieved CCE was 88.1%, which is the range of the reported CCE values (generally between 80-92%) for waste gasification in fluidized beds operating up to 800°C (Kwon et al., 2010). The CGE was 104.5%, which is much higher than reported CGE values for SRF gasification in fluidized bed gasifiers that vary between 70% and 85% at best (Khosasaeng and Suntivarakorn, 2017; Materazzi et al., 2016; Valin et al., 2019) thanks to solar energy chemical storage.

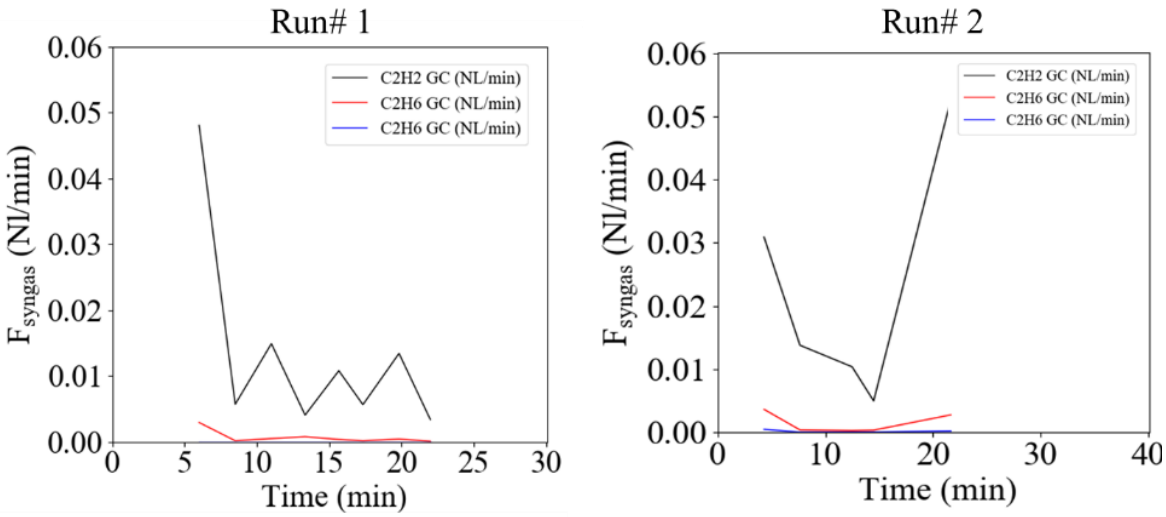

Figure II.37 GC analysis of CnHm during Runs#1-2

To study the flexibility of the solar process and its ability to deal with solar energy variations, a small amount of O_2 to burn around 33% of the feedstock was added to the system in Run#2 at time t=13 min. O_2 injection was expected to elevate and stabilize the reactor temperature at a higher set point value. The reactor temperatures during Runs#1-2 are presented in Figure II.38. While temperature was quit stable in Run#1, the hybrid operation showed a fluctuating temperature pattern in Run#2. The fluctuations were increased significantly during the hybrid phase and were due to the rapid combustion of the particles. In fact, the consumption of the particles was faster than the injection process leading to sharp temperature increases and decreases by about 80°C. During the hybrid phase of Run#2, T3 temperature increased only slightly and unsteadily, as a consequence, the desired effect of increasing and stabilizing the reactor temperature at a higher set point value through partial feedstock oxycombustion was not overly effective due to the injection issues. In return, the impact on the gas composition was considerable and affected essentially the H_2 and CO_2 gas content.

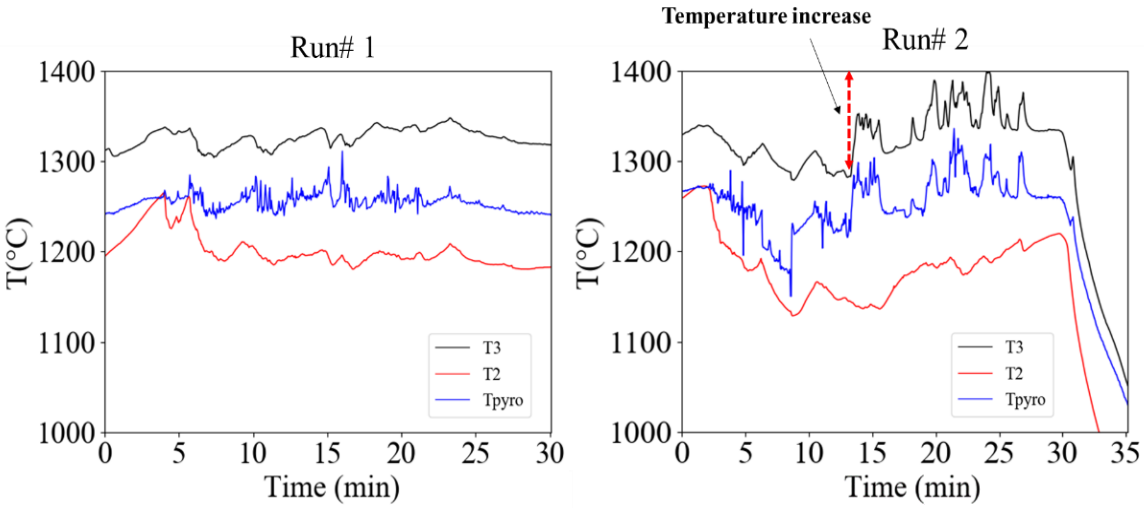

Figure II.38 Temperature measurements during Runs#1-2: T3, T2 and Tpyro

Figure II.39-a shows the gas volume fractions before and after hybridization. The H_2 volume fraction decreased by 24% (58.9%-40.0%) and CO_2 increased by more than 5 times (3.5%-24.0%), CO concentration was only slightly affected with a decrease of 6% (33.8%- 31.8%). The CCE and the CGE of Run#2 integrated over the whole experiment duration declined as compared to Run#1 and were respectively 78.5% and 78.0%. This was possibly due to higher entrainment of smallest reacting particles (including char and finest unreacted SRF particles) due to residence time decrease after the injection of O_2 and the decline of syngas calorific value as less SRF was steam-gasified.

Finally, to assess the repeatability of the measurements, the syngas composition of the Run#1 and Run#2-allothermal were compared in Figure II.39-b. It can be observed that globally the composition did not much vary expect for the CO_2 that was somewhat larger and CH_4 that was slightly lower during Run#1 (CO_2: 7%-4%; CH_4: 2%-3%).

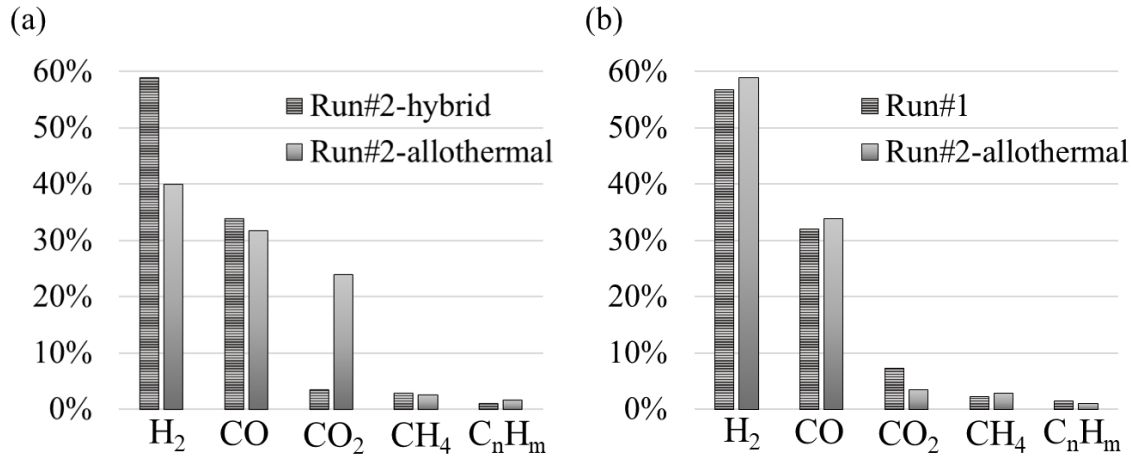

Figure II.39 (a) Syngas composition during Run#2 (Allothermal vs. Hybrid phase; (b) Syngas composition (Run#1 vs Allothermal part of Run#2)

In review, first solar-only and solar hybrid experiments on SRF particles were performed. The results were promising and showed both high syngas quality and suitable performance.

Nonetheless, the continuous process suffered significantly from the instability of injection that particularly affected the hybrid process. The use of more complex systems for the continuous injection of SRF powders is often required and achieved thanks to vibratory/fluidization systems or pneumatic conveyors. An innovative solution proposed by Perret and Chataing (Perret and Chataing, 2019) for SRF injection in entrained flow reactors consists in transporting the particles first in the form of pellets at low temperature to an in-situ grinder that crushes the particles just before the injection. This avoids blockage in the hopper/screw feeder without the need of more complex technologies.

Another encountered issue concerned ash agglomeration at the bottom of the conical cavity (Figure II.40).

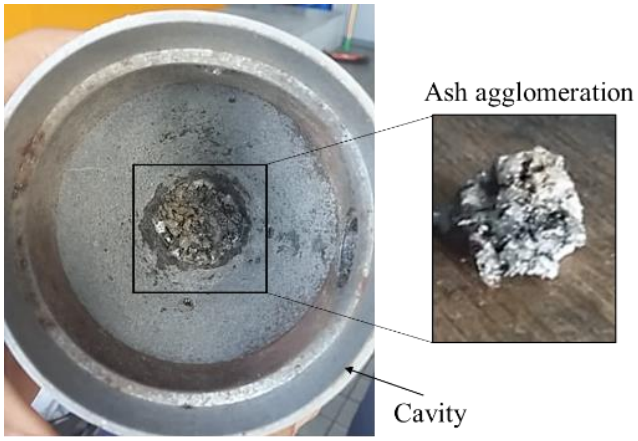

Figure II.40 Top view photography of the solar cavity after Run#2

The melting ashes agglomerated around the packed Al_2O_3 bed just above the gas injection tube, this should be correctly managed to avoid obstructing or blocking the gas passage.[7] A patent application has been filed in this sense. It proposed a new spouted bed variant that allows continuous ash evacuation during solar operation. The 3D model was used to perform preliminary flow simulations for concept validation. The new reactor variant is described in ANNEX 1.

II.5 Conclusions

In this chapter, a novel spouted bed solar reactor for beech wood and waste gasification was studied using high temperature experimentation and numerical modelling. It was organized in three parts. In the first one, a comprehensive 3D steady state CFD model accounting for the reactor hydrodynamic, thermal and chemical aspects was developed. The CFD model is the first attempt to compare the direct and indirect heating modes on the grounds of 3D multiphysics numerical simulations and experimental validation. It showed a maximum discrepancy of 10% for the outlet syngas composition in comparison with experimental results and the carbon conversion efficiency was slightly overestimated for the direct heating

[7] This issue was not encountered with the wood sample during the experiments thanks to its very low ash fraction <wt. 0.5%.

mode. The detailed analysis of the 3D gas-particle flow provided new insights into the solar operation of the novel jet spouted bed reactor. The model confirmed that the desired vigorous cyclic movement of the particles was well established and that such reactor configuration (especially direct heating) provides optimal particles exposure to solar radiations while enabling solid residence time increase. Moreover, it stressed that directly heating the reactor improves heat and mass transfer rates and results in higher reaction zone temperature, which promotes the formation of hydrogen and carbon monoxide. A more extensive experimental and CFD study on various operating conditions remains to be done, in particular, to study the impact of temperature, carrier gas and oxidant flow rates on the conversion. Since hydrodynamics in the two configurations (direct and indirect) is somewhat different due to the emitter plate, the observed trends may vary. Paths for improving the model were also highlighted, even if they should be accompanied by greater computing capabilities to speed up the calculations. Finally, simulations allowed determining possible reactor improvement strategies to alleviate the entrainment of the smallest particles and enhance phase mixing and heat and mass transfer rates.

In the second part, hybrid solar/autothermal gasification was simulated and experimentally tested for the first time. Oxy-combustion coupled to solar heating appeared to be a suitable option in order to control the reactor temperature. 3D CFD steady state simulations of the reactive gas-particle flow allowed providing better understanding about the hybrid reactor operation with emphasis on the effects of O_2 injection on the 3D temperature field, species distribution and the prediction of the output syngas composition. Following these results, transient 2D CFD thermal simulations were carried out to determine the temperature evolution and the dynamic response of the reactor during the transition from solar-only to hybrid solar combustion operation, a simple on/off control strategy for biomass and oxygen supply allowed to elevate and maintain constant the final cavity temperature. Experimental tests under real concentrated solar flux were thereafter conducted in direct and indirect heating modes at different initial temperatures ranging from 1200°C to 1350°C. The goal was to assess the ability of hybridization to elevate the process temperature and to analyze the impact of oxygen injection on the reactor throughput. The switch from allothermal to hybrid (solar/ combustion) mode resulted in sharp temperature rise but lowered significantly the syngas yields (especially H_2) while CO_2 increased noticeably, in agreement with CFD predictions. Accordingly, O_2 injection should be used only when the available solar irradiation is insufficient to optimally convert the biomass feedstock. Furthermore, the observed decline of syngas quality due to hybridization can be an issue and needs to be mitigated to optimize process reliability and performance. This study represents the first successful attempt to control a hybrid continuous thermochemical reactor under real low and variable solar irradiation conditions, which paves the way for continuous solar gasification processes.

In the third and last part, first SRF solar and solar hybrid gasification experiments were performed under direct solar flux at 1300°C. The results were promising and showed both high syngas quality and good performance. These experiments allowed identifying technical issues to be addressed regarding SRF transport and injection that was highly unstable. The

melting of ashes at the bottom of the cone was another issue encountered with the SRF particles, which for longer experiments can compromise the continuity of the process. In practice, the management of ash-related problems is essential in the design of thermochemical reactors for reliable operation. Indeed, it presents major risks that encompass multiple aspects such as slag formation, bed agglomeration (when bed materials are used, e.g. in fluidized beds) and corrosion of heat transfer surfaces. From these first observations, experimental results and with the help of the 3D CFD model, a new reactor geometry was proposed to continuously evacuate the melting ashes during operation. Although a thorough experimental study on the new reactor variant remains to be done, the proposed concept presents a first step for the reactor to treat more varied loads such as waste and low-grade fuels. Future work will focus on the improvement of the reactor design thanks to numerical simulations and high temperature experimentations. The co-gasification of wood biomass and SRF will also be studied as an efficient strategy to limit the formation of ash while providing potential synergistic benefits for enhancing gasification performance.

III. CHAPTER 3

Experimental and numerical investigation of inert bed materials effects in a high-temperature conical cavity-type reactor for continuous solar-driven steam gasification of biomass

III.1 Introduction

This study was undertaken following the results of Chapter 2 in which a novel kW scale dilute solar spouted bed reactor was simulated for the first time. In the preceding work, the reactor was initially empty and the continuously injected biomass particles were the only spouted particles inside the cavity. The results showed that the dilute spouted bed was suitable to continuously convert the biomass feedstock with a high carbon conversion efficiency approaching ~80%, and the efficient storage of solar energy in the form of a readily transportable fuel was confirmed. With the support of the developed 3D multiphysics model, improvement strategies were proposed to enhance the phase mixing, to limit the finest char particles entrainment and to homogenize the reactor temperature. In fact, most of the incoming solar radiations were absorbed directly by the reactor cavity walls while the gases and biomass particles absorbed a smaller portion of the solar power input. Moreover, the low gas velocities in the annular zone of the cone implied a low convective heat transfer coefficient at the near wall region. In order to address these issues and with the aim of homogenizing the reactor temperature, the use of inert particles (set at the bottom of the conical cavity in the form of spouted or packed-beds) appeared to be judicious to achieve higher reaction extents and heat transfer rates. Therefore, in this work, different inert bed materials were tested for the first time to study their impact on the allothermal (solar-only) continuous gasification of wood particles. Prior to the experimental study, the gas/particles flow dynamics at real processing conditions was investigated using Computational Fluid Dynamics (CFD) modelling. Two thermal CFD models were developed with Fluent© to simulate the flow through the inert packed and spouted bed particles in interaction with radiation and gas. These simulations were completed by cold tests on a replicated transparent PMMA (PolyMethyl Methacrylate) cavity mockup to validate the CFD predictions (at ambient temperature) and confirm the effective mixing of the wood and bed particles. Thereafter, high temperature solar experiments were carried out at the CNRS-PROMES solar furnace under real direct concentrated solar flux. Results in terms of syngas yield, composition, biomass conversion and reactor performance metrics were discussed in light of the numerical simulations. The experimental test bench including the reactor, the solar facility and the metrology is described in Chapter 2.

The results presented in this section were published in *Chemical Engineering Science* (Boujjat et al., 2020a)

III.2 Bed materials

In chapter 2, simulations using 3D CFD multiphysics modelling of the reactor (without bed materials) predicted a cavity wall temperature hundred degrees higher than the inner reaction zone temperature. Moreover, the lightest particles were rapidly entrained towards the outlet by the high velocity jet, which penalized the biomass conversion and syngas yields. Notable gradients in both steam concentration and gas temperature between the central spout region and the annular zone were also pointed out by the model, leading to strong variations in the particles conversion rate. With the aim of achieving higher reactor performance and better use of solar energy, inert bed materials set in the form of spouted or packed beds were considered. The

spouted flow regime is expected to increase the reaction zone temperature and to enhance the gas/wood particles phase mixing. The packed-bed configuration is used to broaden the gas stream at the cavity bottom, which should reduce the central gas jet velocity (thus increase the gas residence time) and limit the entrainment of the reacting particles, when compared with an empty cavity configuration. Figure III.1 provides an illustration of the three studied hydrodynamic configurations: dilute spouted bed (chapter 2), spouted and packed beds.

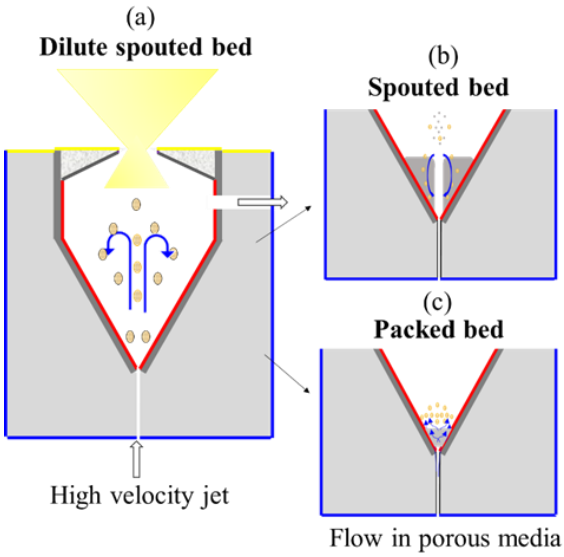

Figure III.1 Illustration of particles effects on the gasification process: (a) Dilute spouted bed, (b) Spouted bed (with inert powders), (c) Packed bed (inert particle bed at the bottom)

Figure III.2 Studied inert bed and wood biomass particles

The bed particles used for this study were alumina particles (3 mm and 125 µm mean diameter), 300 µm SiC and olivine particles, and 200 µm sand particles (Figure III.2). The olivine main compounds include MgO, SiO_2, CaO (0.4% max) and Fe_2O_3. The mass fractions of Mg, Si and Fe were respectively 28.5%, 17.5% and 7%. Both SiC and olivine particles were thermally treated at 1000°C in presence of air to ensure inertness regarding the biomass thermochemical reactions of pyrolysis and gasification.

The particles characteristics are summarized in Table III.1

Table III.1 Inert particles characteristics at 1400°C

	Alumina (Al_2O_3)	Silicon carbide (SiC)	Olivine	Silica sand (SiO_2)
ρ_s ($kg.m^{-3}$)	3950	3210	3270	1442
λ_s ($W.m^{-1}.°C^{-1}$)	7	15	0.6	2.2
$c_{p,s}$ ($J.kg^{-1}.°C^{-1}$)	795	1320	1220	1225
d_s (mm)	3.00 or 0.125	0.30	0.30	0.20

III.3 Modelling

III.3.1 Geometry, mesh and boundary conditions

Prior to the high temperature experiments, multiphysics simulations of the three configurations (empty cavity, inert packed-bed and spouted-bed particles) were performed to analyze the gas/solid flow behavior under real processing conditions using the same bottom and upper (at the window) gas flow rates as in experiments with a solar power input of 0.9 kW. The reactor geometry was created based on the reactor design (composed of different zones: alumina cap, insulation, cavity walls, and fluid/gas injection, reaction and exit zones). Figure III.3 shows the global 2D geometry and Boundary Conditions (BCs). A flow rate of 2 $NL.min^{-1}$ is set for the upper Ar window inlet and of 0.2 $NL.min^{-1}$ of Ar + 0.2 $g.min^{-1}$ of steam for the bottom spouting gas inlet. All the gases were injected at an initial temperature of 25°C. The outlet pressure was equal to the atmospheric pressure (around 860 hPa). To simulate the gasification reactions, a volumetric heat sink ($S_{rxn}=F_{biomass}.\Delta H_{rxn}/V_{fluid}$) was applied to the fluid region. The enthalpy of the steam gasification reaction for the considered biomass was ΔH_{rxn} = 0.84 $MJ.mol^{-1}$. A no-slip boundary condition at the reactor walls was used for the gas phase. The packed bed was simulated using the porous zone technique to model both the fluid flow and heat transfer through the packed bed considered as a porous medium (characterized by a fixed porosity). The top surface of the bed can potentially interact with discrete phase particles (such as char particles) via rebound/reflect BC. The spouted particles were modelled by the Eulerian approach. The interaction of the particles with the cavity walls was modelled by the Johnson and Jackson (Johnson and Jackson, 1987) wall boundary condition. This wall boundary condition involved two important parameters: the specularity coefficient, Φ, that specified the shear condition at the walls, and the particle–wall restitution coefficient, e_w, that described the dissipation of the solids kinetic energy with the wall by collisions. In this work, Φ and e_w were assumed both equal to 0.9.

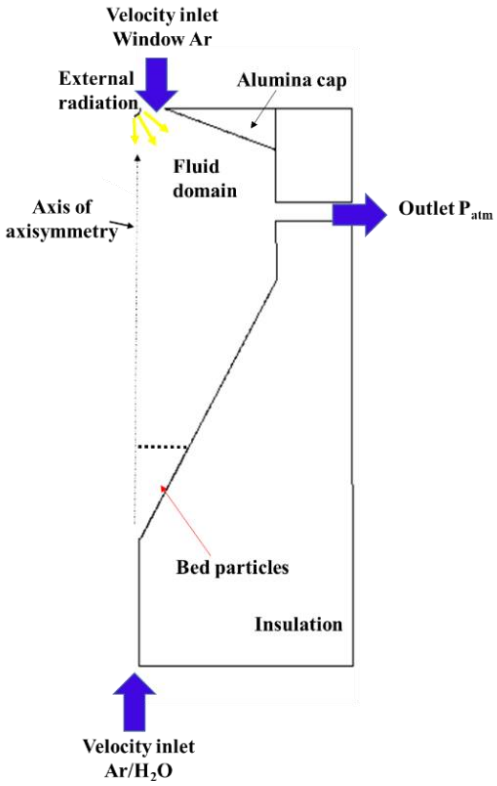

Figure III.3 2D Axisymmetric geometry of the reactor

A grid of 10521 quadrilateral and triangular elements was generated. The average mesh skewness was 8.2×10^{-2} with a standard deviation of 9.2×10^{-2}. The average orthogonal quality was 0.95 with a standard deviation of 6.7×10^{-2}. Grid resolution was very important to increase model accuracy. A preliminary sensitivity study of simulation outputs to the reactor mesh allowed choosing the optimal cell size inside the cavity (gas phase/reaction zone) to accurately solve the gradients in the spout (central) region of the reactor where sharp changes in terms of velocity, temperature and species molar fraction occur (cf. section II.2.4). A mesh size of around 0.8-0.9 mm offered a good compromise between numerical precision and computational time. Therefore, the grid size in the inlet tube was set to 0.15 mm and it was increased (with a growth ratio of 1.2) to 0.8 mm inside the conical cavity. For fluidized bed gasifiers, a cell size of about 12 times the average particle size was able to effectively capture the gas-particles flow hydrodynamics (Gelderbloom et al., 2003; Ismail et al., 2018; Wang, 2008). In this study, the spouted bed particles size was in the range of 125 µm to 300 µm; therefore, the generated mesh met also this criterion.

Two thermal CFD models were developed. The first one simulated the fluid flow through the porous packed bed. In this model, the packed bed particles were modelled through a momentum sink, which depends on the permeability (ζ) and the porosity of the medium (δ). A blending between the energy of fluid and solid particles was considered for the governing transport equation determining the temperature in the packed bed region. The model allowed also to track discrete char particles in space by solving in a Lagrangian reference frame the discrete particles momentum and energy equations. The second model used the Eulerian-Eulerian (granular) approach to simulate the directly-irradiated spouted bed particles. The flow was therefore

described by conservation equations written for each phase separately (gas and granular). Momentum, energy and radiative intensity transport equations used in the modelling of the packed and the spouted powders are provided in detail in Table III.2 and Table III.3. They can be found in the Fluent© theory guide, although a work of organization/grouping of equations, selection and coupling between physical models has been carefully carried out. Furthermore, some terms in the equations are not provided explicitly in the theory guide; they were thus completed, clarified and validated by taking contact with the ANSYS support team. The 2D approach was preferred in this part of the work because it involves the modelling of the powders by a transient Eulerian Granular approach, which requires significant computational resources. 2D modelling simplifies the calculation substantially and allows obtaining information on the flow dynamics in a faster but valuable way. Similarly, chemistry has been integrated by a source term applied homogeneously over the entire cavity domain. This further simplifies the calculations and reduces the computational time.

III.3.2 Mathematical formulation

Simulations were performed with and without the injection of discrete phase char particles for the empty and packed-bed configurations. The injection of char particles gives insights into the effect of the inert packed bed on the reacting particles flow patterns. Table III.2 lists the model equations where subscripts 'g' and 's' stand for gas and solid (packed particles).

Table III.2 Governing equations (empty and packed-bed configurations)

Continuity equation	$\frac{\partial \rho_g}{\partial t} + \nabla.\left(\rho_g v_g\right)=0$	*III.1*
Navier-Stokes equation	$\frac{\partial \rho_g v_g}{\partial t} + \nabla.\left(\rho v_g\left(v_g\right)\right) = -\nabla p + \nabla.\left(\overline{\overline{\tau_g}}\right) + \rho_g g + S_{packed\_bed}$	*III.2*
	With $\overline{\overline{\tau}}_g = \mu_g[(\nabla. v_g + \nabla {v_g}^T)] - \frac{2}{3}\nabla v_g.\overline{\overline{I}}$	*III.3*
Energy equation	$\frac{\partial(\delta\rho_g E_g + (1-\delta)\rho_s E_s)}{\partial t} + \nabla.\left(v\left(\rho_g E_g + p\right)\right) = \nabla.\left((\delta.\lambda_g - (1-\delta).\lambda_s).\nabla T - \sum h_{g,j} j_{g,j}\right) + S_{rad,g} + S_{rxn}$	*III.4*
Gas species transport	$\frac{\partial \rho_g Y_i}{\partial t} + \nabla.\left(\rho_g v_g Y_i\right) = \nabla.\left(\rho_g D_{i,m} \nabla Y_i\right)$	*III.5*
Radiation equation	$\nabla.(I.l) + (a_g + a_{char}).I(s,l) = \frac{a_g.\sigma_{rad}T^4}{\pi} + E_{char} + \frac{\sigma_{char}}{4.\pi}.\int_0^{4.\pi} I(s,l).\Phi_{isotropic}(l,l')d\Omega$	*III.6*
DPM char particles	$\frac{dv_{char}}{dt} = F_D\left(v_g - v_{char}\right) + \frac{g.(\rho_{char}-\rho_g)}{\rho_{char}}$	*III.7*
	$m_{char}c_{p,char}\frac{dT_{char}}{dt} = h.A_{char}\left(T_{g,\infty} - T_{char}\right) + \sigma_{rad}A_{char}\varepsilon_{char}\left({\theta_R}^4 - {T_{char}}^4\right)$	*III.8*

Where S_{packed_bed} (in Eq.III.2) is the momentum sink due to the pressure loss across the randomly packed-bed particles. This pressure loss is generally expressed by Eq.III.9:

$$S_{packed\_bed,i} = -\frac{\mu}{\zeta}.v_i - \frac{1}{2}.C_i\rho\,|v_i|.v_i \qquad III.9$$

Where ζ is the permeability of the packed bed and C_i the coefficient of inertial resistance, the latter parameter can be neglected in case of low Re numbers. Hence, only the first term of this

equation was considered (Re<100)[8] and the permeability of the medium was estimated according to the Kozeny-Carman equation with $\zeta \sim \{ {180.(1-\delta)^2}/{d^2{}_s.\delta^3} \}$, δ the fluid porosity assumed equal to 0.37 (δ=1 for the empty configuration), d_s is the average particles diameter (considered here equal to 3 mm). E_g and E_s are the gas and the packed particles total energy. λ_g and λ_s are the thermal conductivities of the gas and of the packed particles (Al_2O_3).

For the spouted bed configuration, the equations in Table III.3 were solved. Both the gas and the solid phases were considered. The Eulerian-Eulerian treatment was used for modelling the solid/gas system thanks to conservation laws written for both solid and gas phases at each cell of the CFD domain. Each cell was characterized by a phasic volume fraction α representing the space occupied by the corresponding phase. This model did not allow a direct calculation of the properties of each solid particle in the domain, but rather provided information on the effective property (such as temperature, velocity, etc.) of the solids at a cell as calculated by the conservation equations. Each cell contained a given number of particles that defined the solid volume fraction.

Table III.3 Governing equations (spouted particles configuration)

Continuity equation	Fluid phase $\frac{\partial \alpha_g \rho_g}{\partial t} + \nabla.\left(\alpha_g \rho_g v_g\right) = 0$	*III.10*
	Solid phase $\frac{\partial \alpha_s \rho_s}{\partial t} + \nabla.\left(\alpha_s \rho_s v_s\right) = 0$	*III.11*
	$\alpha_s + \alpha_g = 1$	*III.12*
Momentum equations	Fluid phase $\frac{\partial \alpha_g \rho_g \vec{v}_g}{\partial t} + \nabla.\left(\alpha_g \rho_g \vec{v}_g.\vec{v}_g\right) = -\alpha_g.\nabla p + \nabla.\bar{\bar{\tau}}_g + \alpha_g \rho_g \vec{g} + \beta(\vec{v}_s - \vec{v}_g)$	*III.13*
	Solid phase $\frac{\partial \alpha_s \rho_s \vec{v}_s}{\partial t} + \nabla.\left(\alpha_s \rho_s \vec{v}_s.\vec{v}_s\right) = -\alpha_s.\nabla p - \nabla p_s + \nabla.\bar{\bar{\tau}}_s + \alpha_s \rho_s \vec{g} + \beta(\vec{v}_g - \vec{v}_s)$	*III.14*
Granular temperature equation	$\frac{3}{2}\left[\frac{\partial \alpha_s \rho_s \theta_s}{\partial t} + \nabla.\left(\alpha_s \rho_s \vec{v}_s.\theta_s\right)\right] = \left(-p_s \bar{\bar{I}}. + \bar{\bar{\tau}}_s\right):\nabla \vec{v}_s + \nabla.\left(k_{\theta_s}.\nabla \theta_s\right) - \gamma_{\theta_s} + \varphi_{gs}$	*III.15*
Gas species transport	$\frac{\partial \alpha_g \rho_g Y_{i,g}}{\partial t} + \nabla.\left(\alpha_g \rho_g \vec{v}_g.Y_{i,g}\right) = \nabla.(\nabla \alpha_g \rho_g Y_{i,g})$	*III.16*
Energy equation	Fluid phase $\frac{\partial \alpha_g \rho_g E_g}{\partial t} + \nabla.\left(\alpha_g \rho_g \vec{v}_g.E_g\right) = \nabla.(\lambda_g.\nabla T_s) + Q_{g,s} + S_{rad,g} + S_{rxn}$	*III.17*
	Solid phase $\frac{\partial \alpha_s \rho_s E_s}{\partial t} + \nabla.\left(\alpha_g \rho_g \vec{v}_g.E_s\right) = \nabla.(\lambda_s.\nabla T_s) + Q_{g,s} + S_{rad,s}$	*III.18*
Radiative equation	$\nabla.(I.s) + (a_g + a_s + \sigma_s).I(s,\mathrm{l}) = \{(1-\alpha_s).a_g + \alpha_s.a_s\}.\frac{\sigma_{rad}\{(1-\alpha_s).T_g + \alpha_s.T_s\}^4}{\pi} + \frac{\sigma_s}{4.\pi}.\int_0^{4.\pi} I(s,l).\Phi_{isotropic}(l,l')d\Omega'$	*III.19*

[8] cf. ANNEX 1 for Re number estimation

Constitutive Equations		
Solid pressure	$p_s = 2.\rho_s.(1+e_{ss}).{\alpha_s}^2.g_{0,ss}.\theta_s$	*III.20*
Solid stress tensor	$\bar{\bar{\tau}}_s = \alpha_s.\mu_s.[(\nabla.\vec{v}_s + \nabla {v_s}^T)] + (\alpha_s.\lambda_s - \frac{2}{3}\alpha_s.\mu_s)\nabla.\vec{v}_s\bar{\bar{I}}$	*III.21*
Solid shear viscosity	$\mu_s = \mu_{s,kin} + \mu_{s,col}$	*III.22*
Kinetic viscosity	(Gidaspow et al.,1991) $\mu_{s,col} = \frac{4}{5}.\alpha_s.\rho_s.d_s.g_{0,ss}(1+e_{ss})(\frac{\theta_s}{\pi})^{1/2}$	*III.23*
Collisional viscosity	(Syamlal et al., 1993) $\mu_{s,kin} = \frac{\alpha_s.d_s.\rho_s.\sqrt{\pi\theta_s}}{6.(3-e_{ss})}[1+\frac{2}{5}.\alpha_s.g_{0,ss}(1+e_{ss})(3e_{ss}-1)]$	*III.24*
Bulk viscosity	$\lambda_s = \frac{4}{3}.\alpha_s.\rho_s.g_{0,ss}.(1+e_{ss}).(\frac{\theta_s}{\pi})^{1/2}$	*III.25*
Radial distribution	$g_{0,ss} = [1-\left({\alpha_s}/{\alpha_{s,max}}\right)^{1/3}]^{-1}$	*III.26*
Momentum exchange coefficient	(Huilin and Gidaspow, 2003) $\beta = \Psi.\beta_{Ergun} + (1-\Psi).\beta_{Wen\&Yu}$	*III.27*
	$\Psi = \frac{1}{2} + \frac{\arctan(262.5(\alpha_s-0.2))}{\pi}$	*III.28*
	$\beta_{Ergun} = 150\frac{\mu_g.{\alpha^2}_s}{{d^2}_s.\alpha_g} + 1.75\frac{\alpha_s.\rho_g}{d_s}\lvert\vec{v}_s - \vec{v}_g\rvert$ *for* $\alpha_g \le 0.8$	*III.29*
	$\beta_{Wen\&Yu} = \frac{3}{4}\frac{C_D.\alpha_s.\alpha_g.\rho_g}{d_s}\lvert\vec{v}_s - \vec{v}_g\rvert{\alpha_g}^{-2.65}$ *for* $\alpha_g > 0.8$	*III.30*
	$C_D\begin{cases}\frac{24}{\alpha_g.Re_s}[1+0.15.(\alpha_g.Re_s)^{0.687} & Re_s < 1000\\ 0.44 & Re_s \ge 1000\end{cases}$	*III.31*
Granular temperature conductivity	(Syamlal et al., 1993) $k_{\theta_s} = \frac{15\alpha_s.d_s.\rho_s.\sqrt{\pi\theta_s}}{4.(41-33\eta)}[1+\frac{12}{5}.\eta^2.(4\eta-3).\alpha_s.g_{0,ss} + \frac{16}{15\pi}(41-33\eta).\eta.\alpha_s.g_{0,ss}]$	*III.32*
	and $\eta = \frac{1}{2}.(1+e_{ss})$	*III.33*
Energy collision dissipation	(Gidaspow et al., 1991) $\varphi_{gs} = -3\beta\theta_s$	*III.34*
Interphase heat transfer	$Q_{s,g=}h_{s,g}(T_s - T_g)$	*III.35*
	With $h_{s,g} = \frac{6.\lambda_s\alpha_s.\alpha_g.Nu_s}{d_p^2}$	*III.36*
	(Gunn, 1978) $Nu_s = (7-10.\alpha_s+5{\alpha_s}^2).\left(1+0.7{Re_s}^{0.2}.{Pr}^{1/3}\right) + \left(1.33-2.4.\alpha_s+1.2\alpha_s^2\right).{Re_s}^{0.7}.{Pr}^{1/3}$	*III.37*
Radiation source terms	Fluid phase: $S_{rad,g} = a_g.(\int_0^{4\pi} I.d\Omega - 4.\sigma_{rad}{T_g}^4)$	*III.38*
	Gas phase: $S_{rad,s} = a_s.(\int_0^{4\pi} I.d\Omega - 4.\sigma_{rad}{T_s}^4)$	*III.39*

The gas local absorptivity a_g in the radiative heat transfer equation (RTE) was calculated as a function of the mass fraction of water vapor and carbon dioxide using the Fluent© WSGGM-Domain based model as these two gases are the most absorbing/emitting gases in the mixture and are considered to represent the overall radiation/gas phase interaction. The spouted particles radiation absorption and scattering coefficients (a_s and σ_s) were calculated by Eqs.III.40-III.41 with $Q_{ab,\lambda}$, $Q_{sc,\lambda}$ the efficiencies of absorption and scattering. As $d_s/\lambda >> 1$, the geometric regime was applied and $Q_{ab,\lambda} = Q_{sc,\lambda} \sim 1$ (Bohren and Huffman, 2007). These equations were coupled to the Fluent© solver via external User Defined Functions (UDFs).

$$a_s = {}^{3}/_{2} \cdot \alpha_s \cdot {Q_{ab,\lambda}}/{d_s} \qquad \textit{III.40}$$

$$\sigma_s = {}^{3}/_{2} \cdot \alpha_s \cdot {Q_{sc,\lambda}}/{d_s} \qquad \textit{III.41}$$

In regions of high particles concentration, the diffusion becomes dependent on the distance between the particles. A method exists to introduce in the RTE corrected absorption and scattering efficiencies and phase function (Auger et al., 2000). This allows taking into account the effects of the near-field dependent scattering, which increases the accuracy of the predictions at the expense of the computational cost. In this study and for the sake of simplification, these aspects were not considered.

The variations in the fluid physical properties according to temperature were taken into account. The gas density was modeled by the ideal gas law and the kinetic theory was used to calculate intrinsic viscosities, thermal conductivities and mass diffusivities of each gas.

III.3.3 Numerical procedure

The commercial package Fluent© v19.1 was used. The Finite-Volume Method (FVM) was adopted and integral balance equations were formulated for each control volume. The transient conservation equations for both granular and gas phases were solved with a time step of 10^{-4} s for Eulerian-Eulerian approach. A time step of 10 s was used for solving the energy equation for the solid components of the reactor (alumina cap, insulation, cavity walls). The reactor was first heated to a stationary temperature, then, the granular materials were patched into the fluid domain with an initial temperature of 1000°C to speed up the convergence. The phase coupled SIMPLE algorithm, which is an extension of the SIMPLE algorithm for multiphase flow, was used for the pressure–velocity coupling and correction. The momentum, volume fraction and energy equations were discretized by a first-order upwind scheme. A convergence criterion of 10^{-4} for each scaled residual component was specified for the relative error between two successive iterations for the continuity and the momentum equations. For the energy and radiation, a convergence criterion of 10^{-6} was used. The granular and gas phase average temperatures were also monitored for confirming the complete convergence. They should reach periodic and statistically constant values. Concerning the empty and the fixed bed configurations, the governing equations were solved in steady state with the coupled solver. Due to the low Re number (<100) inside the cavity, a laminar solver was selected for all the cases for solving the conservation equations.

III.4 Results and discussion

III.4.1 Numerical study

Figure III.4 shows the temperature field inside the solar reactor for a solar power input of 0.9 kW_{th}. It was observed that for the two configurations, the cavity walls reached an average temperature of around 1230°C while the gas phase average temperature was around 930°C. The empty cavity was characterized by a central gas jet reaching a temperature of around 700°C at the center of the conical part of the cavity, which was relatively colder than the annular region.

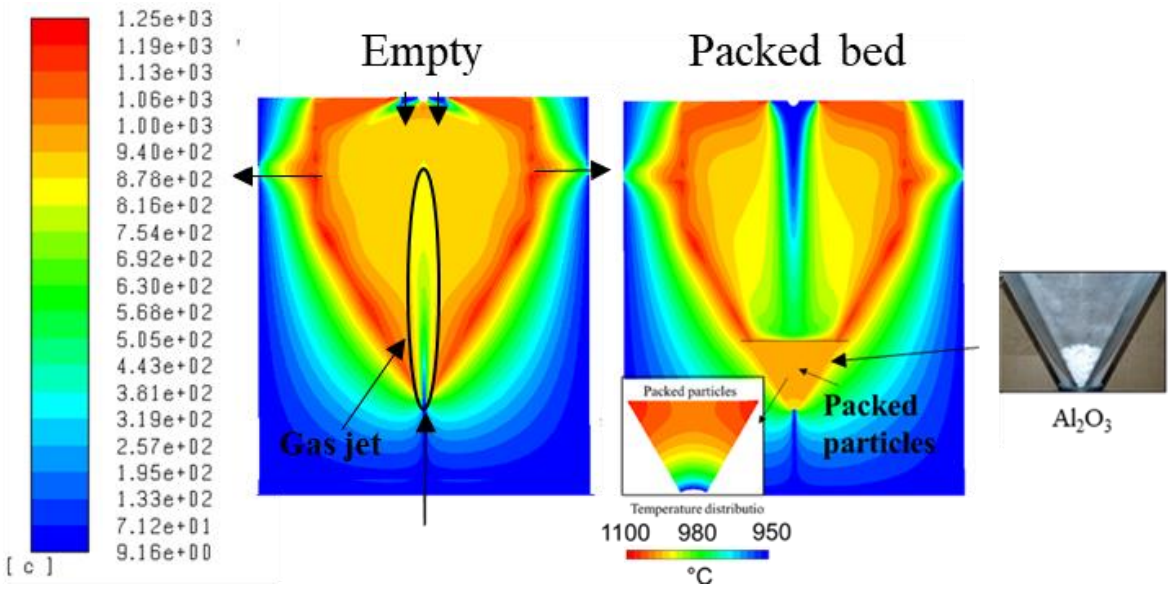

Figure III.4 Temperature distribution: empty vs. packed bed

In the packed bed configuration, the gas phase temperature reached the same temperature (around 700°C) above the porous medium due to the cold window inlet Ar flow rate. The porous zone model allowed to simulate heat transfer through the porous packed bed (composed of 3 mm alumina particles). Accordingly, the bed top surface temperature was estimated at 1000°C at its center and approached 1100°C nearby the cavity walls. Due to the thermal resistance of the packed particles, and to the cooling of the bottom of the bed by the entering cold gases, the bed bottom temperature was lower (around 950°C).

The gas velocity magnitude field inside the reactor is presented in Figure III.5. The simulations revealed a significant attenuation of the inlet gas flow velocity when using the packed particles. The gas jet velocity at the cone entrance was about 8 $m.s^{-1}$. It then decreased to less than 0.5 $m.s^{-1}$ just above the bed. The Ar flow from the top of the reactor flowed downward to hit the bed top surface with a velocity of around 0.3 $m.s^{-1}$. It then flowed with the inlet gases towards the outlet along the cavity walls. The steam distribution inside the reactor and the inlet gas (water steam+argon) pathlines for the two configurations are presented in Figure III.6. In the empty configuration, the central cavity region exhibited the highest water steam concentration, whereas the packed bed broadened the inlet gas streamlines over the entire cavity section, suggesting improved homogenization of chemical kinetics in the whole cavity region.

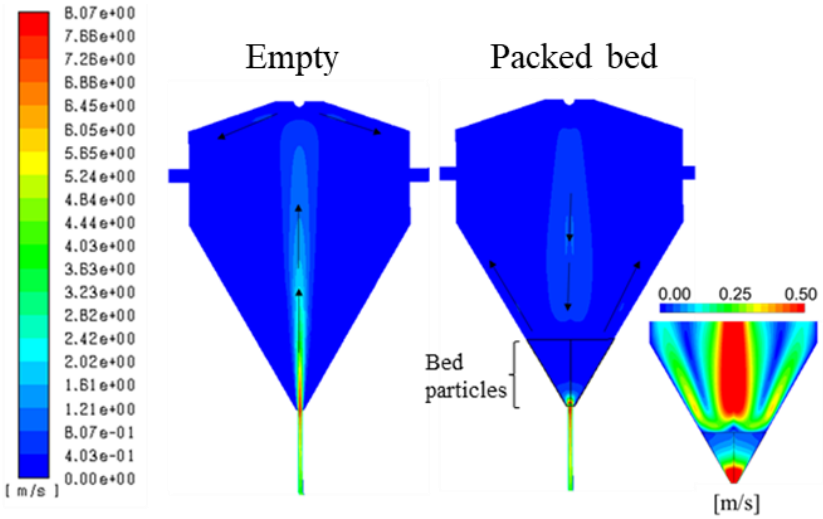

Figure III.5 Velocity magnitude field: empty vs. packed bed

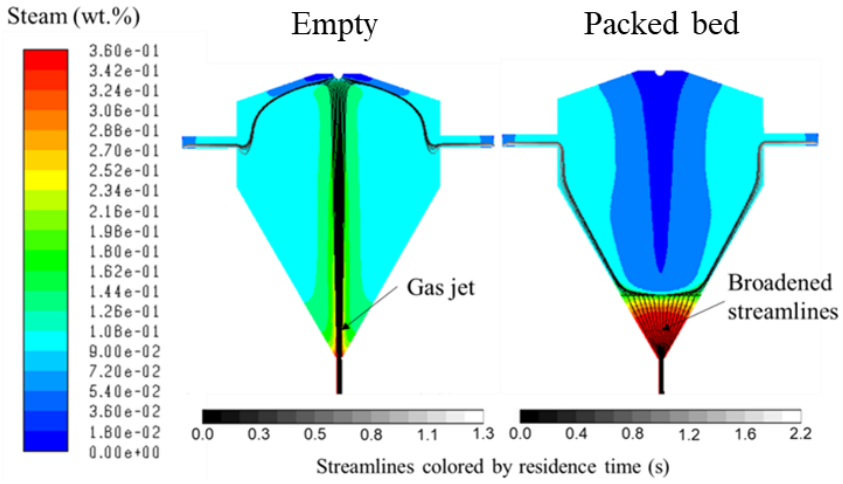

Figure III.6 Steam distribution and inlet gas streamlines

To assess the trajectories of char particles inside the empty and the packed bed cavity, non-reacting particles were tracked for a few seconds using the Discrete Phase Model (DPM) approach. The char particles characteristics were: d_{char}=0.35 mm, ρ_{char}=144 kg.m^{-3}, $c_{p,char}$=1000 J.°C^{-1}.kg^{-1}. They were injected from the top of the reactor for the packed bed configuration and from the center of the gas jet for the empty configuration (Figure III.7-b). A mass flow rate of 0.05 g.min^{-1} of char was continuously injected. Figure III.7-a shows the temperature of a tracked char parcel as function of time for the two hydrodynamic configurations and Figure III.7-b shows the particles trajectories colored by particles velocity. For the empty case, the simulations predicted a fluctuating temperature pattern depending on the location of the particles in the reaction zone. In fact, particles were entrained cyclically toward the source of radiation with a velocity of 1.7 m.s^{-1}, and their temperature could thus reach crest values above 1500°C. When reverting to the bottom of the reactor due to gravity, they were cooled to 900°C by the inlet jet gases. On the contrary, in the packed bed configuration, the particles settled rapidly just after injection on the top of the bed. Their temperature is therefore constant at around 1150°C.

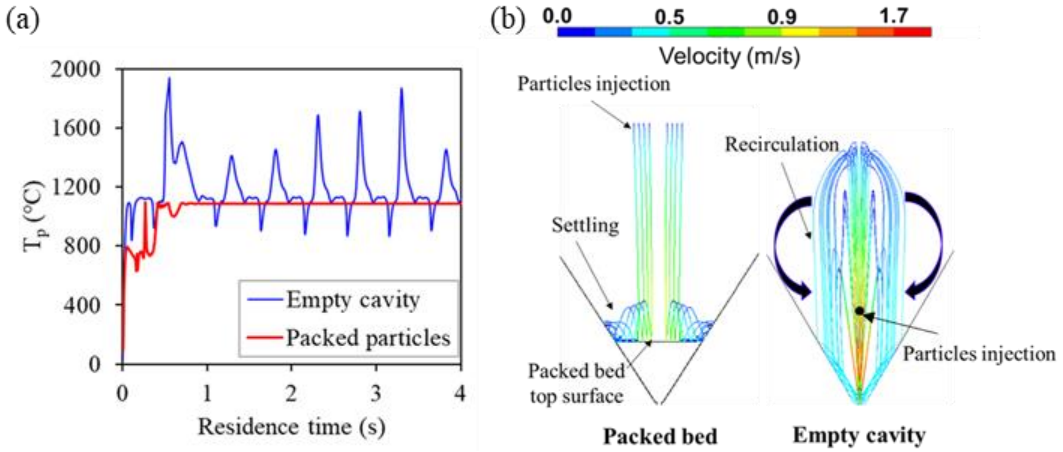

Figure III.7 (a) DPM temperature; (b) DPM trajectories colored by particles velocity magnitude

This clearly confirmed the interest of using the packed Al_2O_3 particles to limit the entrainment of the particles. The spouted bed configuration was studied at cold and at real processing conditions. Prior to the CFD simulations, cold tests were carried out at ambient conditions with air on a transparent PMMA cavity mockup to visualize the mixing of the particles and determine the minimum spouting conditions. The obtained results for a 10g bed of SiC and Al_2O_3 particles are summarized in Figure III.8.

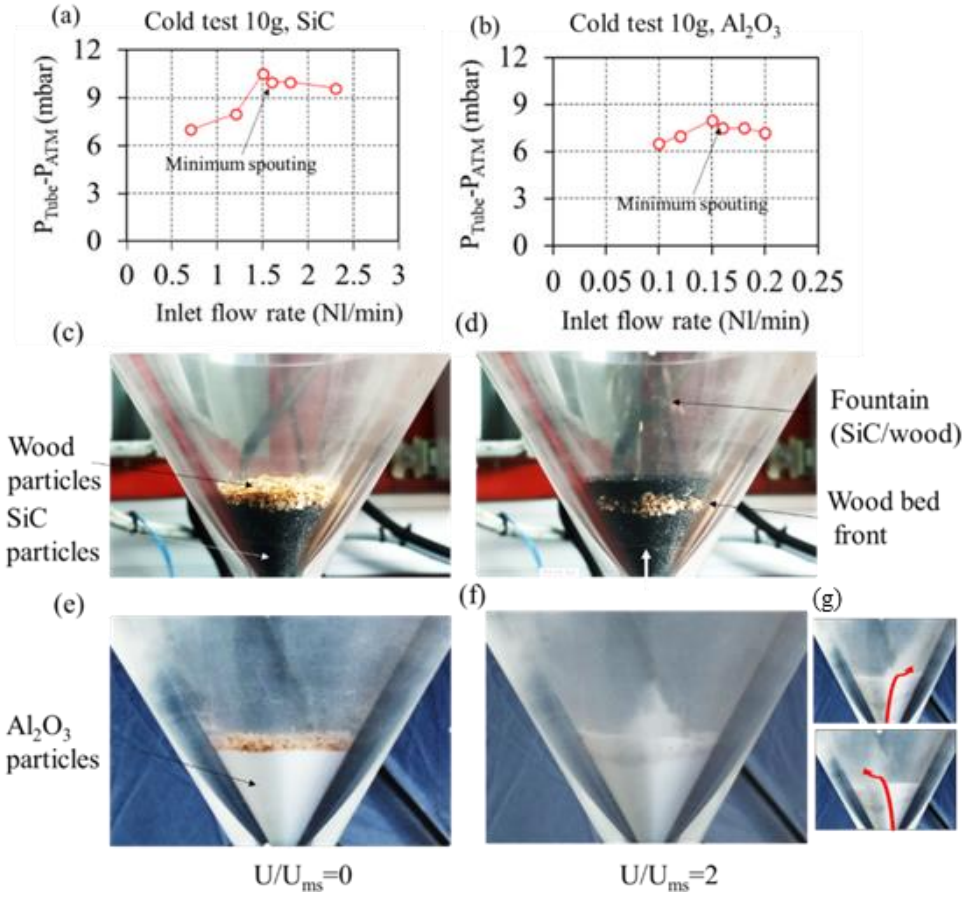

Figure III.8 Experimental cold tests on a replicated PMMA cavity mockup (10g of inert particles)

The bed minimum spouting velocity was determined by plotting the bed pressure drop as function of the inlet gas flow rate. Figure III.8-a,b show the measured pressure drop vs. the air flow rate for a 10g bed of 300 µm SiC and 125 µm Al_2O_3 particles. It can be observed that by increasing the gas flow rate, the total pressure drop increased until reaching a maximum value that initiated the spouting of the particles (around 11 mbar for SiC and around 8 mbar for Al_2O_3 bed). Accordingly, minimum spouting flow rates of 1.5 NL.min^{-1} ($v_{exp,SiC}$=7.42 m.s^{-1}) and 0.16 NL.min^{-1} ($v_{exp,Al2O3}$=0.85 m.s^{-1}) were measured for the SiC and Al_2O_3 particles.

In Figure III.8-c,e, a thin layer of wood particles was set at the top of the inert bed to visualize the stirring of the wood particles for U/U_{ms} ~2. A very stable spouting regime and well-ordered mixing of the particles was observed with the SiC particles, whereas the Al_2O_3 particles showed 3D instabilities that distorted the central gas jet path. As a result, the fountain height was constantly varying and changing its position, as illustrated in Figure III.8-g. This undermined the particles recirculation from the top of the bed to the bottom. Such spouting instabilities were observed in previous studies (Olazar et al., 1992) and were due to different interdependent factors such as too large or too small cone angles. They could also occur when the height of the bed exceeded the maximum spoutable height, or when the spouted powders diameter was too small to be fluidized in a coherent and stable fashion. These results were compared to 2D axisymmetric CFD simulations using the Eulerian approach. Figure III.9 shows the spouted bed particles space distribution for different inlet gas flow rates. The cyclic particle-flow recirculation pattern through the three distinct regions (central spout, annular zone and fountain above the bed surface) was well reproduced by the Eulerian model. The predicted minimum spouting flow rate was 1.5 NL.min^{-1} for the SiC bed ($v_{sim,SiC}$=7.95 m.s^{-1}) and 0.23 NL.min^{-1} for the Al_2O_3 bed ($v_{sim,Al2O3}$=1.22 m.s^{-1}).

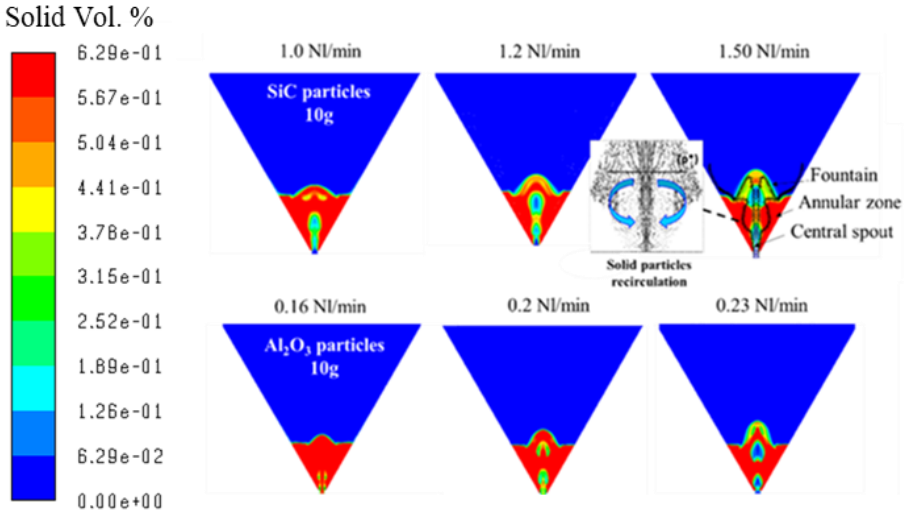

Figure III.9 Spouted bed particles space distribution for different inlet air flow rates (10 g of inert particles, t=2s)

These predictions were in agreement with the experimentally measured values for SiC within an error range of 4% and slightly overestimated the minimum spouting flow rate by about 0.07 NL.min^{-1} for the Al_2O_3 particles. The observed discrepancies for the Al_2O_3 particles were associated to the aforementioned flow perturbations (Figure I.8-g) that potentially facilitated the

gas passage through the annular region. Such 3D instabilities were not reproduced by the 2D axisymmetric model.

Subsequently, the reactor was simulated under real processing conditions (same bottom and upper gas flow rates as experiments) with a solar power input of 0.9 kW_{th} and with 10g of spouted bed mass for comparison with empty and packed bed configurations. The obtained temperature distribution is presented in Figure III.10-a,b for Al_2O_3 and SiC spouted particles. Just as the two previous hydrodynamic configurations (empty and packed bed), the reactor cavity walls reached an average temperature of 1230°C. Unlike the empty configuration where the central gas jet reached only 700°C at the conical part of the reactor, the central gas jet when using the spouted particles reached high temperatures up to 1180°C right away.

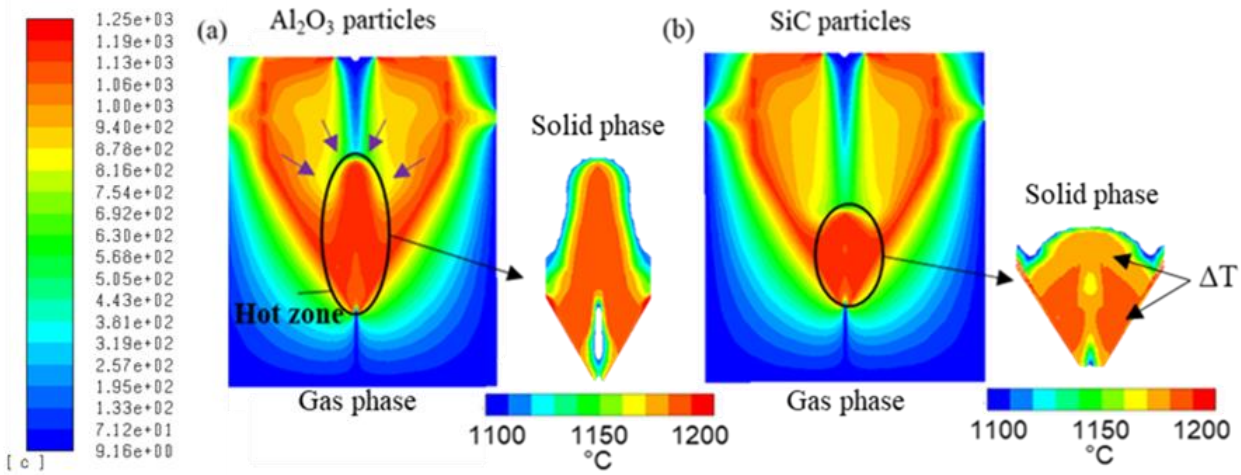

Figure III.10 Temperature distribution (gas and solid phases): (a) 125µm-Al_2O_3 particles; (b) 300µm-SiC particles

By comparing the simulations between Al_2O_3 and SiC, the alumina particles allowed increasing the gas phase temperature over a larger area. This is because the alumina particles were better spouted thanks to their lower diameter. Moreover, their temperature was more homogeneously distributed, whereas small gradients were noticed for SiC particles (Figure III.10-b), arising from the less pronounced stirring of the SiC particles inside the cavity. This is confirmed by the different fountain heights depending on the particles diameter (Figure III.11-b,d).

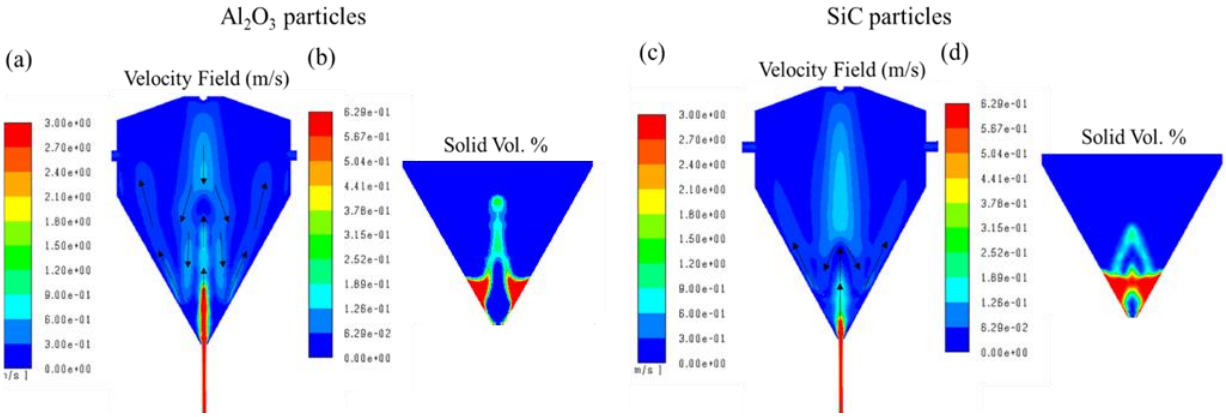

Figure III.11 Gas velocity field and solid volume fraction: (a,b) 125 µm-Al_2O_3 particles, (c,d) 300 µm-SiC particles

Indeed, the fountain height of the Al_2O_3 bed was two to three times higher than the fountain height of the SiC particles. Moreover, the central gas flow (bottom jet zone) was more attenuated by the SiC particles that somehow deflected part of the flow towards the annular zone (Figure III.11-a,c). For readability reasons, the velocity magnitude field was plotted in a range of 0-3 $m.s^{-1}$. However, due to the heating of the gases inside the injection tube, the gas velocity increased from 3 $m.s^{-1}$ (at the inlet of the injection tube) to values above 9 $m.s^{-1}$ at the cone entrance for both 10g beds (Figure III.12). This value is hence higher than the minimum spouting velocities (Figure III.9); therefore, the spouting regime was largely achieved with the current experimental flow rates.

The spouting gases ($Ar+H_2O$) pathlines colored by velocity magnitude are presented in Figure III.12.

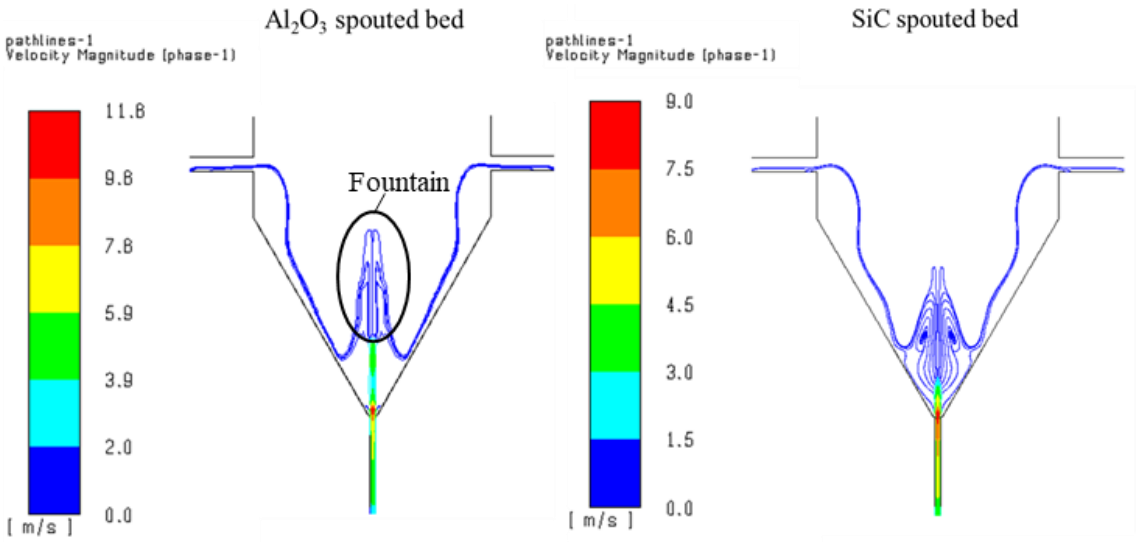

Figure III.12 Spouting gases pathlines colored by velocity magnitude

It clearly showed that for the Al_2O_3 particles, the flow crosses the bed mainly from its center to reach the fountain zone, while the SiC spouted particles distribute part of the flow towards the annular region. Thereafter, the spouting gases interact with the upper window inlet flow to get routed all along the cavity walls towards the gas exit. A complementary comparative study of the three configurations (including sand and olivine) based on hydrodynamic criteria only is provided in ANNEX 2.

Overall, the simulations evidenced the benefits of using inert materials in the form of spouted particles to increase the reaction zone temperature while ensuring an efficient stirring of the particles. The experimental gas flow rates were high enough to spout the 10g bed. A slight increase of the inlet argon flow rate is recommended for the largest particles to better disperse them in the upper part of the cavity. Further increase of the spouting flow rate for the smallest bed particles can possibly impair the process by entraining them out of the conical cavity. The observed flow instabilities during cold tests for the Al_2O_3 spouted particles were not predicted by the 2D model. They are expected to negatively affect the heat transfer through the bed at high temperature.

III.4.2 Experimental study

Different experimental runs were performed to study the effect of the inert bed particles on biomass conversion and syngas composition. The experimental conditions at 1200°C (Runs#1-7) and 1300°C (Runs#8-11) are recapped in Table III.4.

Table III.4 Operating conditions of the directly irradiated reactor (1200 and 1300 °C, 10g of inert materials)

Run#	$T_{operating}$ (°C)	Bed material		Bed configuration	Wood feeding rate ($g.min^{-1}$)	Bottom Ar flow rate ($NL.min^{-1}$)	H_2O flow rate ($g.min^{-1}$)
		material	size			Jet gases	
1	1200	Empty	-	Dilute spouted bed	1.2	0.2	0.2
2	1200	Al_2O_3	3mm	Packed bed	1.2	0.2	0.2
3	1200	Al_2O_3	125µm	Spouted bed	1.2	0.2	0.2
4	1200	SiC	300µm	Spouted bed	1.2	0.2	0.2
5	1200	SiC	300µm	Spouted bed	1.2	0.3	0.2
6	1200	Olivine	300µm	Spouted bed	1.2	0.2	0.2
7	1200	Sand	300µm	Spouted bed	1.2	0.2	0.2
8	1300	Al_2O_3	3mm	Packed bed	1.2	0.2	0.2
9	1200-1300	Al_2O_3	125µm	Spouted bed	1.2	0.2	0.2
10	1300	Al_2O_3	125µm	Spouted bed	1.2	0.2	0.2
11	1300	SiC	300µm	Spouted bed	1.2	0.2	0.2

The Carbon Conversion Efficiency (CCE, I.7), the Cold Gas Efficiency (CGE, I.8) and the Solar-to-Fuel Efficiency (SFE, I.9) metrics were used to evaluate the performance of the reactor for each of the hydrodynamic configurations. The uncertainty on the CCE, CGE and SFE were estimated by differentiating their mathematical formulas (Eqs. III.42-III.44).

$$\Delta CCE = \frac{(\Delta \sum_{i \neq H_2} \bar{m}_{c\ in\ i} + CCE.\Delta m_{c\ in\ dry,biomass})}{m_{c\ in\ dry,biomass}} \quad III.42$$

$$\Delta CGE = \frac{(\Delta \sum_i LHV_i.\bar{m}_i + CGE.LHV_{dry,biomass}.\Delta m_{dry,biomass})}{LHV_{biomass}.m_{dry,biomass}.} \quad III.43$$

$$\Delta SFE = \frac{(\Delta \sum_i LHV_i.\bar{m}_i + SFE.[LHV_{dry,biomass}.\Delta m_{dry,biomass} + \Delta Q_{solar}])}{(Q_{solar} + LHV_{dry,biomass}.m_{dry,biomass})} \quad III.44$$

With $\Delta m_{dry,biomass}=0.5\%.m_{dry,biomass}$ (Time=0min). ΔQ_{solar} (J) was estimated assuming an instantaneous error on the solar power input of ±0.1 kW. The total error was therefore deduced by multiplying 0.11 kW_{th} by the experiment duration (t_f). The uncertainty on the mass $\bar{m}_i$ of each species was deduced from the error made on the total volume of each gas (V_i) (Eq.III.45). With $\Delta F_{i,j}$ the absolute error made at each time step Δt_j on the volume flow rate of a species 'i' and $x_{i,j}$ the instantaneous gas volume fractions.

$$\Delta V_i = \sum_j \Delta t_j . \Delta F_{i,j} = \sum_j \Delta t_j . \{\frac{x_{i,j}}{x_{Ar,i}} . \Delta F_{Ar} + \frac{F_{Ar,i}}{x_{Ar,i}} . \left(\Delta x_{i,j} + \frac{x_{i,j}}{x_{Ar,i}} . \Delta x_{Ar,i}\right)\} \quad \textit{III.45}$$

The initial wood sample mass was 30g for all the runs except in Run#7 where only 15.6g of wood was solar gasified (Table III.5). The $(S/B)/(S/B)_{st}$ mole ratio was equal to 1.24 based on Eq.II.1.in all the experiments to insure a slightly overstoichiometric wood/steam mixture.

After solar tests, the material mass balance was checked systematically by comparing the initial mass of fed reactants (biomass and water) with the mass of products outputs (syngas components, excess water and entrained char/soot/tar trapped in bubbler and filters). Overall, the mass balance closure was higher than 84% for all the experimental runs as shown in Table III.5.

Table III.5 Mass balance Runs#1-11

Run#	Reactants (g)		Products (g)		Mass balance closure
	Biomass	H_2O	Gas products	Residues in outlet reactor components	
1	30.0	6.8	25.5	12.6	103.6%
2	30.0	6.8	26.9	8.3	93.3%
3	30.0	7.0	27.0	6.2	88.2%
4	30.0	6.8	24.6	7.3	86.8%
5	30.0	6.3	24.1	6.6	84.8%
6	30.0	7.7	26.8	5.9	86.8%
7	15.6	3.5	13.4	5.8	99.3%
8	30.0	6.7	27.4	7.7	95.6%
9	30.0	6.1	26.8	6.5	92.2%
10	30.0	6.7	26.8	7.8	94.3%
11	30.0	6.9	26.7	6.9	91.1%

The reactor temperature as measured by T3 (inside the cavity) for Runs#1-11 is plotted in Figure III.13-a,b. The temperature was effectively maintained around the set point values (maximum mean deviation of 14°C in Run#6). Due to the insufficient solar heating in Run#9, the reactor temperature declined from 1300°C to values approaching 1200°C showing the highest mean deviation of 29°C. Pyrometer measurements (T_{pyro}) are plotted in Figure III.14. T_{pyro} indicated strong fluctuations in temperature for the spouted-bed configuration because the pyrometer pointed directly at the bed top surface. Given the spouting of particles and the continuous feeding of fresh biomass, such fluctuations given by the optical pyrometer were expected (for simplification, the same emissivity of 1 was assumed for all the measurements, although in practice the emissivity is dependent on the materials properties and temperature). The fluctuations were lowered when the packed Al_2O_3 particles were used (Run#2).

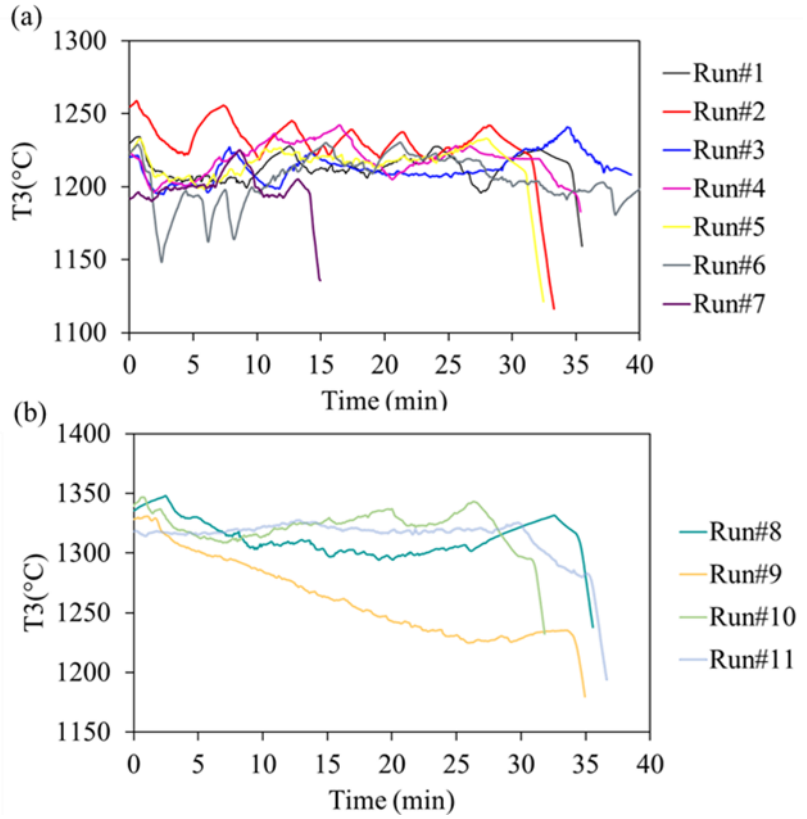

Run#	T	$\sum \frac{T-\bar{T}}{n}$
1	1213°C	7°C
2	1229°C	11°C
3	1213°C	7°C
4	1218°C	9°C
5	1217°C	6°C
6	1203°C	14°C
7	1201°C	6°C

Run#	T	$\sum \frac{T-\bar{T}}{n}$
8	1312°C	11°C
9	1255°C	29°C
10	1314°C	6°C
11	1313°C	10°C

Figure III.13 T3 measurements for Runs#1-11 at 1200°C and 1300°C (left); Average and mean deviation of temperature (right)

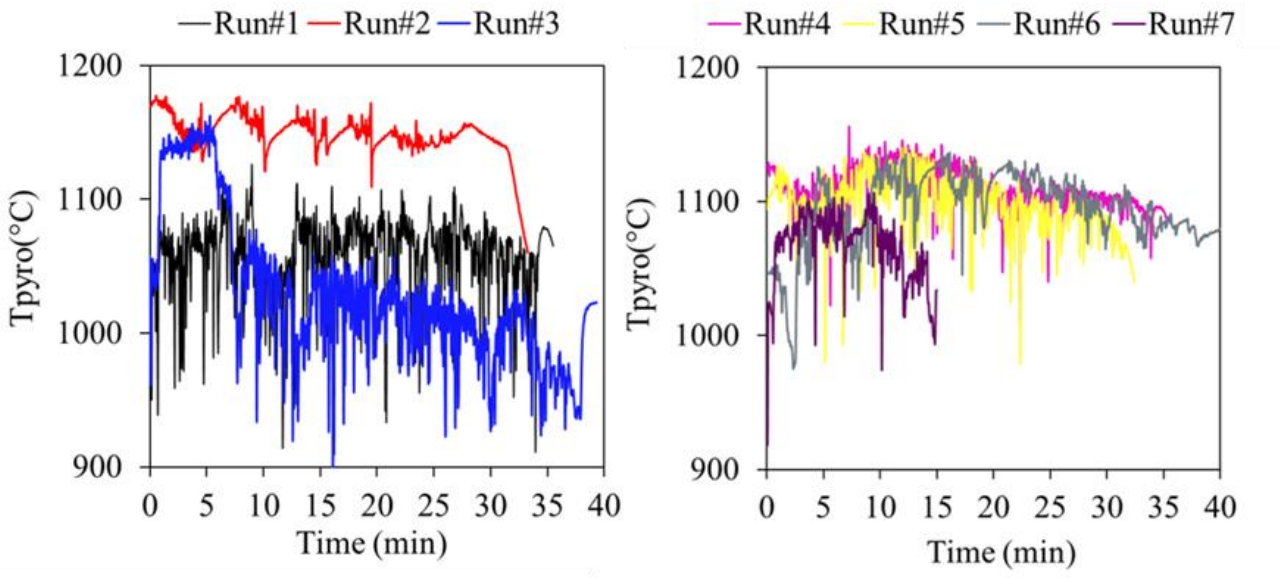

Figure III.14 Pyrometer measurements for Runs#1-7 (1200°C)

Figure III.15 shows the calculated performance metrics and the gas composition for the different hydrodynamic configurations at 1200°C (Runs#1-7). The carbon conversion in the empty case (Run#1) reached 79.3% and the syngas produced was essentially composed of H_2 and CO. The H_2 and CO volume fractions were respectively 51.6% and 38.3%. The use of the packed and

spouted bed of Al_2O_3 particles (Runs#2-3) increased the CCE up to 84.7%. In contrast, the CCE declined to 75.5% with the spouted 300-µm SiC (Run#4).

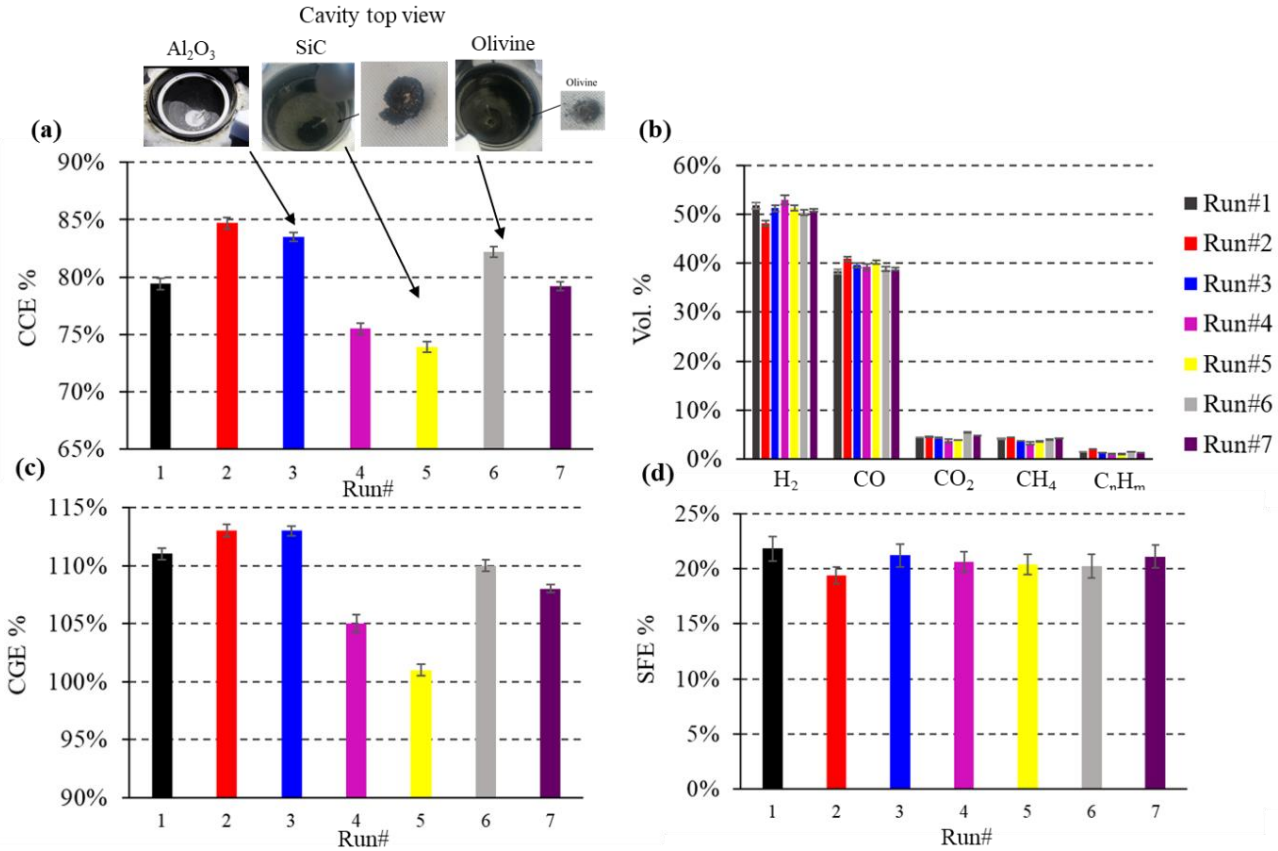

Figure III.15 (a) CCE and top view of the cavity at the end of the experiments (for Al_2O_3, SiC and olivine); (b) Gas composition; (c) CGE; (d) SFE (Runs#1-7 at 1200°C)

The increase of the spouting carrier gas flow rate (from 0.2 NL.min^{-1} in Run#4 to 0.3 NL.min^{-1} Run#5) decreased even more the CCE to 73.9%. While the alumina particles remained intact at the end of the experiments and showed chemical inertness, the SiC bed suffered from sintering and adhered to the cavity walls (Figure III.15-a). This can also be due to possible side reactions that may occur between SiC and water (forming either $SiO_2 + CH_4$ or $SiO_{(g)} + 2H_2 + CO$, the former being the most thermodynamically favorable). The expected effect of improving the stirring of SiC particles by increasing the carrier gas flow rate was therefore hardly achieved and only impaired the gas and solid residence times.

The olivine sample in Run#6 also stuck but to a lesser extent on the cavity walls and its color turned from brown/red (due to the presence of iron oxides) to grey (Figure III.15-a), suggesting poor chemical inertness at high temperatures. The CCE in Run#6 was still higher than the CCE of the empty cavity and reached 82.2%. The silica sand bed in Run#7 was the least resistant material, as the cavity was found almost empty at the end of the experiment, presumably due to attrition and the formation of fused silica during spouting, caused by particles exposure to high-flux radiation in the upper cavity region. The results in terms of CCE and syngas composition were therefore very similar to Run#1.

In general, the bed materials only slightly influenced the gas composition and in all cases, the main syngas components remained H_2 and CO, whereas CO_2, CH_4 and C_nH_m (mainly C_2H_2) were produced in smaller amounts. The Al_2O_3 particles in Run#2 led to the lowest H_2 concentration (~48.1%) while the light hydrocarbons (CH_4 + C_nH_m) volume fraction was the largest (6.4%). The H_2 concentration in Run#4 (SiC particles, 0.2 $NL.min^{-1}$ of spouting carrier gas flow rate) was the highest and reached around 52.9%. This however can be due to the oxidation of SiC by steam, forming additional H_2 in the mixture.

The CGE (Figure III.15-c) followed a similar pattern as the CCE since the gas composition was only slightly modified by the addition of the inert powders. The peak CGE values were obtained in Runs#2-3 (packed and spouted Al_2O_3 particles) and reached 1.13 against 1.11 in Run#1 (empty cavity). The minimum CGE was 1.01 in Run#5 (SiC bed) when the Ar flow rate was set to 0.3 $NL.min^{-1}$. The SFE (Figure III.15-d) reached up to 21.8% in Run#1 (empty cavity) and decreased moderately to a minimum value of 19.4% in Run#2 (packed Al_2O_3 particles) even if the CGE was slightly upgraded.

The total solar energy consumed (Q_{solar}) for gasifying the 30.0g biomass feedstock was 1.76±0.21 MJ in Run#1. It was higher with inert bed materials: 2.23±0.19 MJ in Run#2 (packed Al_2O_3 particles), 2.15±0.24 MJ in Run#3 (spouted Al_2O_3 particles), 1.89±0.21 MJ in Run#4 (spouted SiC particles), 1.83±0.19 MJ in Run#5 (spouted SiC particles) and 2.04±0.25 MJ in Run#6 (spouted olivine particles). Q_{solar} in Run#7 was 0.99±0.11 MJ (because only 15.6g of biomass is gasified). While a small increase of Q_{solar} was observed when using the inert particles probably for heating the bed materials, the uncertainty on Q_{solar} makes it difficult to precisely conclude about the influence of the bed materials on the solar energy consumption and therefore on the SFE.

The effect of temperature on the gasification process was studied in Runs#8-11 with the Al_2O_3 packed particles (Run#8), Al_2O_3 spouted bed particles (Runs#9-10) and with SiC bed (Run#11). Olivine and sand were not tested at this temperature, due to their low stability and resistance to the solar heating. Figure III.16 shows the calculated reactor efficiencies and gas composition at 1300°C.

The temperature increase showed only a little impact on the CCE and CGE for the packed bed configuration (Run#8) but the influence on the gas composition was more pronounced. The CCE and the CGE both slightly declined by less than 1.5% whereas the syngas (H_2 + CO) concentration was improved by 4.3% (from Run#2 to Run#8) due to the enhancement of the kinetic rates of the steam methane and light hydrocarbons reforming ($C_nH_m+nH_2O\rightarrow (m/2+n)\ H_2+nCO$).

The CCE in the Al_2O_3 spouted bed configuration declined with temperature increase, from 83.5% in Run#3 to 81.1% in Run#9 and 80.4% in Run#10. This decrease in CCE was ascribed to the more favored entrainment of the reacting char particles, caused by the lower gas residence time that decreases from 0.54s at 1200°C to 0.51s at 1300°C. Accordingly, the CGE declined in a stepwise fashion in Runs#9-10 to reach 109% in Run#10. Moreover, just as in Run#8, the H_2 + CO volume fraction was improved by 3.2% at the expense of a noticeable decrease in $CH_4+C_nH_m$ by 28.0% (from Run#3 to Run#10). The largest H_2 + CO volume fraction was

achieved with the SiC particles (Run#11) reaching 94.2% against 92.1% in Run#4 (SiC bed-1200°C), with a beneficial effect on the CCE and the GGE that approach values of the Al_2O_3 spouted bed possibly due to their better stirring and absorption of the solar flux at 1300°C.

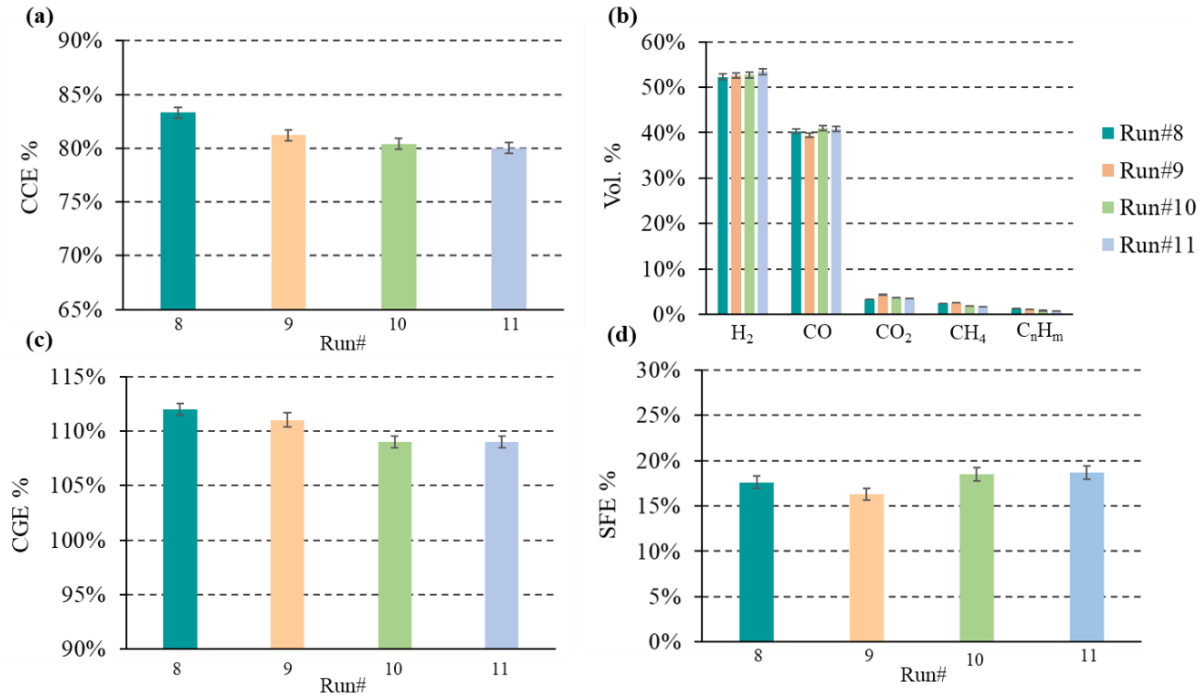

Figure III.16 (a) CCE; (b) Gas composition; (c) CGE; (d) SFE (Runs#8-11 at 1300°C)

For all runs (#8-11), the SFE decreases by more than 10% mainly due to the increase of the solar energy consumption. In fact, the calculated Q_{solar} for Runs#8-11 (1300°C) are higher than in Runs#1-7 (1200°C) and are respectively 2.49±0.20 MJ, 2.68±0.22 MJ, 2.25±0.18 MJ, 2.16±0.18 MJ.

III.4.3 Conclusions

This study focused on solar biomass gasification in a directly-irradiated conical lab-scale reactor and addressed the effect of inert particles on the gasification process. Prior to the experimental study, multiphysics CFD gas-particle flow modelling was developed to explore the impact of inert packed or spouted particles on the reactor thermal and hydrodynamic behavior.

(i) The empty conical cavity (no bed materials) is characterized by a high velocity central gas jet that entrains cyclically the char particles inside the cavity. It offers an excellent exposure to solar radiation evidenced by peak char temperature values but low gas residence time in the central cavity region due to high gas velocities.

(ii) The packed-bed configuration using inert particles at the bottom of the conical cavity significantly attenuates the gas jet speed at the central zone, broadens the gas streamlines and limits the entrainment of the reacting particles.

(iii) The spouted-bed configuration increases the reaction zone temperature and warrants a continuous gas/particles stirring. The finest inert spouted bed particles are more effective in increasing the reaction zone temperature as they are better spatially dispersed.

The experimental part of this study examined five different bed materials at 1200°C and 1300°C.

(i) The empty configuration (no bed materials used) in which only the reacting wood particles are spouted showed a CCE of 79% and a CGE of 111% at 1200°C.

(ii) The Al_2O_3 packed and spouted particles both increased the reactor performance, especially the CCE that reached 85% in the packed bed configuration.

(iii) The SiC bed suffered strongly from sintering and led to the lowest performance with a CCE of 76% and a CGE of 105%.

(iv) Olivine and silica sand were not thermochemically stable at 1200°C, with global performance equivalent to the empty configuration.

(v) The Al_2O_3 beds were the most suitable for the high-temperature process showing good resistance to thermal shocks and chemical inertness.

(vi) The effect of bed materials on the outlet syngas composition at these temperatures remained very low (less than 7% for H_2).

(vii) Increasing temperature to 1300°C improved the syngas quality but globally impaired the CCE, CGE and SFE.

The particles studied in this chapter are widely used in conventional fluidized bed/spouted bed gasifiers (Alauddin et al., 2010). Their use as an efficient heat transfer medium is largely proven below 700°C-900°C. In this work, the particles were subjected to higher temperatures and high solar-flux densities. Although, their potential benefit for enhancing the gasification performance was confirmed at the solar reactor temperature, their resistance to high temperature and thermochemical reactions was questioned. These first results emphasize the importance of the choice of the bed materials that must withstand both the highly oxidizing atmosphere and the high temperature to warrant long-term suitable operation. In order to further study the bed materials, accurate quantification of the mass loss after experiments is essential; in addition, the characterization of the evolution of the particles physico-chemical properties such as density, heat capacity, emissivity, composition etc. would provide key information and relevant data on their physical behavior, durability and thermochemical stability.

Future work should focus on the optimization of the bed particles properties. Low density and high absorption are preferable. New reactor configurations using a confiner can also limit particle entrainment that is a major concern for scale up.

IV. CHAPTER 4

Dynamic simulation and scale up study of a hybrid solar gasifier for biomass steam gasification

IV.1 Introduction

The ability of the solar reactor to operate in both allothermal and hybrid modes was proven numerically and experimentally. The question about its extrapolation arises naturally. Recent studies on up-scaled solar gasification processes focused on liquid fuels, heat, cold and power generation. In this respect, pseudo-dynamic models that assume steady state at each time step and global thermodynamic equilibrium approaches were widely used (Bai et al., 2018; Guo et al., 2015; Kaniyal et al., 2013; Li et al., 2018; Sudiro and Bertucco, 2007; Wang et al., 2019). Despite solar energy variability, up-scaled solar gasification models were based on steady state and pseudo-dynamic approaches that neglect process transients. However, as previously emphasized by Saw et al. (Saw et al. 2017), such models dramatically misestimate the performance, the size and the costs of the plants. Therefore, to achieve a higher degree of relevance, transitional regimes due to large and small parasitic variations of incident solar flux should be integrated in the modelling. Moreover, to cope with the variable nature of solar energy, transient feeding management strategies that precisely control the biomass, steam and oxygen flow rates based on the reactor temperature, syngas demand and optimal use of solar energy need to be investigated. The objective of this study is the scale up and the dynamic modeling of the windowed solar reactor devoted to steam biomass gasification. For this purpose, a dynamic model was formulated based on unsteady mass and energy conservation equations coupled to calculated chemical equilibrium. The time evolutions of the reactor temperature, reactants and products flow rates are determined during three consecutive days at Odeillo in France using representative solar irradiation data. Three biomass, steam and oxygen injection scenarios are discussed to study their impact on the thermochemical behavior of the reactor. The dynamic modeling was first applied to the kW-scale solar reactor for validation and to an industrial reactor for large MW-scale syngas production. Thereafter, the model at MW-scale was used to assess the reactor annual performance in terms of reactants consumption, syngas yield, CO_2 emissions and energy efficiency.

The results presented in this section were published in the *International Journal of Hydrogen Energy* (IJHE) (Boujjat et al., 2020b).

IV.2 Model development

IV.2.1 General principle

The system of differential equations was derived from the unsteady mass and energy conservation equations written for a perfectly stirred reactor considered isothermal. In fact, the blackbody behavior of cavity receivers tends to homogenize the temperature of the reactor walls. The reaction model was taken into account with a chemical equilibrium model that minimizes the system's Gibbs free energy. The reactor model was coded in Python 3. It took as inputs geometrical features (such as the volume of the reactor, thickness of the cavity walls and insulation, aperture size, etc.), DNI (Direct Normal Irradiance) real-time data and the sun's position in the sky represented by both azimuthal (γ) and zenith (α) angles. The latter parameters are relevant to properly model the received solar power during dynamic heating and cooling periods. The Meteonorm© software was used to generate the solar data with a time step of 15

min. The solving of the dynamic equations was performed with the root function of the Python Scipy library. This function was used to find the roots of systems of equations. Among the available methods, the "hybr" method uses the modified Powell method (Jones, 2001), which has shown the best performance in terms of stability for the calculations.

IV.2.2 Model parameters

After model validation with the lab-scale reactor, the dynamic model was used to predict the performance of the up-scaled reactor. Two large-scale solar technology-reactor arrangements are possible, open external and cavity reactors. In the first option, the receiver external surface is directly irradiated by the surrounding mirrors. In the second case, a cavity absorbs the concentrated solar rays through an aperture, thus re-radiation and reflection losses are reduced considerably and the thermal performance is higher. This configuration was thus retained for the extrapolation with a beam down system in which the receiver is located on the ground to facilitate biomass transport and introduction. The solar facility is described in Figure IV.1.

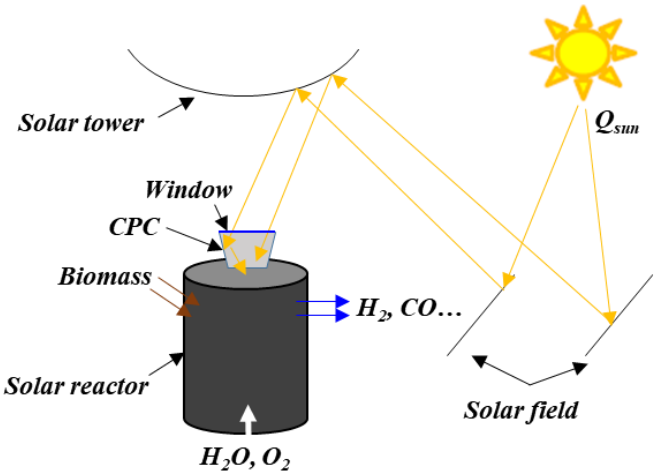

Figure IV.1 Schematic of the up-scaled solar reactor

It was composed of a solar field, a tower and a CPC (Compound Parabolic Collector) set at the top of the reactor. The solar field collected $Q_{sun \rightarrow field}$=10 MW at DNI=1000 W.m^{-2} when the mirrors are normal to sun rays. The solar system was assumed to be able to concentrate the energy 3000 times (i.e. C=3000). This value was also used by other researchers (Rodat, 2010; Romero and Steinfeld, 2012) as it offers a good compromise between performance and technological accessibility in concentrating solar power. A higher value increases the solar power received by the reactor, however at the expense of greater costs and complexity.

The diameter of the aperture was therefore calculated assuming a global optical efficiency ($\eta_{g,opt}$) of 70% (Eq.IV.1):

$$A_{aperture} = \frac{\pi}{4} D_{aperture}^2 = \frac{Q_{sun \rightarrow field}}{\eta_{g,opt} \cdot C \cdot DNI_{max}} \qquad IV.1$$

With DNI_{max}=1000 W.m^{-2}. In order to extrapolate the reactor, the small-scale reactor aperture was first recalculated with the same concentration ratio C of 3000 as the large-scale reactor (Eq.IV.2).

$$A_{aperture,small-scale} = \frac{\pi}{4} D_{aperture,small-scale}^2 = \frac{Q_{sun \rightarrow reactor}}{C \cdot DNI_{max}} \qquad IV.2$$

With $Q_{sun \rightarrow reactor}$ = 1.5 kW_{th} (Eq.IV.2). Thereafter, the ratio between the small-scale cavity diameter and its aperture (designed at C=3000, Eq.IV.2) was held constant during the scale up. The volume of the cavity and its height were sized in order to achieve an average gas residence τ in the order of a minute to promote gas quality and H_2 generation (Saw and Pang, 2012; Wagner et al., 2008) (at T=1200°C and assuming that all the biomass is converted into H_2 and CO, τ_{syngas}=50s at nominal biomass flow rate of 1.0 t/h with a slightly overstoichiometric steam supply $(S/B)/(S/B)_{st}$ equal to 1.24). To estimate the mass of the cavity walls, a constant thickness of 1 cm was considered. The thickness of the thermal insulation was sized in order to keep a temperature of 50°C at the reactor external boundary calculated with an external free convective heat transfer coefficient h=10 $W.m^{-2}.°C^{-1}$. Moreover, to minimize the heat losses through the top of the alumina cap, a 0.5 m refractory layer was added ($\varepsilon_{insu,cap}$=0.35, $\lambda_{insu,cap}$=0.35 $W.m^{-1}.°C^{-1}$). Table IV.1 summarizes the main calculated parameters that were used in the dynamic modelling of the lab-scale and the large-scale reactors.

Table IV.1 Parameters used in the dynamic modeling

Parameters	Lab-scale reactor	Large scale reactor
V_{cavity} (m^3)	$2.40\ 10^{-3}$	139.5
D_{cavity} (m)	$7.80\ 10^{-2}$	6.37
$D_{aperture}$ (m)	$2.00\ 10^{-2}$	2.06
$m_{cavity\ wall}$ (kg)	$3.50\ 10^{-1}$	6218.6
R_{cap} ($°C.W^{-1}$)	4.69	14.41
$R_{cond,\ insulation}$ ($°C.W^{-1}$)	5.88	$1.47\ 10^{-2}$

IV.2.3 Mathematical model formulation

The general unsteady atomic element balance equation for atoms 'j' is given by the following equation (Eq.IV.3):

$$\frac{dN_j}{dt} = \sum_{i=1}^{NC} \nu_{ij} F_i^{in} - \sum_{i=1}^{NC} \nu_{ij} x_i F^{out} \qquad IV.3$$

Where N_j is the number of moles of atoms 'j' inside the cavity at time 't', 'F' is the molar flow rate ($mol.s^{-1}$), 'in' and 'out' indicate the inlet and outlet, respectively. NC is the total number of components (molecules) in the system, ν_{ij} is the stoichiometric coefficient of the "j" atom in the "i" molecule, x_i is the outlet mole fraction of the component "i". In this equation, there is no reaction term because the atoms are conserved.

The syngas composition was calculated at each time step, it was assumed to be equal to that given by chemical equilibrium[9]. As a result, the total number of moles produced for each syngas component (n_j) was expressed as a function of the atomic composition, temperature and pressure inside the reactor (equal to atmospheric pressure). This relationship is expressed by Eq.IV.4:

$$n_j = f_{eq}(N_1, \dots, N_k \dots, N_T, T, P) \qquad IV.4$$

[9] cf. ANNEX 2 for methodology and validation

The chemical equilibrium model was computed by the Python code and was based on the minimization of the system's Gibbs free energy. The nonlinear optimization problem was solved by the numerical procedure SLSQP (Sequential Least SQuares Programming) of the Scipy library following the approach proposed by Kitchin research group at Carnegie Mellon University (https://kitchingroup.cheme.cmu.edu/).

The gases were assumed to be ideal. The total pressure inside the cavity must remain constant. The ideal gas law (Eq.IV.5) was hence used to calculate the total amount of moles of gaseous species in the reactor n_g.

$$n_g = \sum_{i=1}^{NCg} n_i = \frac{PV_{Reactor}}{RT} \qquad IV.5$$

The energy balance equation (Eqs.IV.6-IV.7) was also solved to predict the reactor temperature. It was applied to the reactor cavity volume (reaction zone) and walls as proposed by Charvin et al. (Charvin et al., 2008a) (Figure IV.2).

$$\frac{dE}{dt} = \frac{dU_{wall} + \sum_{i=1}^{NC} n_i . u_i(T)}{dt} = \sum_{i=1}^{NC} F_i^{in} h_i(25°C) - \sum_{i=1}^{NC} F_i^{out} h_i(T) + Q_{net} \qquad IV.6$$

$$Q_{net} = Q_{sun \rightarrow reactor} - Q_{rad,aperture} - Q_{rad,cap} - Q_{cond,insulation} \qquad IV.7$$

Where E is total energy of the system, U_{wall} is the internal energy of the reactor wall, u_i and h_i are respectively the molar internal energy and enthalpy of the species inside the cavity. $Q_{sun \rightarrow reactor}$ is the solar power input at the receiver, $Q_{cond,insulation}$ are the losses by conduction through insulation, $Q_{rad,aperture}$ are the losses due to re-radiation through the aperture, and $Q_{rad,cap}$ are the losses by radiation at the top of the insulated cap.

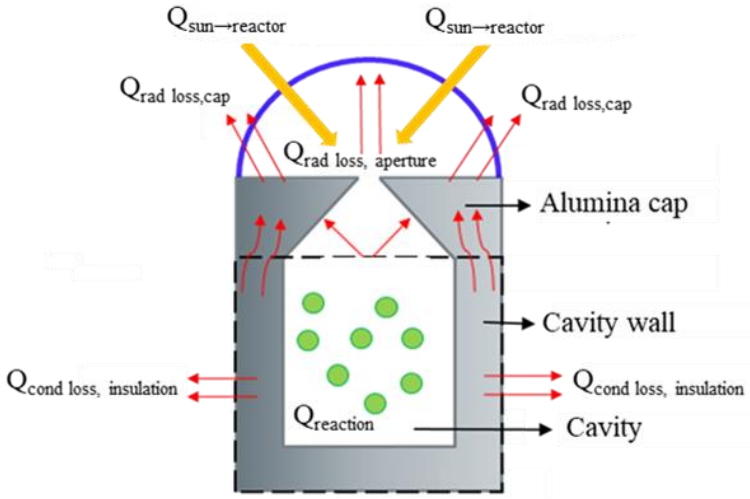

Figure IV.2 Schematic of the reactor thermochemical model.

$Q_{sun \rightarrow reactor}$ was expressed as function of the concentration ratio C, DNI and optical efficiency $\eta_{optical}$ as shown in Eq..

$$Q_{sun \rightarrow reactor} = DNI . C . A_{aperture} . \eta_{optical} \qquad IV.8$$

With $\eta_{optical} = \eta_{field}(\gamma,\alpha).\eta_{beam\ down}$. $\eta_{field}(\gamma,\alpha)$ updated at each time step by 2D linear interpolation of the solar field optical matrix (Figure IV.3) generated by the open source code SAM (System Advisor Model) of the NREL.

It included cosine effects, tracking errors, mirror reflectivity and dirt on mirrors. $\eta_{beam\ down}$ took into account energy losses due to secondary reflection on the beam down system. It was assumed equal to 0.92.

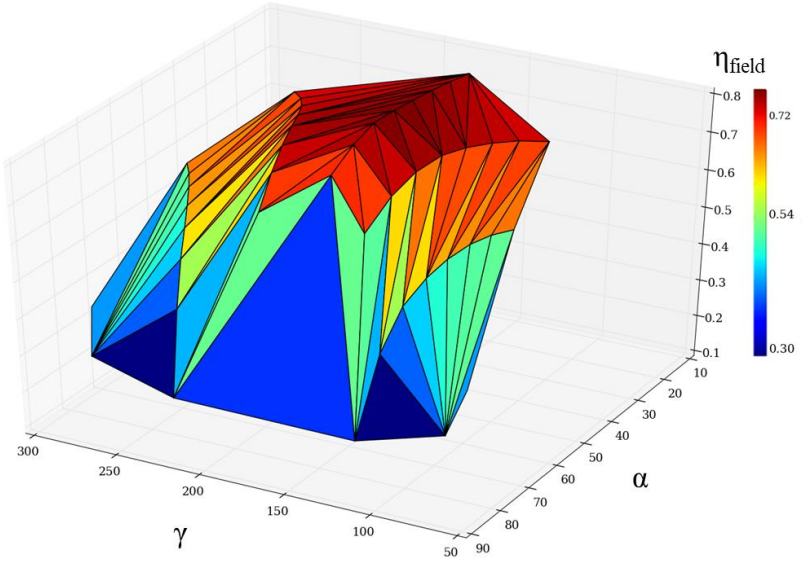

Figure IV.3 Field optical efficiency matrix in Odeillo

The aperture thermal losses were calculated by Eq.IV.9.

$$Q_{rad,aperture} = A_{aperture}\sigma_{rad}.(T^4 - T_\infty^4) \qquad IV.9$$

The losses from the alumina cap ($Q_{rad,cap}$) were calculated by Eq.IV.10.

$$Q_{rad,cap} = \varepsilon_{insu\ cap}.A_{cap}\sigma_{rad}.({T_{cap}}^4 - T_\infty^4) \qquad IV.10$$

The cap effective temperature (T_{cap}) was deduced from Eq.IV.11.

$$Q_{rad,cap} = Q_{cond,cap} + Q_{cavity \to cap} \qquad IV.11$$

$Q_{cond,cap}$ was the heat transferred from the cavity walls to the alumina cap by conduction, it was calculated by Eq.IV.12.

$$Q_{cond,cap} = \frac{T - T_{cap}}{R_{cap}} \qquad IV.12$$

$Q_{cavity \to cap}$ was the net radiative power received by the alumina cap from the radiating cavity walls, deduced from Eq.IV.13.

$$Q_{cavity \to cap} = Q_{cavity \to S_{top}} - Q_{rad,aperture} \qquad IV.13$$

$Q_{cavity \to Stop}$ was the radiation received by the top of the cavity including the one received by the cap and the aperture. It was calculated by the radiative electrical analogy assuming gray bodies heat exchange and considering the three different surfaces of the cylindrical cavity (up, down and lateral surfaces), as depicted in Figure IV.2.

The thermal losses through the insulation were deduced from the following equation (Eq.IV.14):

$$Q_{cond,insulation} = \frac{T - T_{ext}\ (50°C)}{R_{\ cond,insulation}} \qquad IV.14$$

IV.3 Results and discussion

IV.3.1 Model validation at 1.5 $kW_{thermal}$ scale

To validate the model, the simulation results were compared with experimental data obtained during previous experimental campaigns at 1.5 kW scale. The biomass feed-rate was set at 1.2 $g.min^{-1}$ and the water feed-rate at 0.2 $g.min^{-1}$. The total argon flow rate was kept constant at 2.7 $NL.min^{-1}$. The incoming solar power was fixed at 900 W, 1200 W and 1400 W. Simulations were performed using the same boundary and initial conditions until the reactor temperature stabilized to reach steady state. Figure IV.4 shows the steady-state temperature as a function of solar power for the Python model and the measured temperature T3 (inside the cavity).

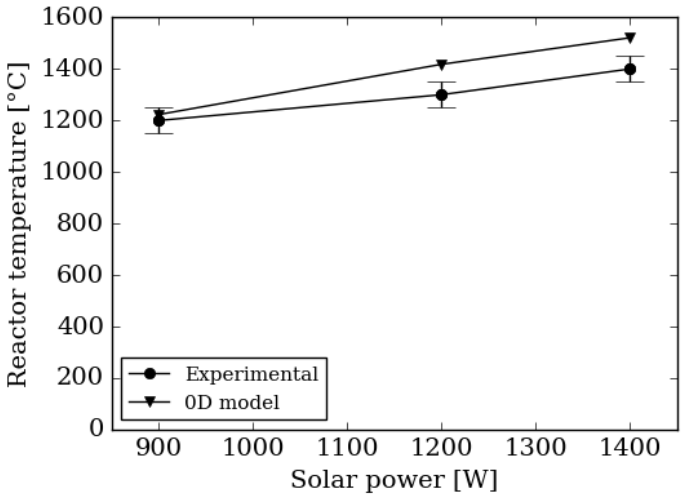

Figure IV.4 Thermal validation of the model.

These results show that the model slightly overpredicts the reactor temperature compared to the experiments. This is especially true with high solar power inputs. Indeed, the relative error on temperature as compared to the experiments is 1.9% at 900 W and 8.6% at 1400 W, which can be due to slightly underestimated thermal losses for example at gas inlets/outlet of the reactor that are not considered in the model. The dynamic behavior of the model was also evaluated. To do so, the simulated reactor cooling after biomass and steam supplies interruption was compared to the experimental cooling. Figure IV.5 shows a comparison of temperature decrease over time during the reactor-cooling phase. Values from T2 (positioned at the external cavity wall) are also plotted.

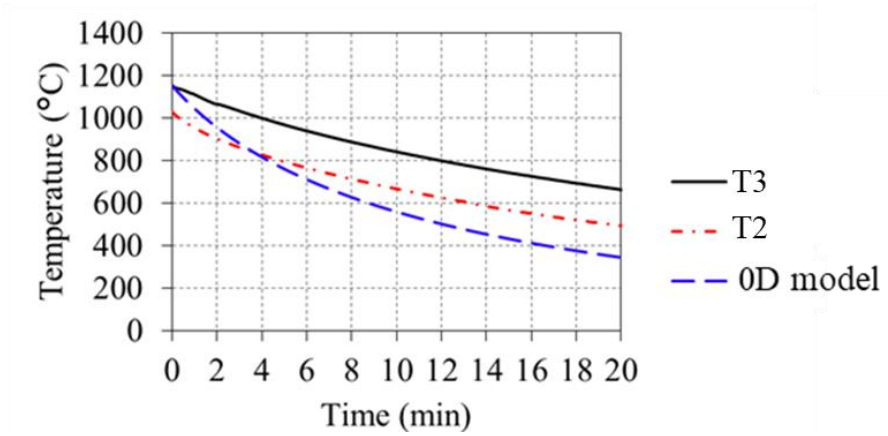

Figure IV.5 Thermal validation of the dynamic model.

The temperature calculated by the model was in agreement with the results of the T2 thermocouple down to around 800°C with a relative error of 8%. The comparison with T3 showed an increasing difference from the beginning of cooling. This may be related to the fact that T3 was inserted inside the cavity and that the heat transfer from the interior of the cavity to the cold outer shell of the reactor takes much longer. Overall, the model reproduced well the main trends that were observed experimentally regarding the reactor thermal behavior, and it was therefore used to extrapolate the reactor.

The experimentally measured syngas yield was also compared to model predictions. Notable differences were observed (Figure IV.6). At 1200°C, the system composition calculated by the equilibrium model showed that almost only H_2 and CO are produced, whereas CH_4 and CO_2 are additionally measured in small amounts during experiments. The Python model composition calculation assumed thermodynamic equilibrium, which is only valid for very long residence times. Actually, the average residence time for the small-scale reactor was estimated at 0.5s (at 1200°C), which means that thermodynamic equilibrium may not be reached, thereby explaining the discrepancy between the calculated and the measured syngas yields. Therefore, kinetic models would be more suitable at this scale. However, due to the targeted high operating temperature and the increased residence time of the up-scaled reactor, the chemical equilibrium assumption is better justified and was thus used in the following.

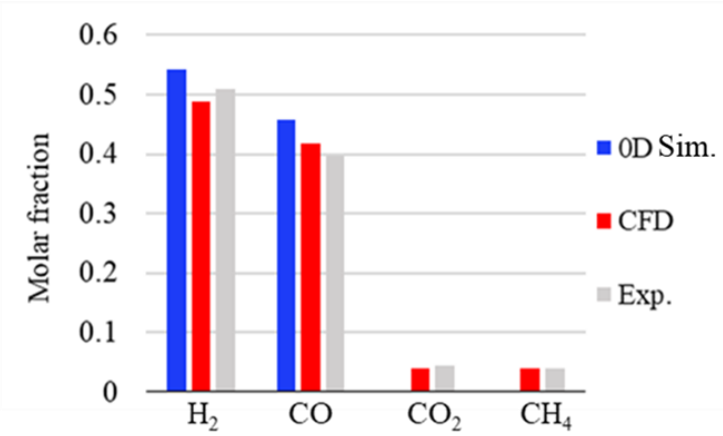

Figure IV.6 Comparison of syngas yields calculated by the 0D chemical equilibrium model, 3D CFD model and the measured experimental values.

IV.3.2 Large-scale reactor simulation

Dynamic simulations of the large-scale reactor were conducted using real solar data (averaged over a 19-year period: 1991-2010) of three consecutive days (4th, 5th and 6th of May in Figure IV.7). The three days were selected as they are characterized by sunny (4 and 6 May) and cloudy days (5 May) thereby allowing getting a better understanding of the reactor operation under stable/high DNI solar radiation conditions (4 and 6 May) and also under unstable (highly variable) solar conditions (5 May). These data were generated by the commercial software Meteonorm©. The yearly variability of DNI at Odeillo for the selected period is 2.5%. Three feeding management strategies were compared. The first one (TOR) was a simple on/off control algorithm. The second one (OPTI) tuned the biomass and steam flow rates in order to thermally stabilize the reactor temperature at 1200°C. The third mode (HYB) used pure oxygen and an additional extra-biomass injection to overcome solar energy fluctuations, thus insuring a continuous conversion of biomass. The three feeding modes were discussed. For all the simulations, the inlet mass flow rate of steam was assumed equal to 0.17 times the raw biomass feeding rate. The solar-to-fuel efficiency (SFE) was used to discuss the performance of the reactor. This metric expresses the ratio of the calorific value contained in the syngas over the total power input that enters the reactor in the form of both solar power and biomass calorific value. When the available solar power is equal to zero, the SFE is equivalent to the Cold Gas Efficiency (CGE).

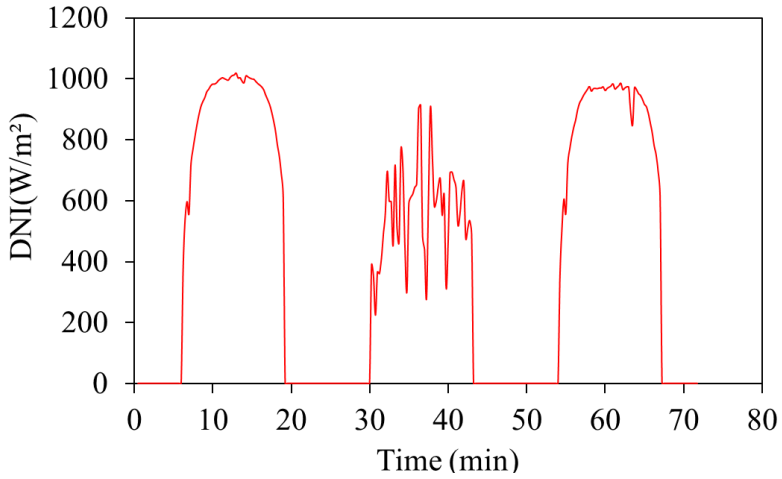

Figure IV.7 Available DNI for 4th, 5th and 6th of May.

IV.3.2.1 TOR allothermal control mode (Tout Ou Rien, on/off control)

In this operating mode, both biomass and steam started being injected when the temperature exceeded an upper threshold. Their injection was stopped when the temperature fell below a lower limit. The chosen upper and lower limits were 1250°C and 1150°C, respectively. There were two main operating steps: one for heating the reactor and the other for gasifying the biomass. During the first step, the only injected gas was the inert carrier gas (Ar for the small-scale reactor and N_2 for the large-scale reactor). Once the temperature reached 1250°C, biomass and steam were fed at a constant nominal flow rate. If, during operation, the temperature decreased below 1150°C, the supplies, except for inert gas, were stopped. During the cooling at night, the top of the reactor was covered to avoid radiation losses from the aperture and the front cover, so as to minimize the heat losses. To study the impact of the biomass and steam

nominal flow rates on the reactor behavior, three biomass feeding rates were selected: 0.5 t/h, 1.0 t/h and 2.0 t/h. Figure IV.8 shows the reactor temperature for the three feeding rates as well as the solar power input.

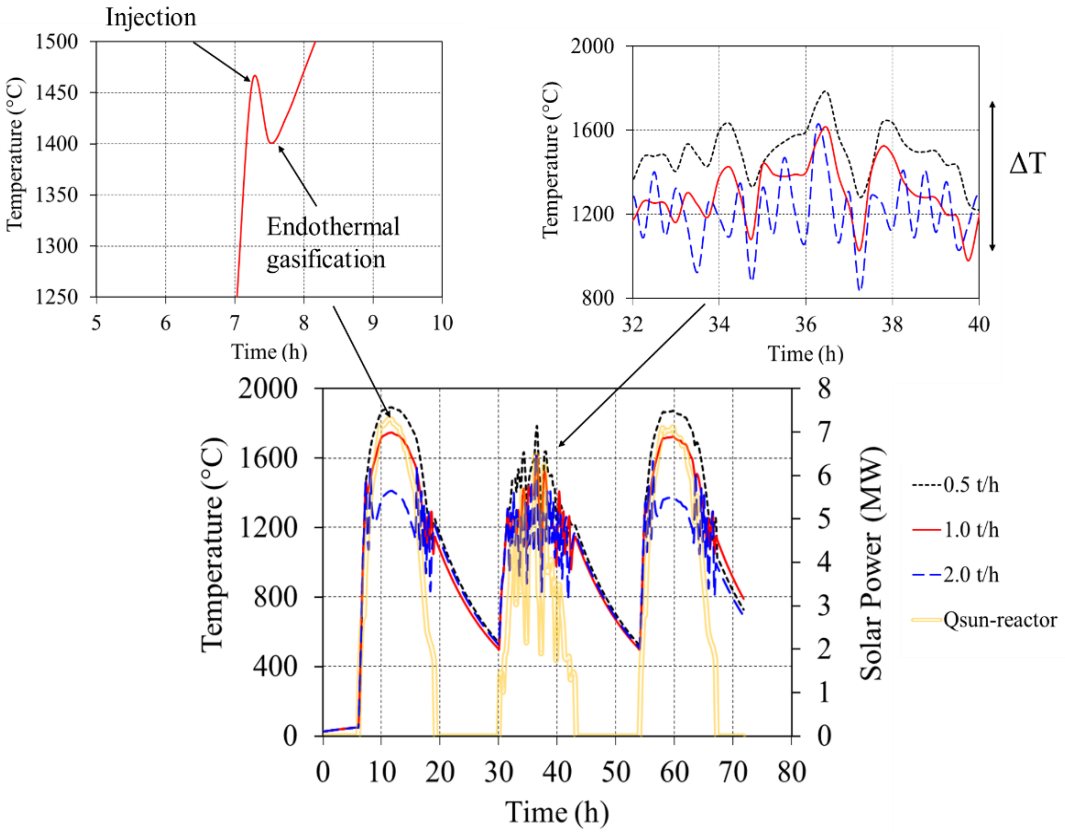

Figure IV.8 Received solar power in cavity and reactor temperature evolution for three biomass feeding rates (0.5 t/h, 1.0 t/h, 2.0 t/h)

The different cooling and heating phases of the reactor are clearly distinguished. The model predicts a duration for reactor heating in the morning between 1h (heating rate of 20°C/min) for days 1 and 3 and 1h30 (heating rate of 13°C.min^{-1}) for day 2. This duration is extremely dependent on the concentration ratio C, the DNI and the quality of the solar collection represented here by the optical efficiency ($\eta_{optical}$). It should be kept in mind that the reactor thermal inertia was exclusively represented by the reactor walls and reaction zone. Hence, this heating duration may be longer because it did not take into account the heating of other reactor components such as the piping and the insulation. Nevertheless, at first approximation, it can be observed that the choice of the nominal biomass flow rate has a strong influence on the reactor crest temperature (1889°C for 0.5t/h, 1752°C for 1.0t/h and 1405°C for 2.0t/h). The minimum achieved temperature during the cooling phase is around 500°C whatever the feeding rates. The second day of the simulation was very cloudy with high fluctuations in DNI, which lead to sharp temperature variations and frequent shutdown and starting up of the installation (Figure IV.9). While the lowest feeding rate (0.5 t/h) allowed converting continuously the biomass with very rare interruptions, the number of interruptions went up from 5 (at 1.0 t/h) to 16 (at 2.0 t/h) by increasing the biomass flow rate.

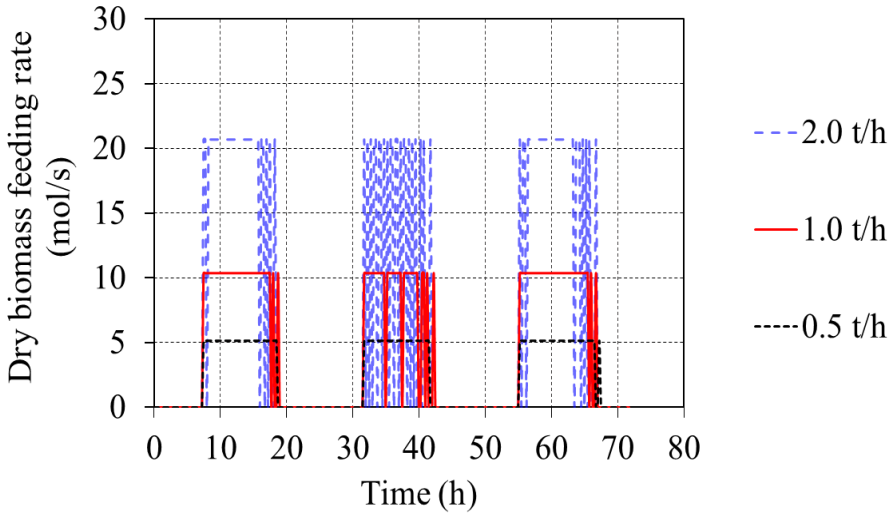

Figure IV.9 On/off control of the biomass-feeding rate

The time averaged SFE (integrated over the three days) attained by the 0.5 t/h, 1.0 t/h and 2.0 t/h is 40%, 59%, and 75% respectively. In fact, as the biomass feeding rate was increased (from 0.5 t/h to 2.0 t/h), the reactor temperature decreased due to the sensible heating of the reactants, the vaporization of the biomass moisture and the endothermal gasification reaction; therefore, the reactor thermal losses were lower and the SFE was greater. However, serious constraints regarding the stability of the process were observed with higher feeding rates.

Therefore, to make full use of solar energy, minimize the heat losses, thermally stabilize the reactor and guarantee a high syngas purity, an optimized control mode of the biomass and steam feeding rates was proposed.

IV.3.2.2 OPTI allothermal control mode (OPTImized)

In this mode, the lower and upper limits for biomass and steam injections were similar to that of the TOR mode values. The feeding flow rates were controlled in such a way that a temperature of 1200°C was maintained as long as possible. The process down time occurred when the biomass supply to maintain the reactor at 1200°C was less than 5% of the nominal flow rate (assumed here to be 1.0 t/h). The biomass feeding rate control was done by solving an optimization problem (Eq.IV.15). The biomass flow rate, $F_{biomass}$, was calculated in order to minimize the difference between the reactor temperature, T, and the setpoint temperature T_C. To achieve this optimization, the secant method was applied using the newton function of the Scipy library. The biomass and steam feeding rates were hence calculated to ensure a fixed temperature T_C=1200°C as depicted in Eq.IV.15.

$$T(F_{biomass}) = T_c \qquad IV.15$$

The achieved temperature during the three days for the OPTI and TOR operations is depicted in Figure IV.10.

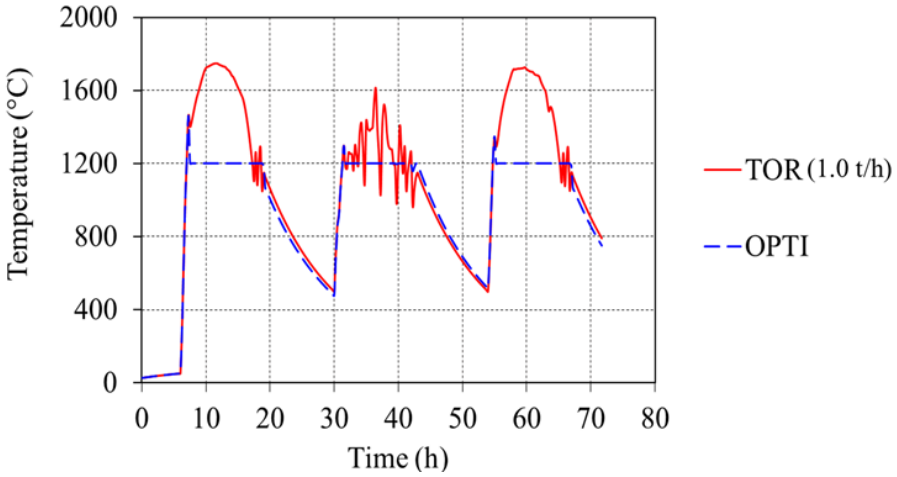

Figure IV.10 Temperature profiles for the TOR and OPTI control modes

The OPTI mode efficiently stabilized the reactor temperature at 1200°C avoiding any system sudden shut down and allowing a smooth and controlled variation of the biomass and steam flow rates. The OPTI scenario also avoided unnecessary reactor overheating that lowers the thermal losses. In addition, the observed sharp variations in temperature depicted in Figure IV.8 during the TOR allothermal operation were eliminated. The calculated dry biomass feeding rate is given in Figure IV.11-a, and the resulting H_2, CO and CO_2 production rates are depicted in Figure IV.11-b. Tars and light hydrocarbons content was negligible due to the high gasification temperature.

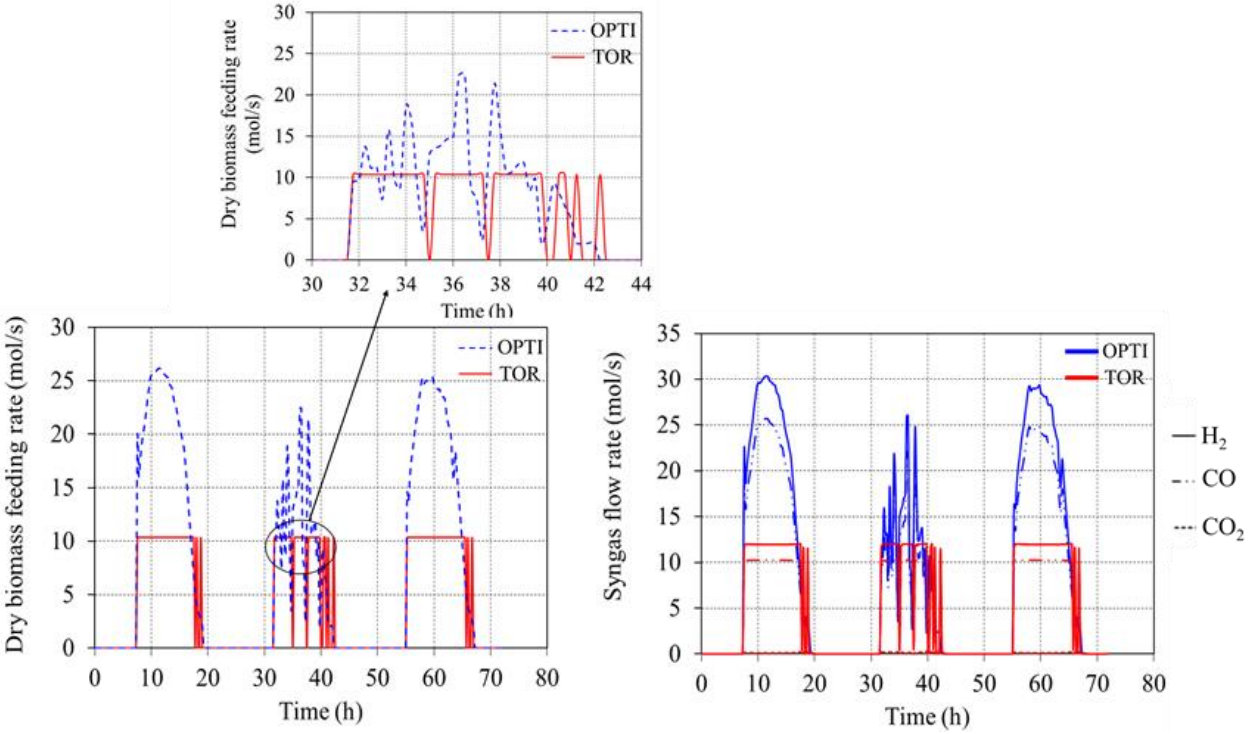

Figure IV.11 Biomass feeding rate and syngas yields for the TOR and OPTI models

The synthesis gas total production increased three-fold for the OPTI mode with a syngas composition that remained almost the same as for the TOR operation. The time-dependent SFE is plotted in Figure IV.12. The SFE increased progressively in the OPTI mode to reach a peak value of nearly 83% at midday when the solar power is at its maximum (i.e. maximum biomass

and steam feeding rates reached and maximum reactor productivity). The TOR mode showed a reverse pattern with at first a continuous decline of the SFE to barely 33% at noon and a consistent increase in the afternoon as the sun sets until shut down.

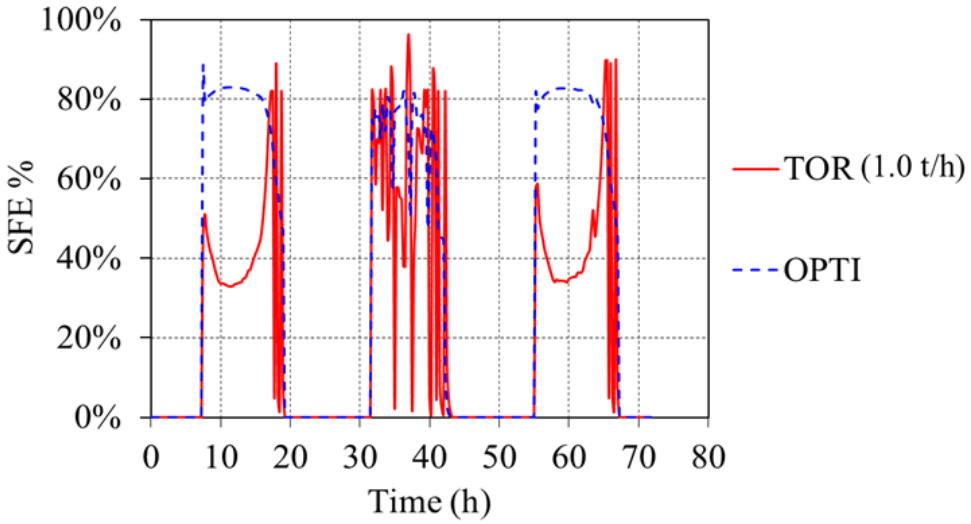

Figure IV.12 SFE for the TOR and OPTI control modes

During cloudy days, both OPTI and TOR modes showed difficulties to operate, thereby resulting in a marked drop in the production yield. To tackle this limitation and to warrant a consistent biomass conversion, process hybridization through combined solar heating and partial feedstock oxy-combustion was proposed. The technical feasibility of the hybrid solar/combustion process was first investigated on the small-scale reactor and O_2 injection during sun-lacking periods was successful to elevate the reactor temperature[10]. Following these first results, the HYB mode was used to counteract solar energy fluctuations for the large-scale reactor while enabling an optimized allothermal biomass conversion during sunny periods.

IV.3.2.3 HYB control mode (HYBridized)

This mode consisted in using OPTI mode when there was sufficient sunlight, otherwise a controlled injection of extra-biomass and pure stoichiometric oxygen was used for partial feedstock combustion to supply the reactor with the missing thermal energy. For studying the HYB mode, the minimum biomass flow rate aimed at being steam solar-gasified is 1.0 t/h. Hence, when the amount of solar energy was unable to steam gasify 1.0 t/h, an additional amount of biomass and stoichiometric pure oxygen was fed into the reactor to assist the solar heating. This way, the gasification temperature was maintained at 1200°C all the time. To minimize the energy losses, the top of the reactor was covered when radiative losses became equal to or higher than the entering solar power. To calculate the extra-biomass injection flow rate, a similar approach to that used in the OPTI mode was applied (Eq.IV.15). The difference was that instead of calculating the biomass flow rate for gasification, it corresponded to the extra-injection of biomass. The resulting temperature profile is plotted in Figure IV.13.

[10] cf. Chapter 2

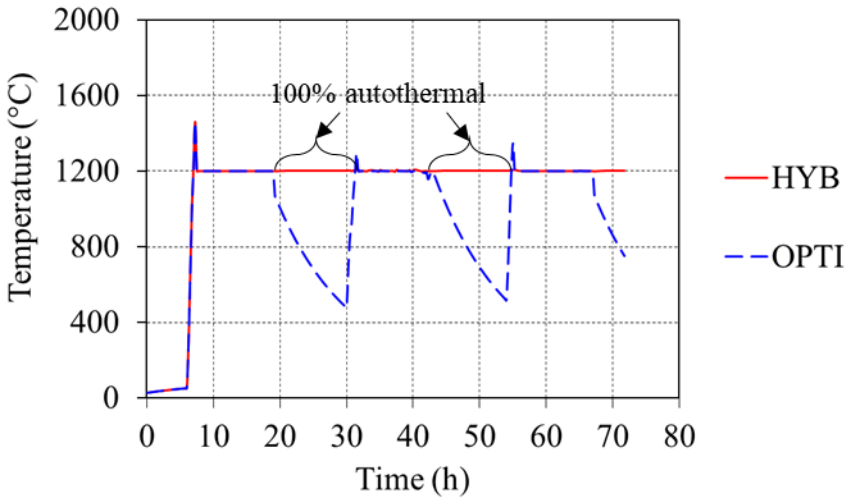

Figure IV.13 Temperature evolution profiles for the OPTI and HYB control modes

It can be seen that transient periods and temperature drops due to cooling at night were eliminated by gradually switching to a full autothermal mode. A constant and stable temperature was this way achieved. Figure IV.14-a shows the biomass, steam and oxygen inlet flow rates and Figure IV.14-b shows the main syngas production rates as a function of time. Oxygen injection took place only at the end of the day for days 1 and 3. The maximum percentage of dry biomass combusted was around 40% to operate the reactor in full autothermal mode (Figure IV.14-c, % of burnt biomass). Accordingly, a SFE (i.e. Cold Gas Efficiency since $Q_{sun \rightarrow reactor}$ = 0 W) of 80% was calculated during the autothermal operation (Figure IV.14-c, SFE), which is in the range of the reported values for conventional autothermal steam gasifiers (Khosasaeng and Suntivarakorn, 2017; Materazzi et al., 2016; Valin et al., 2019). For the second day, oxygen was injected almost all the time due to the low solar input (cloudy day). A considerable gain was achieved in terms of syngas yield as compared to the OPTI mode. Indeed, the total amounts of H_2 and CO were respectively 2281 kmol and 1929 kmol in the OPTI mode; they increased by 52% and 82% in the HYB mode to reach 3462 kmol of H_2 and 3516 kmol of CO. Nonetheless, the syngas composition was significantly impaired. The H_2:CO ratio dropped from 1.2 during the solar-only operation to 0.8 in the 100% autothermal mode (Figure IV.14-c, H_2:CO). The CO_2 production rate also increased notably in the hybrid process from around 0.5 mol.s^{-1} (at peak production capacity) during the solar-only operation to 6 mol.s^{-1} at night.

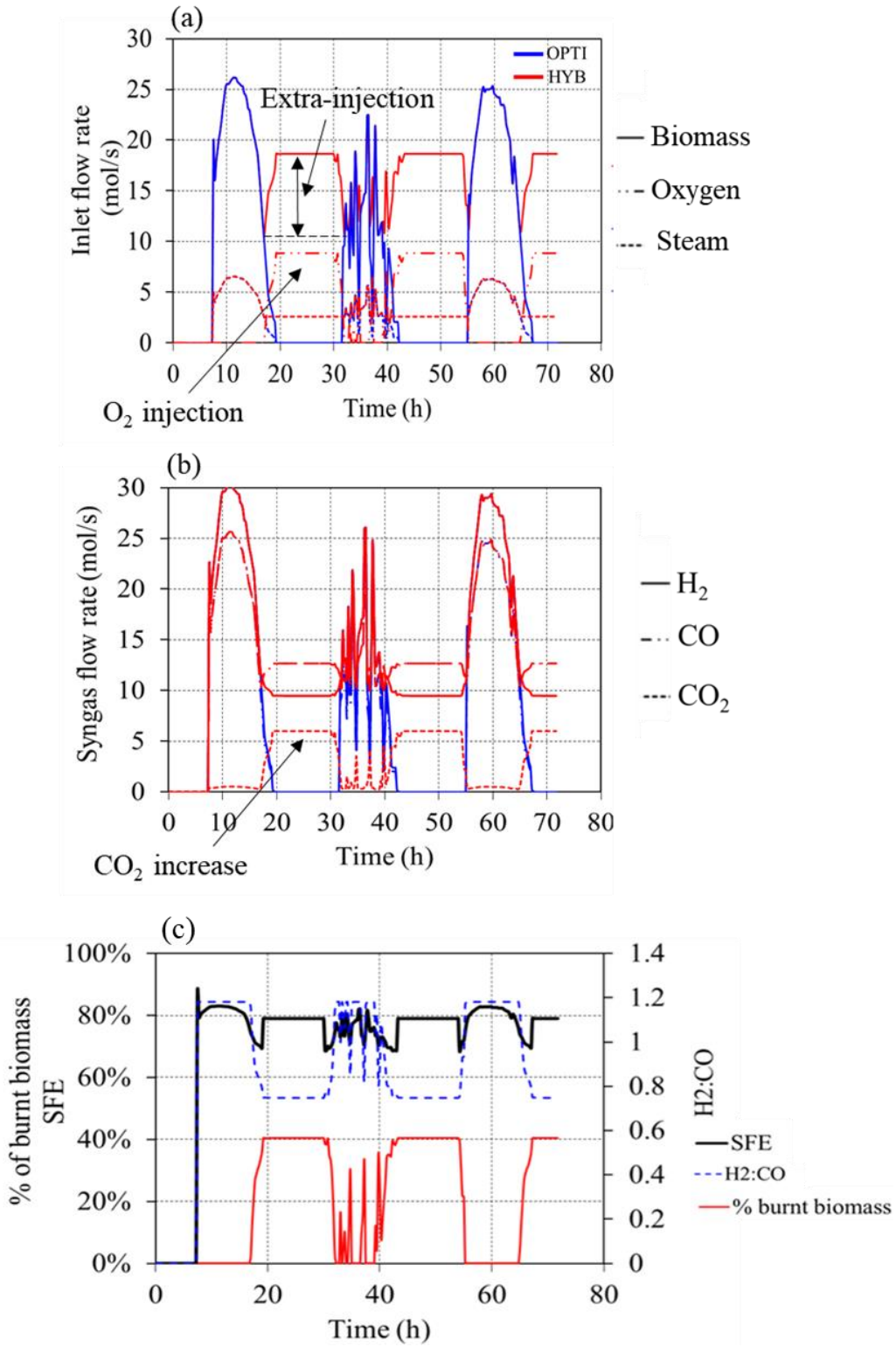

Figure IV.14 (a) Inlet flow rates OPTI vs. HYB; (b) Syngas production rates OPTI vs. HYB; (c) SFE, H_2:CO and % of burnt biomass for the HYB mode

IV.3.3 Annual simulation

In this part, the dynamic model was used to predict the annual gas production and reactants consumption using the OPTI and HYB control modes. The monthly available solar energy ($E_{sun \rightarrow field}$: collected by the field) and the one received by the reactor ($E_{sun \rightarrow reactor}$) are plotted in

Figure IV.15. The ratio $E_{sun \rightarrow reactor}$/ $E_{sun \rightarrow field}$ represents the optical losses caused by the optical matrix and the beam down. Its value varied during the year and reached a maximum of 60% in the summer against about 45-49% in November, December and January. June, August and September were clearly the best-insolated months in the year, showing notably higher energy inputs. The annual simulations were performed with a time step of 15 min.

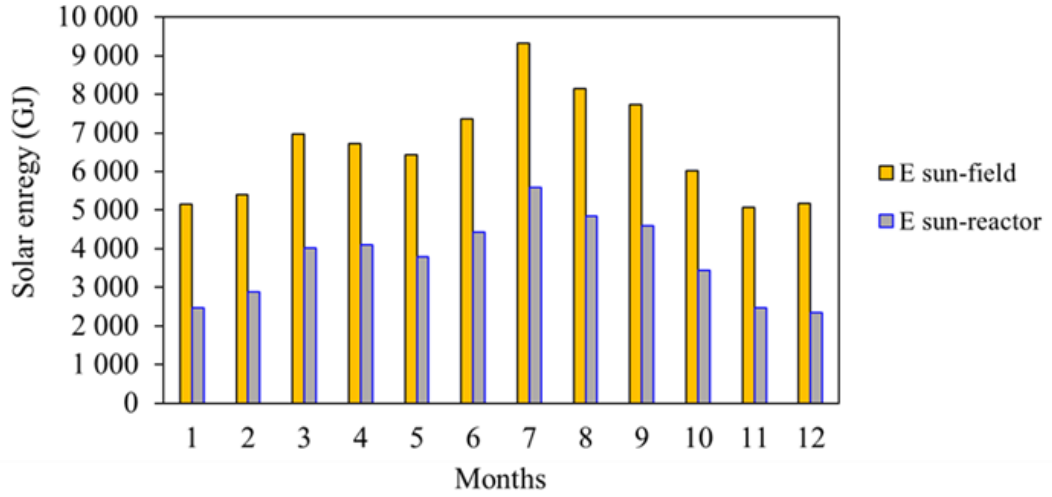

Figure IV.15 Solar energy per month as provided by the Meteonorm© software vs. the solar energy received by the reactor after collection and concentration

Annual simulations were performed assuming a reactor shutdown and restart at the beginning of each month. Figure IV.16 shows the predicted biomass/water/oxygen consumption and gas production yields. In the OPTI mode, the H_2:CO ratio remained constant at 1.2 throughout the year as the gasification occurred exclusively at 1200°C. Moreover, the production was noticeably higher during the summer especially in July, which is due to greater DNI values and longer days. In the hybrid mode, the production of CO was higher than that of H_2. The H_2:CO ratio was lower during the winter approaching 0.8 in December. It increased to 0.9 in July. The HYB mode showed remarkably higher syngas yields (H_2+CO) of 765.8 10^6 moles against 255.9 10^6 moles in the allothermal process. CO_2 represented a significant fraction of syngas reaching up to 16% in the hybrid mode whereas it remained almost negligible (i.e. <0.9%) in OPTI mode. Furthermore, in the allothermal configuration, the gas production capacity throughout the year more than doubled from December to July due to the seasonal variability of solar energy. Hybridization homogenized this trend and showed a production capacity variation of only 6%. The difference between the two processes was also noteworthy with regard to the biomass consumption that increased from 2954 $t_{dry\ biomass}$/year (in the allothermal process) to 13 390 $t_{dry\ biomass}$/year (in the hybrid process). Assuming that all the gas is upgraded into hydrogen, the average daily hydrogen production is equal to 1402.0 kg_{H_2}/day in the allothermal mode and twice higher, i.e 4196.1 kg_{H_2}/day, in the hybrid mode. The round the clock operation of the reactor in the hybrid mode required the combustion of nearly 34% of the biomass feedstock (on dry basis) with an oxygen consumption of 6309 t/year. In practice, the oxygen requirement can be supplied by either an ASU (Air Separation Unit), at the expense of a great investment representing around 15-16% of the total capital cost of autothermal gasification facilities (Adams and Barton, 2011; Kaniyal et al., 2013; Saw et al., 2015), or directly provided by air as a reactant for the combustion reaction. This however may affect to a certain degree the quality

of syngas and the thermal efficiency of the process, and may require a downstream gas separation unit.

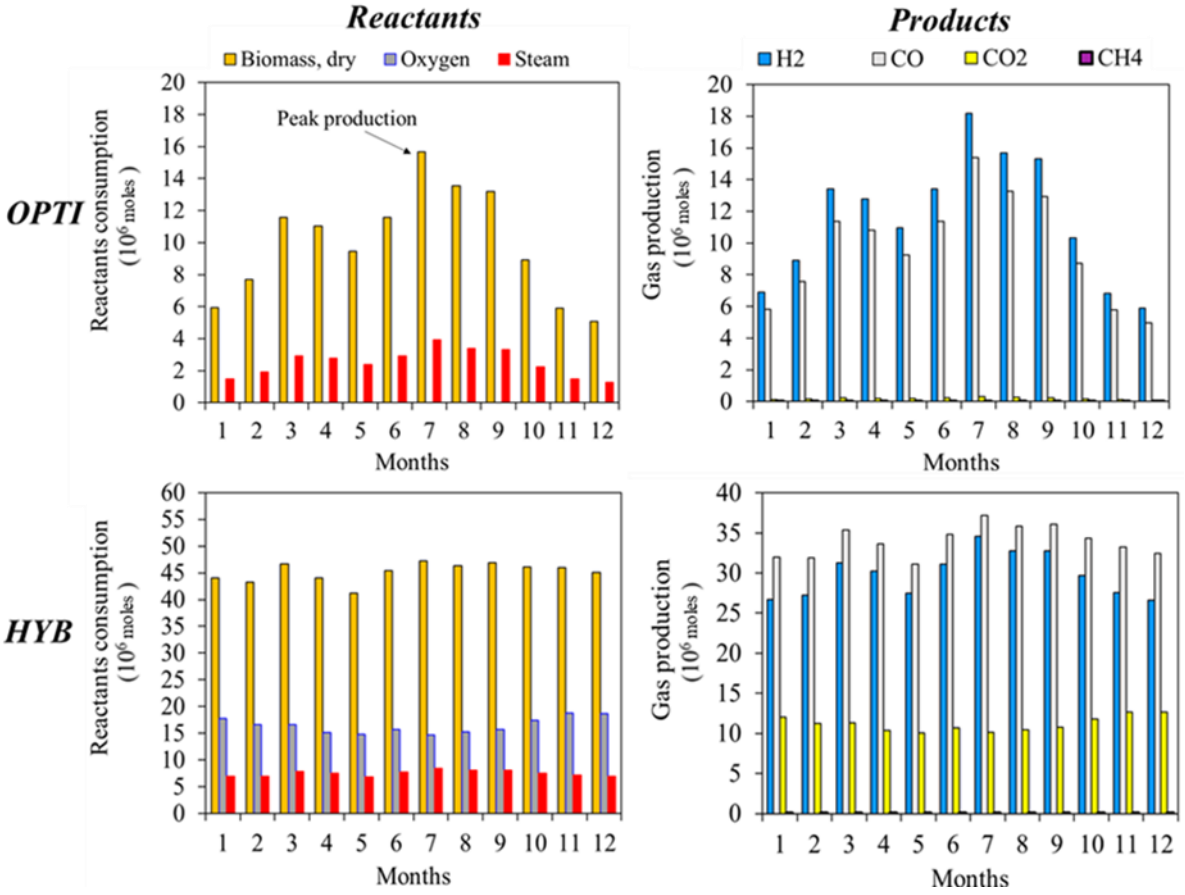

Figure IV.16 Monthly gas yield and biomass/water/oxygen consumption (OPTI vs. HYB)

CO_2 emissions due to the reaction are drastically lowered in the allothermal mode, reaching barely 101 t/year against 5409 t/year in the hybrid mode. This leads to average emission rates of 34 g CO_2/kg of dry biomass in the allothermal mode and 440 g CO_2/kg of dry biomass in the hybrid mode. An autothermal process that continuously converts 1 t/h of dry feedstock (in which 60% is steam gasified and 40% is burnt) would generate 61% more CO_2 than the hybrid process, yielding an emission rate of up to 710 g CO_2/kg of dry biomass. This strongly outlines the interest of process solarization for a drastic and effective reduction of CO_2 emissions, especially when the feedstock is not renewable e.g. waste, plastics, coal, etc.

To deepen the analysis, the reactor energy balance breakdown was studied. To do so, Eq.IV.16 was integrated over the year (Eqs.IV.16-IV.17).

$$\oint \frac{dE}{dt} dt = 0 = \oint \{\sum_{i=1}^{NC} F_i^e h_i(25°C) - \sum_{i=1}^{NC} F_i^s h_i(T)\} dt + \oint Q_{net} dt \qquad \textit{IV.16}$$

$$\oint Q_{net}\, dt = E_{sun \rightarrow reactor} - E_{rad,aperture} - E_{rad,cap} - E_{cond,insulation} \qquad \textit{IV.17}$$

Figure IV.17 shows the predicted energy breakdown distribution in the allothermal and hybrid configurations.

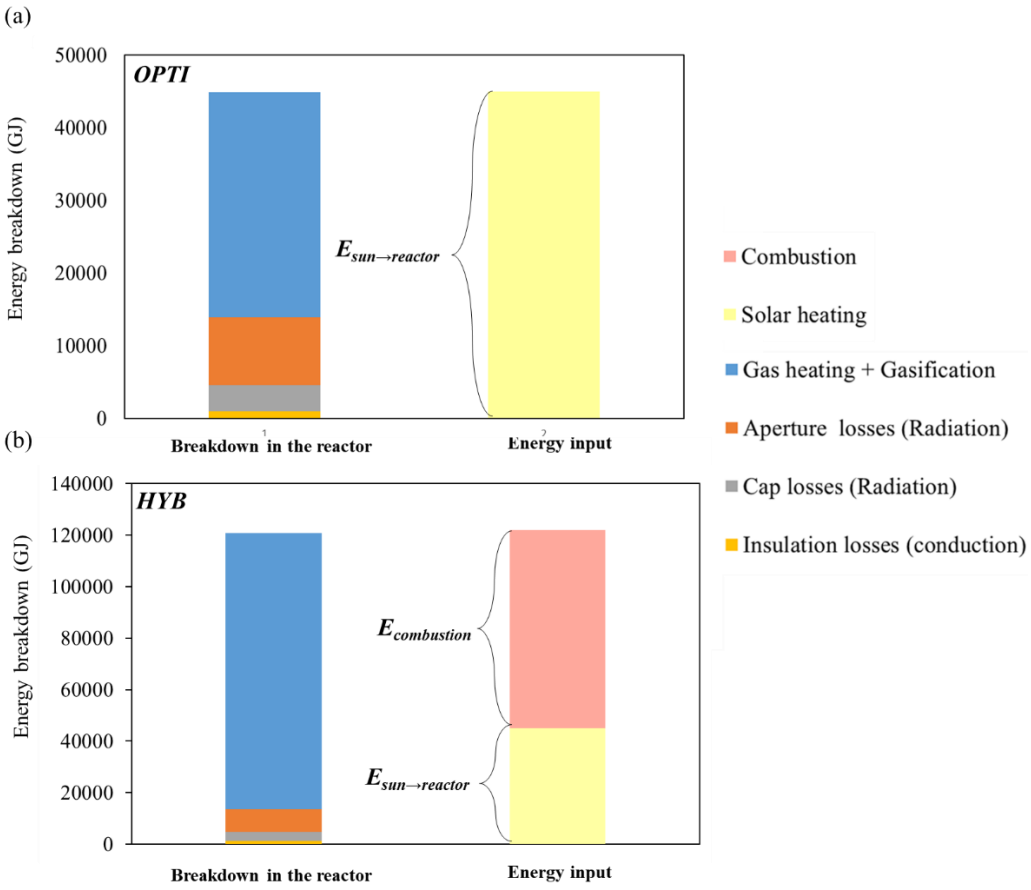

Figure IV.17 Yearly energy breakdown distribution over the reactor components

It can be seen that in both cases, the largest share of the energy input (including solar and combustion) went into the reaction, yielding a thermal efficiency ($E_{heating+gasification}/E_{input}$) of 68% in the allothermal process and of 88% in the hybrid process. The thermal efficiency in the hybrid mode was higher as it drastically reduced the energy losses, especially during autothermal phases thanks to the covering of the reactor top (i.e. no re-radiation losses). Overall, the losses through the cavity aperture were the greatest and contributed to around 66% of the total losses in the two configurations. Additionally, a major heat sink in the allothermal mode was caused by the cooling at night and the heating every morning to restart the process. Equally, in many days of the year (e.g. 9-10 of January, 1-2 of May, and 29-30 of June) the reactor could not reach the biomass injection temperature and therefore all the solar input was dissipated to the environment. The fraction of solar energy received during the periods in which biomass was not injected (i.e. solar energy not used for driving the reaction) was estimated at 14% in the allothermal process. The proportion of solar energy lost in the HYB mode was significantly lower and was estimated at 6% after covering the top of the reactor at the end of each day. Accordingly, a better use of the solar resource was achieved by the hybrid process as the reactor was maintained at 1200°C throughout the year thanks to partial feedstock combustion. This prevented the reactor from any heat losses during cooling and heating phases, which highlights an additional key advantage of process hybridization. However, as can be seen in Figure IV.17-b, this was achieved at the expense of a great supply of energy through combustion by up to 63% of the energy input share. Accordingly, the annual CGE reached 1.38 in the allothermal mode and it decreased to 0.93 in the hybrid mode.

IV.4 Conclusion

Large-scale solar gasification was studied using dynamic process modelling. The study showed the importance of biomass and oxidants flow rates real time monitoring and dynamic control to achieve high productivity and better use of solar energy. Accordingly, three feeding management strategies (TOR, OPTI and HYB) were proposed and discussed. The following conclusions were drawn:

- The TOR mode gasified a constant mass flow rate of biomass when the reactor temperature was above a fixed setpoint value. This mode suffered from significant heat losses due to reactor overheating and large temperature variations. The latter should be alleviated as they may potentially damage the reactor materials.

- The OPTI mode was then considered to overcome TOR issues by stabilizing the reactor temperature at a setpoint value, which reduced considerably the heat losses, while limiting the reactor overheating and increasing the syngas yield. However, both TOR and OPTI modes showed a considerable drop in syngas production during cloudy days and nocturnal hours.

- The HYB mode coupled the OPTI control during sunny periods with a smart injection of biomass and oxygen for partial feedstock combustion to supply the reactor with the deficient process heat during cloudy or night periods. This allowed to counteract sharp DNI variations and ensured a minimum continuous production of H_2 and CO during blackout periods. The gradual addition of oxygen to the system impaired the syngas composition by reducing the H_2:CO ratio and by increasing the CO_2 content.

- The varying syngas composition (especially during hybrid operation) can lead to complications in the gas purification and downstream chemical conversion processes of the produced syngas. Thus, the composition should be adjusted and levelled throughout the operation. To achieve an optimal and stable H_2:CO ratio, a permanent and dynamic coupling of the solar gasification reactor with other hydrogen production processes such as electrolysis and steam methane reforming may be relevant. Another alternative to upgrade the syngas is the utilization of a Water-Gas Shift (WGS) reactor that can dynamically fix the syngas composition to a setpoint value (Meerman et al., 2012). The use of a buffer storage of upgraded syngas and oxygen would smooth the sharp variation of gas flows and facilitate the control of the whole process chain. Very little theoretical and empirical results are available in this field and the dynamic coupling between the different unit operations is still in its infancy.

- The dynamic control of these solar reactors appears to be feasible and the development of intelligent algorithms plays a key role to cope with solar energy fluctuations. Short-term forecasts and accurate forecasts of DNI are vital to correctly apprehend the highly variable solar flux, which constitutes an additional challenge that still needs to be addressed.

- Annual simulations confirmed the interest in hybridization to increase the reactor productivity. The total volume of H_2+CO produced by the hybrid process was 3 times greater than that of the allothermal process but required 4.5 more biomass. The thermal efficiency in the hybrid mode was higher and could reach 88% against 68% in the optimized allothermal mode. The CGE in the hybrid mode was however impaired with a value of 93% against 138% in the allothermal mode.

V.CHAPTER 5

Large-scale hydrogen production from solar-driven steam gasification of biomass: a techno-economic study

V.1 Introduction

Today, around 96% of hydrogen is generated from fossil fuels (78% from natural gas and liquid hydrocarbons and 18% from coal) and only a low proportion of 4% is generated from water electrolysis (IHS Markit, 2018.). In industry, hydrogen is mostly generated using carbon-based CO_2 emitting methods such as steam reforming of light hydrocarbons, partial oxidation (POX) and autothermal reforming (AR) (which is a combination of the two previous processes) followed by coal gasification. Even though being extremely dependent on the price of natural gas, steam reforming remains the most preferred pathway for H_2 production given that it reached a high state of maturity outlined by lower production costs usually below 2$/kg of H_2 including CO_2 capture and sequestration (Safari and Dincer, 2020; Ursua et al., 2012).

Currently, the largest volumes of hydrogen produced or commercially available are consumed in the chemical industry with a share of 63% for the production of ammonia, methanol, polymers and resins industries. Refineries are the second largest hydrogen consumers with a share of more than 30% mainly for hydrocracking and crude oil hydrotreatment. Metallurgical industry consumes around 6% of the share. It is followed by general industries such as semiconductor, glass production, hydrogenation of fates, etc. with a minor share of 1% (Fraile al., 2015).

Hydrogen, used as an intermediate chemical species for the above-mentioned processes, is also seen today as a promising zero-carbon footprint energy vector for massive storage of intermittent renewable energies. Clean, i.e. CO_2-neutral hydrogen, can be produced using biomass or/and water as primary feedstocks. The most mature methods for decarbonized H_2 production are water electrolysis and steam biomass gasification (IEA Bioenergy, 2018). Powered by a renewable energy source such as solar or wind, electrolysis consists in using an electrical current to split water electrochemically into separate streams of H_2 and O_2. Being commercially available for over a century, current commercial electrolysers reach single-stack/module capacities of several megawatts with conversion efficiencies up to 85% (Schmidt et al., 2017). Biomass gasification takes advantages from the extensive accumulated experience of fossil fuels thermochemical gasification, which represents the state of the art for industrial scale H_2 generation. Biomass steam gasification produces a synthesis gas composed of both H_2 and CO at high temperature (>900°C). The syngas therefore needs to be upgraded (shifted to hydrogen) and purified in downstream equipment. According to the IEA Bioenergy's report in 2018 (IEA Bioenergy, 2018), hydrogen production from biomass as a complementary route to increase the share of renewables cannot be accomplished without the full process chain validation at large scale, involving an optimal biomass gasification technology capable of treating and converting a wide range of feedstocks.

Considering the growing demand of biomass in the future, the optimization of the conversion systems to make the best use of biomass is an absolute necessity. A promising way to save the biomass resource while maximizing the yield, the quality and the purity of the synthesis gas consists in using concentrated sunlight as an external source of energy to drive the endothermal thermochemical reactions instead of continually burning a part of the feedstock. The solar process viability for coal and biomass gasification has been thoroughly studied in the last few years and was validated in several research papers and EU projects at both laboratory and pilot

scales (Puig-Arnavat et al., 2013; Taylor et al., 1983b; Zacarías et al., 2010; Z'Graggen et al., 2006). Accordingly, the extrapolation of these solar technologies to larger scales for semi-central or centralized green solar hydrogen production is auspicious in the future in view of the increasing decarbonized hydrogen demand. Although being more environmentally friendly by definition than the conventional autothermal biomass gasification process, the question of the solar process economic feasibility and competitiveness arises. On the one hand, the solar process allows producing a high quality synthesis gas with a higher gas output per unit of feedstock, and on the other hand, the solar process is highly dependent on an intermittent heat source, which requires an initial substantial investment. The question is therefore not simple and requires detailed investigation to highlight both technical aspects related to the management of the heat source variability, and also economic and financial aspects for accurate cost evaluation. In Chapter 4, a dynamic mathematical model of an up-scaled MW solar gasifier was developed. The model was used to assess the transient behavior of the reactor during three successive days with and without cloud cover. Different reactants feeding management strategies were proposed and compared with the aim of achieving enhanced syngas productivity and optimized use of solar energy. The OPTI mode controlled the supplies (biomass and steam) in order to stabilize the reactor temperature around a set point value (assumed to be 1200°C) as long as possible. The HYB production mode used the OPTI mode when the solar irradiation was sufficiently high to gasify a minimum biomass flow rate (e.g. 1t/h). Otherwise, the solar heating was assisted by in-situ injection of O_2 to counteract the solar power decline and to maintain the reactor temperature constant all day long. Annual data were thereafter generated and analyzed to evaluate the behavior of the reactor throughout the year, and estimate feedstock consumption and syngas productivity for real solar irradiation conditions.

In this chapter, and to conclude the work, a techno-economic study was carried out using the dynamic model predictions regarding the yearly gas production with the two recalled control strategies (OPTI and HYB). H_2 cost at plant gate for the autothermal (non-solar), hybrid (solar/optimized-combustion) and allothermal (solar-only) processes operating at different design capacities is evaluated using the DOE's H2A tool for hydrogen cost analysis (NREL H2A, 2018). Furthermore, a sensitivity study is performed to figure out the impact of different factors on the cost of hydrogen. Finally, the cost of hydrogen is compared with other solar and non-solar processes for H_2 generation.

V.2 Solar hydrogen cost model

V.2.1 General principle

The DOE's H2A tool used in this study is based on the Discounted Cash Flow (DCF) rate of return method. DCF analysis finds the present value of expected future cash flows using a discount rate. The Internal Rate of Return (IRR) is the discount rate that cancels the Net Present Value (NPV). The NPV calculation (Eq.V.1) converts all the expected future cash flows of a project into their 'present value', i.e. their value at the initial time, at the very beginning of the project. Then, all the present values are added together to characterize the overall value of the company's project, in other words, the profitability of the project. The NPV is the cash flow generated at the end of the project.

$$NPV = -I + \sum_{p=1}^{p=N} \frac{F_p}{(1+i)^p} \quad V.1$$

with I, the investment, F_p, the cash flow for year p, N, the total duration of the project (years), 'i', the discount rate (it reflects the cost of capital, so it may take the value of the market interest rate for a comparable duration even though this value is often discussed). In the DOE's tool, 'i' is fixed and the model calculates the minimum hydrogen price such that the NPV cancels.

The starting point is a reference conventional (non-solar) biomass gasification process previously developed by Mann & Steward from the NREL (Spath et al., 2005). The minimum cost of hydrogen was calculated with an indirectly-heated steam woody biomass gasifier (based on a dual fluidized bed technology). The process model included biomass treatment and injection units, the reactor, gas compressors and scrubbing units followed by a steam methane reformer (SMR), water gas shift reactors (WGS) and a Pressure Swing Absorption (PSA) unit to reach hydrogen purity above 99.9%. Hydrogen was thereafter compressed to 70 bar prior to shipment through a pipeline. In order to minimize the plant water consumption, the water contained in the syngas was recovered at different points of the cycle. Moreover, part of the electricity needed by the chemical plant was generated by recovering heat from the high temperature syngas. A heat-recovery system using a steam turbine and a generator was therefore coupled to the chemical units. More details about the energy/materials inflows and outflows can be found in (Spath et al., 2005). The solarization of such chemical process impacts a number of factors including the capital investment, the O&M costs, and the plant biomass, water and electricity consumptions. These factors were estimated and integrated to the previously developed cost model using the dynamic simulation results (for yearly productivity estimation) as well as previously reported CST (Concentrated Solar Tower) plants running costs.

V.2.2 Model assumptions

V.2.2.1 Basic flow diagram

The solar powered chemical process was modeled using the real solar data (averaged over a 19-year period: 1991-2010) of Odeillo, in the Pyrénées-Orientales department in France. This region is characterized by a high duration and quality of sunshine (more than 2500 h/year) with a great purity of atmosphere. The basic process flow diagram is described in Figure V.1. It consisted of a solar plant composed of a heliostat field and reflecting towers (beam down technology), and of a chemical plant for biomass gasification and gas processing/purification. The gasifier was fed by both steam and air. Air injection was considered only when operating in full autothermal or in hybrid (solar-combustion) modes. In the model, gas cleaning and upgrading chemical units (such as WGS, and PSA) were assumed to be able to withstand rapid changes in gas flows and composition.

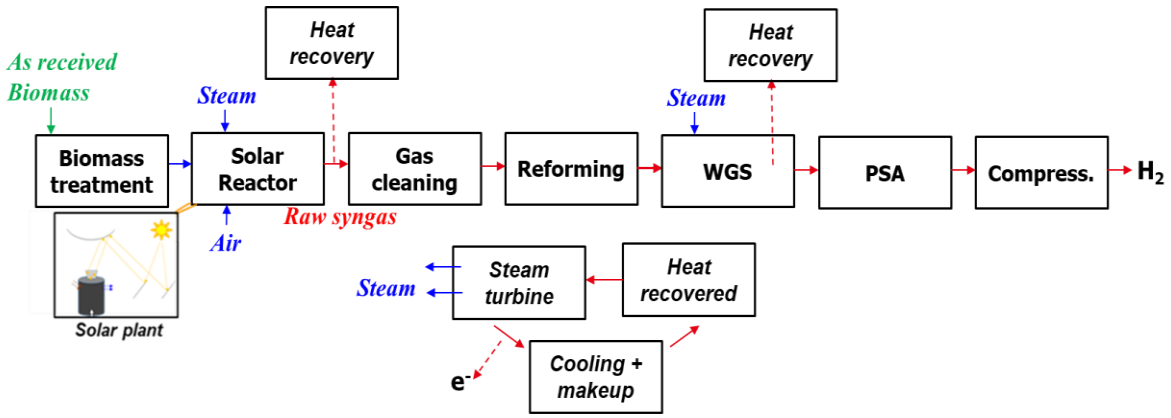

Figure V.1 Biomass solar gasification flow diagram

V.2.2 Capital costs

V.2.2.1 Direct capital costs

The major chemical components costs (installed) at the chemical baseline (defined by a design capacity *DC* of 155 236 kg of H_2 per day) are presented in Table V.1.

These costs were scaled to different design points using Eq.V.2.

$$Component'i'cost_{at\ DC} = Component_{\ at\ chemical\_baseline}\ \ cost.\frac{DC}{Chemical\_baseline\ DC}^{n_{chemical}} \qquad V.2$$

With $n_{chemical}$ = 0.78 (Spath et al., 2005) and DC in kg of H_2/day.

Table V.1 Direct capital costs at chemical baseline (installed, to be scaled)	M€
Feed Handling & Drying	24.57
Gasification, Tar Reforming, & Quench	21.84
Compression & Sulfur Removal	20.28
Steam Methane Reforming, Shift, and PSA	39.39
Steam System and Power Generation	18.72
Cooling Water and Other Utilities	4.42
Buildings & Structures	19.26

The heliostat field cost at *DC* was calculated by Eq.V.3.

$$Heliost\ cost_{at\ DC} = Mirror\ reference\ cost.\ field\ surface_{\ at\ DC} \qquad V.3$$

$$field\ surface_{\ at\ DC} = field\ surface_{\ at\ solar\_baseline}.\frac{DC}{Solar\_baseline_{OPTI,HYB\ DC}} \qquad V.4$$

The mirror reference cost in €/m^2 was assumed equal to 120 €/m^2 based on (SANDIA REPORT, 2007). The solar baseline was defined by a thermal power input on the solar field of 10 MW_{th} (at a DNI of 1000 W/m^2). Thus, the Solar_baseline OPTI, HYB DCs was directly deduced from the previously developed dynamic model[11]. It was estimated at 1402.0 kg H_2/day for the OPTI

[11] cf. Chapter 4

mode and 4196.1 kg H_2/day for the HYB mode. The field surface at solar_baseline was calculated by Eq.V.5.

$$field\ surface_{at\ solar\_baseline} = \frac{Q_{sun \rightarrow field,max}}{DNI_{max}} \quad V.5$$

With $Q_{sun \rightarrow field,max}$=10 MW and DNI_{max}=1000W/m². The tower cost at *DC* was calculated by Eq.V.6.

$$Towers\ cost_{at\ DC} = Tower_{at\ solar\_baseline}\ cost\ . \frac{DC}{Solar\_baseline_{OPTI,HYB\ DC}} \quad V.6$$

As tower costs in the literature are often expressed in € per MWe, *Tower cost* $_{at\ solar\_baseline}$ was deduced from Eq.V.7 assuming a solar-to-electric efficiency $\eta_{solar\text{-}to\text{-}electric}$ of 30% (NREL REPORT, 2012) including the receiver thermal efficiency and a field efficiency η_{field} of 70% (Sudiro and Bertucco, 2007).

$$Tower_{at\ solar\_baseline}\ cost\ = Tower\ cost\ (€/10\ MW_e).(\eta_{opt,field} \cdot \eta_{solar-to-electric}) \quad V.7$$

Tower cost per 10 MW_e was considered equal to 2M€ based on the data provided by Chavez et al. (Chavez et al., 1993) in the Ecostar roadmap.

V.2.2.2.2 Indirect depreciable capital costs

The site preparation, engineering & design, project contingency and up-front permitting costs were calculated by applying a percentage to the sum of the direct capital costs of the overall plant (solar and chemical). These percentages were respectively 2%, 10%, 15%, 15%.

V.2.2.2.3 Non-depreciable capital costs

The cost of land, which can greatly vary depending on the plant's location, was varied from 0.5 €/m² to 50 €/m². A typical serviced land in Odeillo costs up to 150 €/m² while a bare land in rural regions costs only few cents to few euros per m². Eq.V.8 was used to estimate the plant land cost.

$$Land\ cost\ = Chemical\ plant\ land\ cost\ + Solar\ plant\ land\ cost \quad V.8$$

The chemical plant land cost was calculated by Eq.V.9.

$$Chem.land\ cost\ = land\ cost\ per\ m^2 . \frac{DC}{Chemical\_baseline\ DC}^{0.78} . Chem.land\ required_{Chemical\_baseline} \quad V.9$$

Where the chemical plant land required at baseline design capacity was assumed equal to 20.2 hectares. The solar land cost was calculated by Eq.V.10.

$$Sol.land\ cost\ = Cost\ of\ land(€).Solar\ field\ size_{at\ DC} \quad V.10$$

The solar field size at design capacity was considered seven times greater than the heliostat field (Eq.V.4) according to the PS10 plant data in Spain (https://solarpaces.nrel.gov/planta-solar-10).

V.2.2.3 Fixed costs

The total plant staff was calculated by Eq.V.11.

$$Plant\ staff = Chemical\ plant\ staff + Solar\ plant\ staff \quad V.11$$

$$Chemical\ plant\ staff = Baseline\ cap.staff . \frac{DC\ (kg\ H_2/day)}{Chemical\_baseline\ DC\ (kg\ H_2/day)}^{0.25} \quad V.12$$

The staff at baseline capacity was considered equal to 54. The CST plant associated one operator for each 6.25 hectares of mirrors, following the equation provided by Sargent & Lundy (Sargent & Lundy, 2003). The total plant staffing cost was thus deduced assuming a burdened labor cost of 54 €/man.hr. The general and administrative expenses were estimated as 20% of the total plant staffing cost. The property taxes and insurance were assumed equal to 2% of the total capital costs, and the materials maintenance costs and repairs were assumed equal to 0.5% of the project direct capital costs.

V.2.2.4 Utilities, feedstock and variable costs

V.2.2.4.1 Water

Water was used for different purposes beyond its main role as a biomass oxidizer. Water was used to clean (by removing impurities such as particulates and tars residuals) and to shift the syngas into hydrogen. An important amount of water was also used for the cooling of syngas at the exit of the gasification unit and after the last stages of compression. It was also substantially used for heat rejection in the condenser and as a makeup for the steam cycle. Design calculations allowed estimating the process water consumption at about 3.8 L/kg of H_2. The cooling water consumption was considerably higher around 300.0 L/kg of H_2 (Spath et al., 2005). Additional washing water was required for the solar powered chemical plant due to the periodic cleaning of the mirrors. Considering a washing water consumption V_{water} of the heliostat field of 18 $L/MWh_{th,on\ field}$ (Bracken et al., 2015), the amount of required water per kg of H_2 was deduced from Eq.V.13. The total cost of water was hence calculated by Eq.V.14.

$$Washing\ water\ = V_{water} \cdot \frac{Q_{sun \rightarrow field,max}}{Solar\_baseline_{OPTI,HYB}\ DC} \qquad V.13$$

$$Cost\ of\ water\ = (Washing\ + Process\ water).\ C2 + Cooling\ water.C3 \qquad V.14$$

With C2=0.61€/m^3 and C3=0.03€/m^3.

V.2.2.4.2 Electricity

The different chemical plant sections consumed electricity to different extents. Compression of syngas was the most energy-demanding step in the process, representing up to 60% of the total electricity requirement. The heat recovery system allowed generating most of the power. The deficit in electricity was therefore directly supplied by the grid. In conventional CST plants, the electrical requirement comprises the HTF (Heat Transfer Fluid) pumping along with the electricity used for tracking the solar rays, which remains very low. As there is no HTF in the proposed solar gasification concept, and as the energy of the tracking is of minor significance (Hinkley et al., 2013), the electricity requirement of the solar plant was neglected. The overall process electricity requirement (supplied by the grid) was estimated in the previous cost model (Spath et al., 2005) at 0.98 kWh_e/kg of H_2 with a cost of electricity of 0.1 €/kWh.

V.2.2.4.3 Biomass

Biomass consumption varies depending on how the gasifier is heated. In solar gasification, the available solar energy is collected, then concentrated by a field of mirrors and towers to ensure the complete and total conversion of the biomass load. In purely autothermal mode, the reactor is heated solely by burning part of the feedstock. In the hybrid mode, the biomass is partially burned, but in a lesser extent than in pure autothermal mode. The prediction of the biomass

consumption (expressed in $kg_{biomass,\ dry}$/kg of H_2) for the three modes, OPTI, HYB and autothermal, was done based on the annual simulations. The biomass consumption of the three modes (OPTI, HYB, autothermal) used in the economic analysis are respectively, 5.8, 8.7, and 9.7 $kg_{biomass,\ dry}$/ kg_{H_2}.

V.2.2.4.4 Other costs

Other costs include catalysts and bed materials, environmental surcharges, waste treatment and solid waste disposal. These costs are recalled in Table V.2 at the chemical baseline design capacity.

Table V.2 Other variable operating costs	M€
Other materials	7.00
Waste treatment	1.20
Solid waste disposal	0.73
Environmental surcharges	0.13

The scaling to different design capacities followed Eq.V.14 (Spath et al., 2005).

$$Scaled\ variable\ cost = 1.426.\ Baseline\ cost.\frac{DC\ (kg\ H_2/day)}{Chemical\_baseline\ DC\ (kg\ H_2/day)} \qquad V.15$$

V.2.3 Design parameters

Table V.3 shows the calculated design parameters in the three plant configurations.

Table V.3 Comparison between the three studied processes at DC=150 000 kg_{H_2}/day

	Autothermal	Hybrid	Allothermal
Plant size (hectares)	19.7	250.2	748.9
Solar power on field (MW)	-	357.5	1069.9
Biomass consumption (t_{dry}/day)	$1.45\ 10^3$	$1.30\ 10^3$	$0.87\ 10^2$
Water consumption (m^3/day)	$4.58\ 10^4$	$4.60\ 10^4$	$4.63\ 10^4$
Annual Cold Gas efficiency [12]	0.80	0.93	1.38
CO_2 emissions (t/day)[12]	$1.04\ 10^3$	$5.78\ 10^2$	29.5

The plant land surface area dramatically increases by 12 times in the hybrid mode and by up to 37 times in the allothermal mode. The solar power is therefore 67% lower in the hybrid mode compared to allothermal mode, at the expense of a greater biomass requirement. In fact, around $0.43\ 10^3$ t/day more biomass is needed to power the reactor during hybrid and full-autothermal phases, which represents about 30% of the total feedstock consumed by the hybrid process. The interest in the allothermal process lies in its high CGE, which exceeds by far those of the hybrid and autothermal processes. The process water requirement, which includes the heat recovery system for local power generation, is hardly impacted by solarization as water consumption due to mirrors cleaning represents only a small proportion of the total plant water requirement. CO_2 direct emissions due to gasification process (reactor heating and/or gasification reaction) are on the other hand 35 times lower in allothermal solar gasification because no combustion is used

[12] cf. Chapter 4

for process heat supply in this case. The overall carbon balance includes additional greenhouse gas emissions, which are released during the different phases of the solar plants life cycle, i.e. during raw materials extraction, manufacturing and assembly, transport, construction, site improvement, maintenance, replacements, dismantling/disposal and/or recycling, etc. Application of credits for CO_2 mitigation and pollution avoidance will further enable the solar thermochemical technologies to compete favorably with fossil-fuel-based processes or autothermal technologies.

V.3 Results and discussion

V.3.1 Cost assessment

V.3.1.1 Key parameters

The project was assumed to start in 2030 with a construction period of three years. It was financed through equity contributions and dept. All the financial inputs used in the economic study are recapped in Table V.4. Hydrogen cost evaluation was carried out with a fixed operating capacity factor (CF) of 80% (accounting for possible maintenance and outage times). Due to the novelty of the project that may discourage some of the investors, the IRR was varied from 8% to 16%. The impact of equity financing (%) and the IRR on the cost of hydrogen for the three presented configurations is shown in Figure V.2 (at a DC of 150 000 kg H_2/day, a biomass reference price of 0.10 €/kg and a land cost of 12.9 €/m^2).

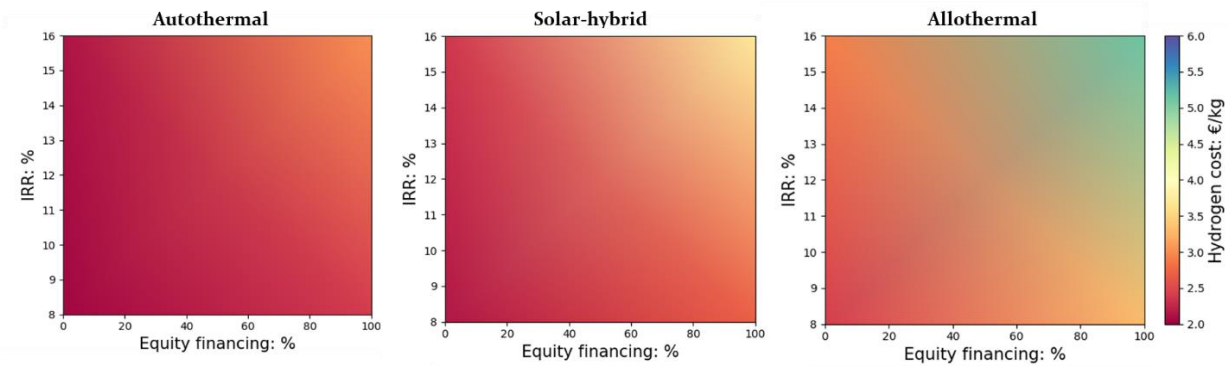

Figure V.2 Impact of equity financing (%) and IRR on the cost of H_2 (DC=150 000 kg H_2/day and a biomass reference price of 0.1 €/kg and land cost of 12.9 €/m^2).

It can be seen that these two parameters have a considerable impact on the price of hydrogen, which varies from 2.41 €/kg_{H_2} to 5.15 €/kg_{H_2} for the solar-only heated process, from 2.15 €/kg_{H_2} to 3.72 €/kg_{H_2} for the hybrid process, and from 2.03 €/kg_{H_2} to 3.02€/kg_{H_2} for the autothermal (non-solar) process. The increase in equity financing (at the expense of less incurred debt) drives up the cost of hydrogen markedly; for instance, for an IRR of 8%, an equity increase from 0% to 100% raises the cost of hydrogen by 37%, 25% and 18% (solar-only, hybrid, and autothermal respectively). The influence of equity percentage on hydrogen price is therefore much greater for the allothermal process that required the largest initial capital investment. In such case, the capital investment of the major pieces of equipment (installed) at *DC*=150 000 kg H_2/day is 335.7 M€, while it is around 201.0 M€ for the hybrid process and only about 137.01 M€ for the non-solar autothermal process. The new shares issued by the increase in

equity contributions give hence more room to launch the investments, but imply on the other hand greater production costs.

Table V.4 Financial inputs

Start-up Time (years)	1
Analysis period & plant life (years)	30
Length of construction period (years)	3
% of Capital spent in 1st, 2nd and 3rd year of construction	8%, 60%, 32%
Depreciation Schedule Length (years)	20
Depreciation Type	MACRS
% of Fixed Operating Costs During Start-up (%)	100%
% of Revenues During Start-up (%)	50%
% of Variable Operating Costs During Start-up	75%
Decommissioning costs (% of depreciable capital investment)	10%
Salvage value (% of total capital investment)	10%
Inflation rate (%)	1,9%
Interest rate on debt	3.7%
Total Tax Rate (%)	25.7%
WORKING CAPITAL (%)	15%

In the following, a percentage of equity of 40% with an IRR of 10% is considered. The overall study reference assumptions are recapped in Table V.5. The breakdown of the direct capital costs of the studied plants is shown in Figure V.3. In the solar-driven processes (solar-only and hybrid solar/autothermal), the heliostat fields hold the largest share of the investment. It contributes to approximately 44% (solar-only) and 24% (hybrid) of the overall direct costs, in agreement with previously reported conventional CST plants values (Pfahl, 2014; Pidaparthi and Hoffmann, 2017). The smallest solar plant size required for the hybrid process leads to a reduced hydrogen price from 2.99 €/kg_{H_2} (allothermal) to 2.48 €/kg_{H_2} (hybrid). The autothermal process is the cheapest with a hydrogen price of 2.25 €/kg_{H_2}.

Table V.5 Reference assumptions

Biomass cost (€/kg)	0.10
Land cost (€/m^2)	12.9
Mirror cost (€/m^2)	120
Tower cost (M€/MW_{th})	0.42
DC (kg H_2/day)	150 000
Electricity cost (€/kWh)	0.10
Water cost (€/m^3)	0.61€/m^3 (process) 0.03€/m^3 (cooling)

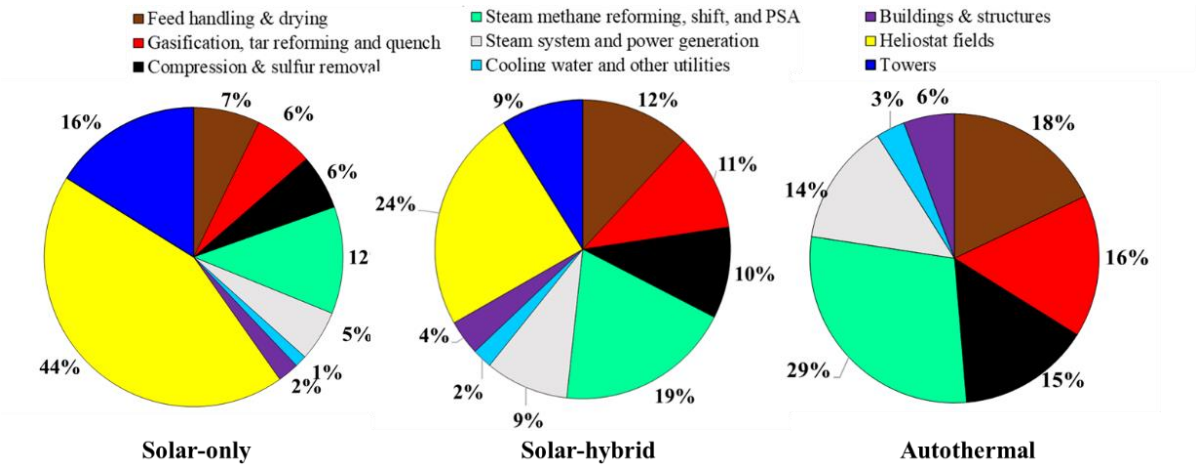

Figure V.3 Direct capital investment breakdown (at reference assumption, Table V.5)

Figure V.4 shows in detail the specific contribution of each item in the plant on the total cost of hydrogen. Solarization increases respectively the capital and the O&M costs by more than three times and up to 46% (in the allothermal configuration). Moreover, the feedstock cost for the hybrid and the autothermal processes is the most predominant, and contributes to nearly 37% and 39% of the total hydrogen production cost (at plant gate). The allothermal process consumes less biomass, and therefore, the feedstock cost is lower representing barely 20%. This is approximately 1.6 times less than for the autothermal process. The impact on the plant variable costs and utilities remains very limited, showing a relative variation of only 2%.

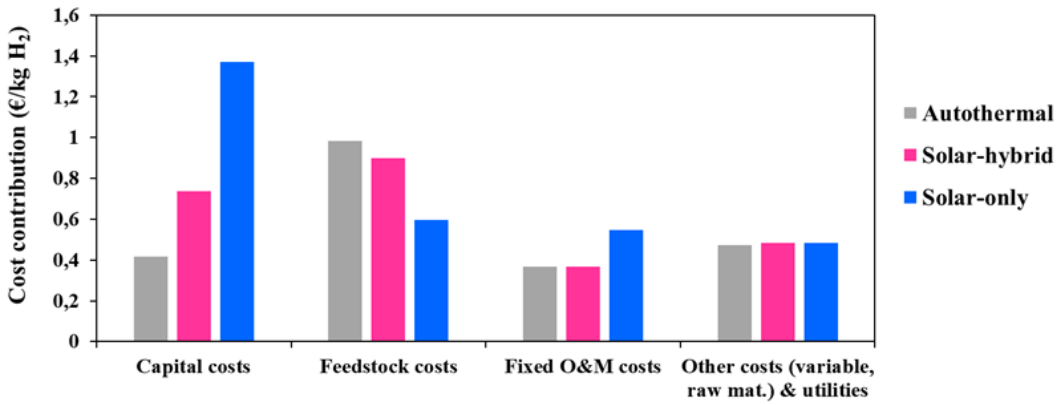

Figure V.4 Specific contribution of each project component

In the following sections, the influence of solar and biomass costs, as major economic factors affecting the minimum hydrogen price, is studied. A sensitivity analysis is carried out on these parameters to examine their impact on the profitability, the competitiveness and the relevance of the projects.

V.3.1.2 Impact of solar investment

The solar investment represents a high proportion of the overall project expenditure, which may be high enough to undermine the solar processes economic attractivity and viability. In the incoming years, and in view of the increasing deployment of solar energy worldwide, the solar investment effort is expected to drop appreciably (SANDIA REPORT, 2007). In fact, innovative designs and new technological solutions are today studied intensely in many research laboratories with the objective of increasing the concentration efficiency and the

durability of the materials. In conjunction with the economy of scale, this should reduce to a certain extent the solar costs for the benefit of solar and solar hybrid gasification. In this respect, the influence of a possible cost reduction of the main solar compounds (i.e. heliostat field and towers) on the minimum hydrogen price was studied (Figure V.5).

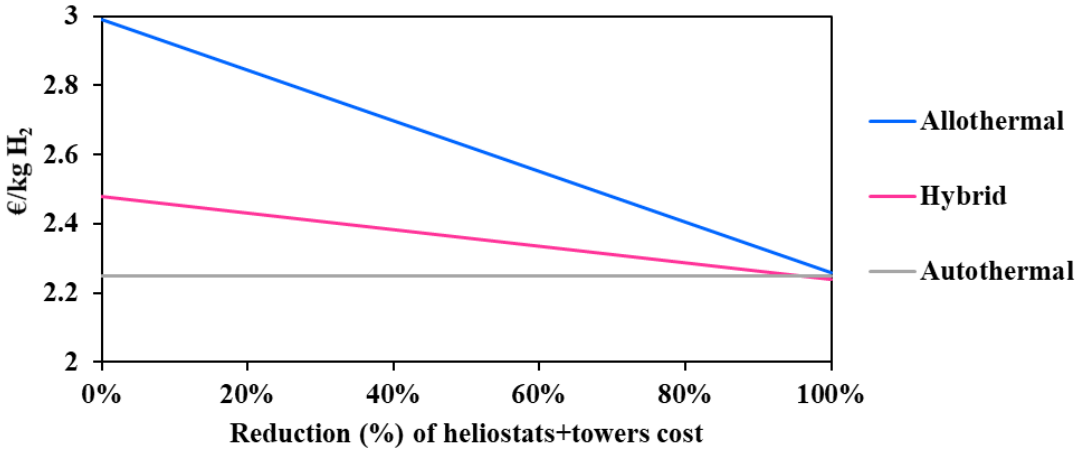

Figure V.5 Impact of solar technologies cost reduction on the hydrogen minimum price

It can be observed in Figure V.5 that the solar allothermal process is the most costly. Moreover, the decline in the heliostats and towers costs reduces the hydrogen minimum price in a more pronounced fashion in the allothermal configuration. In fact, a 50% cost reduction declines the price of hydrogen by 0.37 €/kg_{H_2} for the allothermal process and by 0.12 €/kg_{H_2} for the hybrid process. The intersection between the two curves is achieved only when the cost reduction is beyond 95%, which is practically unattainable. In any case and whatever the cost reduction, solar and solar hybrid hydrogen generation remains more expensive as compared to the conventional autothermal process, which is due to major extra-costs related to the heliostat field and tower, plant land, maintenance and staffing... Design calculations allowed estimating the total area occupied by the solar plants (allothermal and hybrid): the heliostat field surface at DC=150 000 kg H_2/day is estimated at 11.5 km^2 for the allothermal process and at 3.9 km^2 for the hybrid process. This represents nearly 57 and 20 times the required chemical plant land surface. Figure V.6 shows the impact of the land cost (varied between 0.5 €/m^2 to 50 €/m^2) on the hydrogen minimum price. The graphic shows the importance of the choice of land, which apart from being highly irradiated and allowing for continuous biomass supply, must be economically profitable. In fact, a quite significant decrease in the cost of hydrogen from 2.99 €/kg_{H_2} at reference land cost (12.9 €/m^2) to 2.63 €/kg_{H_2} at 0.5 €/m^2 is observed for the allothermal process. As the hybrid plant occupies a smaller area, the hydrogen minimum price decreases less markedly by 0.16 €/kg_{H_2} against 0.36 €/kg_{H_2} in the allothermal process. On the other hand, the autothermal configuration is almost insensitive to land cost, showing a relative H_2 price variation of less than 0.5%. Additionally, a 50% reduction of the heliostats and solar towers costs, combined with a lower land cost below 0.5 €/m^2 allows reaching an area of competitiveness where the three processes meet. This could also correspond to a more favorable plant site in which the solar resource is greater e.g. Chilean desert although the cost of water may be somewhat higher in desert locations.

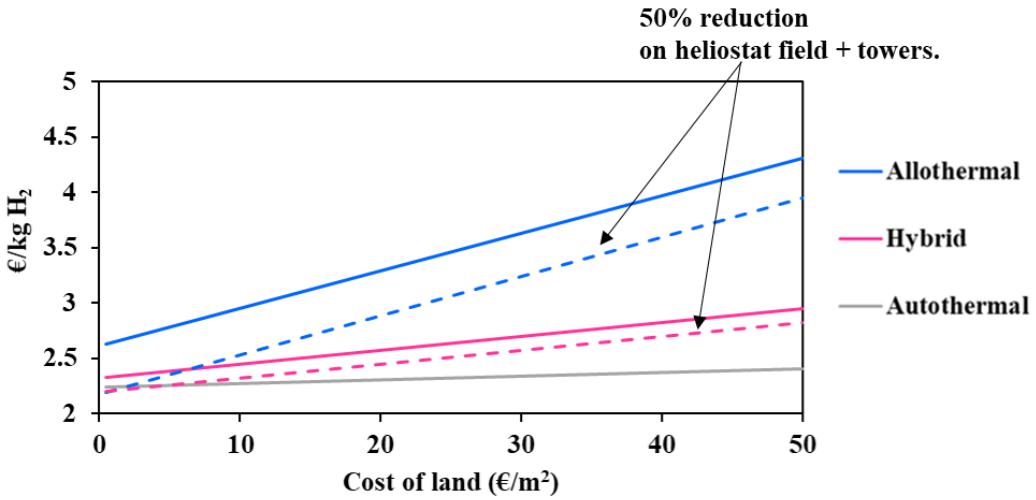

Figure V.6 Impact of land cost on the hydrogen minimum price (solid lines: reference assumptions, Table V.5; Chain-dotted lines: 50% cost reduction on heliostats and towers)

Another important parameter affecting the level of solar investment is the plant design capacity. This parameter was varied in Figure V.7 from 20 000 kg H_2/day to 150 000 kg H_2/day to analyze its impact on the solar/chemical direct costs and on the hydrogen minimum price.

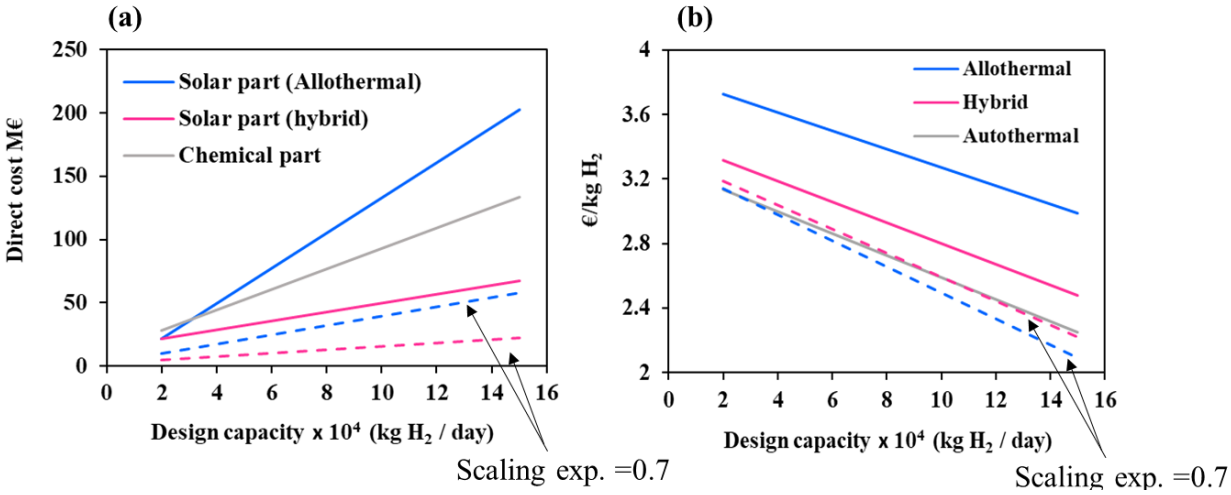

Figure V.7 (a) Direct costs at different design capacities separated in two parts: solar and chemical; (b) Hydrogen minimum price for different design capacities and impact of scaling factor

It can be observed that the solar direct costs of allothermal process grow at least two times faster than the hybrid process solar direct costs and the chemical facilities costs (reaching a maximum value of 202.3 M€). Conversely, the increase in plant design capacity reduces the hydrogen minimum price by up to 25%, 34%, and 39% for the allothermal, hybrid, and autothermal processes, respectively. Additionally, due to the sharp rise in the solar facilities costs, the relative difference in hydrogen minimum price between the solar processes and the autothermal process goes up from 18% (allothermal) and 6% (hybrid) at 20 000 kg H_2/day to 32% (allothermal) and 10% (hybrid) at 150 000 kg H_2/day. This suggests that upon scale up, the competitive gap between the conventional and the solar processes increases. However, this may be due solely to the linearity assumption that was adopted in (Eqs.V.3-V.6) between the solar costs and the production capacity. As a matter of fact, solar costs prediction is not straightforward and relies on uncertain data. Generally speaking, heliostats field scale up

depends on many factors such as the design of individual mirrors, their number, their arrangement, their sub-composition and their reflective properties, etc. Larger solar fields impair the quality of concentration and suffer from amplified atmospheric attenuation (due to a greater heliostat-to-receiver slant path) (Lovegrove and Stein, 2012). At the same time, larger solar fields involve higher solar power inputs that allow using larger cavity receivers (i.e. gasification reactors), which reduce the energy losses (due to a better absorption of radiation) and thus positively impact the solar costs. A power law with a global scaling exponent factor of 0.7 accounting for these trends was previously used by Kromer et al. (Kromer et al., 2011) for assessing hydrogen cost of several solar thermochemical processes. The impact of this value on the solar costs and on hydrogen minimum price is shown in Figure V.7 Results show that the trends strongly vary with the scaling exponent. The solar costs decline by approximately 72% for the allothermal process and by 60% for the hybrid process at 150 000 kg H_2/day. In the same way, the hydrogen price for the allothermal process sharply drop to 2.09 €/kg_{H_2} at 150 000 kg/day against 2.22 €/kg_{H_2} for the hybrid process and 2.25 €/kg_{H_2} for the autothermal process. This highlights the necessity of a proper field layout optimization during the scale up to maximize the energy/materials savings and further reduce the hydrogen cost.

The feedstock cost is another crucial parameter to be studied (Figure V.4). Its impact on hydrogen cost is presented in the following section.

V.3.1.3 Impact of feedstock cost

The cost of the feedstock is a key dynamic parameter that evolves with different factors such as local supply chains, resource availability, sustainability criteria, political choices or competing uses of biomass. In this part of the study, the biomass price was varied in the 0-1 €/kg interval to cover a large range of woody and non-woody biomasses (such as waste and Solid Recovered Fuels) and also a potential increase in the resource price (due for instance to the increasing pressure on the resource in the incoming years). Figure IV.8 shows the hydrogen cost as a function of the biomass price for the three studied processes (at reference conditions represented by solid lines). Two additional scenarios are considered, the first one assumes a 50% cost reduction of the heliostat field and towers (at reference land cost) and the second one assumes (in addition) a land cost of 0.5 €/m^2. Two zones on these graphs can be observed for each of the considered solar scenarios, one zone when the biomass price is below a critical value and one zone when the resource price is above. In the first zone, the autothermal mode prevails and imposes lower production costs. In the second zone, a significant reversal trend in favor of the solar processes occurs. Table V.6 shows the critical biomass prices at the intersection between the autothermal and solar processes curves. It can be seen that the trend turnaround occurs faster in the allothermal process than in the hybrid one at reference assumptions. In fact, it takes place at a biomass critical price of 0.29 €/kg (for the allothermal mode, which represents 3 times the reference biomass price), against 0.37 €/kg for the hybrid configuration. By reducing the solar equipment cost by 50%, the turnaround biomass price decreases by about 31% for the allothermal mode and by 38% for the hybrid mode (at reference land cost). It decreases even more by a total of 69% (allothermal) and 84% (hybrid) when the land cost is set to 0.5 €/m^2. In the latter scenario, the turnaround occurs earlier in the hybrid process.

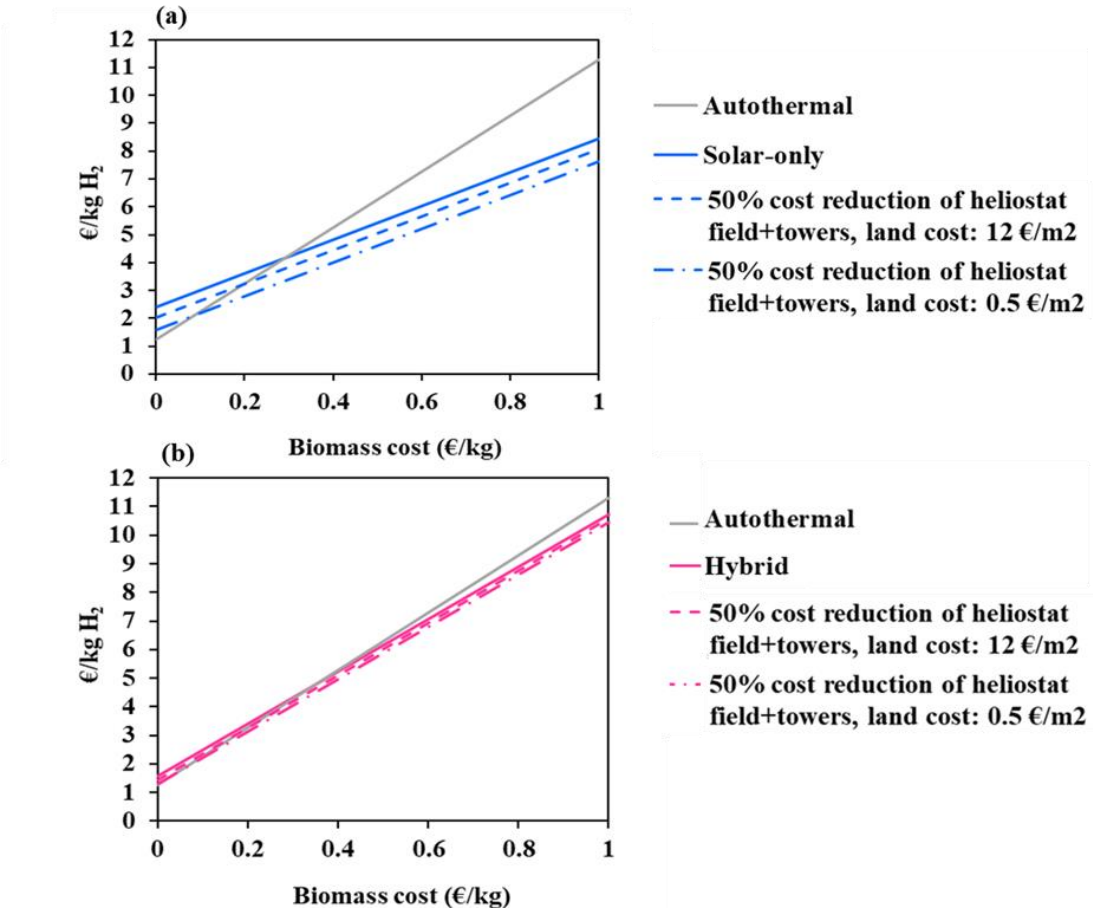

Figure V.8 Impact of biomass cost on hydrogen minimum price; (a)-allothermal, (b)-hybrid

Table V.6 Turnaround biomass price (€/kg): autothermal/solar, DC=150 000 kg H_2/day

	Autothermal/Allothermal	Autothermal/Hybrid
Reference assumptions	0.29	0.35
+50% reduction on (heliostats+towers), land cost= 12.9 €/m^2	0.20	0.23
+50% reduction on (heliostats+towers), land cost= 0.50€/m^2	0.09	0.06

In summary, the analysis shows that a slight increase in the price of the feedstock undermines the autothermal process. The better use of biomass provided by the solar processes clearly limits the increase in hydrogen cost, especially when it is combined with lower solar plant and land costs. Zero or even negative-priced feedstocks remain on the other hand more profitable using the conventional autothermal process. However, in case of waste gasification, CO_2 emissions and environmental impact should be considered if carbon is not renewable (e.g. plastic waste). Direct CO_2 emissions released by the solar processes are negligible or significantly lower than those from the current autothermal processes. Solar gasification processes have thus favorable long-term prospects because they avoid or reduce costs for CO_2 mitigation and pollution abatement. Moreover, due to the more heterogeneous nature of waste, its conversion implies additional costs, to deal with syngas impurities, especially the H_2S content that is a major corrosive constituent. More costly reactor materials and gas cleaning units are thus required for waste feedstocks.

V.3.1.4 Impact of environmental subsidies

As shown in Table V.3, solar gasification avoids respectively 3.08 kg and 6.73 kg of CO_2 (due to reaction) per kilogram of H_2 in hybrid and allothermal processes, which is significant. Although a detailed analysis has not yet been published comparing the three processes based on environmental criteria, important and achievable CO_2 emissions mitigation is greatly expected thanks to solar heating. In fact, a conventional CSP tower plant generates barely 38 g of CO_2/kWh_e (Burkhardt et al., 2012), which is by far (more than 10 times) lower than the 750-900 g of CO_2/kWh_e generated by conventional IGCC (Integrated Gasification Combined Cycles) power plants when no CO_2 capture is considered. Capture/sequestration of 80% of CO_2 during operation decreases the net emissions to about 200 g of CO_2/kWh_e, resulting in a total saving of more than 550 g of CO_2/kWh_e (Ordorica-Garcia et al., 2006). In this sense, solar-driven processes can drastically reduce the GHG (Greenhouse gas) emissions, which allows them to take advantage of carbon pricing and environmental subsidies to improve to their economic balance and their competitiveness. Indeed, application of credits for CO_2 mitigation and pollution avoidance will further enable the solar thermochemical technologies to compete favorably with conventional processes. Carbon price varies from country to country (https://carbonpricingdashboard.worldbank.org/map_data), and in France, it is estimated at 100 €/t CO_2 in 2030 according to Quinet REPORT. In Europe, carbon prices are expected to double by 2021 and even quadruple to reach up to 55€/t CO_2 as stipulated in the Paris climate agreement (Carbon Tracker REPORT, 2018). In this section, the impact of possible capital subsidies due to CO_2 emission reduction is studied. The total subventions were calculated on the basis of the amount of CO_2 that would have been emitted by the conventional process. For allothermal gasification, the subvention was estimated at 14.74 M€ (6.73x150 000x80%x365x50/1000) and at about 6.74 M€ for the hybrid process (3.08x150 000x80%x365x50/1000) for DC=150 000 kg H_2/day, a capacity factor of 80% and a capital subsidy of 50€ t/CO_2. Figure V.9 shows the impact of CO_2 subsidies on hydrogen cost.

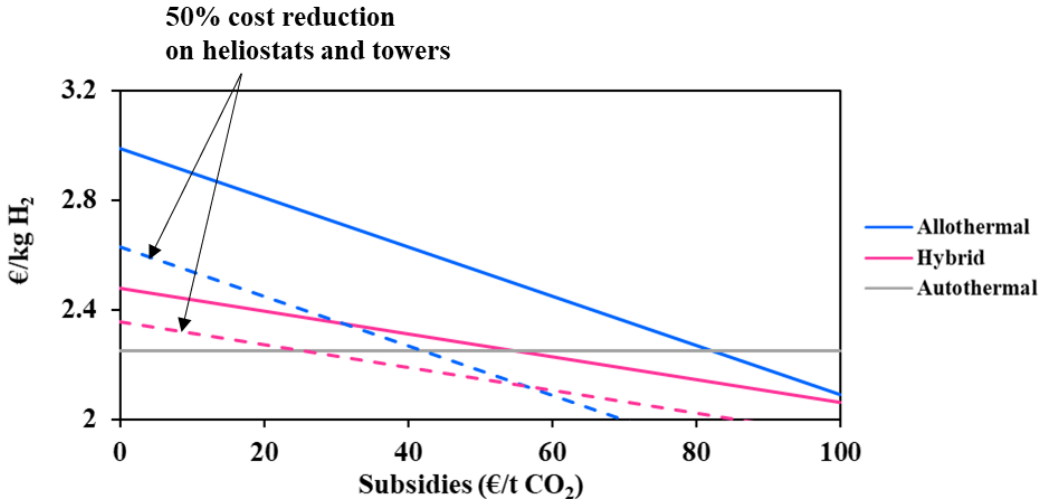

Figure V.9 Impact of CO_2 subsidies on hydrogen cost

At reference conditions, the intersection between the curves (autothermal and solar processes) takes place at CO_2 subventions of 82 €/tCO_2 (allothermal) and 55 €/tCO_2 (hybrid). Considering a cost reduction on heliostats and towers of 50% and a fixed environmental subsidy of 30€/tCO_2, the biomass turnaround price goes down to 0.14 €/kg and 0.09 €/kg (lower than

reference cost ~0.1 €/kg) for the allothermal and hybrid processes, respectively. This confirms that subsidies can play a key role in the reduction of solar hydrogen costs.

V.3.2 Comparison with other hydrogen production methods

This part of the study gives insights into hydrogen production costs with different technologies such as biomass gasification, coal gasification, natural gas reforming and water electrolysis (based on a solid oxide technology). Previously developed NREL cost models were used for this purpose (https://www.nrel.gov/hydrogen/h2a-production-models.html). The financial inputs of all the technologies are the same as those presented in Table V.4 and the operating capacity factor is fixed to 80%. To focus on the comparison with low carbon technologies, the considered coal gasification and natural gas reforming models integrate carbon capture and sequestration units that remove CO_2 from syngas before storing it in underground reservoirs. The reference primary resources costs used in this section are: biomass cost=0.1€/kg, coal cost=0.04€/kg, NG cost=0.01€/kWh, electricity cost for electrolysis =0.10€/kWh. Figure V.10 shows the hydrogen minimum price of the different technologies. The grey bars show the sensitivity to the primary resource price (electricity price for electrolysis, process water was fixed to 0.61€/m^3) when it increases from zero to twice the reference cost.

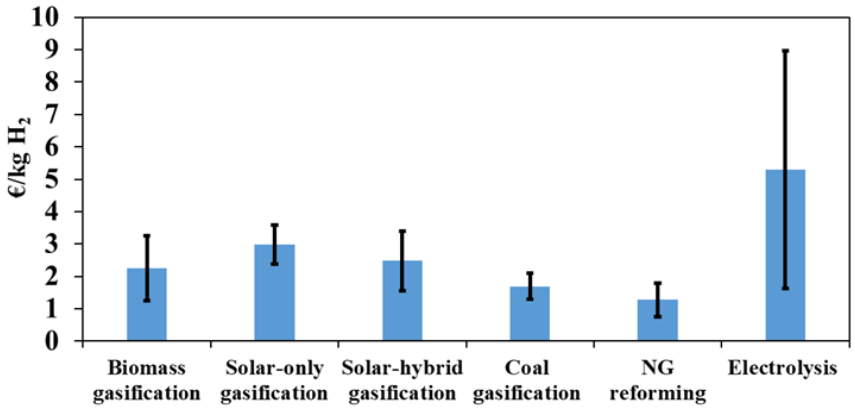

Figure V.10 Hydrogen production cost and sensitivity on the primary resource cost (electricity for electrolysis) when ranging from zero to twice the reference cost (Table V.4)

It can be seen that natural gas reforming is the most profitable process so far with a hydrogen production cost of only 1.28 €/kg. This process is followed by coal (1.69 €/kg) and biomass gasification. The difference between these three processes is mainly due to two factors: the cost of the primary resource and the capacity of the plant. Clearly, due to the low fossil fuels cost, fossil-based processes are the most competitive on the market. Moreover, very large plants can be envisaged, which lowers the price of hydrogen even further thanks to the economy of scale. The cost of hydrogen produced by electrolysis is much higher than that of the other processes (5.48 €/kg), and it shows moreover a greater sensitivity to primary resource cost. It can be seen that for a zero resource cost, the price of hydrogen produced by electrolysis decreases drastically to 1.68 €/kg, making this technology potentially more competitive when recovering and valorizing unusable electricity (due for example to lack of demand and storage). Although coal gasification plant capacity is 7 times larger than that of biomass gasification (and therefore benefits from the economy of scale), it appears that for low feedstock costs, hydrogen price is

almost the same in both configurations. This is due to the extra-costs entailed by CO_2 capture and sequestration operations (which are not considered in biomass gasification). Finally, NG reforming with CO_2 capture and sequestration is the cheapest process with a hydrogen cost a way below than that of coal and biomass gasification (solar and non-solar), making this technology the most economically attractive at present for decarbonized hydrogen generation.

It is essential to recall that other solar thermochemical processes are prospected for the generation of solar fuels. The number of publications in this field considerably increased by more than five times since 2000 (Yadav and Banerjee, 2016). This brought significant insights regarding the technical feasibility and the possibilities of scale up. A number of economic studies were carried out to estimate the cost of hydrogen using different solar thermochemical technologies. Although initial assumptions differ from one study to another regarding plant site, solar materials cost, operating hours, installations costs and optical/thermal efficiencies, etc., the calculated values estimate the prices and their sensitivity to the input parameters. Möller et al. (Möller et al., 2006) analyzed solar steam reforming of natural gas for the production of 103.8 Million Nm^3/year (i.e. ~25 594 kg/day) of hydrogen. The study showed that the solar process allows to save 40% of the fuel compared to the conventional process with hydrogen cost less than 0.05 €/kWh LHV of H_2 (~1.67 €/kg of H_2). Similarly, Rodat et al., (Rodat, 2010) studied solar thermal decomposition of natural gas at plant design capacity of 436 kg of H_2/day. Hydrogen cost was about 1.42 $/kg and showed a great sensitivity to carbon blacks (which are the process byproducts) selling price. The study determined carbon blacks minimum cost that makes solar thermal decomposition of natural gas competitive with solar and conventional reforming processes. Baykara et al. (Baykara and Bilgen, 1985) compared commercial, hybrid and solar coal gasification processes for the production of hydrogen. The plants were designed to produce 10^7 GJ of H_2 per year (~228 310 kg/day). The study showed that the commercial process (based on partial feedstock combustion) is the most cost effective with a hydrogen price of 0.94 $/kg, which is 5.2% and 6.3% lower than the hybrid and solar (only) process and is in some respects consistent with the present study outcomes. Other researchers took a keen interest in the thermochemical splitting of water using high temperature solar heat. Single-step direct thermolysis at temperatures beyond 2500°C being hardly feasible, thermochemical cycles technologies were rather considered. This process involves several reactional intermediates, which are regenerated during the cycles to lower the water dissociation temperature. Over 280 cycles were developed and screened to select the most suitable ones for the coupling with concentrated solar thermal energy (Abanades et al., 2006). Among the most promising cycles that were studied from an economic perspective, zinc, ferrite, and sulphur cycles were proposed. Charvin et al. (Charvin et al., 2008b) studied two-step (ZnO/Zn and Fe_3O_4/FeO) and three-step (Fe_2O_3/Fe_3O_4) thermochemical cycles driven by concentrated solar energy. The economic study was performed with a design capacity ranging from 50 kg/h to 250 kg/h of H_2. The analysis gave a hydrogen production cost between 7.98 $/kg to 14.75 $/kg of H_2 depending on process intensification and on the targeted hydrogen productivity. In a similar study, Steinfield (Steinfeld, 2002) analyzed hydrogen production cost via two-step water-splitting ZnO/Zn redox system, and hydrogen price was around 5 $/kg at a design capacity of 61 Million-kWh/year (~5014 kg/day), which is somewhat larger than Charvin et al. design capacity and therefore lowers hydrogen price. Solar hydrogen production cost from hybrid-sulfur cycle and a metal

oxide-based cycle was studied and compared to that of commercial electrolysis (powered by a CSP plant with a thermal storage capacity of 4.5h) by Graf et al. (Graf et al., 2008). The metal oxide-based cycle hydrogen cost ranged between 3.5€/kg to 12.8€/kg and thus covers the ranges calculated by Charvin et al. (2008b) and Steinfeld (2002). It showed the greatest cost variability due to high demand of the metal oxide. Hydrogen cost for hybrid sulfur cycle was the lowest and ranged between 3.9 €/kg to 5.6 €/kg. Water electrolysis was highly influenced by the cost of electricity with a hydrogen price between 2.1 €/kg and 6.8 €/kg.

Overall, it appears from these results that to date, solar thermochemical processes are far from being competitive with conventional processes based on fossil fuels (coal and natural gas). Major challenges remain to improve the efficiency of the processes. It concerns the cost of the solar concentrators, which represents a significant part of the investment and the cost of the receiver, which in many cases must withstand high temperatures in the presence of highly corrosive chemical species. Another challenge to meet concerns the solar reactors design that should minimize the heat losses and maximize the chemical conversion for a better use of the solar resource. The recycling of chemicals in thermochemical cycles that impose a high degree of purity and a precise control of phases and constituents separation is another issue to properly manage and solve. Carbon-based solar thermochemical technologies generally show lower hydrogen production costs. These processes, which by definition are less harmful to the environment, offer the possibility to extend the lifespan of fossil resources on earth and can play a role in the transition towards a zero carbon economy.

V.4 Conclusion

A techno-economic study of solar and solar hybrid gasification was carried out. The study was based on the discounted cash flow rate of return method to calculate the minimum hydrogen production cost. At first, the most important solar parameters were identified, and they were then integrated to a previously developed autothermal gasification cost model. The new solarized cost model was thereafter used to examine the profitability and the cost effectiveness of each of the studied heating configurations (i.e. allothermal, hybrid and autothermal). A sensitivity analysis of the main cost-influencing factors was carried out. The analysis showed that at the current biomass reference cost (considered equal to 0.1 €/kg), the most competitive scenario (in which solar hydrogen cost is lower than conventional hydrogen) assumes a cost reduction of 50% of the heliostats and towers costs with a land cost of 0.5 €/m^2, which is today clearly challenging and requires an important economic effort. However, the analysis also showed that an increase in the biomass cost by a factor of 2 to 3 significantly undermines the profitability of the autothermal process, in favor of solar gasification, which becomes more competitive without any substantial economic and financial efforts. A comparative analysis with other solar and non-solar clean technologies was carried out. It confirmed that the two most economically-favorable processes for hydrogen generation are those based on fossil fuels with CO_2 capture and sequestration. These processes will therefore certainly make the greatest contribution in the hydrogen market in the near future. Nonetheless, fossil fuels are neither universally available nor inexhaustible and depend on a large number of strategic and geopolitical parameters that remain uncertain, sensitive and hardly predictable. Moreover, carbon sequestration is not without risk for the environment and human health. Leakage during

transport and storage is possible and the long-term process performance is uncertain especially in case of large-scale development. These represent major constraints to circumvent in order to ensure security and sustainability. Renewable technologies are today hardly competitive with fossil-based technologies and require more effort to gain in efficiency, durability and cost effectiveness. Government policy incentives have also a major role to play through the use of mechanisms like carbon credits, renewable energy credits, capital subsidies, and reverse auctions. This way, the financial viability of the sustainable path can be improved.

CONCLUSION & PERSPECTIVES

These three years were organized to study a novel solar thermochemical gasifier based on the principle of spouted bed reactors. The goal was to bring new insights into the reactor operation in order to improve its performance, flexibility and industrial integration. The state of the art and previous work on the solar reactor allowed defining number of points and research axes to be investigated during the thesis. Accordingly, different stages of development of the technology were discussed and analyzed thanks to combined numerical modelling and lab-scale experimentations. The accomplished work and the main results are summarized below:

At first, a comprehensive 3D CFD model of the lab-scale solar reactor was developed. The model took into account the coupled momentum, heat and mass transfer and the chemical reactions (pyrolysis, heterogeneous char gasification/combustion and gas-phase reaction kinetics) along with the continuous particle injection. The reacting particles were tracked in space and time using the Discrete Phase Model (DPM) to thoroughly analyze their trajectories and flow patterns when undergoing pyrogasification reactions. Validation allothermal experiments on beech wood particles were carried out in both direct and indirect heating modes at a temperature of 1200°C. The maximum relative discrepancy with the experiments was below 10% for the outlet syngas composition. The results provided a clear overview on the solar conversion of the woody particles in the solar-radiated cavity and confirmed the suitability of the technology to operate under optimal solar conditions thanks to relevant thermochemical and hydrodynamic features.

In a second step, the 3D multiphysics model was used to simulate a new hybrid operating mode that makes use of in-situ combustion reactions to assist the solar heating and address the issue of solar energy intermittency and daily variability. The operational feasibility of the process was first demonstrated thanks to numerical modelling and was confirmed through lab-scale directly and indirectly irradiated experimentations. The achieved results represent the first successful attempt to control a hybrid thermochemical reactor operating under real low and variable solar input. The analysis showed that O_2 injection is a relevant solution for the dynamic control of the reactor temperature. However, it considerably affects the syngas yields with an important drop in H_2 and a sharp rise in CO_2 yields.

Following these results, Solid Recovered Fuels (SRF) solar-only and solar hybrid gasification was explored for the first time to evaluate the ability of the reactor to treat more varied loads with a high ash content. Waste particles solar conversion was successfully achieved yielding high-quality syngas (H_2:CO~1.8) and suitable performance (Carbon Conversion Efficiency =88% and Cold Gas Efficiency =105%). However, the process suffered from ash melting/agglomeration issues and injection instabilities that undermined the continuity of the process. Solutions from the literature were proposed and a patent has been filed in order to improve the solar reactor flexibility in converting both biomass and waste feedstocks.

With the aim of improving the phase mixing, gas and solid residence times and the overall particles conversion, the use of inert bed materials as a heat transfer medium appeared judicious.

This solution was examined first using 2D Eulerian CFD simulations that model the solid inert particles (spouted or packed) in interaction with radiation and gas flow. Then, it was further investigated using cold and high temperature on-sun experimentations with five different inert bed materials. The simulations provided information on the gas-inert particles flow and mixing, temperature, oxidant concentration and velocity field inside the solar cavity. Solar tests showed a relative increase in the Carbon Conversion Efficiency by up to 8% using the Al_2O_3 particles (spouted or packed). The impact on the syngas composition remained globally very low with a maximum relative variation less than 7% for H_2.

Given the promising simulation and experimental outcomes, the reactor was extrapolated to MW scale for industrial syngas production. A dynamic 0D model of the reactor was developed accordingly to determine the temperature and syngas products evolution during continuous operation in both solar-only and hybrid modes. Three reactants feeding management strategies were proposed and studied: TOR (on/off), OPTI (OPTImized) and HYB (HYBridized) to deal with the variable nature of solar energy. OPTI (allothermal) and HYB (solar/autothermal) control modes allowed reaching the highest performances thanks to dynamic control of the supplies that stabilizes the reactor temperature, minimizes the heat losses and maximizes the productivity. The HYB mode resulted in the highest syngas yields outperforming both allothermal and conventional autothermal gasification. Annual simulation for the prediction of reactants consumption and syngas production was also achieved with the developed dynamic model.

In the last part of the work, the economic feasibility of the process at large scale for centralized H_2 production was assessed. H_2 production cost from solar-only, hybrid and autothermal biomass gasification was evaluated under various economic scenarios. The results showed that an increase in the biomass cost by a factor of 2 to 3 significantly undermines the profitability of the autothermal process, in favor of solar hybrid and solar-only gasification. A comparative study involving other solar and non-solar processes concluded on the profitability of fossil-based processes and in particular, natural gas reforming that shows a H_2 cost below 1.28 €/kg (including carbon capture and sequestration), against 2.5€/kg and 3.0 €/kg in hybrid and solar-only biomass gasification process. However, in view of the increasingly stringent environmental regulations, and noting the urgency of the climate change, the sustainable path knows today extensive research and development to gain in efficiency and cost-effectiveness. Massive deployment of concentrated solar energy across the world in the coming years can significantly reduce the cost of the solar materials and components (heliostats) and thus alleviate the financial cost of solar gasification.

This work provides new information on the operation of the solar reactor at both small and large scales and the objectives of the thesis were achieved. However, there are still many questions to be resolved requiring further research. Accordingly, it is worth conducting future work on the following aspects:

Modelling:

- The improvement of the 3D CFD model by considering a more detailed chemistry can provide a more rigorous and accurate representation of the reaction system especially tars, soot, light hydrocarbons and combustion reactions.

- The determination of optimized solution strategies and input data with no significant effect on the numerical solution would lighten the calculations.

- The use of an Equivalent Reactor Network (ERN) can be considered to speed up the calculations while accurately capturing the chemistry of the solar reactor. The ERN represents the solar cavity by a group of Perfectly Stirred Reactors (PSRs) and Plug Flow Reactors (PFRs) on which detailed chemistry mechanisms are directly and efficiently applied (Das et al., 2020).

- The modeling of waste particles solar gasification and the integration of additional physical mechanisms such as molten particles splashing on walls and agglomeration of ashes at the bottom of the cone would provide a better description and understanding of the experimental data.

- The dynamic modelling of the unsteady phases of the reactor (due for example to drop of DNI, variation in wood/water flow rates, oxygen injection, etc.) using multiphysics CFD simulations would improve understanding leading to a better control and handling of the transient periods.

Optimization:

- Strategies for optimizing the geometry of the reactor were identified during this thesis (e.g. use of a confiner and lateral oxidant injection). These solutions can be simulated, improved and complemented in future work in order to conceive a new optimized solar cavity that achieves enhanced performances and deals with any type of charge.

- The control of the gas and biomass flow rates is necessary for improving the productivity of the solar reactor. Thus, intelligent control algorithms need to be developed and tested experimentally to optimize the particles solar/solar hybrid conversion thanks to a precise control of temperature, oxidants concentration, residence time etc. while dealing with the variable solar input.

- A more extensive parametric study on the spouted bed (empty cavity, or with inert particles) for both beechwood/waste particles gasification (and cogasification) at different constant solar inputs would allow to determine optimal operating conditions in terms of temperature, oxidants (including steam and oxygen), biomass/waste and carrier gas flow rates that are most favorable for the reaction. The achieved results can be used to support and guide the developed control algorithms.

Extrapolation:

- The dynamic simulation of the chemical plant at large scale for a particular application e.g. hydrogen or liquid fuels generation can clarify the coupling between the different chemical units and quantify (under specific assumptions) the impact of the solar transients on the whole chemical process.

- The dynamic process model may integrate syngas storage units to mitigate the impact of syngas flows variation, especially if it integrates chemical units such as F-T synthesis that requires very stable input conditions (H_2:CO~2).

- An economic and environmental analysis of the process for the generation of various molecules such as methanol and liquid fuels based on the dynamic process simulation results can justify the relevance of the technology. A comparative study with other conventional processes can help identify the processes in which solar gasification is most profitable.

Concerning the experimental part, the chemical analysis of carbon can determine if the particles are completely pyrolyzed prior to entrainment. As previously, mentioned, the dynamic control of the process is an essential point to be investigated; the experimental test bench needs to be improved consequently. Further research is required to up-scale the reactor. The extrapolation to pilot/demonstration scale e.g. 100 kW_{th} is essential to validate the reliability of the process and equipment during long time operation. Various scale-up problems can be identified and resolved, preparing the industrial scale extrapolation safely, reliably and efficiently.

The work carried out during this thesis shows the interest and the potential profitability of the use of solar energy for the valorization of carbonaceous resources by thermochemical gasification and the production of clean synthetic fuels. In recent decades, and due to climate change and depletion of fossil fuels, advances and technical innovations have appeared to ensure efficient conversion of the solar resource. To date, it is mainly direct power generation technologies that are being promoted and developed. More generally, this energy source is not only promising for gasification but also for the decarbonization of endothermic chemical processes such as reforming, thermal dissociation, and also metallurgical processes requiring very high temperatures. It is therefore important to pay particular attention to these innovative processes to accelerate their development and deployment at large scale. This is how we conclude with the quotation from T. Edison (1931) "*I'd put my money on the sun and solar energy. What a source of power! I hope we don't have to wait until oil and coal run out before we tackle that*".

REFERENCES

Abanades, S., Charvin, P., Flamant, G., Neveu, P., 2006. Screening of water-splitting thermochemical cycles potentially attractive for hydrogen production by concentrated solar energy. Energy 31, 2805–2822. https://doi.org/10.1016/j.energy.2005.11.002

Achkari, O., El Fadar, A., 2020. Latest developments on TES and CSP technologies – Energy and environmental issues, applications and research trends. Appl. Therm. Eng. 167, 114806. https://doi.org/10.1016/j.applthermaleng.2019.114806

Adams, T.A., Barton, P.I., 2011. Combining coal gasification and natural gas reforming for efficient polygeneration. Fuel Process. Technol. 92, 639–655. https://doi.org/10.1016/j.fuproc.2010.11.023

Agoua, E., Perre, P., 2010. MASS TRANSFER IN WOOD: IDENTIFICATION OF STRUCTURAL PARAMETERS FROM DIFFUSIVITY AND PERMEABILITY MEASUREMENTS. J. Porous Media 13. https://doi.org/10.1615/JPorMedia.v13.i11.80

Ahn, D.H., Gibbs, B.M., Ko, K.H., Kim, J.J., 2001. Gasification kinetics of an Indonesian sub-bituminous coal-char with CO2 at elevated pressure. Fuel 80, 1651–1658. https://doi.org/10.1016/S0016-2361(01)00024-2

Alauddin, Z.A.B.Z., Lahijani, P., Mohammadi, M., Mohamed, A.R., 2010. Gasification of lignocellulosic biomass in fluidized beds for renewable energy development: A review. Renew. Sustain. Energy Rev. 14, 2852–2862. https://doi.org/10.1016/j.rser.2010.07.026

Altzibar, H., Estiati, I., Lopez, G., Saldarriaga, J.F., Aguado, R., Bilbao, J., Olazar, M., 2017. Fountain confined conical spouted beds. Powder Technol. 312, 334–346. https://doi.org/10.1016/j.powtec.2017.01.071

Altzibar, H., Lopez, G., Bilbao, J., Olazar, M., 2014. Operating and Peak Pressure Drops in Conical Spouted Beds Equipped with Draft Tubes of Different Configuration. Ind. Eng. Chem. Res. 53, 415–427. https://doi.org/10.1021/ie402031t

Arganbright, D.G., Resch, H., 1971. A review of basic aspects of heat transfer under impinging air jets. Wood Sci. Technol. 5, 73–94. https://doi.org/10.1007/BF01134220

Auger, J.C., Stout, B., Lafait, J., 2000. Dependent light scattering in dense heterogeneous media. Phys. B Condens. Matter 279, 21–24. https://doi.org/10.1016/S0921-4526(99)00657-2

Bacelos, M.S., Freire, J.T., 2008. Flow regimes in wet conical spouted beds using glass bead mixtures. Particuology 2, 72–80. https://doi.org/10.1016/j.partic.2008.01.001

Bai, Z., Liu, Q., Gong, L., Lei, J., 2018. Thermodynamic and economic analysis of a solar-biomass gasification system with the production of methanol and electricity. Energy Procedia, Cleaner Energy for Cleaner Cities 152, 1045–1050. https://doi.org/10.1016/j.egypro.2018.09.118

Bamford, C.H., Crank, J., Malan, D.H., 1946. The combustion of wood. Part I. Math. Proc. Camb. Philos. Soc. 42, 166–182. https://doi.org/10.1017/S030500410002288X

Barrio, M., Hustad, J.E., 2008. CO2 Gasification of Birch Char and the Effect of CO Inhibition on the Calculation of Chemical Kinetics, in: Progress in Thermochemical Biomass Conversion. John Wiley & Sons, Ltd, pp. 47–60. https://doi.org/10.1002/9780470694954.ch3

Basu, P., 2010. Biomass Gasification and Pyrolysis: Practical Design and Theory. Academic Press.

Baumlin, S., 2006. Craquage thermique des vapeurs de pyrolyse-gazéification de la biomasse en réacteur parfaitement auto-agité par jets gazeux. Vandoeuvre-les-Nancy, INPL.

Baykara, S.Z., Bilgen, E., 1985. Synthesis gas and H2 production from solar gasification of albertan coal. Energy Convers. Manag. 25, 391–398. https://doi.org/10.1016/0196-8904(85)90002-0

Bell, D.A., Towler, B.F., Fan, M., 2011. Coal gasification and its applications, 1st ed. ed. Oxford, U.K William Andrew/Elsevier.

Bellan, S., Kodama, T., Matsubara, K., Gokon, N., Cho, H.S., Inoue, K., 2018a. Thermal performance of a 30 kW fluidized bed reactor for solar gasification: A CFD-DEM study. Chem. Eng. J. https://doi.org/10.1016/j.cej.2018.10.111

Bellan, S., Matsubara, K., Cho, H.S., Gokon, N., Kodama, T., 2018b. A CFD-DEM study of hydrodynamics with heat transfer in a gas-solid fluidized bed reactor for solar thermal

applications. Int. J. Heat Mass Transf. 116, 377–392. https://doi.org/10.1016/j.ijheatmasstransfer.2017.09.015
Bellouard, Q., 2017. Biomass valorization into energy vector through solar thermochemical conversion (Theses). Université de Perpignan Via Domita.
Bellouard, Q., Abanades, S., Rodat, S., 2017a. Biomass Gasification in an Innovative Spouted-Bed Solar Reactor: Experimental Proof of Concept and Parametric Study. Energy Fuels 31, 10933–10945. https://doi.org/10.1021/acs.energyfuels.7b01839
Bellouard, Q., Abanades, S., Rodat, S., Dupassieux, N., 2017b. A high temperature drop-tube and packed-bed solar reactor for continuous biomass gasification. AIP Conf. Proc. 1850, 100001. https://doi.org/10.1063/1.4984458
Bellouard, Q., Rodat, S., Abanades, S., Ravel, S., Frayssines, P.-É., 2018. Design, simulation and experimental study of a directly-irradiated solar chemical reactor for hydrogen and syngas production from continuous solar-driven wood biomass gasification. Int. J. Hydrog. Energy. https://doi.org/10.1016/j.ijhydene.2018.04.147
Bilbao, J., Olazar, M., Romera, A., 1987. Design and Operation of a Jet Spouted Bed Reactor with Continuous Catalyst Feed in the Benzyl Alcohol Polymerization.
Billaud, J., 2015. Gazéification de la biomasse en réacteur à flux entrainé : études expérimentales et modélisation (thesis). Ecole nationale des Mines d'Albi-Carmaux.
Billaud, J., Valin, S., Peyrot, M., Salvador, S., 2016. Influence of H2O, CO2 and O-2 addition on biomass gasification in entrained flow reactor conditions: Experiments and modelling. Fuel 166, 166–178. https://doi.org/10.1016/j.fuel.2015.10.046
Bonnie, J.M., Sanford, G., Martin, A.R., 1993. Coefficients for Calculating Thermodynamic and Transport Properties of Individual Species (NASA Technical Memorandum No. 4513).
Boudet, N., Marion, P., Roy-Auberger, M., 2009. Gazéification du charbon. Tech. Ing.
Boujjat, H., Rodat, S., Chuayboon, S., Abanades, S., 2020a. Experimental and CFD investigation of inert bed materials effects in a high-temperature conical cavity-type reactor for continuous solar-driven steam gasification of biomass. Chem. Eng. Sci. 228, 115970. https://doi.org/10.1016/j.ces.2020.115970
Boujjat, H., Rodat, S., Chuayboon, S., Abanades, S., 2019a. Numerical simulation of reactive gas-particle flow in a solar jet spouted bed reactor for continuous biomass gasification. Int. J. Heat Mass Transf. 144, 118572. https://doi.org/10.1016/j.ijheatmasstransfer.2019.118572
Boujjat, H., Rodat, S., Chuayboon, S., Abanades, S., 2019b. Experimental and numerical study of a directly irradiated hybrid solar/combustion spouted bed reactor for continuous steam gasification of biomass. Energy 189, 116118. https://doi.org/10.1016/j.energy.2019.116118
Boujjat, H., Yuki Junior, G.M., Rodat, S., Abanades, S., 2020b. Dynamic simulation and control of solar biomass gasification for hydrogen-rich syngas production during allothermal and hybrid solar/autothermal operation. Int. J. Hydrog. Energy. https://doi.org/10.1016/j.ijhydene.2020.01.072
Bracken, N., Macknick, J., Tover-Hastings, A., Komor, P., Gerritsen, M., Mehta, S., 2015. Concentrating Solar Power and Water Issues in the U.S. Southwest (Technical Report No. NREL/TP-6A50-61376).
Brezinsky, K., Pecullan, M., Glassman, I., 1998. Pyrolysis and Oxidation of Phenol. J. Phys. Chem. A 102, 8614–8619. https://doi.org/10.1021/jp982177+
Bruckner, A.P., 1985. Continuous duty solar coal gasification system using molten slag and direct-contact heat exchange. Sol. Energy 34, 239–247. https://doi.org/10.1016/0038-092X(85)90061-1
Burkhardt, J.J., Heath, G., Cohen, E., 2012. Life Cycle Greenhouse Gas Emissions of Trough and Tower Concentrating Solar Power Electricity Generation. J. Ind. Ecol. 16, S93–S109. https://doi.org/10.1111/j.1530-9290.2012.00474.x
Carbon Tracker REPORT, 2018. Carbon Countdown: Prices and Politics in the EU-ETS [WWW Document]. Carbon Tracker Initiat. URL https://carbontracker.org/reports/carbon-countdown/ (accessed 7.20.20).
Chan, W.-C.R., Kelbon, M., Krieger, B.B., 1985. Modelling and experimental verification of physical and chemical processes during pyrolysis of a large biomass particle. Fuel 64, 1505–1513. https://doi.org/10.1016/0016-2361(85)90364-3

Charvin, P., Abanades, S., Neveu, P., Lemont, F., Flamant, G., 2008a. Dynamic modeling of a volumetric solar reactor for volatile metal oxide reduction. Chem. Eng. Res. Des. 86, 1216–1222. https://doi.org/10.1016/j.cherd.2008.05.009

Charvin, P., Stéphane, A., Florent, L., Gilles, F., 2008b. Analysis of solar chemical processes for hydrogen production from water splitting thermochemical cycles. Energy Convers. Manag. 49, 1547–1556. https://doi.org/10.1016/j.enconman.2007.12.011

Chavez, P., Kolb, G., Meinecke, W., 1993. Second generation central receiver technologies.

Chen, L., 2009. Fast pyrolysis of millimetric wood particles between 800°C and 1000°C (thesis). Lyon 1.

Cheynet, B., Chevalier, P.-Y., Fischer, E., 2002. Thermosuite. Calphad 26, 167–174. https://doi.org/10.1016/S0364-5916(02)00033-0

Cortazar, M., Alvarez, J., Lopez, G., Amutio, M., Santamaria, L., Bilbao, J., Olazar, M., 2018. Role of temperature on gasification performance and tar composition in a fountain enhanced conical spouted bed reactor. Energy Convers. Manag. 171, 1589–1597. https://doi.org/10.1016/j.enconman.2018.06.071

Cortazar, M., Lopez, G., Alvarez, J., Amutio, M., Bilbao, J., Olazar, M., 2018a. Advantages of confining the fountain in a conical spouted bed reactor for biomass steam gasification. Energy 153, 455–463. https://doi.org/10.1016/j.energy.2018.04.067

Cortazar, M., Lopez, G., Alvarez, J., Amutio, M., Bilbao, J., Olazar, M., 2018b. Advantages of confining the fountain in a conical spouted bed reactor for biomass steam gasification. Energy 153, 455–463. https://doi.org/10.1016/j.energy.2018.04.067

Craig F. Bohren, Donald R. Huffman, 2007. Absorption and Scattering of Light by Small Particles, in: Absorption and Scattering of Light by Small Particles. John Wiley & Sons, Ltd, pp. i–xiv. https://doi.org/10.1002/9783527618156.fmatter

CSP Projects Around the World - Solarpaces [WWW Document], n.d. URL https://www.solarpaces.org/csp-technologies/csp-projects-around-the-world/ (accessed 7.5.20).

Cui, H., Grace, J.R., 2008. Spouting of biomass particles: A review. Bioresour. Technol. 99, 4008–4020. https://doi.org/10.1016/j.biortech.2007.04.048

Dai, S., Chang, Z., Chang, C., Akhatov, J.S., Li, X., 2019. Numerical study on the directly-irradiated vortex reactor for solar CO2 coal gasification. Sol. Energy 188, 573–585. https://doi.org/10.1016/j.solener.2019.06.035

Dall'Ora, M., Jensen, P.A., Jensen, A.D., 2008. Suspension Combustion of Wood: Influence of Pyrolysis Conditions on Char Yield, Morphology, and Reactivity. Energy Fuels 22, 2955–2962. https://doi.org/10.1021/ef800136b

Das, B., Bhattacharya, A., Datta, A., 2020. Kinetic modeling of biomass gasification and tar formation in a fluidized bed gasifier using equivalent reactor network (ERN). Fuel 280, 118582. https://doi.org/10.1016/j.fuel.2020.118582

Delgado, J., Aznar, M.P., Corella, J., 1996. Calcined Dolomite, Magnesite, and Calcite for Cleaning Hot Gas from a Fluidized Bed Biomass Gasifier with Steam: Life and Usefulness. Ind. Eng. Chem. Res. 35, 3637–3643. https://doi.org/10.1021/ie950714w

Deng, Z., Xiao, R., Jin, B., Huang, H., Shen, L., Song, Q., Li, Q., 2008. Computational Fluid Dynamics Modeling of Coal Gasification in a Pressurized Spout-Fluid Bed. Energy Fuels 22, 1560–1569. https://doi.org/10.1021/ef7007437

Di Blasi, C., 2009. Combustion and gasification rates of lignocellulosic chars. Prog. Energy Combust. Sci. 35, 121–140. https://doi.org/10.1016/j.pecs.2008.08.001

Di Blasi, C., 2008. Modeling chemical and physical processes of wood and biomass pyrolysis. Prog. Energy Combust. Sci. 34, 47–90. https://doi.org/10.1016/j.pecs.2006.12.001

Di Blasi, C., 1998. Comparison of semi-global mechanisms for primary pyrolysis of lignocellulosic fuels. J. Anal. Appl. Pyrolysis 47, 43–64. https://doi.org/10.1016/S0165-2370(98)00079-5

Di Blasi, C., 1997. Influences of physical properties on biomass devolatilization characteristics. Fuel 76, 957–964. https://doi.org/10.1016/S0016-2361(97)00096-3

Di Blasi, C., 1993. Modeling and simulation of combustion processes of charring and non-charring solid fuels. Prog. Energy Combust. Sci. 19, 71–104. https://doi.org/10.1016/0360-1285(93)90022-7

Dömény, J., Koiš, V., Dejmal, A., 2014. Microwave Radiation Effect on Axial Fluid Permeability in False Heartwood of Beech (Fagus sylvatica L.). BioResources 9, 372–380.
Elfasakhany, A., Klason, T., Bai, X.S., 2008. Modelling of pulverised wood combustion using a functional group model. Combust. Theory Model. 12, 883–904. https://doi.org/10.1080/13647830802094344
Erkiaga, A., Lopez, G., Amutio, M., Bilbao, J., Olazar, M., 2013. Steam gasification of biomass in a conical spouted bed reactor with olivine and γ-alumina as primary catalysts. Fuel Process. Technol. 116, 292–299. https://doi.org/10.1016/j.fuproc.2013.07.008
État de l'art de la production et de l'utilisation de combustibles solides de... [WWW Document], 2012. . ADEME. URL https://www.ademe.fr/etat-lart-production-lutilisation-combustibles-solides-recuperation (accessed 7.21.20).
Fermoso, J., Stevanov, C., Moghtaderi, B., Arias, B., Pevida, C., Plaza, M.G., Rubiera, F., Pis, J.J., 2009. High-pressure gasification reactivity of biomass chars produced at different temperatures. J. Anal. Appl. Pyrolysis, Pyrolysis 2008 85, 287–293. https://doi.org/10.1016/j.jaap.2008.09.017
Fernández-García, A., Cantos-Soto, M.E., Röger, M., Wieckert, C., Hutter, C., Martínez-Arcos, L., 2014. Durability of solar reflector materials for secondary concentrators used in CSP systems. Sol. Energy Mater. Sol. Cells 130, 51–63. https://doi.org/10.1016/j.solmat.2014.06.043
Fletcher, E.A., Moen, R.L., 1977. Hydrogen- and Oxygen from Water. Science 197, 1050–1056. https://doi.org/10.1126/science.197.4308.1050
Fraile Daniel, Lanoix Jean-Christophe, Maio Patrick, Rangel Azalea, TORRES Angelica, 2015. Overview of the market segmentation for hydrogen across potential customer groups, based on key application areas.
Fuller, E.N., Schettler, P.D., Giddings, J.C., 1966. NEW METHOD FOR PREDICTION OF BINARY GAS-PHASE DIFFUSION COEFFICIENTS. Ind. Eng. Chem. 58, 18–27. https://doi.org/10.1021/ie50677a007
Fushimi, C., Wada, T., Tsutsumi, A., 2011. Inhibition of steam gasification of biomass char by hydrogen and tar. Biomass Bioenergy 35, 179–185. https://doi.org/10.1016/j.biombioe.2010.08.017
Gadsby, J., C Hinshelwood, Sykes, K.., 1946. The kinetics of the reactions of the steam-carbon system. London.
Gao, X., Zhang, Y., Bao, F., Li, B., Zhao, Y., Ke, C., Jiang, B., 2018. CFD modeling of sawdust gasification in a lab-scale entrained flow reactor based on char intrinsic kinetics. Part 1: Model development. Chem. Eng. Process. - Process Intensif. 125, 280–289. https://doi.org/10.1016/j.cep.2018.02.017
Gauché, P., Rudman, J., Mabaso, M., Landman, W.A., von Backström, T.W., Brent, A.C., 2017. System value and progress of CSP. Sol. Energy, Progress in Solar Energy Special Issue: Concentrating Solar Power (CSP) 152, 106–139. https://doi.org/10.1016/j.solener.2017.03.072
Gelderbloom, S.J., Gidaspow, D., Lyczkowski, R.W., 2003. CFD Simulations of bubbling/collapsing fluidized beds for three Geldart Groups. AIChE J. 49, 844–858. https://doi.org/10.1002/aic.690490405
Gidaspow, D., Bezburuah, R., Ding, J., 1991. Hydrodynamics of circulating fluidized beds: Kinetic theory approach (No. CONF-920502-1). Illinois Inst. of Tech., Chicago, IL (United States). Dept. of Chemical Engineering.
Gokon, N., Ono, R., Hatamachi, T., Liuyun, L., Kim, H.-J., Kodama, T., 2012. CO2 gasification of coal cokes using internally circulating fluidized bed reactor by concentrated Xe-light irradiation for solar gasification. Int. J. Hydrog. Energy, 12th CHEC 37, 12128–12137. https://doi.org/10.1016/j.ijhydene.2012.05.133
Gómez-Barea, A., Leckner, B., 2010. Modeling of biomass gasification in fluidized bed. Prog. Energy Combust. Sci. 36, 444–509. https://doi.org/10.1016/j.pecs.2009.12.002
Gore, R., Crowe, C., 2012. Observations on the flow in a confined coaxial jet, in: 1st National Fluid Dynamics Conference. American Institute of Aeronautics and Astronautics. https://doi.org/10.2514/6.1988-3591

Graf, D., Monnerie, N., Roeb, M., Schmitz, M., Sattler, C., 2008. Economic comparison of solar hydrogen generation by means of thermochemical cycles and electrolysis. Int. J. Hydrog. Energy 33, 4511–4519. https://doi.org/10.1016/j.ijhydene.2008.05.086

Gregg, D.W., Taylor, R.W., Campbell, J.H., Taylor, J.R., Cotton, A., 1980. Solar gasification of coal, activated carbon, coke and coal and biomass mixtures. Sol. Energy 25, 353–364. https://doi.org/10.1016/0038-092X(80)90347-3

Grønli, M.G., Melaaen, M.C., 2000. Mathematical Model for Wood PyrolysisComparison of Experimental Measurements with Model Predictions. Energy Fuels 14, 791–800. https://doi.org/10.1021/ef990176q

Guizani, C., Escudero Sanz, F.J., Salvador, S., 2015. Influence of temperature and particle size on the single and mixed atmosphere gasification of biomass char with H2O and CO2. Fuel Process. Technol. 134, 175–188. https://doi.org/10.1016/j.fuproc.2015.01.031

Guizani, C., Valin, S., Billaud, J., Peyrot, M., Salvador, S., 2017. Biomass fast pyrolysis in a drop tube reactor for bio oil production: Experiments and modeling. Fuel 207, 71–84. https://doi.org/10.1016/j.fuel.2017.06.068

Gunn, D.J., 1978. Transfer of heat or mass to particles in fixed and fluidised beds. Int. J. Heat Mass Transf. 21, 467–476. https://doi.org/10.1016/0017-9310(78)90080-7

Guo, P., Saw, W., van Eyk, P., Ashman, P., Nathan, G., Stechel, E., 2015. Fischer-tropschliquid Fuel Production by Co-gasification of Coal and Biomass in a Solar Hybrid Dual Fluidized Bed Gasifier. Energy Procedia, International Conference on Concentrating Solar Power and Chemical Energy Systems, SolarPACES 2014 69, 1770–1779. https://doi.org/10.1016/j.egypro.2015.03.147

Hathaway, B.J., Davidson, J.H., 2017. Demonstration of a prototype molten salt solar gasification reactor. Sol. Energy 142, 224–230. https://doi.org/10.1016/j.solener.2016.12.032

Hathaway, B.J., Kittelson, D.B., Davidson, J.H., 2014. Development of a Molten Salt Reactor for Solar Gasification of Biomass. Energy Procedia, Proceedings of the SolarPACES 2013 International Conference 49, 1950–1959. https://doi.org/10.1016/j.egypro.2014.03.207

Helman, U., 2017. Chapter 26 - Economic and Reliability Benefits of Solar Plants, in: Jones, L.E. (Ed.), Renewable Energy Integration (Second Edition). Academic Press, Boston, pp. 351–372. https://doi.org/10.1016/B978-0-12-809592-8.00026-3

Hinkley, J.T., Hayward, J.A., Curtin, B., Wonhas, A., Boyd, R., Grima, C., Tadros, A., Hall, R., Naicker, K., 2013. An analysis of the costs and opportunities for concentrating solar power in Australia. Renew. Energy 57, 653–661. https://doi.org/10.1016/j.renene.2013.02.020

Horn, C., Roy, K., Frank, P., Just, T., 1998. Shock-tube study on the high-temperature pyrolysis of phenol. Symp. Int. Combust., Twenty-Seventh Sysposium (International) on Combustion Volume One 27, 321–328. https://doi.org/10.1016/S0082-0784(98)80419-0

Huilin, L., Gidaspow, D., 2003. Hydrodynamics of binary fluidization in a riser: CFD simulation using two granular temperatures. Chem. Eng. Sci. 58, 3777–3792. https://doi.org/10.1016/S0009-2509(03)00238-0

Hydrogen - Chemical Economics Handbook (CEH) | IHS Markit [WWW Document], 2018. URL https://ihsmarkit.com/products/hydrogen-chemical-economics-handbook.html (accessed 7.14.20).

Ibrahimoglu, B., Cucen, A., Yilmazoglu, M.Z., 2017. Numerical modeling of a downdraft plasma gasification reactor. Int. J. Hydrog. Energy 42, 2583–2591. https://doi.org/10.1016/j.ijhydene.2016.06.224

IEA Bioenergy, 2018. Hydrogen from biomass gasification (No. Task 33).

IRENA, 2017. Renewable Energy Statistics 2017 [WWW Document]. Publ.-Energy-Stat.-2017. URL /publications/2017/Jul/Renewable-Energy-Statistics-2017 (accessed 7.5.20).

IRENA, 2012. Renewable Power Generation Costs in 2012: An Overview [WWW Document]. Publ.-Power-Gener.-Costs--2012--Overv. URL /publications/2013/Jan/Renewable-Power-Generation-Costs-in-2012-An-Overview (accessed 7.5.20).

Ismail, T.M., Abd El-Salam, M., Monteiro, E., Rouboa, A., 2018. Fluid dynamics model on fluidized bed gasifier using agro-industrial biomass as fuel. Waste Manag. 73, 476–486. https://doi.org/10.1016/j.wasman.2017.06.018

Iwasaki, T., Suzuki, S., Kojima, T., 2014. Influence of Biomass Pyrolysis Temperature, Heating Rate and Type of Biomass on Produced Char in a Fluidized Bed Reactor. Energy Environ. Res. 4, p64. https://doi.org/10.5539/eer.v4n2p64

Janajreh, I., Al Shrah, M., 2013. Numerical and experimental investigation of downdraft gasification of wood chips. Energy Convers. Manag., Global Conference on Renewable energy and Energy Efficiency for Desert Regions 2011 "GCREEDER 2011" 65, 783–792. https://doi.org/10.1016/j.enconman.2012.03.009

Jeong, H.J., Seo, D.K., Hwang, J., 2014. CFD modeling for coal size effect on coal gasification in a two-stage commercial entrained-bed gasifier with an improved char gasification model. Appl. Energy 123, 29–36.

Johnson, P.C., Jackson, R., 1987. Frictional–collisional constitutive relations for granular materials, with application to plane shearing. J. Fluid Mech. 176, 67–93. https://doi.org/10.1017/S0022112087000570

Jones, E., Oliphant, T., Peterson, P., 2001. Open Source Scientific Tools for Python [WWW Document]. URL https://www.scipy.org/ (accessed 2.4.20).

Joseph O. Hirschfelder, Charles F. Curtiss, R. Byron Bird, 1964. The Molecular Theory of Gases and Liquids | Wiley [WWW Document]. Wiley.com. URL https://www.wiley.com/en-us/The+Molecular+Theory+of+Gases+and+Liquids-p-9780471400653 (accessed 8.20.20).

Kaniyal, A.A., van Eyk, P.J., Nathan, G.J., Ashman, P.J., Pincus, J.J., 2013. Polygeneration of Liquid Fuels and Electricity by the Atmospheric Pressure Hybrid Solar Gasification of Coal. Energy Fuels 27, 3538–3555. https://doi.org/10.1021/ef400198v

Kelbaliyev, G.I., 2011. Drag coefficients of variously shaped solid particles, drops, and bubbles. Theor. Found. Chem. Eng. 45, 248–266. https://doi.org/10.1134/S0040579511020084

Keown, D.M., Favas, G., Hayashi, J., Li, C.-Z., 2005. Volatilisation of alkali and alkaline earth metallic species during the pyrolysis of biomass: differences between sugar cane bagasse and cane trash. Bioresour. Technol. 96, 1570–1577. https://doi.org/10.1016/j.biortech.2004.12.014

Kharaghani, A., Le, K.H., Tran, T.T.H., Tsotsas, E., 2019. Reaction engineering approach for modeling single wood particle drying at elevated air temperature. Chem. Eng. Sci. 199, 602–612. https://doi.org/10.1016/j.ces.2019.01.042

Khosasaeng, T., Suntivarakorn, R., 2017. Effect of Equivalence Ratio on an Efficiency of Single Throat Downdraft Gasifier Using RDF from Municipal solid waste. Energy Procedia, 2017 International Conference on Alternative Energy in Developing Countries and Emerging Economies 138, 784–788. https://doi.org/10.1016/j.egypro.2017.10.066

Kikuchi, K., Suzuki, A., Mochizuki, T., Endo, S., Imai, E., Tanji, Y., 1985. Ash-agglomerating gasification of coal in a spouted bed reactor. Fuel 64, 368–372. https://doi.org/10.1016/0016-2361(85)90426-0

Klose, W., Wölki, M., 2005. On the intrinsic reaction rate of biomass char gasification with carbon dioxide and steam. Fuel 84, 885–892. https://doi.org/10.1016/j.fuel.2004.11.016

Kodama, T., Gokon, N., Enomoto, S., Itoh, S., Hatamachi, T., 2010. Coal Coke Gasification in a Windowed Solar Chemical Reactor for Beam-Down Optics. J. Sol. Energy Eng. 132. https://doi.org/10.1115/1.4002081

Kodama, T., Kondoh, Y., Tamagawa, T., Funatoh, A., Shimizu, K.-I., Kitayama, Y., 2002. Fluidized Bed Coal Gasification with CO2 under Direct Irradiation with Concentrated Visible Light. Energy Fuels 16, 1264–1270. https://doi.org/10.1021/ef020053x

Kojima, T., Assavadakorn, P, Furusawa, T, 1993. Measurement and evaluation of gasification kinetics of sawdust char with steam in an experimental fluidized bed. Fuel Process. Technol.

Kromer, M., Roth, K., Takata, R., Chin, P., 2011. Support for Cost Analyses on Solar-Driven High Temperature Thermochemical Water-Splitting Cycles. (No. D0535). TIAX LLC.

Kruesi, M., Jovanovic, Z.R., dos Santos, E.C., Yoon, H.C., Steinfeld, A., 2013. Solar-driven steam-based gasification of sugarcane bagasse in a combined drop-tube and fixed-bed reactor – Thermodynamic, kinetic, and experimental analyses. Biomass Bioenergy 52, 173–183. https://doi.org/10.1016/j.biombioe.2013.03.003

Ku, X., Li, T., Løvås, T., 2015. CFD–DEM simulation of biomass gasification with steam in a fluidized bed reactor. Chem. Eng. Sci. 122, 270–283. https://doi.org/10.1016/j.ces.2014.08.045

Ku, X., Li, T., Løvås, T., 2014. Eulerian–Lagrangian Simulation of Biomass Gasification Behavior in a High-Temperature Entrained-Flow Reactor. Energy Fuels 28, 5184–5196. https://doi.org/10.1021/ef5010557
Kucuk, H., Midilli, A., Kilic, A., Dincer, I., 2014. A Review on Thin-Layer Drying-Curve Equations. Dry. Technol. 32, 757–773. https://doi.org/10.1080/07373937.2013.873047
Kumar, U., Salem, A.M., Paul, M.C., 2017. Investigating the thermochemical conversion of biomass in a downdraft gasifier with a volatile break-up approach. Energy Procedia, Proceedings of the 9th International Conference on Applied Energy 142, 822–828. https://doi.org/10.1016/j.egypro.2017.12.132
Kwon, E., Westby, K.J., Castaldi, M.J., 2010. Transforming Municipal Solid Waste (MSW) Into Fuel via the Gasification/Pyrolysis Process. Presented at the 18th Annual North American Waste-to-Energy Conference, American Society of Mechanical Engineers Digital Collection, pp. 53–60. https://doi.org/10.1115/NAWTEC18-3559
Letcher, T.M., 2020. Future Energy: Improved, Sustainable and Clean Options for Our Planet. Elsevier.
Li, C., Suzuki, K., 2009. Tar property, analysis, reforming mechanism and model for biomass gasification—An overview. Renew. Sustain. Energy Rev. 13, 594–604. https://doi.org/10.1016/j.rser.2008.01.009
Li, X., Shen, Y., Kan, X., Hardiman, T.K., Dai, Y., Wang, C.-H., 2018. Thermodynamic assessment of a solar/autothermal hybrid gasification CCHP system with an indirectly radiative reactor. Energy 142, 201–214. https://doi.org/10.1016/j.energy.2017.09.149
Liu, H., Cattolica, R.J., Seiser, R., 2016. CFD studies on biomass gasification in a pilot-scale dual fluidized-bed system. Int. J. Hydrog. Energy 41, 11974–11989. https://doi.org/10.1016/j.ijhydene.2016.04.205
Liu, H., Elkamel, A., Lohi, A., Biglari, M., 2014. Effect of Char Combustion Product Distribution Coefficient on the CFD Modeling of Biomass Gasification in a Circulating Fluidized Bed. Ind. Eng. Chem. Res. 53, 5554–5563. https://doi.org/10.1021/ie404239u
Lopez, G., Cortazar, M., Alvarez, J., Amutio, M., Bilbao, J., Olazar, M., 2017. Assessment of a conical spouted with an enhanced fountain bed for biomass gasification. Fuel 203, 825–831. https://doi.org/10.1016/j.fuel.2017.05.014
Lopez, G., Erkiaga, A., Amutio, M., Bilbao, J., Olazar, M., 2015. Effect of polyethylene co-feeding in the steam gasification of biomass in a conical spouted bed reactor. Fuel 153, 393–401. https://doi.org/10.1016/j.fuel.2015.03.006
Loutzenhiser, P.G., Muroyama, A.P., 2017. A review of the state-of-the-art in solar-driven gasification processes with carbonaceous materials. Sol. Energy, Advances in Solar Thermochemistry 156, 93–100. https://doi.org/10.1016/j.solener.2017.05.008
Lovegrove, Stein, 2012. Concentrating Solar Power Technology [WWW Document]. URL https://www.sciencedirect.com/book/9781845697693/concentrating-solar-power-technology (accessed 7.14.20).
Lu, D., Yoshikawa, K., Ismail, T.M., Abd El-Salam, M., 2018. Assessment of the carbonized woody briquette gasification in an updraft fixed bed gasifier using the Euler-Euler model. Appl. Energy 220, 70–86. https://doi.org/10.1016/j.apenergy.2018.03.063
Luan, Y.-T., Chyou, Y.-P., Wang, T., 2013. Numerical analysis of gasification performance via finite-rate model in a cross-type two-stage gasifier. Int. J. Heat Mass Transf. 57, 558–566. https://doi.org/10.1016/j.ijheatmasstransfer.2012.10.026
Mahinpey, N., Gomez, A., 2016. Review of gasification fundamentals and new findings: Reactors, feedstock, and kinetic studies. Chem. Eng. Sci. 148, 14–31. https://doi.org/10.1016/j.ces.2016.03.037
Makibar, J., Aranzazu R., F.-A., Diaz, L., Gartzen, L., Olazar, M., 2011. Pilot scale conical spouted bed pyrolysis reactor: Draft tube selection and hydrodynamic performance - ScienceDirect [WWW Document]. URL https://www.sciencedirect.com/science/article/pii/S0032591011006826 (accessed 4.11.18).
Manyà, J.J., Velo, E., Puigjaner, L., 2003. Kinetics of Biomass Pyrolysis: a Reformulated Three-Parallel-Reactions Model. Ind. Eng. Chem. Res. 42, 434–441. https://doi.org/10.1021/ie020218p

Marinov, N.M., Pitz, W.J., Westbrook, C.K., Vincitore, A.M., Castaldi, M.J., Senkan, S.M., Melius, C.F., 1998. Aromatic and Polycyclic Aromatic Hydrocarbon Formation in a Laminar Premixed n-Butane Flame. Combust. Flame 114, 192–213. https://doi.org/10.1016/S0010-2180(97)00275-7

Markowski, Kaminski, 1983. Hydrodynamic characteristics of jet-spouted beds - Markowski -The Canadian Journal of Chemical Engineering - Wiley Online Library [WWW Document]. URL http://onlinelibrary.wiley.com/doi/10.1002/cjce.5450610318/full (accessed 1.8.18).

Materazzi, M., Lettieri, P., Taylor, R., Chapman, C., 2016. Performance analysis of RDF gasification in a two stage fluidized bed–plasma process. Waste Manag., Refuse Derived Fuel/Solid Recovered Fuel 47, 256–266. https://doi.org/10.1016/j.wasman.2015.06.016

Mathur, K.B., Gishler, P.E., 1955. A technique for contacting gases with coarse solid particles. AIChE J. 1, 157–164. https://doi.org/10.1002/aic.690010205

Meerman, J.C., Ramírez, A., Turkenburg, W.C., Faaij, A.P.C., 2012. Performance of simulated flexible integrated gasification polygeneration facilities, Part B: Economic evaluation. Renew. Sustain. Energy Rev. 16, 6083–6102. https://doi.org/10.1016/j.rser.2012.06.030

Miller, R.S., Harstad, K., Bellan, J., 1998. Evaluation of equilibrium and non-equilibrium evaporation models for many-droplet gas-liquid flow simulations. Int. J. Multiph. Flow 24, 1025–1055.

Milne, T.A., Evans, R.J., Abatzaglou, N., 1998. Biomass Gasifier "'Tars'": Their Nature, Formation, and Conversion (No. NREL/TP-570-25357; ON: DE00003726). National Renewable Energy Laboratory, Golden, CO (US). https://doi.org/10.2172/3726

Möller, S., Kaucic, D., Sattler, C., 2006. Hydrogen Production by Solar Reforming of Natural Gas: A Comparison Study of Two Possible Process Configurations. J. Sol. Energy Eng. 128, 16–23. https://doi.org/10.1115/1.2164447

Morf, P., Hasler, P., Nussbaumer, T., 2002. Mechanisms and kinetics of homogeneous secondary reactions of tar from continuous pyrolysis of wood chips. Fuel 81, 843–853. https://doi.org/10.1016/S0016-2361(01)00216-2

Mühlen, H.-J., van Heek, K.H., Jüntgen, H., 1985. Kinetic studies of steam gasification of char in the presence of H2, CO2 and CO. Fuel 64, 944–949. https://doi.org/10.1016/0016-2361(85)90149-8

Mularski, J., Pawlak-Kruczek, H., Modlinski, N., 2020. A review of recent studies of the CFD modelling of coal gasification in entrained flow gasifiers, covering devolatilization, gas-phase reactions, surface reactions, models and kinetics. Fuel 271, 117620. https://doi.org/10.1016/j.fuel.2020.117620

Müller, F., Poživil, P., Eyk, P.J. van, Villarrazo, A., Haueter, P., Wieckert, C., Nathan, G.J., Steinfeld, A., 2017. A pressurized high-flux solar reactor for the efficient thermochemical gasification of carbonaceous feedstock. Fuel C, 432–443. https://doi.org/10.1016/j.fuel.2016.12.036

Muroyama, A.P., Guscetti, I., Schieber, G.L., Haussener, S., Loutzenhiser, P.G., 2018. Design and demonstration of a prototype 1.5kWth hybrid solar/autothermal steam gasifier. Fuel 211, 331–340. https://doi.org/10.1016/j.fuel.2017.09.059

Myöhänen, K., Palonen, J., Hyppänen, T., 2018. Modelling of indirect steam gasification in circulating fluidized bed reactors. Fuel Process. Technol. 171, 10–19. https://doi.org/10.1016/j.fuproc.2017.11.006

Nagashima, H., Ishikura, T., Ide, M., 2009. Effect of the tube shape on gas and particle flow in spouted beds with a porous draft tube. Can. J. Chem. Eng. 87, 228–236. https://doi.org/10.1002/cjce.20150

Nakod, P., 2013. CFD Modeling and Validation of Oxy-Fired and Air-Fired Entrained Flow Gasifiers.

Nocquet, T., 2012. Torréfaction du bois et de ses constituants : expériences et modélisation des rendements en matières volatiles (phd).

Nowakowska, M., 2014. Conversion thermique des goudrons provenant de la gazéification de la biomasse (phdthesis). Université de Lorraine.

NREL H2A, 2018. H2A: Hydrogen Analysis Production Models | Hydrogen and Fuel Cells | NREL [WWW Document]. URL https://www.nrel.gov/hydrogen/h2a-production-models.html (accessed 7.7.20).

NREL REPORT, 2012. Utility-Scale Concentrating Solar Power and Photovoltaics Projects: A Technology and Market Overview (Technical Report No. NREL/TP-6A20-51137).
Olazar, M., López, G., Altzibar, H., Aguado, R., Bilbao, J., 2009. Minimum spouting velocity under vacuum and high temperature in conical spouted beds. Can. J. Chem. Eng. 87, 541–546. https://doi.org/10.1002/cjce.20183
Olazar, M., San Jose, M.J., Aguayo, A.T., Arandes, J.M., Bilbao, J., 1992. Stable operation conditions for gas-solid contact regimes in conical spouted beds. Ind. Eng. Chem. Res. 31, 1784–1792. https://doi.org/10.1021/ie00007a025
Olazar, M., San Jose, M.J., Penas, F.J., Aguayo, A.T., Bilbao, J., 1993. Stability and hydrodynamics of conical spouted beds with binary mixtures. Ind. Eng. Chem. Res. 32, 2826–2834. https://doi.org/10.1021/ie00023a053
Ollero, P., Serrera, A., Arjona, R., Alcantarilla, S., 2003. The CO2 gasification kinetics of olive residue. Biomass Bioenergy 24, 151–161. https://doi.org/10.1016/S0961-9534(02)00091-0
Ordorica-Garcia, G., Douglas, P., Croiset, E., Zheng, L., 2006. Technoeconomic evaluation of IGCC power plants for CO2 avoidance. Energy Convers. Manag. 47, 2250–2259. https://doi.org/10.1016/j.enconman.2005.11.020
Pandey, K.M., Chaurasiya, R., 2017. A review on analysis and development of solar flat plate collector. Renew. Sustain. Energy Rev. 67, 641–650. https://doi.org/10.1016/j.rser.2016.09.078
Paterson, N., Reed, G.P., Dugwell, D.R., Kandiyoti, R., 2002. Gasification Tests With Sewage Sludge and Coal/Sewage Sludge Mixtures in a Pilot Scale, Air Blown, Spouted Bed Gasifier 197–202. https://doi.org/10.1115/GT2002-30013
Perret, C., Chataing, T., 2019. Systeme d'alimentation en poudre a partir de granules, procede et installation de gazeification de charge de matiere carbonee dans un reacteur a flux entraine (rfe) utilisant un tel systeme. FR3059572B1.
Pescheux, A.-C., Le Baron, E., Raccurt, O., 2019. Characterization of different Moroccan sands to explain their potential negative impacts on CSP solar mirrors. Sol. Energy 194, 959–968. https://doi.org/10.1016/j.solener.2019.11.020
Pfahl, A., 2014. Survey of Heliostat Concepts for Cost Reduction. J. Sol. Energy Eng. 136. https://doi.org/10.1115/1.4024243
Piatkowski, N., Wieckert, C., Steinfeld, A., 2009. Experimental investigation of a packed-bed solar reactor for the steam-gasification of carbonaceous feedstocks. Fuel Process. Technol. 90, 360–366. https://doi.org/10.1016/j.fuproc.2008.10.007
Pidaparthi, A., Hoffmann, J., 2017. Effect of heliostat size on the levelized cost of electricity for power towers. AIP Conf. Proc. 1850, 030038. https://doi.org/10.1063/1.4984381
Pozzobon, V., Salvador, S., Bézian, J.J., El-Hafi, M., Le Maoult, Y., Flamant, G., 2014. Radiative pyrolysis of wet wood under intermediate heat flux: Experiments and modelling. Fuel Process. Technol. 128, 319–330. https://doi.org/10.1016/j.fuproc.2014.07.007
Puig-Arnavat, M., Tora, E.A., Bruno, J.C., Coronas, A., 2013. State of the art on reactor designs for solar gasification of carbonaceous feedstock. Sol. Energy 97, 67–84. https://doi.org/10.1016/j.solener.2013.08.001
Qi, T., Lei, T., Yan, B., Chen, G., Li, Z., Fatehi, H., Wang, Z., Bai, X.-S., 2019. Biomass steam gasification in bubbling fluidized bed for higher-H2 syngas: CFD simulation with coarse grain model. Int. J. Hydrog. Energy 44, 6448–6460. https://doi.org/10.1016/j.ijhydene.2019.01.146
Quinet, 2008. Rapport de la commission présidée par A. Quinet, La valeur tutélaire du carbone, Centre d'Analyse Stratégique, 2008.
Ranz, Marshsal, 1952. Evaporation from Drops, Part I and Part II", Chemical engineering progress. ed.
REN21, 2019. RENEWABLES 2019 GLOBAL STATUS REPORT [WWW Document]. URL https://www.ren21.net/gsr-2019 (accessed 7.5.20).
REN21, 2014. RENEWABLES 2014 GLOBAL STATUS REPORT [WWW Document]. URL https://www.ren21.net/gsr-2014 (accessed 7.5.20).
Roberts, D.G., Harris, D.J., 2007. Char gasification in mixtures of CO2 and H2O: Competition and inhibition. Fuel 86, 2672–2678. https://doi.org/10.1016/j.fuel.2007.03.019
Rodat, S., 2010. Production d'hydrogène et de noirs de carbone par décomposition thermique de gaz naturel dans des réacteurs solaires.

Romankov, Rashkovskaya, 1979. Drying in Suspension State.
Romero, M., Steinfeld, A., 2012. Concentrating solar thermal power and thermochemical fuels. Energy Environ. Sci. 5, 9234–9245. https://doi.org/10.1039/C2EE21275G
Ross, R.J., 2010. Wood handbook : wood as an engineering material. USDA For. Serv. For. Prod. Lab. Gen. Tech. Rep. FPL- GTR-190 2010 509 P 1 V 190. https://doi.org/10.2737/FPL-GTR-190
S. A. Morsi, A. J. Alexander, 1972. An investigation of Particle trajectories in Two-Phase Flow Systems., 55(2):193-208. ed. J. Fluid Mech.
Safari, F., Dincer, I., 2020. A review and comparative evaluation of thermochemical water splitting cycles for hydrogen production. Energy Convers. Manag. 205, 112182. https://doi.org/10.1016/j.enconman.2019.112182
San Jose, M.J., Olazar, M., Penas, F.J., Bilbao, 1994. Segregation in Conical Spouted Beds with Binary and Ternary Mixtures of Equidensity Spherical Particles - Industrial & Engineering Chemistry Research (ACS Publications) [WWW Document]. URL http://pubs.acs.org/doi/abs/10.1021/ie00031a025 (accessed 1.8.18).
San Jose, Olazar, M., Aguayo, A.T., Bilbao, J., 1991. Design and Hydrodynamics of Conical Jet Spouted Beds.
SANDIA REPORT, 2007. Heliostat Cost Reduction Study (No. SAND2007-3293).
Sangtong-ngam, K., Narasingha, M.H., 2008. Kinetic Study of Thai-lignite Char Gasification Using the Random Pore Model, International journal of science and technology. ed.
Sargent & Lundy, 2003. Assessment of Parabolic Trough and Power Tower Solar Technology Cost and Performance Forecasts (No. NREL/SR-550-34440).
Saw, Kaniyal, A., van Eyk, P., Nathan, G., Ashman, P., 2015. Solar Hybridized Coal-to-liquids via Gasification in Australia: Techno-economic Assessment. Energy Procedia, International Conference on Concentrating Solar Power and Chemical Energy Systems, SolarPACES 2014 69, 1819–1827. https://doi.org/10.1016/j.egypro.2015.03.158
Saw, W.L., Guo, P., van Eyk, P.J., Nathan, G.J., 2017. Approaches to accommodate resource variability in the modelling of solar driven gasification processes for liquid fuels synthesis. Sol. Energy, Advances in Solar Thermochemistry 156, 101–112. https://doi.org/10.1016/j.solener.2017.05.085
Saw, W.L., Pang, S.S., 2012. Influence of mean gas residence time in the bubbling fluidised bed on the performance of a 100-kW dual fluidised bed steam gasifier. Biomass Convers. Biorefinery 2, 197–205. https://doi.org/10.1007/s13399-012-0036-4
Sazhin, S.S., 2006. Advanced models of fuel droplet heating and evaporation. Prog. Energy Combust. Sci. 32, 162–214. https://doi.org/10.1016/j.pecs.2005.11.001
SCACCHI Gérard, BOUCHY Michel, FOUCAUT Jean-François, ZAHRAA Orfan, FOURNET René, 2011. Cinétique et catalyse [WWW Document]. Libr. Lavoisier. URL https://www.lavoisier.fr/livre/chimie/cinetique-et-catalyse-2-ed/scacchi/descriptif-9782743013929 (accessed 7.6.20).
Schmidt, O., Gambhir, A., Staffell, I., Hawkes, A., Nelson, J., Few, S., 2017. Future cost and performance of water electrolysis: An expert elicitation study. Int. J. Hydrog. Energy 42, 30470–30492. https://doi.org/10.1016/j.ijhydene.2017.10.045
Septien, S., Escudero Sanz, F.J., Salvador, S., Valin, S., 2018. The effect of pyrolysis heating rate on the steam gasification reactivity of char from woodchips. Energy 142, 68–78. https://doi.org/10.1016/j.energy.2017.09.114
Septien, S., Valin, S., Peyrot, M., Dupont, C., Salvador, S., 2014. Characterization of char and soot from millimetric wood particles pyrolysis in a drop tube reactor between 800°C and 1400°C. Fuel 121, 216–224. https://doi.org/10.1016/j.fuel.2013.12.026
Septien, S., Valin, S., Peyrot, M., Spindler, B., Salvador, S., 2013. Influence of steam on gasification of millimetric wood particles in a drop tube reactor: Experiments and modelling. Fuel 103, 1080–1089. https://doi.org/10.1016/j.fuel.2012.09.011
Silaen, A., Wang, T., 2010. Effect of turbulence and devolatilization models on coal gasification simulation in an entrained-flow gasifier. Int. J. Heat Mass Transf. 53, 2074–2091. https://doi.org/10.1016/j.ijheatmasstransfer.2009.12.047

Singh, R.I., Brink, A., Hupa, M., 2013. CFD modeling to study fluidized bed combustion and gasification. Appl. Therm. Eng. 52, 585–614. https://doi.org/10.1016/j.applthermaleng.2012.12.017
Skjøth-Rasmussen, M.S., Glarborg, P., Østberg, M., Johannessen, T., Livbjerg, H., Jensen, A., Christensen, T.S., 2004. Formation of polycyclic aromatic hydrocarbons and soot in fuel-rich oxidation of methane in a laminar flow reactor. Combust. Flame 136, 91–128. https://doi.org/10.1016/j.combustflame.2003.09.011
Spath, P., Aden, A., Eggeman, T., Ringer, M., Wallace, B., Jechura, J., 2005. Biomass to Hydrogen Production Detailed Design and Economics Utilizing the Battelle Columbus Laboratory Indirectly Heated Gasifier. (No. TP-510-37408). NREL Report.
Spreutels, L., Chaouki, J., Bertrand, F., Haut, B., Legros, R., 2016. Gas residence time distribution in a conical spouted bed. Powder Technol., Fluid-particle systems A special issue to commemorate the retirement of Professor John R. Grace 290, 62–71. https://doi.org/10.1016/j.powtec.2015.07.033
Steinfeld, A., 2002. Solar hydrogen production via a two-step water-splitting thermochemical cycle based on Zn/ZnO redox reactions. Int. J. Hydrog. Energy 27, 611–619. https://doi.org/10.1016/S0360-3199(01)00177-X
Steinfeld, A., Meier, A., 2004. Solar Fuels and Materials, in: Cleveland, C.J. (Ed.), Encyclopedia of Energy. Elsevier, New York, pp. 623–637. https://doi.org/10.1016/B0-12-176480-X/00322-3
Sudiro, M., Bertucco, A., 2007. Synthetic Fuels by a Limited CO2 Emission Process Which Uses Both Fossil and Solar Energy. Energy Fuels 21, 3668–3675. https://doi.org/10.1021/ef7003255
Sue-A-Quan, T.A., Cheng, G., Watkinson, A.P., 1995. Coal gasification in a pressurized spouted bed. Fuel 74, 159–164. https://doi.org/10.1016/0016-2361(95)92649-Q
Syamlal, M., Rogers, W., O`Brien, T.J., 1993. MFIX documentation theory guide (No. DOE/METC-94/1004). USDOE Morgantown Energy Technology Center, WV (United States). https://doi.org/10.2172/10145548
Tagutchou, J.-P., 2008. Gazéification du charbon de plaquettes forestières : particule isolée et lit fixe continu (thesis). Université de Perpignan.
Taylor, R.W., Berjoan, R., Coutures, J.P., 1983a. Solar gasification of carbonaceous materials. Sol. Energy 30, 513–525. https://doi.org/10.1016/0038-092X(83)90063-4
Taylor, R.W., Berjoan, R., Coutures, J.P., 1983b. Solar gasification of carbonaceous materials. Sol. Energy 30, 513–525. https://doi.org/10.1016/0038-092X(83)90063-4
Teixeira, G., 2012. Gazéification de charbon de granules de bois : comportement thermochimique et mécanique d'un lit fixe continu (phd).
Tian, M., Su, Y., Zheng, H., Pei, G., Li, G., Riffat, S., 2018. A review on the recent research progress in the compound parabolic concentrator (CPC) for solar energy applications. Renew. Sustain. Energy Rev. 82, 1272–1296. https://doi.org/10.1016/j.rser.2017.09.050
Tomaszewicz, M., Tomaszewicz, G., Sciazko, M., 2017. Experimental study on kinetics of coal char–CO2 reaction by means of pressurized thermogravimetric analysis. J. Therm. Anal. Calorim. 130, 2315–2330. https://doi.org/10.1007/s10973-017-6538-3
Trieb, F., Schillings, C., O'Sullivan, M., Pregger, T., Hoyer-Klick, C., 2009. Global potential of concentrating solar power. SolarPACES.
Ursua, A., Gandia, L.M., Sanchis, P., 2012. Hydrogen Production From Water Electrolysis: Current Status and Future Trends. Proc. IEEE 100, 410–426. https://doi.org/10.1109/JPROC.2011.2156750
Valin, S., Ravel, S., Pons de Vincent, P., Thiery, S., Miller, H., 2019. Fluidized bed air gasification of solid recovered fuel and woody biomass: Influence of experimental conditions on product gas and pollutant release. Fuel 242, 664–672. https://doi.org/10.1016/j.fuel.2019.01.094
Van de steene, L., Tagutchou, J.P., Escudero Sanz, F.J., Salvador, S., 2011. Gasification of woodchip particles: Experimental and numerical study of char–H2O, char–CO2, and char–O2 reactions. Chem. Eng. Sci. 66, 4499–4509. https://doi.org/10.1016/j.ces.2011.05.045
Van der Drift, A., Boerrigter, H., Coda, B., Cieplik, M.K., Hemmes, K., 2004. Entrained flow gasification of biomass. Ash behaviour, feeding issues, system analyses (Technical Report) | ETDEWEB [WWW Document]. URL https://www.osti.gov/etdeweb/biblio/20479502 (accessed 7.6.20).

van Heek, K.H., Mühlen, H.-J., 1991. Chemical Kinetics of Carbon and Char Gasification, in: Lahaye, J., Ehrburger, P. (Eds.), Fundamental Issues in Control of Carbon Gasification Reactivity, NATO ASI Series. Springer Netherlands, Dordrecht, pp. 1–34. https://doi.org/10.1007/978-94-011-3310-4_1
Vander Wal, R.L., Tomasek, A.J., 2004. Soot nanostructure: dependence upon synthesis conditions. Combust. Flame 136, 129–140. https://doi.org/10.1016/j.combustflame.2003.09.008
Vigouroux, R.Z., 2001. Zanzi R., « Pyrolysis of biomass ».
Wagner, N.J., Coertzen, M., Matjie, R.H., van Dyk, J.C., 2008. Chapter 5 - Coal Gasification, in: Suárez-Ruiz, I., Crelling, J.C. (Eds.), Applied Coal Petrology. Elsevier, Burlington, pp. 119–144. https://doi.org/10.1016/B978-0-08-045051-3.00005-1
Wang, G., Silva, R.B., Azevedo, J.L.T., Martins-Dias, S., Costa, M., 2014. Evaluation of the combustion behaviour and ash characteristics of biomass waste derived fuels, pine and coal in a drop tube furnace. Fuel 117, 809–824. https://doi.org/10.1016/j.fuel.2013.09.080
Wang, J., 2008. High-resolution Eulerian simulation of RMS of solid volume fraction fluctuation and particle clustering characteristics in a CFB riser. Chem. Eng. Sci. 63, 3341–3347. https://doi.org/10.1016/j.ces.2008.03.041
Wang, J., Ma, C., Wu, J., 2019. Thermodynamic analysis of a combined cooling, heating and power system based on solar thermal biomass gasification☆. Appl. Energy 247, 102–115. https://doi.org/10.1016/j.apenergy.2019.04.039
Weinstein, L.A., Loomis, J., Bhatia, B., Bierman, D.M., Wang, E.N., Chen, G., 2015. Concentrating Solar Power. Chem. Rev. 115, 12797–12838. https://doi.org/10.1021/acs.chemrev.5b00397
Whitaker, S., 1977. Simultaneous Heat, Mass, and Momentum Transfer in Porous Media: A Theory of Drying, in: Hartnett, J.P., Irvine, T.F. (Eds.), Advances in Heat Transfer. Elsevier, pp. 119–203. https://doi.org/10.1016/S0065-2717(08)70223-5
Wieckert, C., Obrist, A., Zedtwitz, P. von, Maag, G., Steinfeld, A., 2013. Syngas Production by Thermochemical Gasification of Carbonaceous Waste Materials in a 150 kWth Packed-Bed Solar Reactor [WWW Document]. https://doi.org/10.1021/ef4008399
Williams, P.T., Besler, S., 1996. The influence of temperature and heating rate on the slow pyrolysis of biomass. Renew. Energy 7, 233–250. https://doi.org/10.1016/0960-1481(96)00006-7
Wu, F., Yang, C., Che, X., Ma, X., Yan, Y., Zhou, W., 2020. Numerical and experimental study of integral multi-jet structure impact on gas-solid flow in a 3D spout-fluidized bed. Chem. Eng. J. 393, 124737. https://doi.org/10.1016/j.cej.2020.124737
Wu, H., Liu, Q., Bai, Z., Xie, G., Zheng, J., Su, B., 2020. Thermodynamics analysis of a novel steam/air biomass gasification combined cooling, heating and power system with solar energy. Appl. Therm. Eng. 164, 114494. https://doi.org/10.1016/j.applthermaleng.2019.114494
Xiao, P., Guo, L., Zhang, X., Zhu, C., Ma, S., 2013. Continuous hydrogen production by biomass gasification in supercritical water heated by molten salt flow: System development and reactor assessment. Int. J. Hydrog. Energy 38, 12927–12937. https://doi.org/10.1016/j.ijhydene.2013.04.139
Xiao, Y., Xu, S., Tursun, Y., Wang, C., Wang, G., 2017. Catalytic steam gasification of lignite for hydrogen-rich gas production in a decoupled triple bed reaction system. Fuel 189, 57–65. https://doi.org/10.1016/j.fuel.2016.10.078
Xiong, Q., Zhang, J., Xu, F., Wiggins, G., Stuart Daw, C., 2016. Coupling DAEM and CFD for simulating biomass fast pyrolysis in fluidized beds. J. Anal. Appl. Pyrolysis 117, 176–181. https://doi.org/10.1016/j.jaap.2015.11.015
Xue, Q., Fox, R.O., 2014. Multi-fluid CFD modeling of biomass gasification in polydisperse fluidized-bed gasifiers. Powder Technol. 254, 187–198. https://doi.org/10.1016/j.powtec.2014.01.025
Yadav, D., Banerjee, R., 2016. A review of solar thermochemical processes. Renew. Sustain. Energy Rev. 54, 497–532. https://doi.org/10.1016/j.rser.2015.10.026
Ye, B., Lim, C.J., Grace, J.R., 1992. Hydrodynamics of spouted and spout-fluidized beds at high temperature. Can. J. Chem. Eng. 70, 840–847. https://doi.org/10.1002/cjce.5450700504
Yogev, A., Kribus, A., Epstein, M., Kogan, A., 1998. Solar "tower reflector" systems: A new approach for high-temperature solar plants. Int. J. Hydrog. Energy 23, 239–245. https://doi.org/10.1016/S0360-3199(97)00059-1

Yu, L., Lu, J., Zhang, X., Zhang, S., 2007. Numerical simulation of the bubbling fluidized bed coal gasification by the kinetic theory of granular flow (KTGF). Fuel 86, 722–734. https://doi.org/10.1016/j.fuel.2006.09.008

Zacarías, L., Steinfeld, A., Vidal, A., Denk, T., 2010. Upscaling of a 500kW Solar Gasification Plant. Presented at the 18th World Hydrogen Energy Conference, International Association for Hydrogen Energy (IAHE).

Z'Graggen, A., Haueter, P., Trommer, D., Romero, M., de Jesus, J.C., Steinfeld, A., 2006. Hydrogen production by steam-gasification of petroleum coke using concentrated solar power—II Reactor design, testing, and modeling. Int. J. Hydrog. Energy 31, 797–811. https://doi.org/10.1016/j.ijhydene.2005.06.011

Zhong, W., Xiao, R., Zhang, M., 2006. Experimental study of gas mixing in a spout-fluid bed. AIChE J. 52, 924–930. https://doi.org/10.1002/aic.10708

VI. ANNEX 1

VI.1 Comparison between REACSOL design and literature recommendations

Table VI.1 compares the main REACSOL design features with those recommended for conical spouted beds.

Table VI.1 REACSOL design features vs. main literature recommendations

	Recommendations (Olazar et al., 1992)	REACSOL
Inlet design	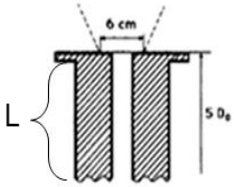	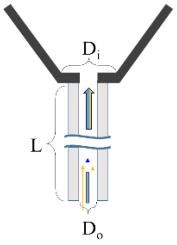
Injection tube length (L)	$L>5.D_o$	L=34 mm (Argon injection) and D_o=2 mm
Inlet diameter	$1/2<D_o/D_i<5/6$ $1<D_o/d_p<80$	$D_o/D_i=1/2$ D_o/d_p ~ 2 considering 1 mm diameter wood particles
Cone angle (γ)	28°< γ <45°	γ =60°

For a stable operation, the inlet design should be properly designed and should consist in an inlet tube of a diameter D_o fixed to a D_i diameter cone base. The injection tube needs to be cylindrical (not convergent) and its tip should not protrude beyond the conical base, which is the case for REACSOL. A small capillary inserted in the injection tube is used in the solar reactor to allow water liquid droplets injection. Under the effect of temperature, water evaporates and mixes with a stream of carrier gas (Ar) flowing through the annular zone of the tube. This does not seem to be an issue as long as a minimum distance of $5.D_o$ was respected between the capillary tip and the conical base to stabilize the flow. In REACSOL, a minimum distance of 2 cm (between the capillary and the cone base) was insured. It is recommended that the D_o/D_i ratio is between 1/2 and 5/6. REACSOL has a ratio of 1/2, which is at the lower limit but remains reasonable. The D_o/d_p ratio varies with the treated particles; globally, in the present thesis, the studied wood particles have an average diameter of 1 mm leading to a ratio $D_o/d_p=2$ which is in the recommended interval. Finally, narrow conical angles are recommended to optimize the stirring, for REACSOL, an angle of 60° was selected. The shallow configuration was preferred to minimize the thermal gradients and approach the black body behavior.

VI.2 Time scale characteristics

In order to describe the transfer phenomena inside the solar reactor, characteristic time scales and dimensionless numbers were calculated prior to detailed numerical simulation. Table VI.2 recaps the gas flow assumptions and the wood properties used in the calculations.

Table VI.2 Gas flow and wood properties assumptions

Gas	Mixture composition	6 vol.% of H_2O, 94% vol.% Ar
	Inlet: temperature-velocity-length	25°C-8.5 $m.s^{-1}$-2 mm
	Spout zone: temperature-velocity-length	600°C-2.0 $m.s^{-1}$-6 mm
	Annular zone: temperature-velocity- length	1000°C-0.1 $m.s^{-1}$-3.3 mm
	Operating pressure (P_{op})	860 hPa
Wood	Density ($\rho_{,wood}$)	650 $kg.m^{-3}$
	Heat capacity ($c_{p,wood}$)	1500 $J.°C^{-1}.kg^{-1}$
	Thermal conductivity (λ_{wood})	0.1 $W.m^{-1}.°C^{-1}$ (Ross, 2010)
	Emissivity (ε_{wood})	0.9 (Pozzobon et al., 2014)
	Permeability(K_{wood})	10^{-11}-10^{-13} m² (Dömény et al., 2014)
	Porosity (ω_{wood})	0.5 (Agoua and Perre, 2010)
	Tortuosity (τ_{wood})	1.5 (Nocquet, 2012)

For the sake of simplicity, the gas was composed of argon, being predominant inside the solar reactor and steam (e.g. 2.7 NL_{Ar}/min from window, hopper and alumina injection tube, 0.15 g_{steam}/min from the alumina injection tube). Gas mixture properties (μ, ρ, λ, c_p) were thereafter computed at different temperatures using the python *thermo package software*, details about the software correlations and equations can be found in (Bell, 2016). In order to get an appropriate approximation of the studied beech wood particles, wood properties such as emissivity, porosity, tortuosity, permeability and thermal conductivity were taken from the published literature on beech wood.

VI.2.1 Fluid dynamics

To get insights into the change in the flow dynamics and to quantify the level of turbulence inside the solar reactor, three Reynolds (Re) numbers were calculated: at the inlet tube, at the central spout and at the annular zone (Figure VI.1).

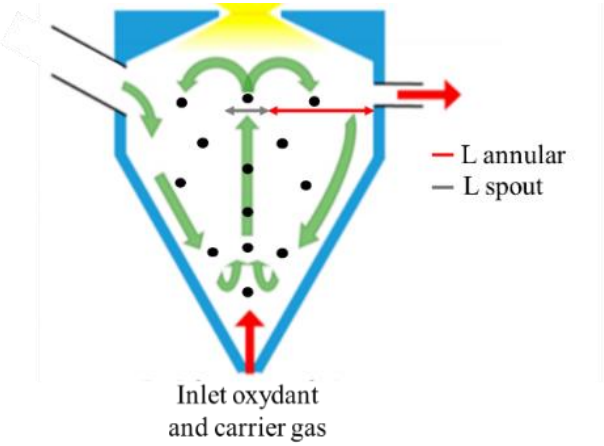

Figure VI.1 Particle trajectories inside the reactor and characteristic lengths definitions

The Reynolds number compares the time scale of the momentum transfer due to molecular diffusion and the momentum transfer by flow advection. It is expressed by Eq.VI.1

$$Re_k = \frac{\rho V_k L_k}{\mu} \qquad VI.1$$

Table VI.3 shows the calculated Re values for the three distinct regions of the reactor

Table VI.3 Reynolds number at different regions of the reactor

k	T (°C)	$\rho(kg.m^{-3})$	μ *(Pa.s)*	V_k (m.s^{-1})	L_k (m)	Re_k
Inlet	100	1.07	$2.68.10^{-5}$	8.5	0.002	680
Spout	600	0.46	$5.05.10^{-5}$	2	0.006	109
Annular	1000	0.31	$7.23.10^{-5}$	0.1	0.033	14

A continuous decline of Re throughout the cavity is highlighted with peak viscous effects at the annular region. These dissipative effects are expected to be more pronounced at the near hot wall regions where gas density is lower and viscosity is higher. The reactor small dimensions, small flow rates and high temperature are the three important factors that result in the low Reynolds numbers, which substantially limits the impact of turbulence on heat/mass transfer and mixing inside the solar-radiated cavity.

VI.2.2 Thermochemistry

The thermochemical conversion of a woody particle is the result of a number of physico-chemical mechanisms (Figure VI.2) (Klose and Wölki, 2005; Ollero et al., 2003; Scacchi al., 2011).

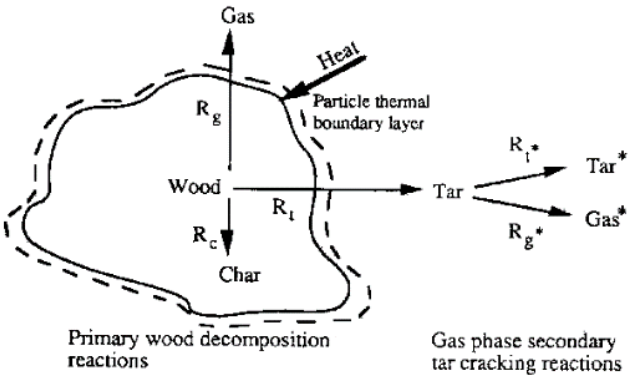

Figure VI.2 Reacting carbonaceous particle schematic

These mechanisms occur inside and outside the particle. In the beginning, the reactants are transported to the particle outer surface (through its boundary layer). Then, the reactants enter the particle porous matrix. If the thermochemical conditions are favorable (i.e. $\Delta G_{reaction}(T,P)<0$), surface chemical reactions take place at rate determined primarily by the particle temperature thanks' to a gas absorption/desorption mechanism. The produced vapors leave the particle firstly from its core to the solid/gas interface and secondly from the interface to the surrounding environment.

To gain a better understanding of the reactor operation, the importance of these mechanisms and their inherent contribution to the overall (i.e. apparent) process kinetics was evaluated. To do so, characteristic time scales of heat and mass transfer were calculated by dimensional analysis (Eqs.VI.2-VI.6). Pyrolysis and gasification time scales were deduced from first-order Arrhenius-like kinetic laws in which the time scale is equal to the inverse of the kinetic constant k (Eqs.VI.7-VI.8). The study was performed at the two regions of the reactor (spout and annular) following the assumptions of Table VI.2 and considering spherical particles.

The characteristic time scale equations are summarized below (Eqs.VI.2-VI.6).

External thermal convection: $t_{ext\ th\ conv} = \frac{\rho_{\mathrm{wood}}\, c_{\mathrm{p,wood}}\, d_{\mathrm{wood}}}{h_{th,c}}$ *VI.2*

External thermal radiation: $t_{ext\ th\ rad} = \frac{\rho_{\mathrm{wood}}\, c_{\mathrm{p,wood}}\, d_{\mathrm{wood}}}{h_{rad}}$ *VI.3*

Internal thermal conduction $t_{int\ th\ cond} = \frac{\rho_{\mathrm{wood}}\, c_{\mathrm{p,wood}}\, d_{\mathrm{wood}}{}^2}{\lambda_{wood}}$ *VI.4*

Internal mass convection: $t_{int\ mass\ conv} = \frac{\mu\, .d_{wood}{}^2}{P_{op} K_{wood}}$ *VI.5*

Internal mass diffusion $t_{int\ mass\ diff} = \frac{d_{\mathrm{wood}}{}^2}{D_{eff}}$ *VI.6*

Pyrolysis: $t_{py} = 1/A_{py}.e^{\frac{-E_{a,py}}{RT}}$ *VI.7*

Steam gasification: $t_{gasif} = 1/P_{ox}{}^{n}.A_{gasi}.e^{\frac{-E_{a,gasif}}{RT}}$ *VI.8*

$h_{th,c}$ in Eq.VI.2 is the thermal convection coefficient, it was calculated from the correlation of Ranz and Marshall (Ranz and Marshsal, 1952) (Eq.VI.9) assuming a spherical particle of a diameter d_{wood}.

$Nu = \frac{h_{th,c}.d_{fuel}}{\lambda} = 2 + 0.57.Re_{wood}{}^{1/2}.\mathrm{Pr}^{1/3}$ *VI.9*

h_{rad} in Eq.VI.3 is the radiative heat transfer coefficient, it was calculated under the assumption of grey body radiation according to Eq.VI.10 with T_{wall} =1200°C and $\varepsilon_{cavity,wall}$=0.7 (Table VI.1).

$$h_{rad} = \frac{\sigma_{rad}\left({T_{wall}}^2 + {T_{wood}}^2\right)}{\left(\frac{1}{\varepsilon_{wall}} + \frac{1}{\varepsilon_{wood}} - 1\right)\left(T_{wall} - T_{wood}\right)} \quad \textit{VI.10}$$

D_{eff} ($m^2.s^{-1}$) in Eq.VI.6 is the gas effective diffusivity; this parameter depends on the particle porosity, tortuosity and on the gas diffusivity (Eq.VI.11). Strictly speaking, gas diffusivity is a parameter that is specific to each gas in the mixture, since not all gases diffuse at the same rate. Here, the global diffusivity coefficient D was approximated by $D_{CO,Ar}$ involving CO and Ar. In fact, as these gases are largely present in the mixture, they were used to give a rough estimate of the global diffusivity. In this sense, $D_{CO,Ar}$ was calculated using the empirical equation (Eq.VI.12) of Fuller et al. (Fuller et al., 1966). With $\sum v$ the species atomic and structural diffusion-volume of gases.

$$D_{eff} = \frac{\omega_{wood}}{\tau_{wood}}.D \quad \textit{VI.11}$$

$$D_{CO,Ar} = 10^{-3}.\frac{T^{1.75}\sqrt{\left(\frac{1}{M_{w,CO}} + \frac{1}{M_{w,Ar}}\right)}}{P_{op}.\left\{\left(\sum v_{CO}\right)^{\frac{1}{3}} + \left(\sum v_{Ar}\right)^{\frac{1}{3}}\right\}^2} \quad \textit{VI.12}$$

The kinetic data of pyrolysis (Eq.VI.7) were: $A_{py}=1.5.10^4\ s^{-1}$ and $E_{a,py}$ =55kJ.mol^{-1} They were taken from the work of Wang et al. (Wang et al., 2014) who studied high temperature (T~1100°C) fast pyrolysis (Residence time ~1.7s) of different types of biomasses. The kinetic data of steam gasification (Eq.VI.8) were taken from the work of Kojima et al. (Kojima et al., 1993) who studied biomass char steam gasification in a fluidized bed reactor. The kinetic parameters were: n=0.41, $A_{gasif}=1773 s^{-1}.Pa^{-0.48}$ and $E_{a,gasif}=1.79.10^3$ kJ.mol^{-1}.

From this, six dimensionless numbers were computed. Table VI.4 shows the calculated dimensionless numbers for two wood particle diameters.

The Biot number Bi (Eq.IV.13) compares thermal conduction and thermal convection time scales. Its value is globally close to unity. The difference between the spout and annular regions is only slightly noticeable. In fact, even if the characteristic velocity of the annular zone is much lower than that of the spout zone (which greatly undermines convection), gas properties at higher temperature (μ/ρ (600°C) =$1.1.10^{-4}$ $m^2.s^{-1}$, μ/ρ (1000°C) =$2.3.10^{-4}$ $m^2.s^{-1}$; λ (600°C) =0.04 W.m^{-1}.°C^{-1}, λ (1000°C) =0.06 W.m^{-1}.°C^{-1}) are more interesting for heat transfer and therefore compensate the lower gas velocity. Moreover, Bi decreases with the particle diameter, reaching a minimum of 1.16 in the spout region due to a lower particle thermal inertia. Based on these results, heat conduction is an important limiting factor hindering heat propagation throughout the particle. Intraparticle thermal gradients may occur and affect to a certain extent, the reaction kinetics and the course of the reaction.

The estimation of the Boltzmann number Bo (Eq.VI.14) is insightful as the reactor is heated at above 1200°C. The Bo number compares the importance of thermal convection over radiation. The results show that both transfer modes are present during the conversion, and their contribution varies with the considered temperature and particle diameter.

Table VI.4 Dimensionless numbers

			Spout ***($T_{gas,wood}$ =600°C, V=2 m.s^{-1})***				***Annular*** ***($T_{gas,wood}$ =1000°C, V=0.1 m.s^{-1})***			
			d_{wood} (mm)							
Eqs			***0.1***		***1.0***		***0.1***		***1.0***	
VI.13	*Bi*	$t_{int,th\ cond}/t_{ext\ th\ conv}$	1.16		1.78		1.31		1.45	
VI.14	*Bo*	$t_{ext\ th\ rad}/t_{ext\ th\ conv}$	4.50		0.70		3.41		0.38	
VI.15	*Pe*	$t_{int\ mass\ diff}/t_{mass\ conv}$	***Permeability K_{wood} (m^2)***							
			10^{-13}	***10^{-11}***	***10^{-13}***	***10^{-11}***	***10^{-13}***	***10^{-11}***	***10^{-13}***	***10^{-11}***
			3.38	338.29	3.38	338.29	1.22	122.24	1.22	122.24
VI.16	*Le*	$t_{int,\ mass\ conv}/t_{int,th\ cond}$	$6.02.10^{-4}$	$6.02.10^{-6}$	$6.02.10^{-4}$	$6.02.10^{-6}$	$8.62.10^{-4}$	$8.62.10^{-6}$	$8.62.10^{-4}$	$8.62.10^{-6}$
VI.17	Da_{py}	$t_{int,th\ cond}/t_{py}$	0.74		74.66		8.07		807.96	
VI.18	Da_{gasif}	$t_{int,th\ cond}/t_{gasif}$	$4.63.10^{-8}$		$4.63.10^{-6}$		$1.00.10^{-4}$		0.01	

In fact, at d_{wood}=0.1mm, the characteristic time of external radiation is 3 to 5 times greater than that of convection (depending on the location inside the reactor), thus convection prevails mostly for the smallest particles. On the other hand, calculations at d_{wood}=1.0mm showed a trend reversal in the heating process, with a slightly more significant impact of radiation over thermal convection, especially in the annular zone.

The Peclet Pe (Eq.VI.15) and the Lewis Le (Eq. VI.16) numbers are also interesting to quantify. The former compares the time scale of internal mass transport by convection to the one taking place by diffusion, and the latter compares the convective mass transport time scale to that of heat conduction. The analysis of these numbers is carried out assuming two different coefficients of permeability (K_{wood}: 10^{-11}, 10^{-13} m²) as they vary a lot depending on the wood's nature and origin, its treatment and even during the thermochemical conversion. In all cases, Pe is greater than unity, meaning that the mass transport occurs predominantly inside the particle by convection. In fact, at K_{wood}= 10^{-11} m², the convective mass transport is hundreds of times higher than that of diffusion. It decreases to values approaching 1 by K_{wood} decrease to 10^{-13} m². Moreover, Pe in the annular region is 2-3 times lower than that in the spout zone. Due to enhanced gas diffusion. The very low Le values (i.e. <<1) confirm that under the reactor operating conditions, heat conduction is critically limiting the conversion of the woody particles.

Finally, heat conduction time scale is compared to that of the reaction (pyrolysis and gasification) thanks' to the calculation of the Damköhler number Da (Eqs.VI.17-VI.18). Large Da numbers (>>1) mean that the reaction is very fast and takes place as soon as the heat wave hits the particle active sites. In such configuration, the reactive front advances progressively into the unreacted biomass. This is largely verified for pyrolysis occurring above 1000°C especially for larger particle diameters. However, at lower temperature (i.e. in the spout) and for the smallest particles, chemical kinetic limitations can be expected as the Da_{py} number is less than unity. Da_{gasif} is on the other hand extremely low regardless of temperature and particle size. In fact, the gasification time scale was substantially higher than that of pyrolysis e.g. at 1000°C t_{gasif} ~15 min while t_{py}~0.012s.

The calculated Da_{gasif} values would in reality be somewhat higher than those indicated in (without changing anything to the conclusions drawn) as gasification concerns primary char particles, which under the effect of pyrolysis are thermally less resistant (i.e. lower density, heat capacity, size etc.).

VI.3 Patent applications

VI.3.1 Heat exchange intensification

A feature outlined thanks to 3D simulations especially in the indirect heating mode is shown in Figure VI.3-a, Run#1. It concerns the gas streamlines that impinge upon the emissive plate at the center. This flow configuration is known to provide optimal heat transfer rates (Arganbright and Resch, 1971) in thermal applications thereby offering the possibility to enhance the energy transfer from the emissive plate to the gas phase through enhanced thermal convection. The heat exchange can be further intensified in the studied reactor configuration thanks to the

reduction of cylindrical part height and also, the structuration of the plate (Figure VI.3-b). A patent application has been filed in this sense.

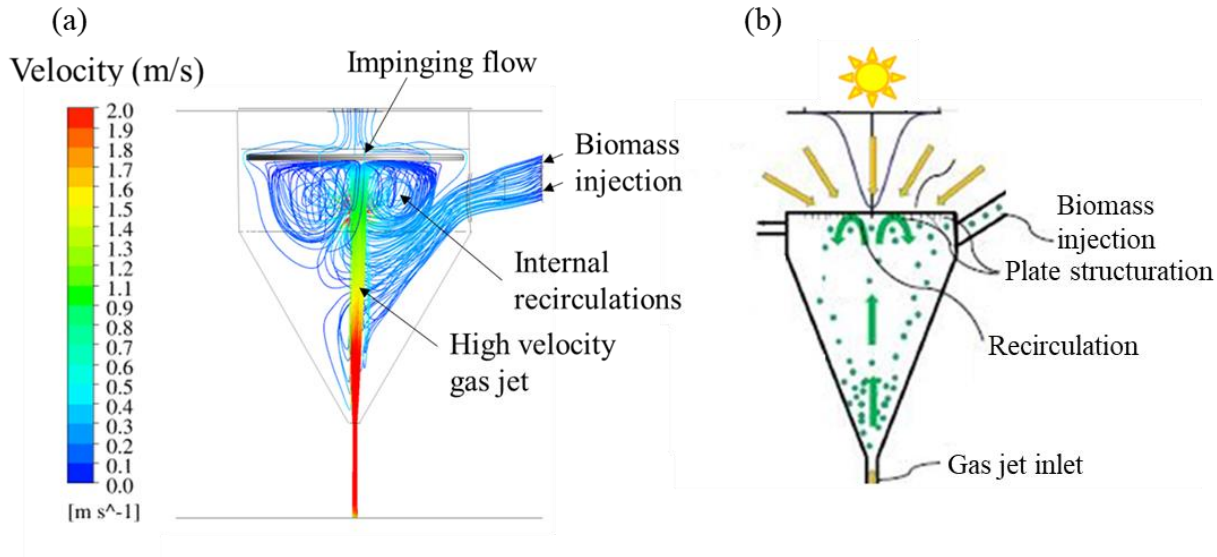

Figure VI.3 (a) Gas streamlines impinging upon the emissive plate (Indirect, Run#1 cf. section II.2); (b) New concept of a solar cavity with a structured emissive plate impinged by a gas jet

VI.3.2 Melting ash continuous evacuation

The proposed concept aims at continuously evacuating the melting ashes while insuring waste particles spouting. The principle is described in Figure VI.4 and Figure VI.5.

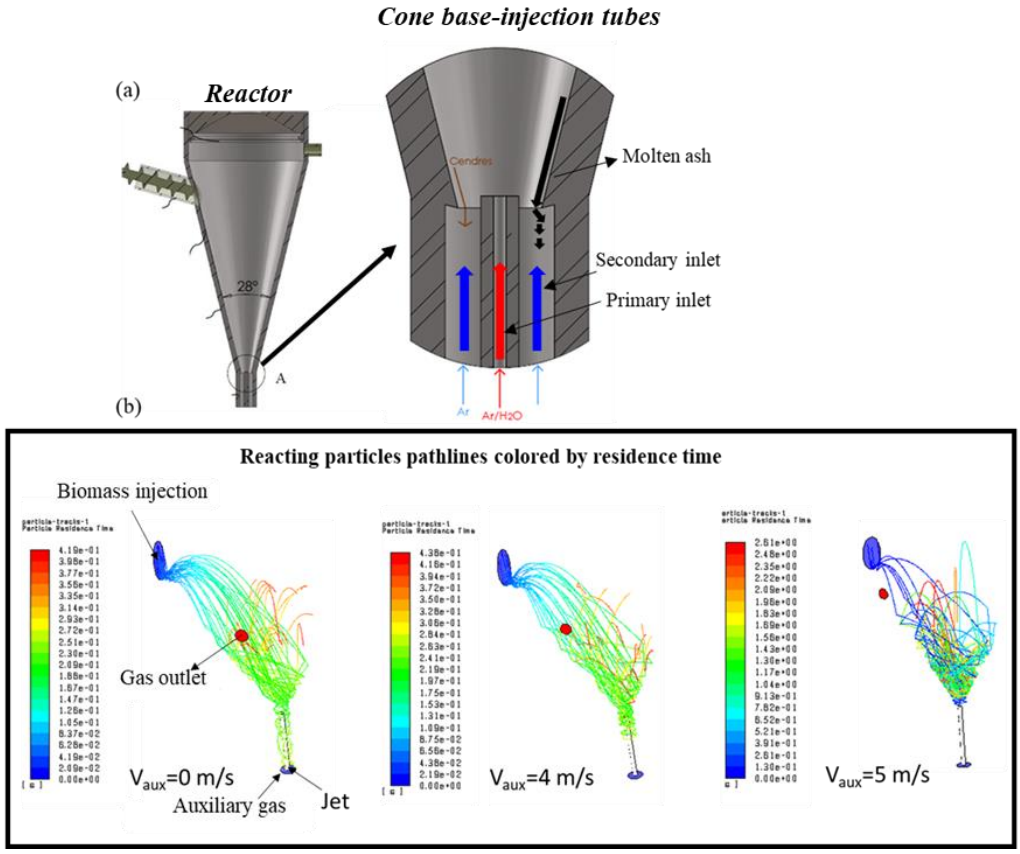

Figure VI.4 (a) New jet spouted bed reactor with improved ash removal; (b) sensitivity study using CFD of the impact of auxiliary gas inlet flow rate on the reacting particles pathlines

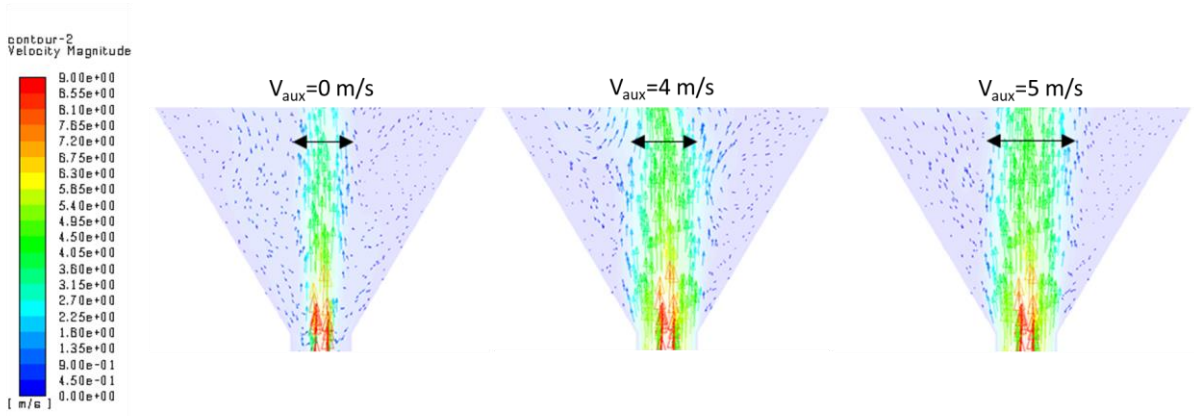

Figure VI.5 Impact of auxiliary gas velocity on the gas jet structure at the outlet of the injection tube

This technological variant is characterized by two gas inlets. The primary jet inlet (Ar/H_2O) is the main gas inlet. The secondary annular gas inlet allows molten ash continuous discharge. A minimum flow of auxiliary gas needs however to be injected into the secondary orifice to prevent the reacting particles from escaping downwards as shown in the simulations in Figure VI.4. These simulations were performed with biomass spherical particles of 650 $kg.m^{-3}$ density, a diameter of 1 mm and a flow rate of 2 $g.min^{-1}$. The velocity of the oxidizing gas jet in the central main tube was set to 9 $m.s^{-1}$ and the reactor operated at isothermal conditions (energy equation not solved to speed up the calculation) of 1000°C. The auxiliary gas jet velocity was increased from 0 $m.s^{-1}$ to 5 $m.s^{-1}$ to maintain the particles in the reaction zone.

VII. ANNEX 2

VII.1 Bed materials hydrodynamic simulations

A comparative study of the different powders flow dynamics (i.e SiC, Al_2O_3, olivine and sand) was carried out based on a purely hydrodynamic model (only momentum equations were solved to speed up calculations). Accordingly, gas (mixture of Ar and steam, see section III.3 for BCs, window flow rate set to 0 NL.min^{-1}) physical properties (ρ, μ) were assumed constant and were calculated at a fixed temperature. The choice of this temperature is important as it affects the velocity that spouts the beds (due to gas expansion) which in turn strongly influences the gas-particles flow patterns (Olazar et al., 2009). In the studied configuration, the gas flow entered the injection tube at ambient temperature where it was heated before reaching the cone entrance. The achieved temperature near the cone entrance in the empty configuration was around 400°C (cf. section II.2.6). This value was used as rough estimate of the actual temperature at which the spouting takes place. Under these conditions, the inlet gas velocity was calculated by Eq.VII.1. Where $\dot{m}_{exp}$ is the experimental inlet mass flow rate of Ar and H_2O. x_{H_2O} is the volume fraction of steam and $A_{\text{inlet tube}}$ the surface area of the alumina tube.

$$V_{inlet,spouting} = (\dot{m}_{Ar} + \dot{m}_{H_2O})_{exp} \Big/ \{(1 - x_{H_2O}).\rho_{Ar}(400°C) + x_{H_2O}.\rho_{H_2O}(400°C).A_{inlet\ tube}\} \quad \textit{VII.1}$$

The predicted solid particles space distributions for a 10g bed of SiC, Al_2O_3 olivine and sand are shown in Figure VII.1.

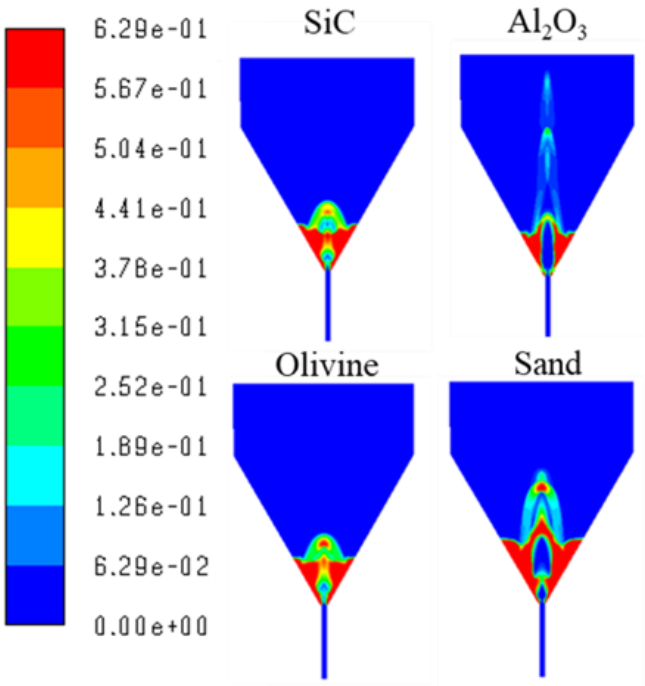

Figure VII.1 Inert particles space distribution (on volume basis) at experimental conditions (Time=2s), $V_{inlet,spout}$=6.91 m.s^{-1} cf. Chapter 3.

It is observed that the inlet gas flow rate was high enough to spout all the powders in a cyclic fashion without risk of entraining the finest ones (Al_2O_3 and sand) by the gas central jet stream. Moreover, for the SiC particles, the simulations pointed out that even if the inlet gas velocity was lower than the minimum spouting velocity measured during the cold tests, the spouting could still occur due to the increase in the gas kinematic viscosity. Furthermore, it is noted that the Al_2O_3 particles reached the highest degree of mixing with a fountain height that is three to four times the fountain height of the SiC and olivine particles while it roughly doubled the fountain height of the sand particles. Finally, as the olivine and SiC particles had very close characteristics (in terms of diameter and density); their solid flow patterns were almost identical.

The gas velocity magnitude is plotted in Figure VII.2 at a horizontal plan (p) for the empty, the Al_2O_3 and SiC spouted beds, and for the Al_2O_3 packed bed. Globally, for the empty and the Al_2O_3 spouted bed, the curves had a bell-like shape with peak velocity values approaching 5 $m.s^{-1}$ in the central region. The central gas velocities were significantly lower (~0.5 $m.s^{-1}$) with the SiC particles that somehow diverted the flow towards the annular region due to their larger size. In the packed bed configuration, the gas velocity profile was flattened showing more homogeneously distributed values over plan (p) with the lowest velocities of around 0.05 $m.s^{-1}$.

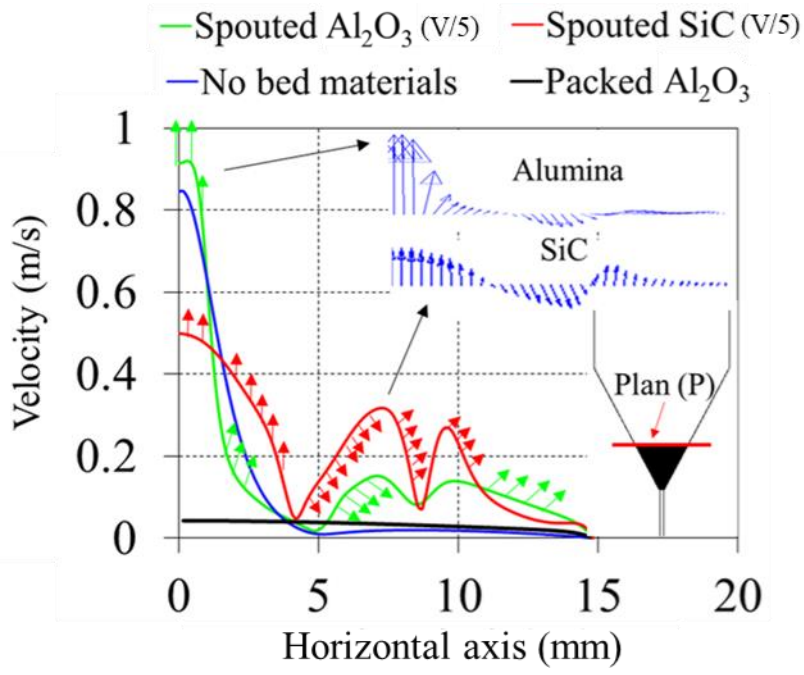

Figure VII.2 Gas velocity magnitude at a horizontal plan (plan (p)), vectors indicate flow direction

VII.2 Chemical equilibrium model for 0D simulations

The equilibrium gas yields were evaluated by minimizing the Gibbs free energy of the system. These calculations were performed using an in-house program developed in Python. The results were validated and compared with the GeMINI (Gibbs Energy MINImizer) software developed by Thermodata of the INPG (Institut National de Physique de Grenoble) and the CNRS (Cheynet et al., 2002). GeMINI is a largely validated chemical equilibrium code.

VII.2.1 Optimization problem formulation

The total free enthalpy of the system was calculated by summing the chemical potentials of each component i with Eq.VII.2, where NC indicates the number of components, n the number of moles and μ the chemical potential.

$$G_{total} = \sum_{i=1}^{NC} n_i \mu_i \qquad VII.2$$

The chemical potentials were obtained thanks to Eq.VII.3. The gases were considered ideal (i.e. ϕ=1). In the case of solids, such as carbon, the second term was not considered.

$$\mu_i = G_i^\circ + RT ln\left(\frac{\phi P_i}{P^\circ}\right) \qquad VII.3$$

Species standard Gibbs enthalpies were estimated based on the species enthalpies and entropies according to Eq.VII.4. The latter were calculated as a function of temperature using Eqs.VII.5-VII.6 (Bonnie et al., 1993).

$$G_i^\circ = H_i^\circ - T \cdot S_i^\circ \qquad VII.4$$

$$\frac{H^\circ(T)}{RT} = -a_1 T^{-2} + \frac{a_2 \ln(T)}{T} + a_3 + \frac{a_4 T}{2} + \frac{a_5 T^2}{3} + \frac{a_6 T^3}{4} + \frac{a_7 T^4}{5} + \frac{b_1}{T} \qquad VII.5$$

$$\frac{S^\circ(T)}{R} = -\frac{a_1 T^{-2}}{2} - a_2 T^{-1} + a_3 \ln(T) + a_4 T + \frac{a_5 T^2}{2} + \frac{a_6 T^3}{3} + \frac{a_7 T^4}{4} + b_2 \qquad VII.6$$

The equilibrium composition was calculated as a function of the atomic quantities in the reactor, pressure and temperature. The components in the reactor must satisfy the atomic balance of the reactor. This condition corresponds to the constraints of the optimization problem, which is represented by Eq.VII.7 , where N_j is the number of moles of atom j and ν_{ij} is the stoichiometric coefficient of an atom j in component i. In this code, only Ar, O_2, H_2O, H_2, CO, CH_4 and CO_2 gas components were considered.

$$N_j = \sum_i \nu_{ij} n_i \qquad VII.7$$

Eq.VII.8 represents the optimization problem and Eq.VII.9 represents the constraint to be met to obtain the chemical equilibrium composition. The partial pressures were calculated as a function of the number of moles using Eq.VII.10, where P is the reactor pressure and g indicates the gaseous components. This optimization problem is nonlinear. To solve it, a similar approach to that described by Kitchin (https://kitchingroup.cheme.cmu.edu/) was adopted. The numerical method used was hence the SLSQP (Sequential Least SQuares Programming) method of the Scipy library of Python.

$$N_j = \min_n \left(F_{obj} = \sum_{i=1}^{NC} \left(\frac{n_i G_i^\circ}{RT} + n_i ln\left(\frac{\phi P_i}{P^\circ}\right) \right) \right) \qquad VII.8$$

$$N_j = \sum_{i=1}^{NC} \nu_{ij} n_i \qquad VII.9$$

$$P_i = P \frac{n_i}{n_{total\ gas}} \qquad VII.10$$

VII.2.2 Validation

The values obtained with the two tools (in-house code and GeMINI) were compared (Table VII.1) at two different temperatures 1200°C and 600°C with a reactive system composed of 1.0 C, 2.35 H and 1.0 O. GeMINI performed the calculations considering all the components in its database (tars, light hydrocarbons etc.). For this reason, other components were predicted. They were not included in Table VII.1 as their quantities were less than 10^{-4} mol. The results show a suitable correlation between the two codes, with relative variations of less than 1% for H_2 and CO (main gases).

Table VII.1 Gas composition validation (0.9 bar, 1.0 C, 2.35 H and 1.0 O)

Components	1200 °C			600 °C		
	Python	Gemini	Relative variation	Python	Gemini	Relative variation
CH_4	1.48E-03	1.43E-03	3.219%	1.06E-01	1.07E-01	0.954%
CO	9.98E-01	9.98E-01	0.003%	1.91E-01	1.90E-01	0.081%
H_2	1.14E+00	1.14E+00	0.008%	6.21E-01	6.20E-01	0.192%
CO_2	3.88E-04	3.82E-04	1.518%	2.51E-01	2.52E-01	0.200%
H_2O	1.09E-03	1.07E-03	2.091%	3.07E-01	3.06E-01	0.279%
C	-	-	-	4.52E-01	4.51E-01	0.305%

The Python code allowed thus estimating the quantities of each component at equilibrium. Moreover, the results were consistent with those calculated by GeMINI and therefore it was integrated to the 0D dynamic physical model of the solar reactor to predict the time-dependent syngas flow rates during operation.

Résumé: La présente thèse propose d'étudier un réacteur solaire à jet pour la gazéification de biomasse de l'échelle du laboratoire à l'échelle industrielle en combinant simulations numériques et expérimentations. Un modèle numérique multiphysique a été développé à l'aide du logiciel de CFD Fluent© pour simuler la gazéification de particules de bois à la vapeur dans le réacteur solaire. Le modèle développé tient compte de l'écoulement diphasique solide/gaz grâce à une approche DPM (Discrete Phase Modelling) en interaction avec le rayonnement et la chimie. Une étape de validation expérimentale à 1200°C a montré des rendements sur gaz froid supérieurs à 1 grâce à la valorisation de l'énergie solaire et un taux de conversion du carbone approchant 80%. Le modèle a permis d'acquérir des informations clés sur le déroulement du processus de gazéification au sein de la cavité solaire et d'identifier des pistes d'amélioration du procédé. L'utilisation de matériaux de lit inertes en suspension dans la cavité s'est avérée judicieuse. Cette piste a été étudiée à la fois par simulation numérique grâce à une approche granulaire Eulérienne, puis sur banc expérimental à 1200°C et 1300°C. Une amélioration maximale relative du rendement carbone de 8% a ainsi été atteinte. L'un des obstacles critiques à l'extrapolation du réacteur est dû à la variabilité de l'énergie solaire qui entrave la continuité du procédé. Afin d'assurer une production continue de gaz indépendamment de la ressource solaire, l'hybridation du réacteur par oxy-combustion partielle de la charge a été étudiée. Il a été montré que l'injection contrôlée d'O_2 durant les périodes de faible énergie solaire est une solution pertinente pour contrôler la température du procédé. Un modèle dynamique 0D a ensuite été développé pour prédire l'évolution de la température et la production de syngaz à l'échelle du MW_{th} selon deux modes de chauffage : solaire et hybride solaire-combustion. Des simulations annuelles ont été par la suite réalisées pour prédire les performances du réacteur, la consommation des réactifs et les volumes de gaz produits. Ces données ont été utilisées pour analyser la faisabilité technico-économique du procédé pour la production industrielle de dihydrogène.

Mots clés : solaire à concentration , gazéification, réacteur à jet, biomasse, gaz de synthèse, hybridation, oxy-combustion, modélisation multiphysique, extrapolation.

Abstract: The present thesis proposes to study a novel spouted bed solar reactor for biomass thermochemical gasification from laboratory to industrial scale by combining numerical simulations and lab-scale experimentations. A multiphysics numerical model of the reactor was developed using the Fluent© software for the simulation of solar steam gasification of wood particles. The model takes into account the two-phase solid/gas flow using the DPM (Discrete Phase Modelling) approach in interaction with radiation and chemistry. An experimental validation step at 1200°C showed a Cold Gas Efficiencies higher than 1 thanks to the efficient valorization of solar energy and a Carbon Conversion Efficiency approaching 80%. The simulations provided a clear overview on the particles solar conversion within the solar cavity and allowed identifying paths for improving the conversion. The use of inert bed materials as a heat transfer medium inside the cavity appeared judicious. This solution was examined both numerically using a granular Eulerian approach, and experimentally at 1200°C and 1300°C. A maximum relative improvement of the carbon conversion efficiency by 8% was this way achieved. The variability of solar energy is one of the critical obstacles hindering the scale-up of the technology. In order to ensure a continuous syngas production whatever the solar resource, the solar reactor was hybridized thanks to partial feedstock oxy-combustion. The study showed that the injection of a controlled amount of O_2 is a relevant solution to overcome solar energy variability and to control the reactor temperature. A dynamic 0D model was then developed to predict the temperature and syngas production evolution at MW_{th} scale according to two heating modes: solar-only and hybrid solar-combustion. Annual simulations were subsequently performed to predict reactor performance, reactants consumption and gas production volumes. These data were used to analyze the technical and economic feasibility of the process for the industrial production of hydrogen.

Keywords: concentrated solar energy, gasification, spouted bed reactor, biomass, synthesis gas, hybridization, oxy-combustion, multiphysics modelling, scale up.